SIZE EFFECTS IN TIN-BASED LEAD-FREE SOLDER JOINTS: KINETICS OF BOND

FORMATION AND MECHANICAL CHARACTERISTICS

by

OUSAMA MOHAMMED OMER ABDELHADI

LEILA LADANI, COMMITTEE CHAIR
CLARK MIDKIFF
KEVIN CHOU
DANIEL FONSECA
BETH TODD
VIOLA ACOFF

A DISSERTATION

Submitted in partial fulfillment of the requirements
for the degree of Doctor of Philosophy in the
Department of Mechanical Engineering
in the Graduate School of
The University of Alabama

TUSCALOOSA, ALABAMA

2013

Abstract

Continuous miniaturization of microelectronic interconnects demands smaller joints with comparable microstructural and structural sizes. As the size of joints become smaller, the volume of intermetallics (IMCs) becomes comparable with the joint size. As a result, the kinetics of bond formation changes and the types and thicknesses of IMC phases that form within the constrained region of the bond varies. Furthermore, the size of the grains becomes comparable with the size of the bond and the bond may only consist of a few grains resulting in an anisotropic behavior. The effect of size of solder joints on mechanical behavior is not clearly understood and contradicting results have been reported. Studies have shown that some size effects introduced strengthening effects while others have shown weakening effects associated with decreasing joint size. While numerous studies have been dedicated to evaluating elastic and plastic properties of a variety of solder alloys in bulk and large-scale (several 100s of microns) joint configurations, very few studies have been directed to address the elastic and plastic properties of joints in the scale of few microns.

This dissertation focuses on investigating combination effects of process parameters and size on kinetics of bond formation, resulting microstructure and the mechanical properties of joints that are formed under structurally constrained conditions.

An experiment is designed where several process parameters such as time of bonding, temperature, and pressure, and bond thickness as structural characteristic, are varied at multiple levels. The experiment is then implemented on the process. Scanning electron microscope (SEM) is then utilized to determine the bond thickness, IMC phases and their thicknesses, and morphology of the bonds. Electron backscatter diffraction (EBSD) is used to determine the grain size in different regions, including the bulk solder, and different IMC phases. Physics-based analytical models have been developed for growth kinetics of IMC compounds and are verified using the experimental results. Nanoindentation is used to determine the mechanical behavior of IMC phases in joints in different scales. Four-point bending notched multilayer specimen and four-point bending technique were used to determine fracture toughness of the bonds containing IMCs. Analytical modeling of peeling and shear stresses and fracture toughness in tri-layer four-point bend specimen containing intermetallic layer was developed and was verified and validated using finite element simulation and experimental results. The experiment is used in conjunction with the model to calculate and verify the fracture toughness of Cu_6Sn_5 IMC materials.

As expected two different IMC phases, η-phase (Cu_6Sn_5) and ε-phase (Cu_3Sn), were found in almost all the cases regardless of the process parameters and size levels. The physics-based analytical model was successfully able to capture the governing mechanisms of IMC growth: chemical reaction controlled and diffusion-controlled. Examination of microstructures of solder joints of different sizes revealed the size of the solder joint has no effect on the type of IMCs formed during the process. Joint size, however, affected the thickness of IMC layers significantly. IMC layers formed in the solder joints of smaller sizes were found to be thicker

than those in the solder joints of larger sizes. The growth rate constants and activation energies of Cu_3Sn IMC layer were also reported and related to joint thickness. In an effort to optimize the EBSD imaging in the multi-layer configuration, an improved specimen preparation technique and optimum software parameters were determined. Nanoindentation results show that size effects play a major role on the mechanical properties of micro-scale solder joints. Smaller joints show higher Young's modulus, hardness, and yield strength and lower work hardening exponents comparing to thicker joints. To obtain the stress concentration factors in a multilayer specimen with IMC layer as bonding material, a four-point bending notched configuration was used. The analytical solutions developed for peeling and shear stresses in notched structure were used to evaluate the stresses at IMC interface layers. Results were in good agreement with the finite-element simulation. The values of interfacial stresses were utilized in obtaining fracture toughness of the IMC material.

Dedication

This dissertation is dedicated to my:

Parents,

Wife,

Sons,

Extended family members,

Colleagues, and

Friends.

A List of Symbols and Abbreviations

ρ	Density
φ	Content of an element in A_pB_q compound layer in mass fraction
A, B	Arbitrary elements
A_pB_q, A_rB_s	Arbitrary IMC compounds
A_i	Total area of ith IMC layer
M	Molar weight
Q	Activation energy
R	Universal gas constant
S	Surface area of the solid in contact with liquid
T	Absolute temperature
c	Concentration of the dissolved substance in the liquid bulk at time (t)
g	Ratio of molar volumes of A_pB_q and A_rB_s IMCs
k	Growth rate constant
n	Growth time exponent
v	Liquid volume
x	Thickness of A_pB_q IMC compound
y	Thickness of A_rB_s IMC compound
c_s	Solubility limit of solid substance B in liquid A at a given temperature
k_d	Dissolution rate constant

k_i	Growth rate constant of ith IMC layer
l_i	Average thickness of the ith IMC layer
l_j	Half thickness of the original or remaining solder bulk
l_{Sn}	Half thickness of the tin consumed in forming IMC layers
w_i	Total length of the ith IMC layer measured on the micrograph image
dt	Time increment
dx	Change in the thickness of A_pB_q layer
dy	Change in the thickness of A_rB_s layer
$x_{dissolution}$	Thickness of the dissolved part of the solid in contact with liquid
$x_{1/2}, y_{1/2}$	Critical values of thickness for an IMC compound layer
E_i (i = 1,2, a)	Elastic modulus of layer 1, 2 and interfacial layer
G	Total energy release rate
G_I, G_{II}	Mode I and II energy release rates
G_i (i = 1,2, a)	Transverse shear moduli of layer "i"
I_{uc}, I_c	Moments of inertia for un-cracked and cracked beams
I_i (i = 1,2)	Second moment of inertia of layer "i"
K_s	Shear stiffness of the interfacial layer
K_I	Mode I stress intensity factor

K_{II}	Mode II stress intensity factor
L	Beam longitudinal length
$M_T(m)$	Total applied moment
$M_i(x)$	Bending moment acts on layer "i"
N_i ($i = 1,2$)	Longitudinal resultant force for layer "i"
P	Concentrated load
$V_T(x)$	Total transverse shear force
b_i ($i = 1,2, a$)	Width of layer "i"
h_i ($i = 1,2, a$)	Thickness of layer "i"
q	Uniformly distributed load
$u_i(x)$ ($i = 1,2$)	Longitudinal displacement at the base of layer 1 and at the top of layer 2 respectively
v_i ($i = 1,2$)	Transverse shear force in layer "i"
$w_i(x)$ ($i = 1,2$)	Vertical displacements of layer "i"
y_i ($i = 1,2$)	Distances from the bottom of layer 1 and the top of layer 2 to their respective neutral axis
δ_{12}	Normal stiffness of the interfacial layer per unit length
$\varepsilon_1(x), \varepsilon_2(x)$	Strains at the base of layer 1 and the top of layer 2 respectively
$\varepsilon_i^M(x), \varepsilon_i^N(x)$ ($i = 1,2$)	Strains induced by bending moment and by the longitudinal forces at layer "i".

$\tau(x)$	Interfacial shear stress
τ_{xy}	Averaged shear stress
$\sigma_p(x)$	Interfacial peeling stress
σ_{yy}	Averaged Normal stress
ν	Poisson ratio

Acknowledgements

I am pleased to have this opportunity to express wholehearted gratitude to my advisor Dr. Leila Ladani, for her support, guidance, and mentorship throughout this work. Her inspiration and patience through the ups and downs have been greatly appreciated. Sincere appreciation is also sent to members of my advisory committee, in no particular order of preference, including Dr. Clark Midkiff, Dr. Kevin Chou, Dr. Daniel Fonseca, Dr. Beth Todd, and Dr. Viola Acoff for their insightful instruction and precious time in the course of this research.

Special thanks are extended to Mr. Johnny Goodwin, Instrumentation Specialist at CAF center for his assistance, training, and creative discussions about SEM and EBSD techniques.

I would also like to thank friends who are former members of Micromechanics Lab at Utah State University, Mr. James Gyllenskog, Mr. Steven Nelson, Mr. Omar Rodriguez, and Mr. Jordan Bentley. Thank you to the current members of Micromechanics Lab at University of Alabama, Mr. Andrew Magee and Mr. Evan Harvey.

Most of all, my heartfelt thanks go to two most important persons in my life, my mother and my father who brought me up to where I am right now. They taught me the first step in my life, gave me endless love and protection, and encouraged me to move on towards a better tomorrow. I cannot express enough gratitude to my beloved wife who scarified her career, time, and effort for me and my two years-old son, Mohammed.

Contents

List of Tables

List of Figures

Chapter 1 : Introduction

1.1 Overview and Background

Soldering in its general form is a technique that is used to join material parts using low melting-point filler material [1]. Solder material is placed in the joining area and then heated to a point greater than its melting point. The melted solder wets the parts and solidifies after the heating source is removed, joining the parts. Most solder materials are made of two or more elements alloyed together. In this case, solder alloys usually have a melting range instead of a single melting point as seen from Sn-Pb phase diagram in Figure 1-1.
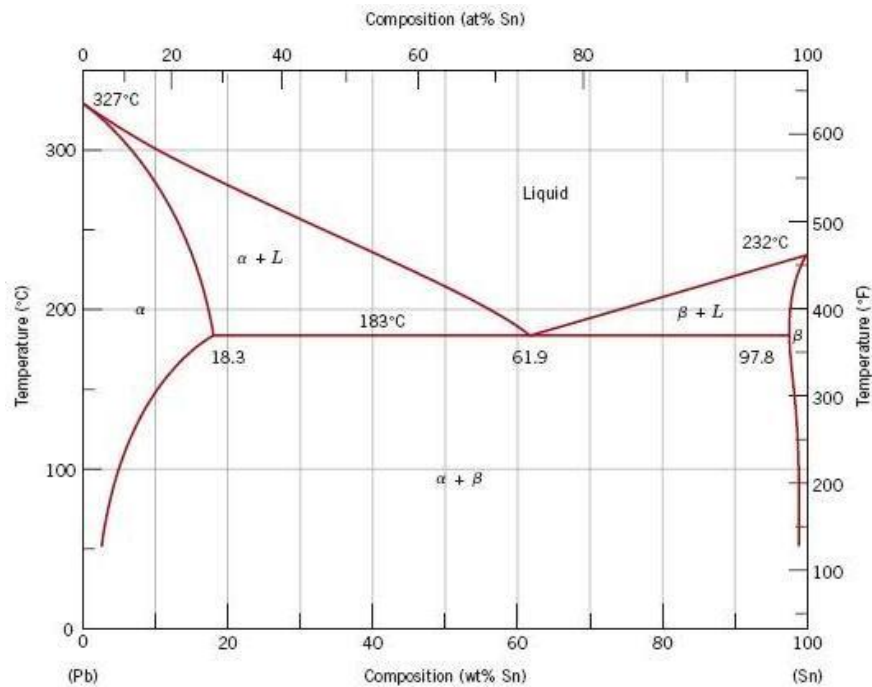
Figure 1-1: Sn-Pb equilibrium phase diagram

The equilibrium phase diagram of any particular soldering system usually shows a clear picture of this melting range which is defined by two lines: the solidus line, which maps the temperatures below which the alloy is a pure solid and the liquidus line, which maps the temperatures above which solder is a pure liquid. Special alloy compositions show a unique melting point and are called eutectic compositions. For Sn-Pb soldering system showing in Figure 1-1, the eutectic composition occurs at 61.9wt.% Sn and at an eutectic temperature of 183°C.

The use of soldering techniques in creating a metallurgical bond between two metallic parts can be dated back thousands of years, though it is difficult to say who first utilized the method. Egyptians applied soldering methods to make their tools, weapons, and gold jewelry as early as 5000 years ago [1]. The Romans and Greeks are known to have introduced tin-lead (Sn-Pb) solder, until recently the most widely used solder alloy [1-2]. Other societies such as the Etruscans, Celts, and Gauls are also known to have used soldering [2]. The main function of these early solder joints was to provide a mechanical connection. With the appearance of microelectronics in the mid-20th century, the new functions of conducting electricity and heat were assigned to the joints. The joints in microelectronics serve to bond two components mechanically, transfer current across the joint, and provide a path to dissipate heat from the packages. The continuing decrease in the size of the packages and the increase in power consumption have introduced new challenges and opportunities in the fields of research and manufacturing of reliable joints.

1.2 Solder Alloys in Electronic Packaging

Solder alloys and soldering processes are used extensively in electronic assembly. Solder alloys must possess a low melting point and provide a unique set of properties to achieve cost-effective

production of reliable electronic assemblies and allow for the joints to perform both mechanical and electrical functions. Traditionally, eutectic or near-eutectic Sn-Pb alloys have been the most widely used solders for electronic packaging. The binary Sn-Pb system offers a variety of technical advantages when compared to other types of soldering alloys. This alloy's relatively low melting temperature of about $183^{\circ}C$, allows the soldering conditions to be compatible with most packaging materials, processing, and technologies. Sn-Pb solder alloy possesses outstanding wetting and spreading capabilities when used on metallic substrates [3]. Joints with satisfactory strength, ductility, stiffness, and fatigue resistance have been built using this solder material [4-8]. Pb can help in reducing the surface tension of pure tin, preventing the transformation of white or β-Sn to gray or α-Sn, and serve as a solvent metal that enables the other joint constituents to form IMCs rapidly [9]. The above mentioned advantages, besides the low cost and availability of lead, account for the large variety of applications of Sn-Pb solders, ranging from personal products to aerospace vehicles and instrumentation.

Sn-Pb solders have been refined by many years of experience. A well-established knowledge base about physical metallurgy, mechanical properties, manufacturing processes, and reliability of this solder type exists. Assembly and soldering equipment infrastructure is almost exclusively engineered with Sn-Pb solder in mind. A good understanding of the Sn-Pb solder behavior has enabled electronic manufacturers to assemble and create small geometry solder joints in high volume and at a competitive cost. Furthermore, joints of Sn-Pb solder alloy have adequate fatigue life and because the alloy has been used in microelectronics for decades, its thermal fatigue behavior is reasonably well understood and both accelerated test data and extensive field data are widely available.

However, due to environmental and toxicological concerns associated with Pb [10], legislations that tax, restrict, or eliminate its use have been enacted. These legislations are one factor that causes the eventual replacement of Pb-based solder alloys to be unavoidable. In Europe and Japan, Pb was banned from electric and electronic equipment as of July 2006 [11-12]. In the USA, although no legislation has been issued to ban Pb usage in electronic products, several environmental agencies have listed Pb among the top chemicals that negatively affect human health [1]. Electronic institutes have drawn a map for lead-free electronic products to encourage industry and academic sectors to develop soldering alloys, processes, techniques, and equipment for the new lead-free generations of electronic devices and products. However, exceptions are made in cases where the substitution of Pb is not possible for scientific or technical reasons or if the environmental and human benefits are outweighed by side effects of substitution [11].

A second factor is the continued trend toward packaging and interconnects miniaturization [13]. It stretches the physical capability of Sn-Pb solder to provide sound and reliable solder joints. Finally, the consumers play an important role in this Pb replacement equation. They prefer "green" products, which give Pb-free electronic devices and products an economical edge over Pb-based ones. All these global legislations and market forces have a fundamental effect on material selection and manufacturing processes in electronic industry.

1.3   Tin-Based Lead-Free Solders

For a smooth transition to Pb-free soldering, several solder alloy systems have been suggested as replacements for Sn-Pb solder alloys [9, 15]. The candidates are evaluated based on a set of criteria that use Sn-Pb eutectic solder alloy as a baseline [9]. Ideally, the proposed Pb-free alloys should fulfill the following major criteria: have a melting point as close to Sn-Pb eutectic as possible, be eutectic or very close to eutectic, have a similar reflow profile during the soldering

4

process, have a sufficient wetting ability to ensure good metallization during the fabrication process of the packages, have the same or exceed the electrical properties of Pb-based solders in order to efficiently transfer the electrical signals, have adequate mechanical properties that show equal or better reliability when compared to Sn-Pb eutectic, and be inexpensive and non-toxic. The development of a good Pb-free solder alloy that displays the desired properties above is not an easy challenge. Until now, no "drop-in" replacement alloys for Sn-Pb eutectic that are suitable for all purposes have been found [16]. Researchers and solder manufacturers started with identifying the element(s) that can replace Pb and produce systems that possess the same properties as Pb-based solder alloys. Based on this approach, a limited number of elements were identified [9]. They are silver (Ag), Cu (Cu), bismuth (Bi), zinc (Zn) and indium (In). Numerous elements with preferred features were eliminated because of either lack of supply (e.g. germanium) or toxicity (e.g. antimony and cadmium) [17, 18]. All of these replacements can be used to construct a Pb-free solder system with Sn as a base element [19]. Sn is preferred over other low melting elements such as In and Bi because of its abundance and low cost with an acceptable melting temperature when it is compared to Pb [9].

The possible alloy systems that can be obtained when elements are combined with Sn will have melting temperatures in the range of 139 ^{o}C to 227 ^{o}C. Candidates such as Sn-Ag, Sn-Cu, Sn-Bi, Sn-Zn, and Sn-In are commonly used as binary solder alloy systems. Alloying elements are sometimes added, to control, modify, or improve some characteristics, creating ternary or even quaternary systems [20]. The binary and ternary alloys based on the Sn-Cu and Sn-Ag alloy systems are leading candidates, in near eutectic and alloyed forms. Others, such as Sn-Bi, Sn-In, and Sn-Zn, show limited uses in electronic packaging due to some drawbacks. Sn-Bi eutectic and Sn-In eutectic have low melting temperatures, 139 ^{o}C and 118 ^{o}C, respectively [21-23]. Due to

their relatively poor high temperature mechanical strength, lack of ductility, and limited availability, these alloys are finding only very limited applications in industry. Sn-Zn and its tertiary alloys with Bi or In have melting points close to the Sn-Pb eutectic alloys [9, 24-25]. Nevertheless, Zn has shown to be prone to oxidation and corrosion in high temperature soldering processes [26] which limits the use of these alloys as a Pb-free solder replacement for volume production. Sn-Cu has been implemented as a low cost product. The primary criteria for this selection were cost and availability in comparison to Sn-Ag alloys [15, 27]. On the other hand, Sn-Cu has been reported to exhibit somewhat inferior mechanical properties and wettability compared to Sn-Ag alloys and its ternary systems [27]. The remaining candidates include the Sn-Ag binary and ternary eutectics of Cu and Bi. The melting point of Sn-Ag is higher than Sn-Pb and therefore tertiary alloys are desirable to obtain a lower melting point [28-29]. Ternary alloys of Cu with Sn-Ag system (Sn-Ag-Cu) have been reported to provide superior performance in the replacement of Sn-Pb systems [29]. Major industrial regions, such as the USA, Europe, Japan, etc. have shown some difference in the preferred Sn-Ag-Cu compositions [15-26].

1.4   Microstructure of Bulk Tin-Based Lead-Free Solder Alloys

It is well known that the mechanical response of a component is strongly linked to its microstructure. Therefore, it is very important to accurately characterize and quantify the microstructural features of tin-based lead-free solders. Much is known about the microstructure of Sn-Pb alloy. Eutectic Sn-Pb, which was the most popular solder until recently, is composed of two phases: lead-rich particulates embedded in a tin-rich matrix [30-31].

However, Pb-free solder alloys possess a microstructure that is very different. Sn-Ag with eutectic composition of 3.5wt.%Ag and a melting temperature at 221 ^{o}C, shows a microstructure

that consists of a β-Sn rich phase and an Ag$_3$Sn IMC upon solidification as seen from Figure 1-2 [32], and confirmed by Sn-Ag phase diagram in Figure 1-3.
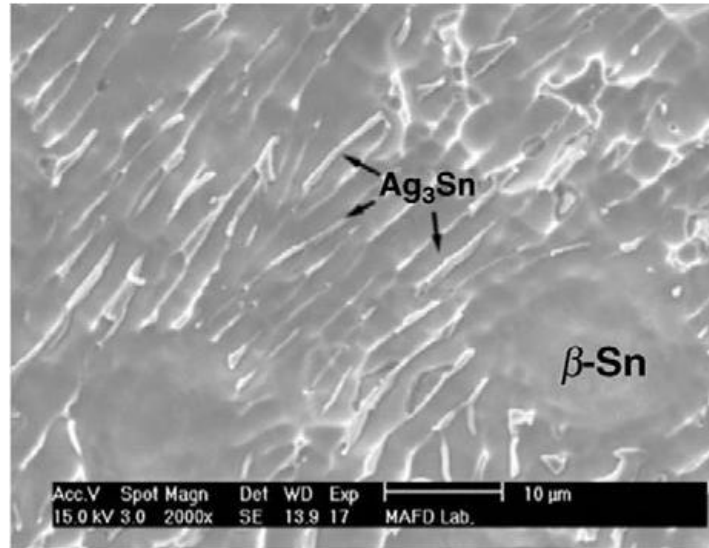
Figure 1-2: SEM image of the microstructure of Sn-3.5wt.% Ag solder alloy [32].
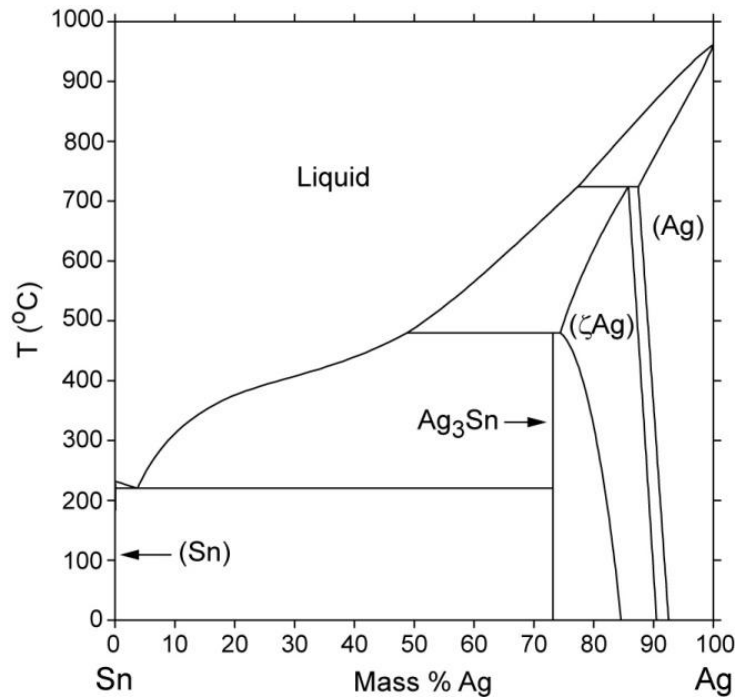
Figure 1-3: Sn-Ag equilibrium phase diagram [1].

Sn-Cu solder alloy also shows two phases when the eutectic composition of Sn-0.7wt.%Cu is solidified from its eutectic melting point 227 ^{o}C. Its microstructure contains Cu_6Sn_5 IMC phase dispersed into a Sn-rich matrix phase as seen in Figure 1-4 [27].
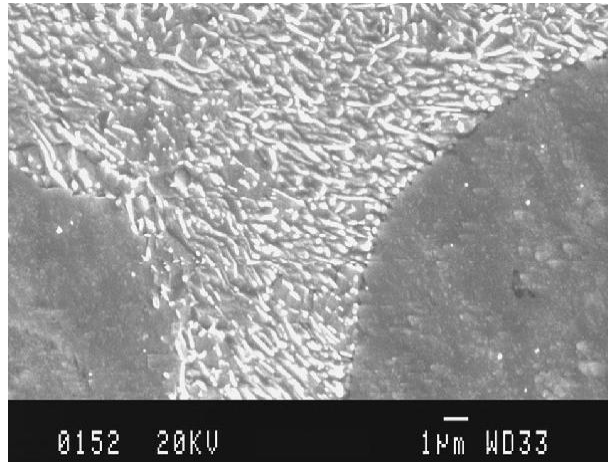
Figure 1-4: SEM image of the microstructure of Sn-0.7wt.% Cu solder alloy [27].

According to the equilibrium phase diagram of Sn-Bi system shown in Figure 1-5, no IMCs are formed when the eutectic composition of Bi-42wt.%Sn is cooled down from the eutectic melting point of 139 ^{o}C to room temperature [33].
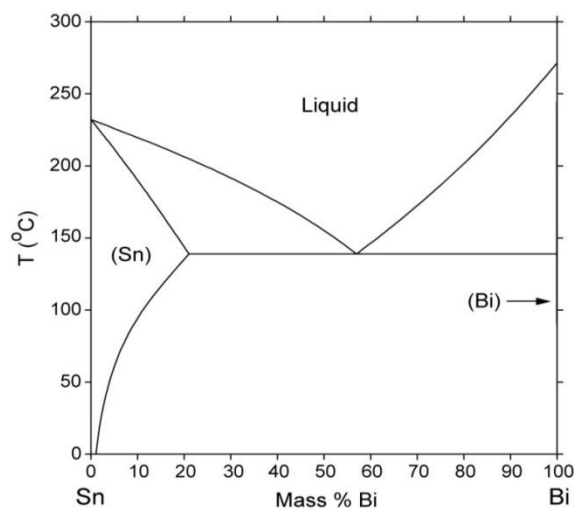
Figure 1-5: Sn-Bi equilibrium phase diagram [1].

Its microstructure, shown by Figure 1-6, is made of two phases, Sn-rich phase with 4wt.%Bi and Bi-rich phase with mostly pure Bi. This is because of the low solubility limit of Sn in Bi in solid solution as shown by Figure 1-5.
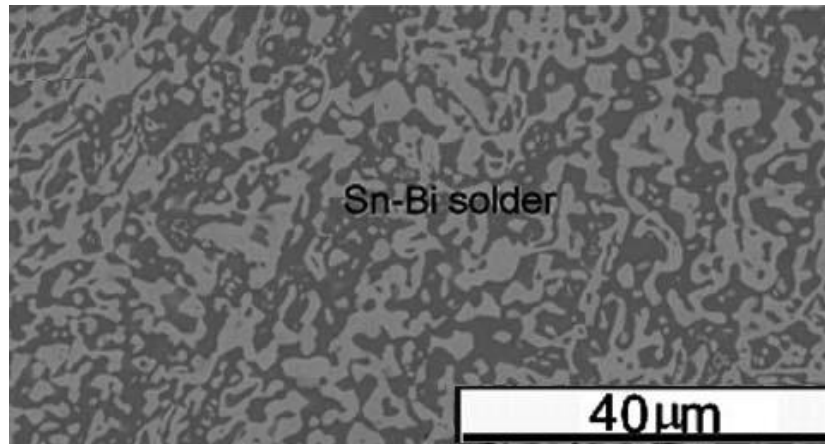
Figure 1-6: SEM image of the microstructure of Bi-42wt.%Sn solder alloy [33].

Eutectic Sn-Zn shows attractive characteristics with a melting temperature at 198 $^{\circ}$C, that is comparable with the melting temperature of Sn-Pb solder alloy (183 $^{\circ}$C). Its eutectic composition occurs at Sn-15wt. %Zn as confirmed by its phase diagram in Figure 1-7. Upon cooling, the microstructure shown in Figure 1-8, consists of a Sn-rich matrix phase and a Zn-rich phase with small amounts of Sn in solid solution [34].

Depending on the substrate material [35-36], both elements can form IMC phases, e.g. when they interact with a Cu substrate. The Sn-In system is also an interesting alternative. Although Sn-In eutectic composition occurs at In-49.1wt.% Sn, In-48wt.% Sn is more commonly used in the electronics industry [22-23]. The microstructure of its eutectic composition with melting temperature of 117 $^{\circ}$C shows two IMC constituents: a β-In rich phase and a γ-Sn rich phase with approximately 45wt. % Sn and 78wt. % Sn solubility limits, respectively.
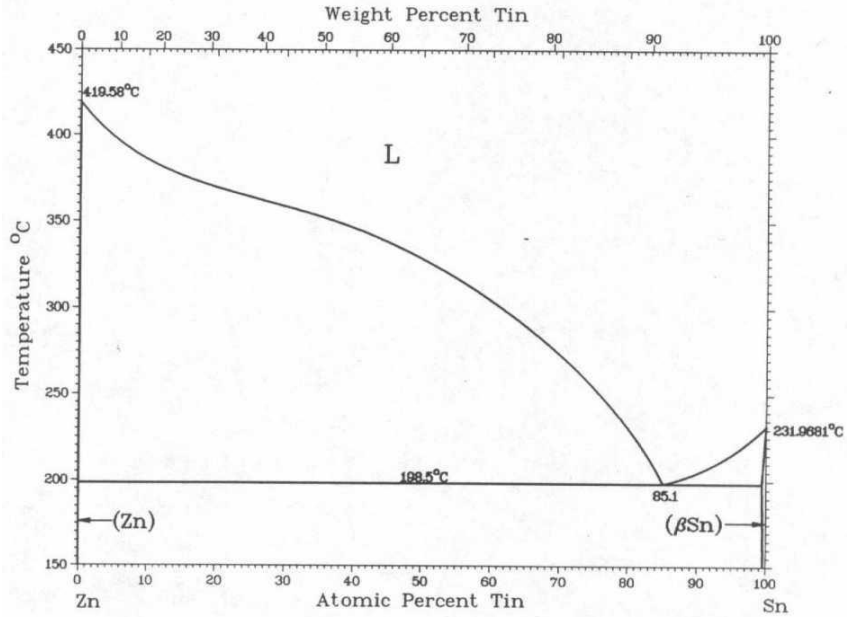
Figure 1-7: Sn-Zn equilibrium phase diagram [1].
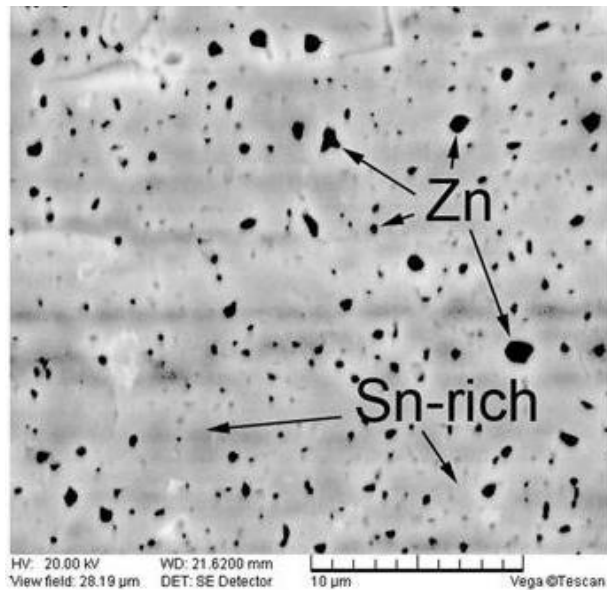
Figure 1-8: SEM image of the microstructure of Sn-9wt.% Zn solder alloy [34]

Using Sn-Ag-Cu solder alloys as an example of a ternary system, the alloy is made of large

amount of tin with relatively small amounts of Ag and Cu [37]. Additives such as Zn and Bi are

sometimes added to control or enhance certain properties [20]. Three possible IMCs could form when Sn-Ag-Cu solder alloy is solidified from its melting temperature. They are embedded into Sn-rich matrix, and their chemical compositions could be extracted from their corresponding equilibrium phase diagrams as seen from Figure 1-3 and Figure 1-9 (a and b) [39], which show Sn-Ag, Sn-Cu, and Cu-Ag systems, respectively. These binary phase diagrams often combined into one ternary phase diagram as shown in Figure 1-10. Ag_3Sn is a result of Sn-Ag reaction, and Cu_3Sn and Cu_6Sn_5 are formed as a result of Cu-Sn reaction. Cu_3Sn requires high amounts of Cu at higher temperature in order to be formed [20]. It should be mentioned here that there is no IMC(s) obtained from Cu-Ag reaction as confirmed by Figure 1-9(b) and Figure 1-10. It is also worth mentioning here that no Sn-Cu MCs will show in the microstructure of Pb-free solder systems that do not contain Cu in their compositions. This means that Cu_6Sn_5 and Cu_3Sn will not form in those bulk systems.
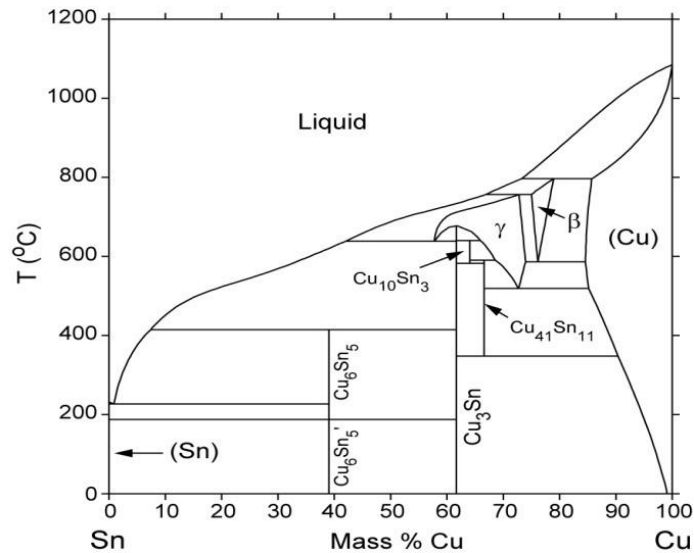
Figure 1-9(a): Equilibrium phase diagram of Sn-Cu system [32].

11
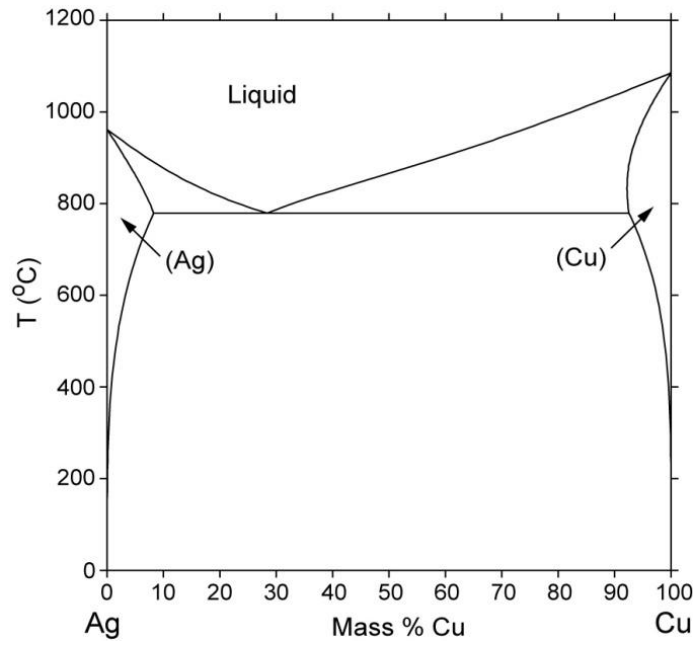
(b)

Figure 1-10(b): Equilibrium phase diagram of Ag-Cu system [32].
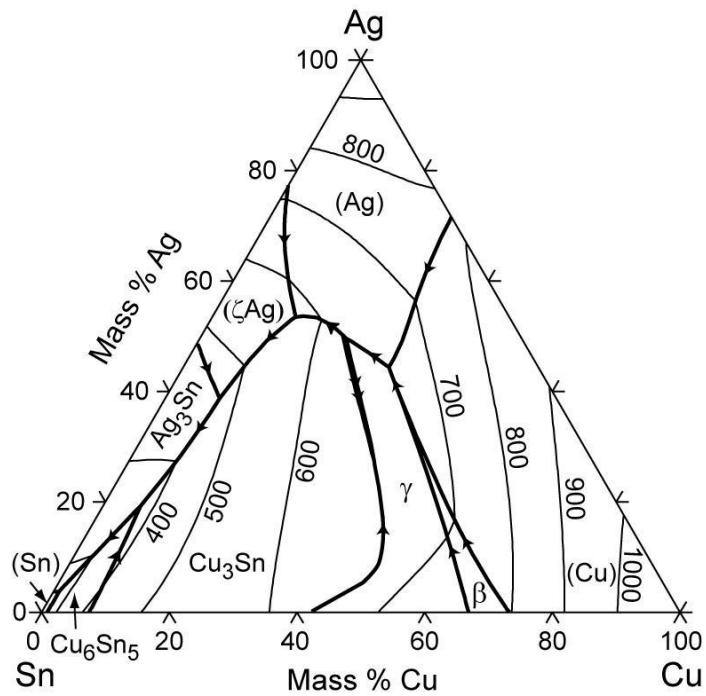
Figure 1-11: Ternary Sn-Ag-Cu phase diagram.

12

1.5   Microstructure of Joint-Configuration Tin-Based Lead-Free Solder Alloys

During the soldering process, molten solder alloy comes into contact and reacts with the substrate material. In most cases, IMCs are formed and are observed at or near the solder/substrate interface as well as in the interior of the solder joints. The composition of the solder alloy and how each of its constituents interacts with the substrate material are the major factors that affect the nature of such compounds. Other factors that may contribute in the nature of this reaction are soldering parameters such as soldering temperature, time, pressure, and cooling rate [40]. These parameters may alter the type and/or the amount of the resulting species in the joint. They may also allow or prevent the formation of certain types of phases. There are a number of substrate materials that are common in electronic packages, such as gold (Au), silver (Ag), palladium (Pd), platinum (Pt), nickel (Ni), and most commonly, copper (Cu).

In Sn-based Pb-free solder alloys the tin is metallurgically active with most metals that are commonly used in electronics packaging and assembly, such as substrate materials. The formation of various IMCs has been explained based upon the equilibrium phase diagram between each of the constituents of solder alloy and the substrate materials. The crystal structure and properties of these IMCs is usually different from those of their elemental components [28-41]. IMCs formed at the solder-substrate interface are needed for successful bond formation. Those IMCs may have morphologies that are different from those formed at the solder joint interior [41]. Sn, Ag, Bi, Zn, and In are the major components of most Sn-based Pb-free solder alloy systems and Cu is the most common substrate material. The following discussion is limited to the study of the microstructure of solder joints when the constituents of solder alloy interact with a Cu substrate and form IMCs.

Sn-Ag/Cu system

As was mentioned earlier, the eutectic composition of the Sn-Ag system shows a microstructure which consists of β-Sn rich and Ag_3Sn IMC phases upon solidification to room temperature, as depicted from Figure 1-3. When this system interacts with a Cu substrate, no Ag-Cu IMCs are formed at the solder-substrate interface, as confirmed by the Ag-Cu phase diagram in Figure 1-9(b). However, Cu-Sn and Sn-Ag IMCs form at the interface due to the chemical reaction between the Cu substrate and Sn and between Ag and Sn, respectively. In addition to the solder-substrate interface, the Sn-Ag IMCs can also form in the interior of the solder. The stable Cu-Sn IMC phases below 300 ^{o}C are Cu_6Sn_5 and Cu_3Sn as shown by the equilibrium phase diagram of Cu-Sn system indicated in Figure 1-9(a). At the eutectic composition, the Cu_6Sn_5 phase is typically formed above the melting point of the solder. However, Cu_3Sn will not form at the eutectic unless a high amount of Cu is available, as in alloys with a large amount of a Cu, e.g. Sn-63%Cu. During fabrication of a solder joint between any Sn-based Pb-free solder alloy and a Cu substrate, a thin layer of Cu_6Sn_5 is found at the solder-Cu interface and a layer of Cu_3Sn is found between Cu and Cu_6Sn_5. Figure 1-11 shows an example of the resulting microstructure in Sn-3.5wt.% Ag/Cu-substrate soldering system [40]. The amount of heat and/or time during the soldering process controls the total volume of secondary Cu-Sn IMC (Cu_3Sn) by allowing specific amounts of Cu to diffuse from the substrate to the melting solder [41]. Aging at low temperatures was also found to activate Cu diffusion and allow for Cu_3Sn to form [31, 44]. In recent years, the nature and growth of interfacial constituents formed at the Sn-Ag/Cu interface have been extensively studied in order to develop an adequate understanding of such phenomena [33-38, 41-48].
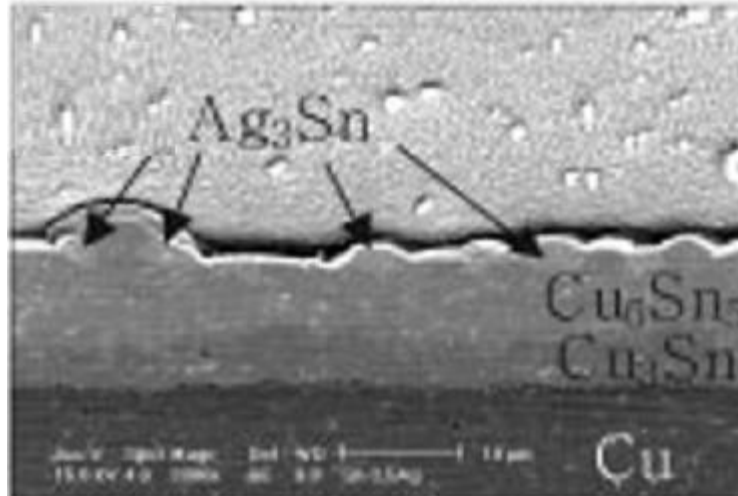
Figure 1-12: SEM image of Sn-3.5wt.% Ag/Cu-substrate solder joint [40].

Sn-Bi/Cu system

There is no formation of IMCs between Bi and Cu or Bi and Sn [39]. When Sn-Bi solder alloy is used to fabricate a joint with a Cu substrate, Cu-Sn IMCs are formed at solder-substrate interface. The nature and growth of such IMCs are very similar to the Sn-Ag/Cu system.

Sn-Zn/Cu system

In addition to the Sn-Cu IMCs such as Cu_6Sn_5 and Cu_3Sn, Sn-Zn IMCs such as CuZn and Cu_5Zn_8 are formed at the solder-Cu interface [35-36].

Sn-In/Cu system

The Cu substrate material can chemically react with both tin and indium. The microstructure that forms in this system has Sn-Cu, Cu-In and Sn-Cu-In IMCs [22].

Sn-Ag-Cu/Cu system

Sn-Ag-Cu/Cu joints show a microstructure that is very similar to its bulk microstructure [48]. In its bulk state, the microstructure of Sn-Ag-Cu consists of a β-Sn matrix in which Sn-Cu IMCs are randomly distributed. In addition, there are layers of Cu_6Sn_5 and/or Cu_3Sn within the bulk solder as well as at the Solder/Cu interface.

1.6 Solid-Liquid Interdiffusion (SoLID) Soldering Process

SoLID process is one of the potential bonding techniques compatible with modern advanced packages such as 3-dimensional integrated circuits (3D-ICs) and wafer-level packaging (WLP). It consists of a layer of low-melting materials which is deposited on top of a high melting substrate layer, respectively. During the bonding process, a pair of doubly deposited materials are placed in contact and heated to a temperature above the melting point of the low-melting material. Upon melting, phase transformation of the liquid component to a higher melting material takes place at the contacting interface. The resulting material, which is IMCs, is required for successful bonding and possesses the desired high temperature and mechanical stabilities. Obtaining a high re-melting point material from low melting temperature bonding is one advantage which increases the significance of SoLID in the electronics industry. Another advantage is that when SoLID is used, undesirable phase transformation and process-induced residual stresses that occur during high-temperature bonding can be avoidable [49]. To implement a SoLID bonding technique and obtain superior joint quality, it is necessary to understand and gain sufficient control of its parameters.

The demand for higher and faster functionality for electronic products has pushed the electronic industry sector towards developing more advanced types of packaging such as WLP and 3D-ICs. Although, these technologies possess several advantages, such as integration of heterogeneous

functions in a single package, utilization of short vertical interconnects, and size miniaturization, moderate and higher temperature gradients and thermal-induced mechanical loads are introduced into the package which could lead to severe reliability issues. The common soft solders cannot be used because of their low thermal stability [38, 45]. New joining methods are needed to produce bonds that withstand such temperatures and loads and to be implemented at low bonding temperature. One way to meet these requirements is by using SoLID method [14].

1.7 Size effects in Soldering and Solder Joints

Miniaturization requires the dimensions of the package components and parts to become smaller and smaller. This is one of the challenges that has brought about increasingly fine pitch interconnects and, accordingly, the size of solder interconnects is being continuously scaled down. It is well known that when one of the component's dimensions approaches a characteristic size of the material's microstructure, mechanical effects occur [50]. Interconnects and some other parts of electronic packages can be considered examples of components that have three small dimensions on the same order of magnitude as the microstructural length scales of their respective materials. Significant changes in the properties and behaviors of such components could take place due to dependence on the scale itself as well as the material's microstructure, and cannot be predicted by macroscopic assessments and evaluations. These effects are commonly called size effects and have been categorized into four areas [50-63]: microstructural effects, gradient effects, surface/interfacial effects, and grain statistics effects.

Microstructural Effects

Microstructural effects are one of the earliest reported effects in which the dimensions of phases and particles in the microstructure play a role in defining the overall performance of a material

17

under consideration. Microstructural effects directly influence the overall behavior of a material which depends on the detailed underlying microstructure, e.g. grain size, distribution, and orientation of each phase and particle in the microstructure. For a given application, material scientists and engineers have used this type of size effect as a tool to improve or fine-tune the desired properties [52]. A variety of models have been proposed to incorporate the microstructural effects [64-67]. In the Hall-Petch model, the material is strengthened by grain refinement to a specific extent. After this point the model breaks down and the strengthening effect is reversed upon further grain refinement. Another model is the Orowan model [68], which incorporates the effect of hard obstacles embedded inside the material's microstructure in terminating the dislocation motion. A third model, the Friedal model [69], applies a precipitation-based strengthening approach on hindering the motion of dislocations and dislocation loops.

Gradient Effects

It is one of the widely discussed size effects, which explains the strengthening behavior observed in many metals at small length scales [53, 70]. While keeping all geometrical proportions identical, downscaling a component will naturally results in an increase of the gradients of the strain. The increase in strain gradients has to be accommodated geometrically in the lattice by curvature, which is intrinsically limited through the lattice structure. Therefore, the only physical manner to accommodate the curvature is by the introduction of extra dislocations in the lattice [53]. The extra dislocations usually denoted as geometrically necessary dislocations (GNDs). Since more stresses are needed to introduce GNDs into the lattice structure which is seen as a strengthening effects.

Surface/Interfacial Constraint Effects

Surface/interfacial effects occur when carriers of plastic deformation and an external boundary or interfacial surface of another material having physical interact. For instance, the formation of a strong or weak boundary layer or interface at a surface of a particular material may facilitate or block dislocation motion during plastic deformation. This size effect has been implemented in many applications where the component's mechanical response was enhanced by obstructing plastic slip using an oxide layer, hard coating, etc. The nature of the physical boundary and the material of interest defines whether the resistance of the component to the applied load and then to the plastic flow is increased or decreased [53, 56, 71]. Small interconnects, thin films, foils, and multi-layered structures are all relatively close to a physical boundary or interface surface. This material behavior with respect to its boundaries motivates surface/interfacial effects which therefore induce a dimensional constraint. It can be expected that in small structures, the dimensional constraint will control the mechanical properties, response, and deformation mechanisms of the components [53].

Grain Statistics Effects

Grain statistics effects are frequently observed in polycrystalline materials upon decreasing dimensions of a structure. For small geometrical dimensions, the number of grains in one of the spatial direction may become small. Therefore, the overall mechanical behavior of the structure becomes dependent on the detailed underlying microstructure such as size, distribution, and orientation of the individual grains. This geometrical constraints-microstructure features interaction is very common in structures with dimensions close to the characteristic microstructural length scale. In general, a lack of statistical microstructural averaging induces a

19

weaker response in metallic foils and ultra-fine sheets. Investigations [58, 70, 72, and 73] have revealed that the yield and hardening properties diminished upon decreasing thickness.

1.7.1 Size Effects on Interfacial Reaction during SOLID Soldering Process.

SoLID bonding for electronic packaging and interconnects was investigated by many researchers as early as mid-1960s [74, 75]. Bernstein et al. demonstrated the feasibility of using SoLID bonding at low-temperature processing conditions to produce high-temperature bonds which can be used in semiconductor and non-semiconductor brazing and bonding applications. The effect of process parameters such as temperature and time were addressed on specimens with dimensions on the order of inches. Since then, other studies exploring the use of SoLID bonding to join base materials such as Ag, Au, Cu, Ni, Pd, etc. have been conducted [76-82]. SoLID joints generally consist of IMC phases, such as Cu_6Sn_5 and Cu_3Sn in Sn-based solder-Cu substrate systems [83]. Despite the fact that IMCs are brittle in nature, SoLID joints are not necessarily less reliable than conventional Sn-based solder joints. This is because the IMCs have a much higher strength [84] and creep resistance than the conventional Sn-based solder alloys. Roman et al [43] investigated SoLID bonding of Ag, Au, and Cu base materials using a variety of commercial solder alloys. Bonds as strong as, or stronger than, the ones obtained by conventional soldering techniques were formed. However, little or no information was available on diffusion rates, IMC formation, and structure. Li et al [83, 85] have investigated the kinetics of the interfacial reaction in a variety of SoLID bonding material-substrate systems at different bonding temperatures and times. Specimens made of 25 μm thick pure Sn foil and 0.1 mm thick pure Cu and Ag foils with other dimensions of 12x10mm were used in their study. Microstructure, evolution, and kinetics of IMCs formed in Ag-Sn-Ag and Cu-Sn-Cu systems were characterized. It was found that microstructural features and growth kinetics of IMCs are

significantly different from those formed in conventional Sn-based solder alloys- Cu substrate systems.

A number of studies have been carried out on SoLID bonding processes to address the effect of process parameters on the reliability and integrity of the solder joints. Ladani et al [86, 87] implemented a full factorial experiment on the SoLID fabrication process to investigate the effect of process parameters such as time, temperature, and pressure on the bond strength and microstructure of Sn-3.5Ag solder bonds. Temperature has been shown to be the most influential factor on the bond strength. Higher strengths are obtained at a fabrication temperature of about 40 ^{o}C higher than the melting point of the low-melting material. The study also showed that IMC formation requires a sufficient Cu concentration, which is achieved through increasing bonding time. IMC growth was also studied through application of a 1-D analytical model. It was found that for complete transformation to IMC, 17 and 28 minute bonding times are sufficient for 20 µm and 240 µm thick-joints, respectively. Bartels et al [76] investigated IMC phase formation in Sn-SoLID. Microstructural and mechanical characterizations of IMC bonds were performed. At longer times and higher temperatures, the IMC formation rate increased. Continuous miniaturization of solder joints in high-density packaging highlights the importance of studying how the joint size affects the joint microstructure and thereby the mechanical behavior and reliability. Sharif et al. and Islam et al. [88, 89] have conducted an investigation to compare the interfacial reaction between under bump metallization (Cu-UBM) material and molten eutectic Sn-Pb and Sn-3.5Ag-0.5Cu solder alloys having different volumes for a range of temperatures and bonding times. It was found that higher solder volumes show a much higher Cu consumption with a higher rate during the initial reflow stage. Smaller solder volumes show a thicker layer of IMC due to the high diffusivity of Cu in molten solder and the higher probability

21

of IMC formation on the existing IMC at the interface. Huang et al. [90, 91] conducted a study on the effect of solder bump geometry on the microstructure of Sn-3.5Ag, Sn-3.8Ag-0.7Cu, and pure Sn/Cu joints fabricated at 240 ^{o}C with different bonding times. It was suggested that solder bump geometry can influence the dissolution kinetics of pad material into the molten solder and, therefore, affecting the resulting microstructure within the bond.

Despite the extensive literature which addresses the kinetics of SoLID bonding processes used to join a variety of solder alloy-substrate material systems, there is limited focus on the effect of bond size and geometry on growth kinetics and the morphology of the interfacial IMCs presented in very small SoLID Pb-free solder interconnects. To date, there have been no studies released which elucidate the effect of joint size on the kinetics of the interfacial reaction in the Sn-based Pb-free solder/Cu systems during SoLID soldering. More studies should be conducted to characterize the microstructure morphology and evolution of IMC during SoLID soldering, derive the kinetic constants of IMCs, and investigate diffusion and growth mechanisms of Cu and IMCs during IMC formation and thickening.

1.7.2   Size Effects on Microstructure of Solder Joints

The combination of the phases present in a material, and their defects, morphology and distribution usually define the microstructure of that material. The material properties and response are ultimately a function of composition of the material, microstructure as well as the thermal, mechanical and chemical histories.

In electronic assembly, one of the processing variables that affect the initial microstructure of the solder is the cooling rate. For eutectic alloys, two phases; Ag_3Sn IMC and Sn-rich, usually solidify at a single temperature and the resulting microstructure is usually lamellar which may be altered to be equiaxed by cooling the solder very quickly as seen from Figure 1-12 [92, 93]. A

22

faster cooling rate produces a finer microstructure since the time is less for diffusion to take place.
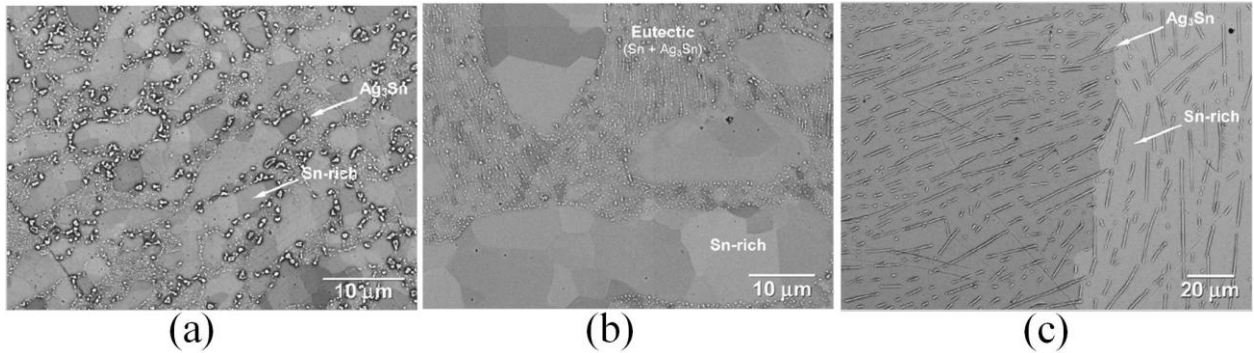
Figure 1-13: SEM images of the effect of cooling rate on the microstructure of Sn-3.5wt.% Ag solder. (a) 24°C/s (water cooling), (b) 0.5°C/c (air cooling), and (c) 0.08 $^{\circ}$C/s (furnace cooling) [92].

For off-eutectic and ternary solder alloys, the resulting phases are more complex due to the difference in the range of solidification and the increasing number of involved elements. Cooling rate can also be controlled by reducing the amount of molten material [94, 95]. Less time is needed for a small volume to cool down due to changes in heat conduction, radiation, and convection rates with volume reduction. Small volumes also amplify the effect of other factors such as defects, voids, and grain [96].

Other factors which may introduce some variation in the initial solder microstructure are solder composition, solder-substrate interaction, and the shape of the joints which can be reflected in their thicknesses. When the characteristic size of the solder joints is decreased, the global mechanical behavior of the solder materials could be changed. This alteration in solder joint response is attributed to the effect of microstructure change that is introduced due to different phenomena. One important phenomenon is the change in the interaction between the solder and the substrate materials at small size joints. This phenomenon is responsible for the IMC formation at the interface. Small gaps between the two soldering species affect the diffusion

process which controls the bond-formation mechanisms [83, 86]. For example, the rate of diffusion of substrate element is higher in which there is a good chance to reach the solder and form IMC. This change of diffusion rate alters the weight percentage of the formed IMC amount in the bond at the expense or diminishing the bulk solder alloy in the joint [83, 97]. It can be expected that at small joint thicknesses, all bulk solder material will be transformed into IMCs [98], and the joint behavior will be controlled by IMC properties and microstructure since they are totally different from solder alloy.

During the last two decades, several investigations characterizing the microstructure of Sn-based Pb-free solder joints have been carried out both experimentally and theoretically.

Wu et al. [97] studied the effect of joint thickness on microstructure and tensile properties of Sn9Zn/Cu joint system. A couple of observations were made. One is that as the joint thickness decreases, a rapid decrease of Zn content in the bulk solder takes place. This is attributed to the metallurgical reaction during reflow process which consumes the Zn to form Cu-Zn IMCs. This significantly changed the solder composition from its eutectic composition to hypoeutectic. Another observation is that the Cu content, which diffuses from the substrate into molten solder, will experience a rapid increase within the bulk solder as the joint thickness decreases, which consequently results in increasing the amount of IMC. Since the Cu/solder interface area is the same in all joints regardless of joint size, the amount of IMCs will be the same in all joints and causes increasing in the IMC volume fraction upon decreasing the joint thickness. All these changes in the phase fractions and element contents in solder joint introduce variations in joint behavior under loading conditions.

Wiese et al. [99, 100] analyzed the microstructure of SnAgCu and Sn-3.5Ag solder systems. It was found that in bulk Sn-Ag-Cu solder specimens the microstructure consists of β-Sn dendrites

surrounded by quasi-eutectic phase. Solder joint specimens exhibit a columnar structure [99]. This difference in microstructure appearance was related to the elemental content in the solder alloy and the nucleation process during solidification. Varying the content of soldering elements could affect the production process of dendritic or columnar microstructures. In bulk solder, rapid crystal growth starts from the center region which was distinguished by a small area with many randomly oriented grains surrounded by large grains. In small joints, the nucleation starts at the solder/substrate interface and proceeds from one side to the other, producing the columnar structure. Furthermore, the solidification process takes less time which causes the microstructure to consist of a large number of small randomly oriented grains. An increase in the number of grain boundaries is expected compared to bulk solder and will be responsible for any possible variation in mechanical response. Zimprich et al. [101, 102] compared the microstructure of solder joints of different sizes. Larger joints showed coarser microstructures compared to small ones. This change was responsible for the pronounced increase in yield and ultimate tensile strengths of their specimen mentioned in the next section.

Huang et al. [94], Kinyanjui et al. [95], and Cho et al. [103], demonstrated the dependency of the solidification process on specimen size and under bump metallurgies (UBM) of Pb-free solder alloys. Decreasing specimen size resulted in rapid solidification of molten alloys because of the under-cooling phenomenon which describes the solidification stage at a temperature that is lower than the equilibrium melting temperature of the alloy system. In their studies, it was found that the degree of under-cooling increases linearly with the decrease of specimen size. This relationship was attributed to the reduction of nucleation probability when specimen size is reduced. It was also found that the UBM plays a role in these studies. The comparison between different UMBs revealed that the degree of under-cooling varies from one UBM to another. In

general, a significant reduction of under-cooling was observed when solders were placed on Cu, Ni and Ag substrates compared to the same solders placed on non-wetted and non-reactive substrate material (e.g. Al). Wetting ability and reactivity between solder alloys and UBM materials introduce variations in nucleation behavior as well. Whether the solder system shows a low or high degree of under-cooling will have direct influence on the resulting microstructure of solder joints as well as their mechanical properties.

Castro et al. [104] observed a substantial change in the morphology of three systems of Sn-Pb solder alloys: hypoeutectic, eutectic, and hypereutectic compositions. There was a critical degree of under-cooling at which a transition from lamellar eutectic to anomalous eutectic occurred in the Sn-Pb system. The former morphology is a result of rapid solidification while the latter one forms due to slow solidification conditions. Yang et al. [105] addressed the effect of joint size on Sn grain features of Pb-free solder alloy such as number of grains across joint thickness, grain orientation, and distribution. These features are critical parameters in determining the thermo-mechanical response of solder joints. It was found that the number of grains is independent of joint size, aging time, and reflows. Generally, the Sn grains show highly preferred misorientation angles. However, Cong et al. [106] arrived to an opposite conclusion in which the number of Sn grains diminished as the joint size decreases.

1.7.3 Size Effects on Mechanical Properties of Solder Joints

The mechanical properties of a material determine the limit of applications in which that material can be effectively used. A material could show different properties in different applications depending on the type and range of loading, shape and size of the component in which the material was used, and heat treatment. The first parameter which can introduce significant changes in material properties is the microstructure as was explained in the previous section. A

26

component material could possess a microstructure that shows different phases with different distribution and grain sizes due to cooling rate, component geometry, and compositions. Investigations on the effect of specimen size on the mechanical properties of solder materials have been done by many researchers [96, 101-102, 107-110]. Bonda et al. [107-108] have shown that bulk data can be used only if the joint size is larger than a certain representative volume. When structure has a volume below this critical size, non-homogeneous deformation and strain localization begin to appear and cause deviation of local strains from applied ones. Gugnoni et al. [96] conducted experimental and numerical studies on the influence of geometrical (plastic) constrains and size effects on the elasto-plastic response of lead-free solder joints. It was explained in this study that when solder gap relative to other dimensions is decreased, triaxial stress field will develop within the solder volume. This triaxiality of stress field can completely modify the overall load-displacement response of the solder joint comparing to bulk/case solder specimen, due to the introduction of a significant apparent hardening. This apparent hardening is usually called constraining effect and strongly depends on the geometry of the solder joint. The experimental results revealed that the stress-strain response of thinner joints shows a much higher ultimate stress as well as a reduced ultimate strain compared with thicker joints and bulk solder specimens. This was due to the possible constraining (plastic constraints) and size effects. Zimprich et al. [101, 102] have conducted tensile and shear tests of solder joints to investigate the occurrence of size effects on mechanical properties. Solder joints of rectangular shape with gap sizes in the range of 25-850 μm were tested. Results showed that as the gap size decreases, a strong increase in ultimate tensile strength and yield strength of tensile samples and shear strength of shear samples was observed and attributed to the Orowan effect. Ranieri et al. [109] investigated the tensile properties of geometrically constrained high aspect ratio Sn-40Pb solder

joints with thicknesses ranging between 0.001-0.006 inches. The plastic constraint, introduced by substrates on the solder material used in joining, was shown to severely change solder joint average tensile strengths which increased by a factor of six compared to the same solder when used in bulk form. Thus the data extracted from bulk samples are not reliable if extremely small solder volumes are considered.

An experimental study performed by Yin et al. [110] showed that an increase of ultimate tensile strength is not always encountered with decreasing thickness-to-diameter ratio shown in Figure 1-13. The ultimate tensile strength of the solder joint increases with decreases in thickness at constant diameter and it nicely follows the Orowan approximation. However, a decrease in ultimate tensile strength was observed when the diameter was decreased at constant thickness. This introduced an inverse size effect. A joint volume effect model, instead, was developed which describes the dependency of a joint's strength on joint volume as displayed Figure 1-14. The figure clearly shows the improvement of ultimate tensile strength with decreasing joint volume in two different solder alloys; Sn-3.0Ag-0.5Cu and Sn-37Pb.

Limeng et al. [111] were able to numerically evaluate fracture properties of solder joints of different sizes under tensile loading conditions. A similar trend to the thickness-to-diameter ratio effect, as elsewhere [110], was observed. The trend showed that the stress intensity factor was decreasing with decreasing thickness at constant diameter and the opposite behavior when diameter is decreased at constant thickness.
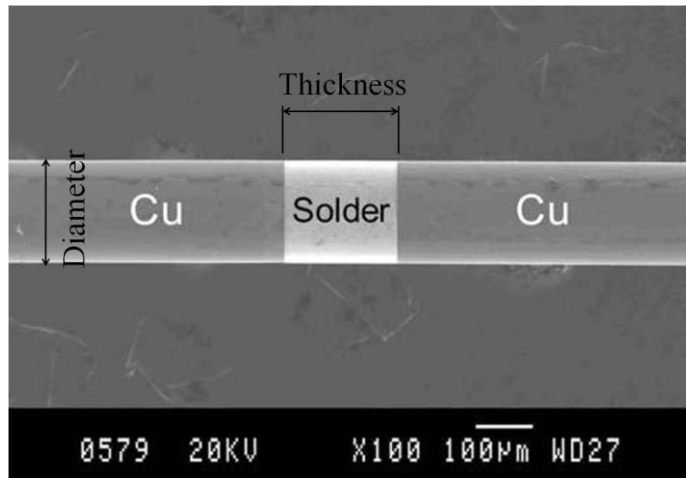
Figure 1-13: SEM images of detailed geometry of Cu/solder/Cu sandwich-structured solder joints [110].
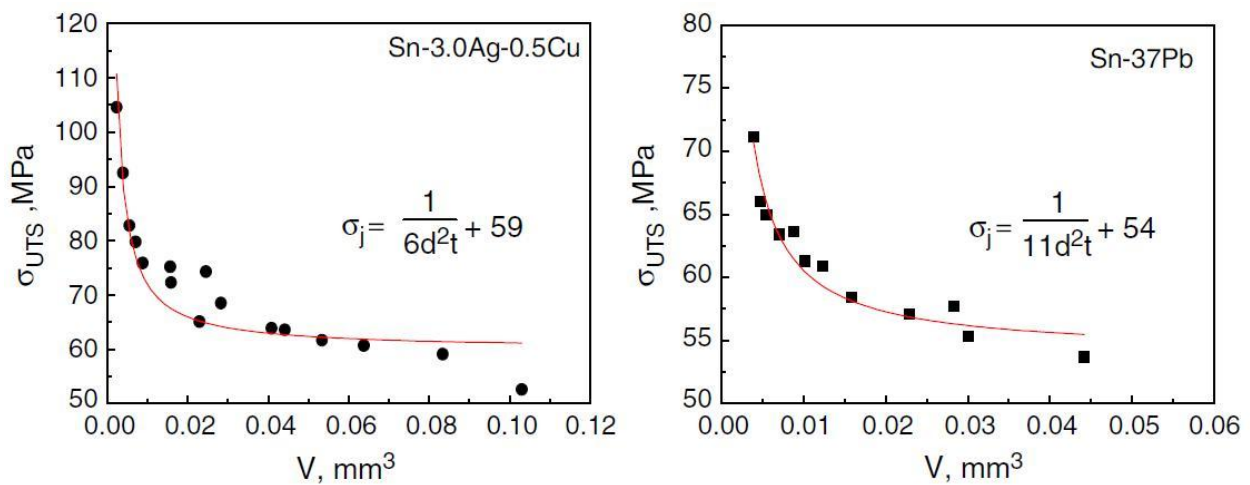
Figure 1-14: Ultimate tensile strength versus solder joint volume for different solder alloys [110].

Ongoing efforts in the electronics industry aim to reduce the size of the components to meet the requirements of modern electronic packaging. The integrity and reliability of interconnects plays a significant role in attaining this goal. These factors are highly affected by the mechanical properties of the interconnect materials. Material data obtained from bulk test specimens are often utilized in many activities such as material selection and design processes, evaluation of the mechanical response, and reliability estimation of joints that are very different in size and

29

shape. Previous studies have shown that the bulk data can be successfully used only if the size of the solder joint is greater than a certain representative volume, which is the smallest volume over which the average deformation of entire substance is still shown [107, 108]. Below this volume, the performance of the joint is strongly dependent on its size. Therefore, the effect of joint size, which at small dimensions could dramatically vary the mechanical properties and performance of solder joints, has to be taken into account when investigations are conducted addressing a reliability or integrity issues.

In most cases, solder joints are made into a thin layer or a small ball of soldering alloy, with a typical size on the order of microns. Testing material properties and mechanical response at such length scales is not an easy task as it requires unique instrumentation and sample preparation [12-14]. Sn-based Pb-free solders have been considered promising alternatives because of their superior resistance to creep and thermal fatigue [112, 113]. During device operation, the mismatch of coefficients of thermal expansion of the different materials in the package causes creep and thermo-mechanical fatigue damage in the joints which could result in premature failure. The mechanical properties as well as fatigue and creep behaviors of the solder joints are significantly influenced by joint size and geometry as well as processing parameters. Thus, an understanding of the relationships between processing parameters and microstructure evolution, mechanical and creep properties, and fatigue life under different loading conditions at small sizes is extremely important. This can help in demonstrating field response and deformation and fracture mechanisms associated with solder interconnects.

1.8 Interfacial Stresses and Fracture Toughness of IMC Material

During the electronic packaging, components are usually stacked in multi-layer structure fashions in which different interconnection methods may be used such as solid SoLID, thermo-

compression bonds, adhesive bonds, soldering, etc. The ability to control and predict the failure

mechanisms in electronic devices is of practical importance. Therefore, the sustainability of the

interconnections to different mechanical and thermo-mechanical stresses in both during

manufacturing and operation is a critical factor to be monitored. It is well known that one of the

major failure causes is the brittle fracture associated with IMC materials formed in most joints

such as solder joints [114, 115]. To quantify the fracture in such brittle materials, theories of

fracture mechanics have developed which give a systematic approach of calculating fracture

toughness based on the type of loading. Failure in electronic devices could be due to stresses

developed by mechanical loading, thermal mismatch, or a combination of both. These stresses

could result in different fracture modes such as tension (mode I), shear (mode II), out-of-plane

shear (mode III), or mixed-mode conditions [116]. Therefore, different experimental techniques

are available to determine the bond strength and fracture characteristics of IMC bonds. In

particular, four-point bend test, Chevron test, and double-cantilever beam test are commonly

used in measuring strength and fracture toughness of interfacial bonds when mixed-mode

loading conditions are under consideration [117, 118]. It is a testing technique that is based on

accounting for the interfacial stresses at the interfaces of IMC bonds during the measurement of

strength and fracture toughness.

In conventional four-point bend test, the fracture toughness of bond material is determined based

on the knowledge of the bending moment. There is no need to address the stresses at the crack

tip or at the interfaces for the bond material. However, understanding the stresses developed at

the interface, and relating these stresses to fracture toughness is scientifically significant. Closed-

form solutions of interfacial stresses such as shear and peeling stresses due to thermal loading

[119- 128] and due to mechanical loading [129-133] have been obtained based on either strength

of materials, theory of elasticity, or classical beam theory. Despite the extensive use of four-point bending test specimens for quantifying bond strength and fracture toughness, no analytical solution is available to determine the interfacial stresses at the interface bond.

1.9 Problem Statement

With miniaturization of modern electronic products and devices, the interconnect density in electronic components and packages has significantly increased resulting in interconnects and joints on the scale of a few microns. The requirements of high integrity and reliability have demanded superior mechanical properties in interconnect materials such as solder alloys. However, the need for miniaturization leads to fundamental changes in the microstructure of solder joints as well as on the resulting mechanical behavior under service conditions. One microstructural change is that the IMC fraction, which is required for successful bond formation, increases as joint size decreases up to a point where the joint completely transforms into IMCs [15], as shown in Figure 1-15. The large reduction in the typical volume of interconnects leads to a situation where the characteristic size of solder joints is comparable to the characteristic size of its microstructure. In this case, the mechanical properties of the solder joint may change significantly due to the scale effects discussed in this chapter. Previous studies of the effect of joint size on mechanical behavior showed contradicting results [97, 134]. It is well known that the properties of solder joints are very different from those of bulk solders. Therefore, properties of bulk solder should not be used for joint design, solder selection, and reliability estimation of electronic packages. To successfully estimate the reliability of solder joints, accurate mechanical properties are needed. To obtain this data, test specimens have to be scaled down to the typical joint sizes used in modern electronic products. Proper mechanical and microstructural characterization tools have to be implemented, rather than the ones used for large structures.
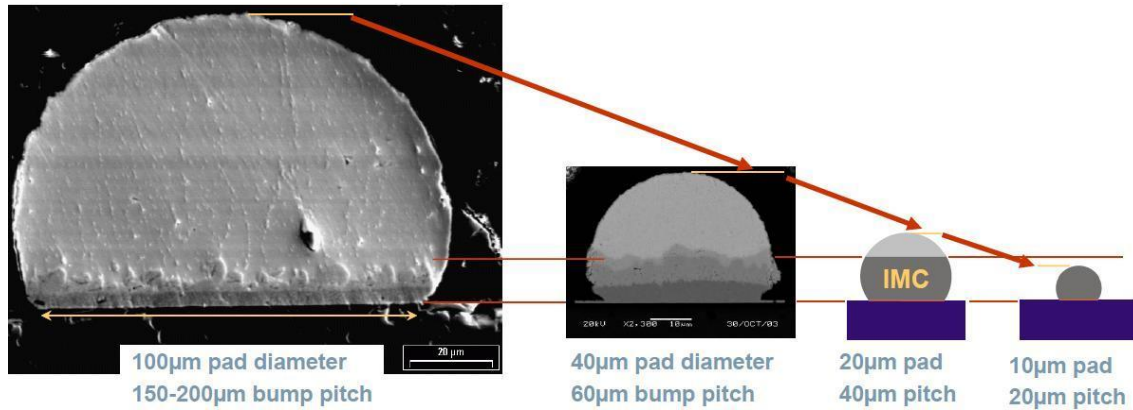
Figure 1-15: The change of IMC fraction as the size of solder joint decreases [1].

Soldering involves a chemical reaction that takes place between molten solder and a substrate. The substrate material dissolves into the molten solder at the contact interface and IMC layers are formed which serve as bonding material for the solder joint. The formation, growth, morphology, and thickness of IMC layers are critical issues for the mechanical properties of solder joints and therefore the integrity of the entire electronic packages [4], particularly when solder joints are very small. Some studies have suggested that solder joint size and geometry could influence the kinetics of the interfacial reaction [23]. Having a better understanding of the effects of solder joint size on the interfacial reactions during SoLID soldering is important. Limited studies on the effect of size and geometry of solder joints on interfacial reaction during conventional soldering were conducted [86, 87]. Other studies, which investigated the kinetics of interfacial reaction during SoLID soldering, were reported [9-11]. Others experimentally and theoretically investigated the effect of process parameters on the mechanical strength and microstructure of SoLID solder joints [9-13]. To date, no data have been reported for the size effects on the interfacial reactions during SoLID soldering.

Despite the brittle nature of IMC compounds which dominate SoLID joints, these joints do not have to be less reliable when compared with conventional solder joints formed using, for

example, reflow or wave soldering methods. Studies have reported different mechanical behaviors of solder joints at small scale [97, 111, 134-136]. Wu et al. [97] reported a weakening effect as joint size decreased while others [111, 134-136] reported a strengthening effect with decrease in joint size. In all of those studies, solder joints were fabricated using conventional techniques and at relatively large sizes compared to the joint sizes common in nowadays electronics. Fundamental investigations of the mechanical properties of SoLID solder joints are needed for reliability and theoretical modeling studies.

1.10 Objectives

Based on the statements above, several critical problems in the area of Sn-based Pb-free solder alloys remain to be solved. Thus, the objectives of this research work are:

1- Investigate size effects on the microstructure of micro-scale Sn-3.5Ag/Cu-substrate joints, interfacial reaction, and resulting phases and morphologies.

2- Understand the growth kinetics of IMC formed in micro-scale Sn-3.5Ag/Cu-substrate soldering joints and determine possible size effects on the kinetics constants, activation energies, and growth mechanisms associated with each IMC layer.

3- Determine any possible size effects on the mechanical properties of different materials in micro-scale Sn-3.5Ag/Cu-substrate soldering joints.

4- Evaluate local mechanical properties of joints consisting of a few grains nanoindentation.

5- Evaluate mechanical properties of single grain IMCs and compare across different grain orientation.

6- Evaluate the fracture toughness of interfacial IMC bond through experiment and modeling

1.11 Dissertation Organization

This is an article-based dissertation. Each chapter presents an article that has been either

published or under review at this time. Chapter 2 presents an experimental characterization of

microstructure and IMCs- growth kinetics in Sn-3.5Ag/Cu-substrate solder joints. The growth

kinetics of IMCs was further investigated analytically using a physics-based analytical model to

determine the governing mechanisms of IMC formation and growth.

In Chapter 3, the size effects on the interfacial reaction in Sn-3.5Ag/Cu-substrate solder joints

are characterized and discussed. An experiment was designed in which three solder joint

thicknesses were fabricated. SEM and energy-dispersive x-ray spectroscopy (EDX) were utilized

in observing IMC morphology, measuring the growth, and identifying IMCs and eutectics.

For further microstructural and mechanical characterization of solder joints, Chapter 4 is devoted

to developing and optimizing the surface preparation procedure that could be used in preparing

solder joints for EBSD analysis. It describes the outline of the polishing steps that should reveal

the best flat, distortion-free surfaces. In addition, an effort has been made to define and optimize

the EBSD processing parameters, in particular the step size and the minimum number of detected

bands, that have the most effect on the reliability of EBSD analysis of solder joints.

Chapter 5 presents an experimental study that has been conducted to evaluate the mechanical

properties of Sn-3.5Ag/Cu-substrate solder joints locally. In particular, the elastic and plastic

properties of IMCs, eutectic solder, and Cu materials have been obtained through

nanoindentation testing. Size effects on mechanical properties of solder joints have also been

addressed in this chapter. The indentation is used to extract properties of single grain Cu6Sn5

IMC layer and compare them in grains with different orientation.

Chapter 6 is dedicated in obtaining stresses in IMC layer in multilayer configuration where IMC layers act as joining material for two other materials. Analytical models are developed to obtain the shear and normal stresses and to use these stresses to determine the fracture toughness of Cu6Sn5 IMC material, using four-point bending method. Results are verified using finite-element simulations and experiments.

The last chapter, Chapter 7, summarizes the primary results, conclusions, and contributions obtained of this study as well as the recommendations for future directions of this research.

Chapter 2 : IMC Growth of Sn-3.5Ag/Cu-Substrate Soldering System: Combined Chemical Reaction and Diffusion Mechanisms

Abstract

The growth kinetics of intermetallic (IMC) compound layers formed between Sn-3.5Ag solders and Cu substrate in soldering process are investigated experimentally and analytically. In order to determine the governing mechanisms of IMC formation, an experiment is designed in which samples are fabricated with bonding temperature varied at three levels of 260, 310 and $360^{o}C$ while time is varied at seven levels between 1 to 240 min. Microstructural analysis is conducted to analyze the IMC thickness and morphology. A physics-based analytical model (Dybkov), in which net growth of each IMC phase is modeled as result of diffusion and partial chemical reaction, is modified for a case of liquid-solid state for two IMC layers. Dissolution of solid IMCs into liquid solder is included in the model. The model is then used to evaluate governing mechanisms of IMC formation and growth and determine the activation energies for formation and growth of different IMC compounds. The chemical reaction and diffusion rate constants have also been evaluated for different intermetallic compounds of Sn-3.5Ag/-Cu-substrate soldering system. Two intermetallic phases were observed during soldering at the interface: η-phase (Cu_6Sn_5) and ε-phase (Cu_3Sn) IMC layers. The thickness of the η and ε IMC phases increase with increasing the soldering time and/or soldering temperature. The increase in the IMC layer thickness during the process is found to obey a linear relationship with time during the chemical reaction-controlled stage of formation of Cu_3Sn IMC layer and it obeys a parabolic

relationship with time during the diffusion-controlled growth stage of formation of both IMC layers. It was shown that as temperature increases, the chemical reaction and diffusion rate constants monotonically increase. Modeling results indicate clear distinction of governing mechanisms of growth at different IMC growth stages with chemical reaction-controlled growth at initial stage and diffusion-controlled growth at final stage of IMC formation. The apparent activation energy calculated for the chemical reaction-controlled growth stage is 20.59 (kJ/mol) for ε IMC phase. For diffusion-controlled growth stage, the activation energy values obtained are 41.98 (kJ/mol) for η IMC phase and 50.10 (kJ/mol) for ε IMC phase. These values slightly differ from values reported in literature where a simple power-law fit is used to extract those quantities. This is expected because unlike present study, the power-law fit does not explicitly incorporate the interaction between the chemical reaction and diffusion mechanisms in IMC growth. The values obtained in the current study are still within the range of the values found in the literature.

Key words: Sn-3.5Ag solders, intermetallic growth, chemical reaction and diffusion kinetics, activation energy.

2.1 Introduction

Solder alloys and soldering processes are used extensively in electronic assemblies. Traditionally, eutectic or near-eutectic Sn-Pb alloys have been the most widely used solders for electronic packaging [1-2]. They offer a variety of technical advantages such as low melting point, outstanding wetting and spreading capabilities, competitive cost, satisfactory strength, ductility, and fatigue resistance [3-9]. Nevertheless, there are legal and technological factors that press for alternative soldering materials and processing approaches. Among these factors are legislations that tax, restrict, or eliminate the use of lead due to the environmental and toxicological concerns associated with the material [10]. Furthermore, continuous

miniaturization of interconnects results in reliability issues [9, 11]. Another factor is the need for stacked soldering of complex assemblies that require different types of solders with different melting temperatures [12].

For a smooth transition to Pb-free soldering, several solder alloy systems have been suggested as replacements for Sn-Pb solder alloys [9, 13]. Candidates such as Sn-Ag, Sn-Cu, Sn-Bi, Sn-Zn, and Sn-In are commonly used as binary solder alloy systems. Alloying elements are sometimes added, to control, modify, or improve characteristics such as melting temperature, microstructure, homogeneity, response to stresses, dissolution rate of base materials, and wettability properties, thus creating ternary or even quaternary systems [1, 14]. The binary and ternary alloys based on the Sn-Cu and Sn-Ag alloy systems are leading candidates, in near eutectic and alloyed forms.

Solder joints play an important role in electronic products by serving as electrical, mechanical, and in some cases thermal connections between components and the board or substrate. With miniaturization of electronics and as the interconnect density increases and more complex geometries are used, reliability issues become even more critical. One of the most critical factors known to affect the reliability of solder joints is the formation of intermetallic (IMCs) compounds between the solder alloys and base materials during the soldering process.

It is well known that the presence of the IMCs between solder alloys and the substrate is an indication and essential requirement of good metallurgical bonding. The mechanical and physical properties of IMCs may substantially differ from those of the solder and substrate. An excessive IMC layer could degrade the reliability of the solder joints due to the inherent brittle nature of IMCs and their tendency to generate structural defects such as Kirkendall voids associated with Cu_3Sn formation, irregular phase formation, and weak interfaces [15-17]. Moreover, continuous

formation of the IMC layers during service operation would also consume the thin film under bump metallization [15] which could exacerbate the long-term reliability of the solder joints. Therefore, knowledge of the solder-substrate chemical reaction and IMC growth in the solder interconnects is extremely important for understanding reliability of the solder interconnects and for the optimization of the soldering processes.

The formation and the growth of IMCs in various solder material systems have been widely investigated over the years [16-32]. Most experimental investigations assume a power law fit for IMC growth [14-15]. In solid-solid interaction, the kinetics of IMC growth usually follows this assumption and it was found that IMC thickness is proportional to the square root of soldering time [16-25]. Similar time dependence is also recognized in literature for liquid-solid interaction with various time exponents [26-28]. Although most of the existing literature has concentrated on this technique, the power law model is not a physics-based model and cannot explain the complicated physics involved in the process of IMC formation and growth [15] such as diffusion mechanisms, and chemical reactions. Such information is important specially when IMC growth is controlled and/or monitored.

Other studies modeled IMC growth using Fick's diffusion law [29-33]. This law relates the mass flux and concentration gradient of the diffusing species through the theory of diffusion. It is assumed that there is instantaneous occurrence of mass flux and chemical reaction. However, a phase lag may exist between the interdiffusion of two dissimilar materials and the chemical reaction at the interface, which is accounted for in Fick-based approach [29]. The diffusion-based approach eliminates some of the weaknesses associated with power law fit. However, it raises some other issues. For example, it is impossible to find a closed-form solution for the developed differential equations describing the thickness growth of IMC layer. Therefore, the

40

solution has been sought through numerical methods [34]. Another issue is the difficulty in interpreting the results obtained by this model due to the assumptions associated with applying the numerical solution [29-30]. Often, the model is simplified to a one dimensional problem which fails to capture the complex physics of the IMC formation. Therefore, more advanced models have to be developed to overcome the drawbacks of available techniques [15, 29].

In this article, a different model, which was developed by Dybkov [35-43] for solid-solid interaction condition, is modified for a case of two different IMC compounds and solid-liquid interaction of IMC with liquid solder to evaluate the kinetics constants of IMC growth. It relies on the assumption that the growth of any IMC layer at the interface between two materials A and B at a given temperature is a result of counter-diffusion of components A and B across its bulk followed by partial chemical reactions between diffusing atoms of one component and surface atoms of another component [35-43]. This model is able to reveal the role of diffusion and chemical reactions in determining the IMC layer growth kinetics. It is chosen in this work because it could be modified to mimic the growth kinetics of one or more layers of IMCs [35-36]. Moreover, it allows for the two sequential growth steps, diffusion and then chemical reaction, to be represented in separate terms, which allows for the possibility of evaluating the diffusion and chemical rate constants separately. It also allows for the effect of the dissolution process to be incorporated in the model, specially, in early IMC formation. In this analysis the model is modified to include the dissolution effect.

2.2 Modeling IMCs Growth

In this study, Dybkov's model is implemented. The model has been used to study the growth kinetics of one and two compound layers in solid state conditions. It has also been used in studying the liquid-solid growth state of one compound layer in which the effect of dissolution is taken into account [35-37]. In our case the model is used to investigate growth kinetics of two

compound layers during liquid-solid reactions such as Cu-Sn reaction which is very popular in soldering industry.

During the soldering process, metallurgical reaction between the liquid solder and substrate material forms a layer of IMC at the solder/substrate interface. The layer growth is due to a continuous alteration of two consecutive steps: diffusion of atoms and subsequent partial chemical reaction. Partial chemical reactions are the reactions that take place at the layer interfaces with the participation of diffusing atoms of one of the components and the surface atoms of another component. In case of the Sn-based solder alloys with the Cu substrate, typically two layers of IMC compounds form. One phase is η- phase (Cu_6Sn_5) which forms first at the interface adjacent to solder followed by ε-phase (Cu_3Sn) which forms adjacent to Cu substrate if higher soldering temperature and/or longer soldering time are applied. A general formulation that can be applied for other similar systems is developed. The reacting elements are denoted by A for the liquid element and B for the solid element. The schematic diagram in Figure 2-1 shows the elements' regions and IMC regions in between these two elements. The growth regions at the interfaces are shown between 1 and 1', 2 and 2', 2 and 2'', and 3 and 3'. The IMC layers thickness are shown by x and y for A_pB_q and A_rB_s IMC compounds accordingly. These two IMC regions are indicated between 1' and 2', and 2'' and 3'.
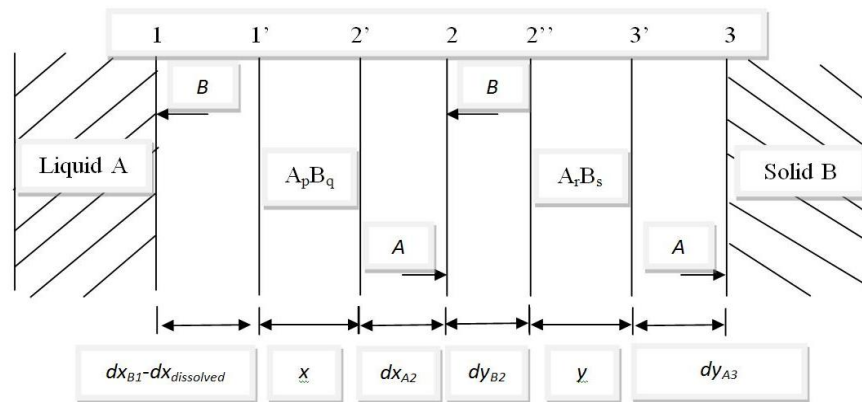
Figure 2-1: Schematic diagram to illustrate the growth of the A_pB_q and A_rB_s compounds between

liquid A and solid B substances.

The A_pB_q represents Cu_6Sn_5 and A_rB_s represents Cu_3Sn compounds in Cu-Sn system. These

layers grow due to four chemical reactions within the interface regions as follows:

Layer formed Interface   Partial chemical reaction

$\quad\quad A_pB_q$ 1-1' $qB + pA = A_pB_q$ (2-1a)

$\quad\quad\quad\quad$ 2'-2 $(sp - qr) A + q\ A_rB_s = sA_pB_q$ (2-1b)

$\quad\quad A_rB_s$ 2-2'' $(sp - qr) B + r\ A_pB_q = pA_rB_s$ (2-1c)

$\quad\quad\quad\quad$ 3'-3 $rA + sB = A_rB_s$ (2-1d)

Reaction (2-1a) governs the formation of the first IMC (A_pB_q) layer at the liquid interface and

also its growth from the original thickness (x) by the amount (dx_{B1}). The numeric subscript, 1,

shows the interface at which the reaction occurs and the alphabetic subscript, B, indicates that it

occurs due to diffusion of element B. This basic notation will be used throughout this discussion.

At interface 2, each IMC layer transforms to the other IMC layer according to reactions (2-1b)

and (2-1c). Reaction (2-1b) governs the formation of the first IMC layer by consuming the

second IMC layer. It causes the thickness (x) of A_pB_q IMC layer to increase by (dx_{A2}).

Simultaneously, the first IMC layer is also consumed to form the second IMC layer (A_rB_s). This

is governed by reaction (2-1c) in which the layer thickness (y) increases by the amount (dy_{B2}). At

the solid interface (interface 3), the second IMC layer forms and grows by a reaction that is

governed by Eq. (2-1d). It causes the thickness (y) of the second IMC layer to increase by the amount (dy_{A3}).

In each partial chemical reaction of Eq. (2-1), two steps have to take place. One is the diffusion of atoms, and the second is the subsequent chemical reaction. Therefore, the time (dt) required for increasing the thickness of any IMC layer, e.g. by amount dx, is the sum of the time of diffusion of the atoms of one of the components, through its bulk or other IMC layer, to the reaction site (dt_{dif}) and the time of their subsequent chemical reaction with the surface atoms (dt_{chem}). Therefore, following equations corresponding to Eq. (2-1) can be written:

$$dt = dt_{dif}^{B \to A_p B_q} + dt_{chem}^{B \to A_p B_q} \qquad (2\text{-}2a)$$

$$dt = dt_{dif}^{A \to A_p B_q} + dt_{chem}^{A \to A_p B_q} \qquad (2\text{-}2b)$$

$$dt = dt_{dif}^{B \to A_r B_s} + dt_{chem}^{B \to A_r B_s} \qquad (2\text{-}2c)$$

$$dt = dt_{dif}^{A \to A_r B_s} + dt_{chem}^{A \to A_r B_s} \qquad (2\text{-}2d)$$

It was assumed that the time of diffusion of atoms (dt_{dif}) is directly proportional to both the change in the thickness of a layer and its existing total thickness [36]. Furthermore, it was assumed that the time of chemical reaction (dt_{chem}) is directly proportional to the change in the layer thickness and independent of its current thickness [36]. These assumptions were used earlier by Dybkov [36] and found to be valid assumptions. Implementation of the assumptions in the following equations:

$$dt = \left(\frac{x}{k_{1B1}} + \frac{1}{k_{0B1}}\right) dx_{B1} \qquad (2\text{-}3a)$$

$$dt = \left(\frac{x}{k'_{1A2}} + \frac{1}{k'_{0A2}}\right) dx_{A2} \tag{2-3b}$$

$$dt = \left(\frac{y}{k'_{1B2}} + \frac{1}{k'_{0B2}}\right) dy_{B2} \tag{2-3c}$$

$$dt = \left(\frac{y}{k_{1A3}} + \frac{1}{k_{0A3}}\right) dy_{A3} \tag{2-3d}$$

The first term in these expressions is the contribution of diffusion while the second term indicates the contribution of chemical reaction. k in these equations denotes the rate constant. The first subscript, 1 or 0, indicates diffusion or chemical reaction respectively, the second subscript, A or B, indicates the diffusing elements, and the third subscript, 1, 2, or 3, shows the interface at which the reaction occurs. k' is also a converted form of the rate constant for the chemical reactions of Eq. (2-1b) or (2-1c) taking into account the amount of atoms required by the chemical reaction. It is given as follows [35-36]:

$$k'_{1A2} = \frac{sp}{sp - qr} k_{1A2} \tag{2-4}$$

During the time (dt), the thicknesses of A_pB_q and A_rB_s layers will respectively increase by

$$dx_+ = dx_{B1} + dx_{A2} \tag{2-5a}$$

$$dy_+ = dy_{B2} + dy_{A3} \tag{2-5b}$$

However, the thickness of the A_pB_q layer decreases by dx_- due to reaction (2-1c) and the thickness of A_pB_q layer decreases by (dy_-) due to reaction (2-1b) as follows:

$$dx_- = \frac{rg}{p} dy_{B2} \tag{2-6a}$$

$$dy_- = \frac{q}{sg} dx_{A2} \tag{2-6b}$$

where g is the ratio of the A_pB_q and A_rB_s molar volumes. The overall change in thickness of the layers during a time period of (dt) is obtained by combining Eq. (2-5a) and (2-6a) for layer A_pB_q and Eq. (2-5b) and (2-6b) for A_rB_s layer.

$$dx = dx_{B1} + dx_{A2} - dx_-$$ (7a)

$$dy = dy_{B2} + dy_{A3} - dy_-$$ (7b)

Substituting Eq. (2-3) and (2-6) into Eq. (2-7), one can obtain the required system of equations that describes the growth rates in the thickness of IMC layers [37]:

$$\frac{dx}{dt} = \frac{k_{0B_1}}{1+\frac{k_{0B_1}x}{k_{1B_1}}} + \frac{k'_{0A_2}}{1+\frac{k'_{0A_2}x}{k'_{1A_2}}} - \frac{rg}{p}\frac{k'_{0B_2}}{1+\frac{k'_{0B_2}y}{k'_{1B_2}}}$$ (2-8a)

$$\frac{dy}{dt} = \frac{k'_{0B_2}}{1+\frac{k'_{0B_2}y}{k'_{1B_2}}} + \frac{k_{0A_3}}{1+\frac{k_{0A_3}y}{k_{1A_3}}} - \frac{q}{sg}\frac{k'_{0A_2}}{1+\frac{k'_{0A_2}x}{k'_{1A_2}}}$$ (2-8b)

The first two terms in these equations represent the rates of growth of an appropriate compound layer at its two interfaces, while the third term reflects the rate of consumption of this layer in the process of formation of an adjacent compound layer.

2.3 The Effect of Layer Dissolution

The melting points of the components of a reaction couple are usually different. Therefore, there is a certain range of temperatures in which one of the components is in the solid state while the other is in the liquid state. If soluble, the solid substance dissolves into the liquid phase. In such a case, the dissolution process affects the growth kinetics of the compound layer(s) at the solid-liquid interface [38-41].

In the case of the under saturated solder melt, the dissolution of the layer formed between liquid A and solid B occurs simultaneously with its growth. The overall change in thickness of the layer

is therefore the difference between the rate of growth of the layer and the rate of its dissolution [36]. The rate of dissolution is described by the following equation [44-45]:

$$\frac{dc}{dt} = k_d \frac{S}{v} (c_s - c) \qquad (2\text{-}9a)$$

or

$$c = c_s \left[1 - \exp\left(-\frac{Sk_d}{v} t \right) \right] \qquad (2\text{-}9b)$$

where c is the concentration of the dissolved substance in the bulk of the liquid at time t, c_s is the solubility of solid element in liquid element at a given temperature, k_d is the dissolution rate constant, S is the surface area of the solid in contact with the liquid, and v is the volume of the liquid.

Equation (2-9) describes the dissolution process in terms of the concentration of the solid element, B, in liquid element, A. To describe the dissolution process in terms of a variation of a linear dimension of a solid specimen (in this case thickness), one needs to use the following equation [36]:

$$c = \frac{\rho_B S x_{dissolution}}{v} \qquad (2\text{-}10)$$

where ρ_B is the density of the solid substance B and $x_{dissolution}$ is the thickness of the dissolved part of the solid. Substitution of Eq. (2-10) into Eq. (2-9) yields the following expression: [16, 36]

$$\frac{dx_{dissolution}}{dt} = \frac{c_s k_d}{\rho_B} \exp\left(-k_d \frac{St}{v} \right) \qquad (2\text{-}11)$$

Integrating Eq. 11 gives the following expression:

$$x_{dissolution} = \frac{c_g v}{\rho_B S}\left[1 - \exp\left(-\frac{k_d St}{v}\right)\right] \qquad (2\text{-}12)$$

If the compound A_pB_q is dissolving in the liquid A, then Eq. (2-11) and Eq. (2-12) are modified to take the following forms [36]:

$$\frac{dx_{dissolution}}{dt} = \frac{c_g k_d}{\rho_{A_pB_q}\varphi}\exp(-at) \qquad (2\text{-}13)$$

$$x_{dissolution} = b_o[1 - \exp(-at)] \qquad (2\text{-}14)$$

where, $b_o = \frac{c_g v}{\rho_{A_pB_q}\varphi S}$, $a = k_d S/v$, and φ is the mass fraction of element B in A_pB_q compound.

Plugging Eq. (2-13) into Eq. (2-8a) reveals the system of mathematical differential equations that describes the growth kinetics of two compounds under conditions of simultaneous dissolution in liquid phase, A, as follows:

$$\frac{dx}{dt} = \frac{k_{oB_1}}{1+\frac{k_{oB_1}x}{k_{1B_1}}} + \frac{k'_{oA_2}}{1+\frac{k'_{oA_2}x}{k'_{1A_2}}} - \frac{rg}{p}\frac{k'_{oB_2}}{1+\frac{k'_{oB_2}y}{k'_{1B_2}}} - \frac{c_g k_d}{\rho_{A_pB_q}\varphi}\exp(-at) \qquad (2\text{-}15)$$

$$\frac{dy}{dt} = \frac{k'_{oB_2}}{1+\frac{k'_{oB_2}y}{k'_{1B_2}}} + \frac{k_{oA_3}}{1+\frac{k_{oA_3}y}{k_{1A_3}}} - \frac{q}{sg}\frac{k'_{oA_2}}{1+\frac{k'_{oA_2}x}{k'_{1A_2}}} \qquad (2\text{-}16)$$

where the initial condition is:

$$x = y = 0 \qquad \text{at} \quad t = 0 \qquad (2\text{-}17)$$

The solution should take into account the critical values of the thickness for the A_pB_q and A_rB_s compound layers [35]. The critical thickness is the thickness of each layer at which the diffusion time equals the time of chemical reaction [35]. Based on this assumption, Eq. (2-3) could be used to extract the critical values of layer thicknesses as follows:

$$x_{1/2}^{(B)} = \frac{k_{1B_1}}{k_{0B_1}} \qquad (2\text{-}18a)$$

$$x_{1/2}^{(A)} = \frac{k'_{1A_2}}{k'_{0A_2}} \qquad (2\text{-}18b)$$

$$y_{1/2}^{(B)} = \frac{k'_{0B_2}}{k'_{1B_2}} \qquad (2\text{-}18c)$$

$$y_{1/2}^{(A)} = \frac{k_{1A_3}}{k_{0A_3}} \qquad (2\text{-}18d)$$

The subscript (1/2) indicates that half of the differential time is spent on transporting the atoms (e.g. atoms B or A) to the reaction site, and the other half is spent on further chemical reaction. The superscript letter indicates the element that is being transported to the reaction site. Using these critical values of thickness, the growth mechanism could be chemical-reaction controlled if thicknesses are smaller than the critical thickness values or diffusion-controlled if the thicknesses are greater than the critical values of thickness. The model developed here is utilized to analyze the data of an experiment conducted on Sn-3.5Ag/Cu solder system.

2.4 Experimental Procedure

2.4.1 Specimen Fabrication
This process involved three steps: design of experiment, specimen design, and bond fabrication. The soldering technique selected for use in this study was reflow soldering. An experiment was

designed in which the process time and temperature were varied in multiple levels. Table 2-1

summarizes the process parameters and their levels. The lowest soldering time that has been used

during joint fabrication at lower temperatures is 2 minutes. This was because poor joints were

formed at lower times.

Table 2-1: Process parameters and their levels used during the fabrication process of specimens.

Run	T,(^{o}C)	Time, (min)	Run	T,(^{o}C)	Time,(min)	Run	T,(^{o}C)	Time,(min)
1		2	8		2	15		1
2		5	9		5	16		2
3		10	10		10	17		5
4	260	15	11	310	15	18	360	15
5		20	12		20	19		20
6		90	13		90	20		90
7		240	14		240	21		240

As identified in many studies, most solder joints, and in particular the Sn-3.5Ag/Cu system

considered in this study, have two distinctive microstructural features. The first is a eutectic

structure consisting of IMC particles such as Ag_3Sn or Cu_6Sn_5 embedded in beta-tin phase. The

second is Cu-Sn IMC layer which consists of Cu_6Sn_5 layer at the solder/Cu interface. Under

particular conditions, Cu_3Sn could co-exist at Cu_6Sn_5-Cu interface. For this purpose and to

fabricate solder bonds containing all possible microstructure features, the process time and

temperature were varied over a wide range.

A simple specimen was designed (Figure 2-2) where two layers of Cu substrates were soldered

together with Sn-3.5Ag solder alloy.
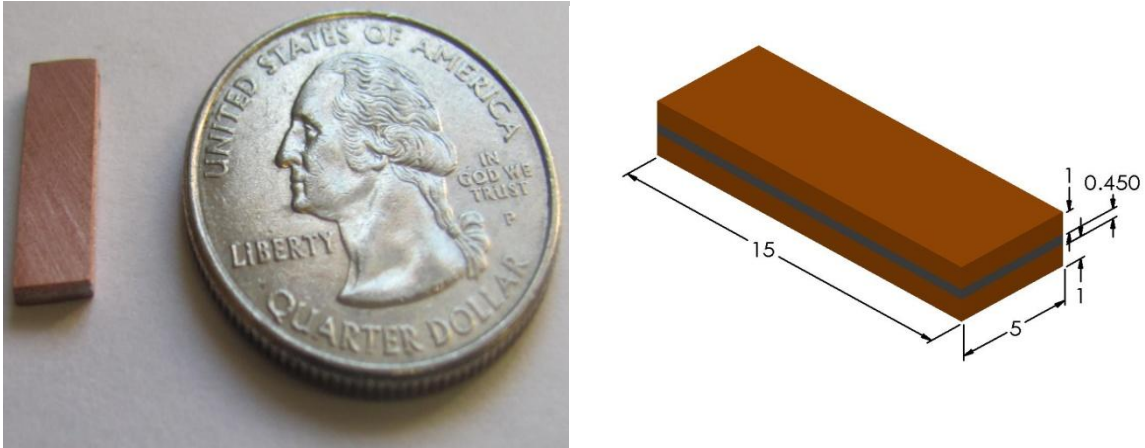
Figure 2-2: (a) Actual specimen design and (b) Drawing of specimen used in the current study. Bottom and top layers are Cu substrates; the sandwiched (grey) layer is Sn-3.5Ag solder joint. Dimensions are in mms.

The amount of solder alloy was adjusted to produce specimens having joints of about 450 μm in thickness. Four bonds were fabricated for each experimental run which gives 84 specimens for 21 runs in total. To fabricate the bonds, the Cu substrates were first prepared. This involved polishing the Cu surfaces up to 1200 grit SiC using standard methods followed by cleaning with isopropyl alcohol. Solder paste was then deposited on the cleaned surface. An activation agent was used to activate the chemical reaction during the soldering process. The two Cu surfaces were then placed in intimate contact in a thermal chamber. Temperature and time were varied based on the design of experiment. After the prescribed amount of time the specimens were cooled to room temperature in air and the bonds were visually inspected to eliminate severely damaged ones.

2.4.2 Microstructure Characterization and Thickness Measurements of IMCs

After the samples were fabricated, regular mounting and polishing procedures were used to prepare metallographic cross-sections for characterization of the interfacial microstructures. A JEOL JSM 7000F scanning electron microscope (SEM) using a backscatter electron signal was employed to view the polished samples and observe and analyze their microstructural features.

51

The IMC formed between the bulk solder and the Cu substrates was identified using an energy-dispersive X-ray spectroscopy (EDX) microanalysis system installed on the SEM. An image analysis method was used to post process the SEM images and measure the IMC and bond-thicknesses.

(a)

(b)

(c)
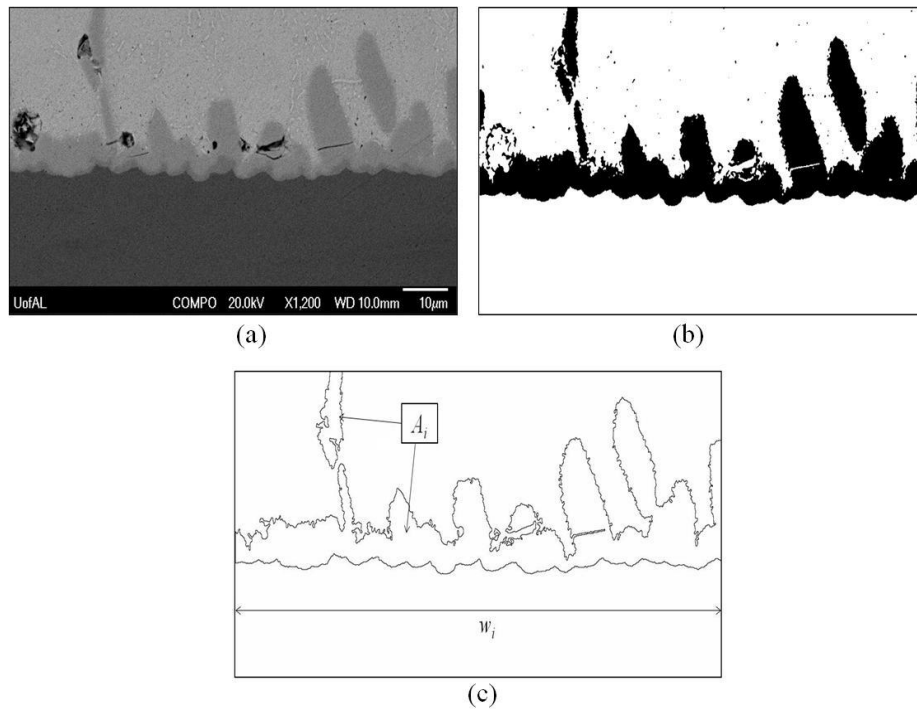
Figure 2-3: (a) SEM image transferred to (b) a binary image, and (c) a graph shows total area and the length of IMC layer.

The post processing steps include [28, 55]: **(1)** enhance the grey-level SEM image of 1280x1024 pixels to clarify the interfaces between the different phase layers, **(2)** produce a binary image from the enhanced image using a suitable threshold to extract the specific layer of the IMC from the others as shown in Figure 2-3(b), **(3)** calculate the areas of the extracted layer after calibrating the image to a known dimension, e.g. the scale on the SEM image , **(4)** divide the area by the length of the image, Figure 2-3(c), to get the average thickness as follows:

$$l_i = \frac{A_i}{w_i} \qquad (2\text{-}19)$$

l_i is the average thickness of the layer i (i = 1 for Cu_6Sn_5 IMC phase or i = 2 for Cu_3Sn IMC phase), A_i and w_i are the area of the layer and width of the SEM image respectively. The total thickness l of the IMC layer is obtained by summing the thickness of the existing IMC phases.

2.5 Results

2.5.1 Interfacial Microstructure

A continuous and bilayer of scalloped η-phase Cu_6Sn_5 adjacent to the solder and ε-phase Cu_3Sn adjacent to the Cu substrate were observed in all the SEM images. To compare the effect of soldering time, SEM micrographs of the bonds fabricated at soldering temperature of 310 $^\circ$C for bond durations from 2 minutes to 240 minutes are shown in Figure 2-4. As soldering time increases, the thickness of both layers of IMC increases. The temperature effect at two different times is illustrated in Figure 2-5.
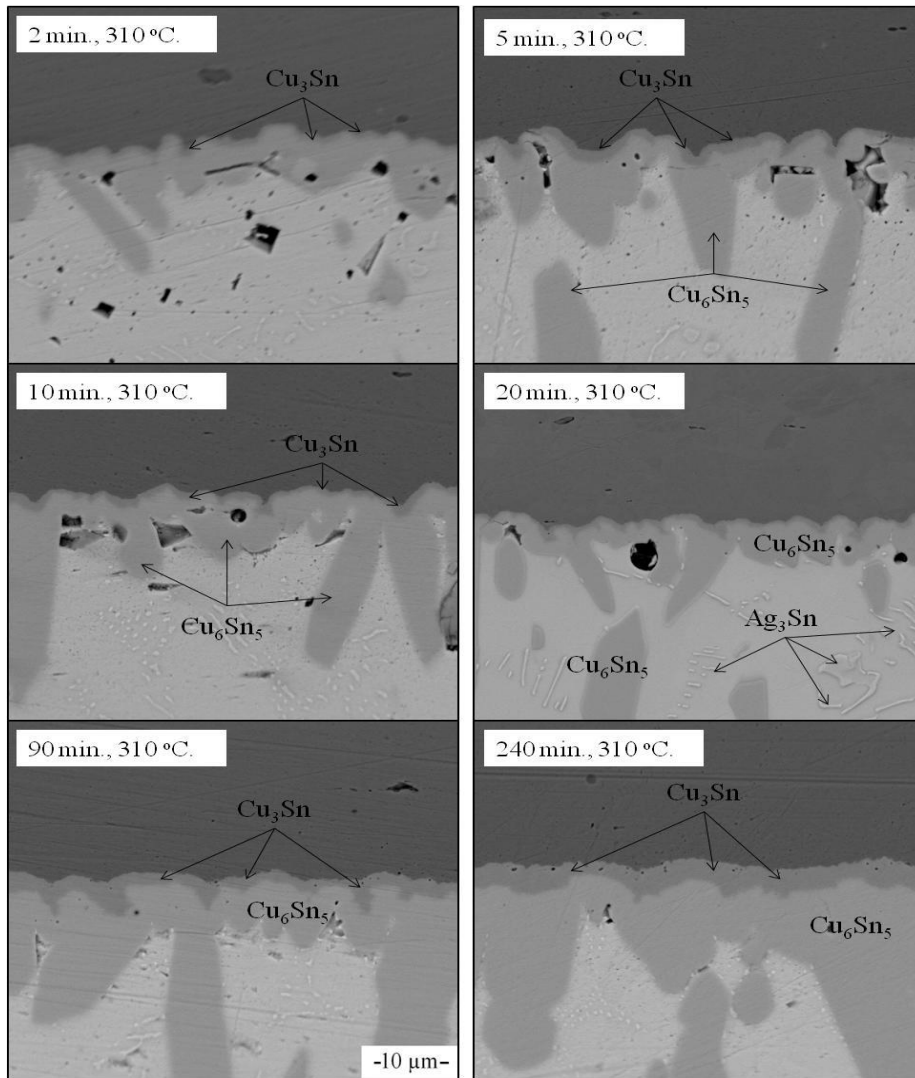
Figure 2-4: SEM backscattered electron images illustrating the microstructure of Sn-3.5Ag/Cu solder joints fabricated at 310 ^{o}C for various soldering times.
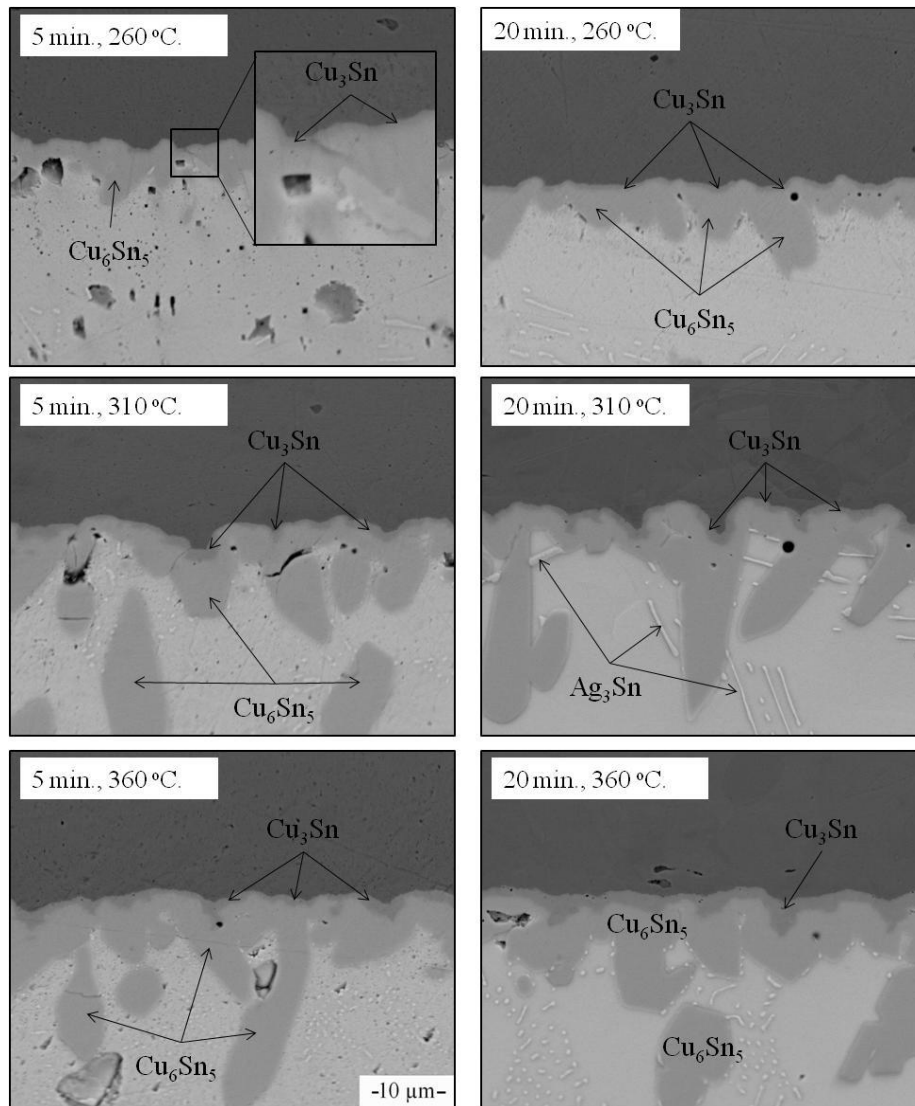
Figure 2-5: Effect of temperature illustrated at two different times, 5 and 20 minutes. SEM backscattered electron images illustrating the microstructure of Sn-3.5Ag/Cu solder joints.

The two phases of IMC are common to all samples soldered for the designated soldering time and temperatures applied in this study. In addition to the η and ε IMC layers located at solder/substrate interface, isolated IMC phase precipitates are observed inside the solder bulk. Also, in Figure 2-5, it was noticed that the thickness of IMC phases show a monotonic increase in thickness as temperature increase. As can be seen from Figure 2-4 and Figure 2-5, the thickness of the Cu_6Sn_5 IMC layer is always larger and less uniform than the thickness of the Cu_3Sn IMC layer. In addition, it is observed that the Cu_3Sn/Cu and Cu_6Sn_5/Cu_3Sn interfaces in

all soldered samples show a slightly wavy interface, see Figure 2-4 and Figure 2-5. The chemical compositions of the IMC phases are presented in Figure 2-6 as identified by means of EDX analysis which confirmed the distinguish between the phases based on the gray level in backscattered SEM micrographs. Figure 2-6(a) confirms that the IMC layer adjacent to Cu substrate is indeed Cu_3Sn IMC which was distinguished from the other IMC by its gray level. Figure 2-6(b) shows the composition of Cu_6Sn_5 which is always adjacent to the bulk solder.

Cu₃Sn		
Element	Wt.%	At. %
CuK	66.38	78.67
SnL	33.62	21.33
Total	100.00	

Full Scale 494 cts Cursor: 0.000   keV

(a)

Cu₆Sn₅		
Element	Wt.%	At. %
CuK	45.58	61.00
SnL	54.42	39.00
Total	100.00	

Full Scale 347 cts Cursor: 0.000   keV

(b)
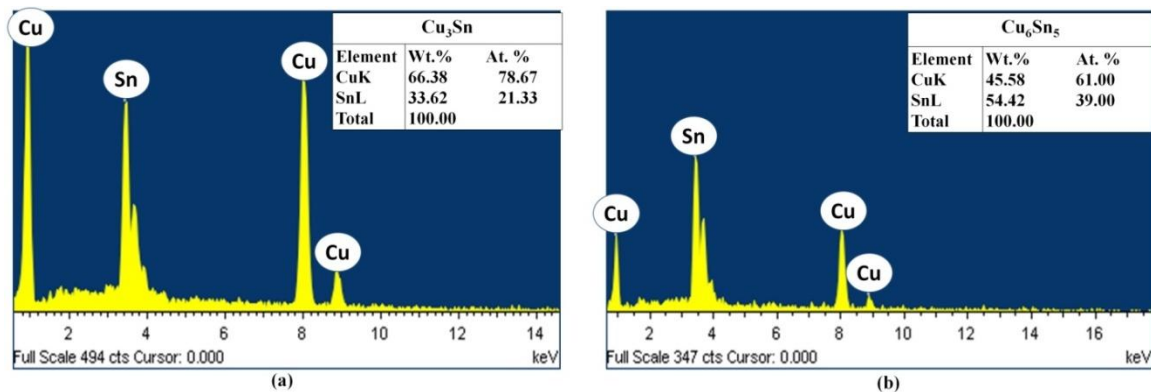
Figure 2-6: EDX analysis indicating the presence of Cu_3Sn (a) and Cu_6Sn_5 (b) IMCs in Sn-3.5Ag/Cu solder joints.

2.5.2 IMC Growth

Average thicknesses of Cu_6Sn_5, Cu_3Sn, and total IMC layers are plotted against bonding time and are shown in Figure 2-7. As can be seen in Figure 2-7(a), the values of average thicknesses of Cu_6Sn_5 interfacial IMC layer were found to monotonically increase following a parabolic law with the soldering time at each bonding temperature. Figure 2-7(b) shows the thickness growth-time relationship for Cu_3Sn IMC layer. It is clear that higher growth rate is obtained at higher bonding temperature. The mean thickness values of interfacial IMC layers were found to increase with the soldering time. Comparing the curves visually, it is clear that growth rate is faster for higher soldering temperatures. The total IMC thickness at highest temperature and longest time is more than 35 μm.
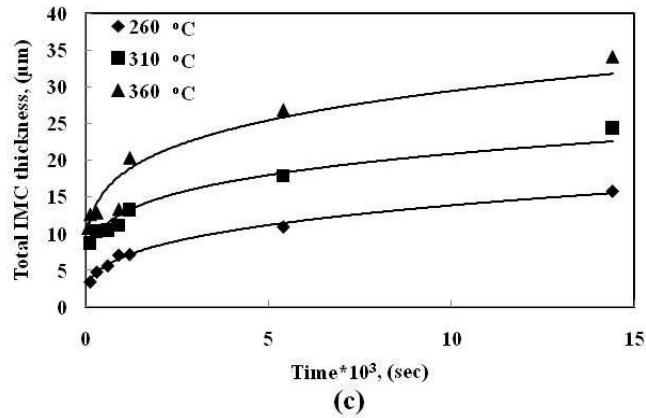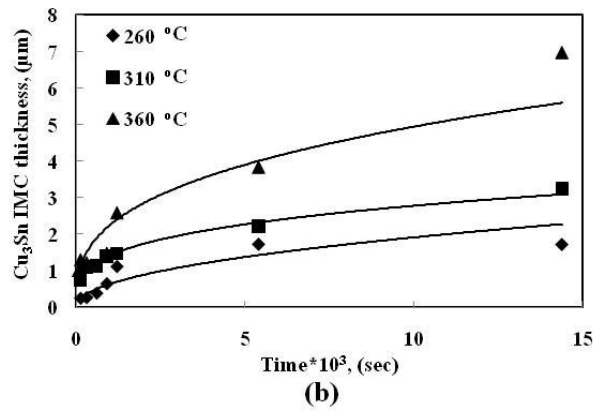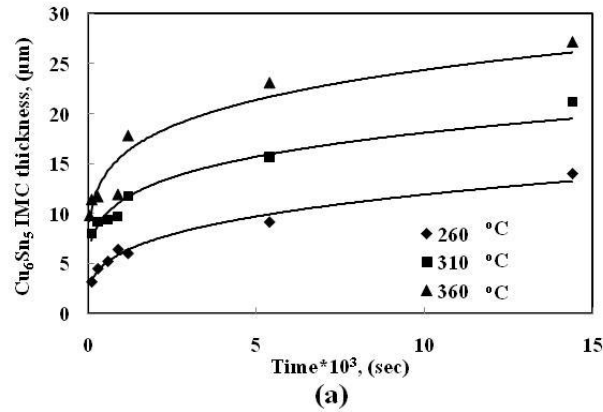
Figure 2-7: Average thickness of (a) Cu_6Sn_5, (b) Cu_3Sn, and (c) total IMC layers as a function of soldering time at different temperatures.

The effect of bonding temperature on the growth rate of IMC layers is shown in Figure 2-8.
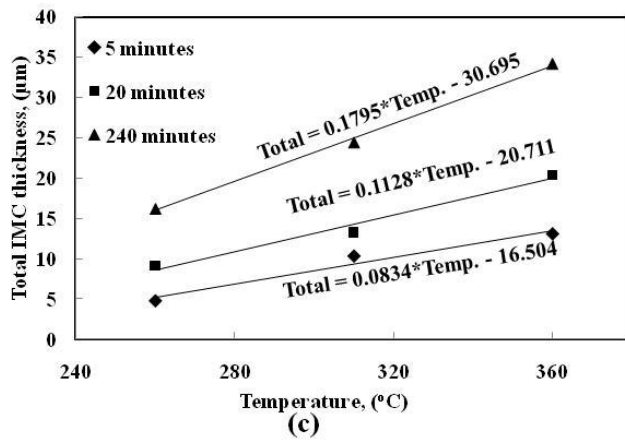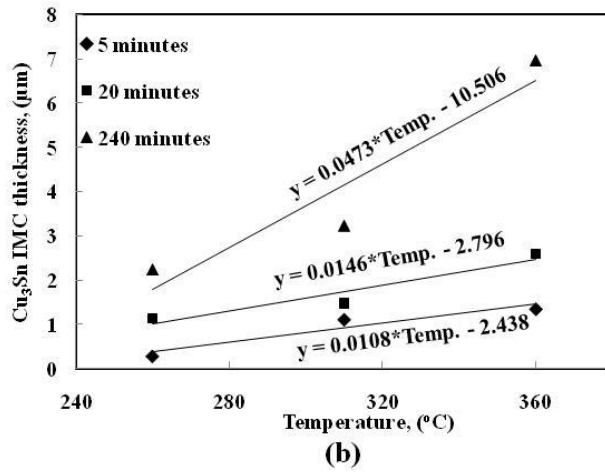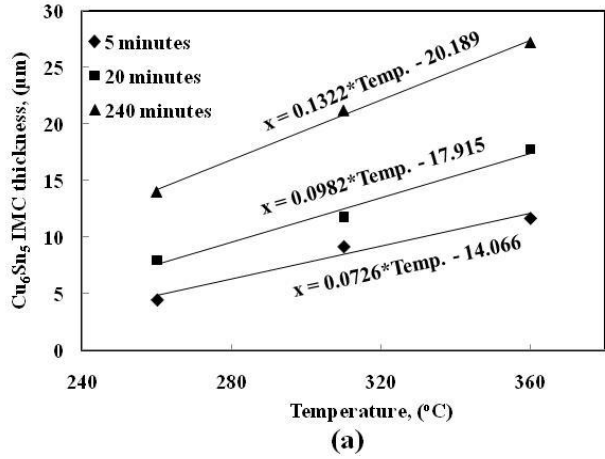
Figure 2-8: Effect of bonding temperature on the growth rate of Cu_6Sn_5 (a) Cu_3Sn (b), and total IMC (c) layers.

Figure 2-8(a) shows the change in thickness of Cu_6Sn_5 IMC layer while Figure 2-8(b) and Figure

2-8(c) show the change of thickness versus bonding temperature at constant times for Cu_3Sn and

total IMC layers, respectively. As can be seen, the mean thickness values of interfacial IMC

layers were found to linearly increase with increasing bonding temperature. A comparison

between the slopes of the lines at different times shows that the effect of temperature is more

pronounced in longer soldering times. This effect is observed in both Cu_6Sn_5 and Cu_3Sn.

2.6 Discussion

2.6.1 Kinetics of Interfacial Reactions
Generally, the thickness of the IMC layer formed during the soldering process is expressed by

the simple parabolic equation:

$$l_i = k_i t^n \tag{2-20}$$

where k_i is the IMC growth rate constant of the appropriate species in the joint, n is the time

exponent, and t is the reaction time. Considerable literature [17-25] is available about solid-state

growth of IMC in solder joints in which Eq.(2-20) has been shown to nicely fit the experimental

results when a time exponent of 0.5 is used. In such a growth state, it is assumed that the rate

controlling process in IMC growth is diffusion during the aging process. In molten solders,

different time exponent values have been obtained, (n = 0.21-0.90), from experimental results

using regression analysis [27-30]. When Eq.(2-20) is applied on the current experimental data,

the following time exponents were obtained: 0.23, 0.37, and 0.25 for growth of Cu_6Sn_5, Cu_3S,

and total IMC, respectively. This model, however, does not consider the complex physics in the

case of molten solder. Therefore, the growth behavior of IMC layers are also modeled using

Dybkov's model.

To successfully use Dybkov's model a few assumptions are made. First, it is assumed that the interfacial reactions which occur at the two Sn-3.5Ag solder/Cu boundaries (at top and bottom Cu layers) are identical. Therefore, half of the sample thickness is considered for IMC growth measurement and modeling. Furthermore, the original thickness of the bulk solder is unknown and is calculated from the remaining thickness of the bulk solder, the formed Cu_6Sn_5, and Cu_3Sn layers as follows [16]:

$$l_{SnAg\_original} = l_{SnAg\_residual} + l_{Sn\_consumed} \qquad (2\text{-}21)$$

where $l_{SnAg\_original}$ is the half thickness of the original solder layer, $l_{SnAg\_residual}$ is the half thickness of the remaining solder layer, and $l_{Sn\_consumed}$ is the half thickness of the tin consumed in forming Cu_6Sn_5, and Cu_3Sn layers, and is found by following equation [16]:

$$l_{Sn\_consumed} = \frac{5\rho_{Cu_6Sn_5}M_{Sn}l_{Cu_6Sn_5}}{\rho_{Sn}M_{Cu_6Sn_5}} + \frac{\rho_{Cu_3Sn}M_{Sn}l_{Cu_3Sn}}{\rho_{Sn}M_{Cu_3Sn}} \qquad (2\text{-}22)$$

where $l_{Cu_6Sn_5}$ and l_{Cu_3Sn} are the measured average thicknesses of the Cu_6Sn_5 and Cu_3Sn layers in each sample, and ρ and M with subscripts Sn, Cu_6Sn_5, and Cu_3Sn are the corresponding densities and molar weights, respectively.

Finally, the effect of the simultaneous dissolution of Cu_6Sn_5 IMC layer and the change of Cu concentration in the molten solder on the kinetics of the interfacial reaction is specified based on Eq.(2-9b) of Section 2.1. The dissolution rate constants, the solubility of Cu in molten solders at different temperatures, and density of Cu, Sn and Cu_6Sn_5 are presented in Table 2-2 [16, 44]. When the right values for the constants are substituted from Table 2-2 into Eq.(2-9b), the time required for the molten solder to saturate with Cu for each bonding temperature can be determined. Based on this equation, saturation times of 4, 3, and 2 minutes are found for the temperatures of 260, 310, and 360 ^{o}C, respectively. Based on these times, it was assumed that the

dissolution effect is negligible after 5 minutes. Using these assumptions, the interfacial reaction is described using Eqs.(2-15) and (2-16).

Table 2-2: Cu dissolution rate, Cu solubility limit, and IMC phase density.

k_d , (m/sec.) [44]			c_s, (wt. %Cu), [44]			ρ, kg/m^3 [16]		
260 ^{o}C	310 ^{o}C	360 ^{o}C	260 ^{o}C	310 ^{o}C	360 ^{o}C	Cu	Sn	Cu$_6$Sn$_5$
8.21E-6	1.09E-5	1.39E-5	1.60	3.025	5.19	8.94	7.29	8.28

According to literature, the chemical reaction-controlled (linear) growth kinetics are observed with thin compound layers up to about 500-600 nm and diffusion-controlled (parabolic) growth are characteristic of much thicker compound layers (1 μm or more) [38-39]. The time-thickness relationship is linear when chemical reaction-controlled and it is parabolic in the diffusion-controlled stage. It was assumed that the time for chemical reaction to take place is directly proportional to the change in the layer thickness while the time for diffusion of atoms is directly proportional to both the change in layer thickness and its existing thickness. Therefore, if IMC growth is under pure chemical reaction mechanism, the partial differential equations describe the growth behavior will be function of change in thickness. Their solution will be first order in layer thickness. In case of a pure diffusion control condition, the partial differential equations governing IMC growth will be function in the change in thickness and the current thickness. Any solution will be second-order in layer thickness. These assumptions have been validated in [36]. The smallest thickness of Cu$_6$Sn$_5$ (seen in Figure 2-7(a)) is beyond 600nm. As a result we assume that Cu$_6$Sn$_5$ IMC layer must have formed under diffusion-controlled mechanism. On the other hand, in several cases Cu$_3$Sn IMC layer thickness was found to be lower than 600nm (refer to Figure 2-7(b)). These cases occur in soldering times smaller than 10 minutes. Therefore, chemical reaction-growth kinetics might be active during IMC formation during this designated

range of bonding time. As it will be shown in the following sections, this assumption is found to give suitable prediction of growth of Cu_3Sn IMC layer using Dybkov's model.

For the soldering times between 1-10 minutes, the highest values of thickness obtained for Cu_3Sn IMC layer was about 650 nm at a bonding temperature of 260 ^{o}C. Therefore, the formation of the compound is believed to be under chemical reaction-controlled mechanisms. For the bonding temperatures of 310 and 360 ^{o}C, the values of thickness for Cu_3Sn IMC layer are close to or greater than 1 μm, thus, the growth is believed to be diffusion-controlled.

Based on these assumptions, IMC thickness growth experiments are divided into two groups: one group is in which the growth of one IMC layer (e.g. Cu_3Sn layer) is under the chemical reaction mechanism while the other layer (e.g. Cu_6Sn_5 (layer) is under diffusion mechanism. It includes the experimental data obtained during bonding times from 1-10 minutes for 260°C. The other group is when both IMC layers are under diffusion-controlled growth kinetics. It includes the experimental data obtained for bonding times greater than 10 minutes. Therefore, the system of differential equation (Eqs.(2-15) and (2-16)) that describes the growth kinetics of IMCs is simplified according to mechanisms that are active during the interfacial reaction.

2.6.2 Combined Chemical Reaction- and Diffusion-Controlled (Paralinear) Growth of the IMC Layers

This condition is for IMC growth time under 10 minutes for bonding temperature of 260°C.

Under this condition, it is assumed that all the A atoms passing across the A_pB_q layer are combined into A_pB_q compound at interface (2'-2) according to reaction (2-1b). The thicker the A_rB_s layer, the greater is the deficit of A atoms. This halts the growth of the A_rB_s layer due to diffusion of component A. Therefore, reaction (2-1d) ceases to occur. As a result A_rB_s grows only at the expanse of component B which means that the second term in Eq.(2-16) has no

physical meaning and it should be omitted. This assumption and the resulting governing

equations are expressed below:

$$x \gg x_{1/2}^{(B)}, x \gg x_{1/2}^{(A)}, \text{and } y \ll y_{1/2}^{(B)} \tag{2-23}$$

This can be transformed into the following inequality:

$$k_{0B1} \gg \frac{k_{1B1}}{x}, k_{0A2}' \gg \frac{k_{1A2}'}{x}, \text{and } k_{0B2}' \ll \frac{k_{1B2}'}{y} \tag{2-24}$$

Then, the system of Eqs.2-15 and 2-16 is simplified into

$$\frac{dx}{dt} = \frac{k_{1B1} + k_{1A2}'}{x} - \frac{rg}{p} k_{0B2}' - \frac{c_s k_d}{\rho_{A_p B_q} \varphi} \exp(-at) \tag{2-25a}$$

$$\frac{dy}{dt} = k_{0B2}' - \frac{q}{sg} \frac{k_{1A2}'}{x} \tag{2-25b}$$

If A is Sn and B is Cu, then $A_p B_q$ is $Cu_6 Sn_5$ and $A_r B_s$ is $Cu_3 Sn$. Therefore, $p = 5$, $q = 6$, $r = 1$, and

$s = 3$. Since k_{1B1} and k_{1A2}' are diffusion rate constants of the $Cu_6 Sn_5$ layer by Cu and Sn

diffusion, respectively, they are given the following combined name, $k_{Cu_6 Sn_5}^{diff}$. Since $Cu_3 Sn$

only forms and grows by reaction (2-1c) under chemical reaction controlled conditions by Cu

diffusion, the growth rate constant under chemical reaction condition is k_{0B2}' which for

simplicity we rename it to $k_{Cu_3 Sn}^{chem}$. The system of Eqs.(2-25) is stated in the following form:

$$\frac{dx}{dt} = \frac{1}{x} k_{Cu_6 Sn_5}^{diff} - \frac{rg}{p} k_{Cu_3 Sn}^{chem} - \frac{c_s k_d}{\rho_{A_p B_q} \varphi} \exp(-at) \tag{2-26a}$$

$$\frac{dy}{dt} = k_{Cu_3 Sn}^{chem} - \frac{q}{sg} \frac{1}{x} k_{Cu_6 Sn_5}^{diff} \tag{2-26b}$$

The unknown quantities in Eqs.(2-26a) and (2-26b) are the growth rate constants

$k_{Cu_6 Sn_5}^{diff}$ and $k_{Cu_3 Sn}^{chem}$. Eq.(2-26a) is uncoupled and its solution could be obtained through

application of standard methods.

2.6.3 Diffusional Growth of the IMC Layers

Thickening of the layers with increasing interaction time of the initial substances A and B leads to a change in the regimes of their growth. At higher thicknesses, greater than the critical values of thicknesses, the regime of growth of the A_pB_q and A_rB_s layers is diffusion controlled with regard to both components A and B.

$$x \gg x_{1/2}^{(B)} \text{ and } x \gg x_{1/2}^{(A)} \tag{2-27a}$$

$$y \gg y_{1/2}^{(B)} \text{ and } y \gg y_{1/2}^{(A)} \tag{2-27b}$$

Consequently, the growth of both layers is due to reactions (2-1b) and (2-1c) taking place at interface 2 whereas reactions (2-1a) and (2-1d) cannot proceed at all because there are no excess diffusing B and A atoms [36]. As a result, the first term in Eq.(2-15) and the second term in Eq.(2-16) lose their physical meaning and are omitted. Simplifying the equations and renaming the diffusion rate constant of Cu_6Sn_5 growth k_{1A2}' and the diffusion rate constant of Cu_3Sn growth, k_{1B2}', $k_{Cu_6Sn_5}^{diff}$ and $k_{Cu_3Sn}^{diff}$ respectively we reached the following system of equations:

$$\frac{dx}{dt} = \frac{1}{x}k_{Cu_6Sn_5}^{diff} - \frac{rg}{p}\frac{1}{y}k_{Cu_3Sn}^{diff} - \frac{c_sk_d}{\rho_{A_pB_q}\varphi}\exp(-at) \tag{2-28a}$$

$$\frac{dy}{dt} = \frac{1}{y}k_{Cu_3Sn}^{diff} - \frac{q}{sg}\frac{1}{x}k_{Cu_6Sn_5}^{diff} \tag{2-28b}$$

Fitting the experimental data designated for diffusion stage to the system of Eq.(2-28), the diffusion-growth rate constants $k_{Cu_6Sn_5}^{diff}$ and $k_{Cu_3Sn}^{diff}$ for Cu_6Sn_5 and Cu_3Sn IMC layers are obtained. Table 2-3 shows the values for all the rate constants obtained using this approach and implementing the experiment results.

Table 2-3: Kinetics constants of IMC diffusional growth in Sn-3.5Ag/Cu solder system

Temp. °C	Chemical-reaction stage	Diffusion stage

	Cu$_3$Sn		k^{diff}, m^2/sec		Q^{diff}, KJ/mol.	
	k^{chem}, m/sec	Q^{chem}, KJ/mol.	Cu$_6$Sn$_5$	Cu$_3$Sn	Cu$_6$Sn$_5$	Cu$_3$Sn
260 ^{o}C	3.81E-10		2.44E-14	2.73E-15		
310 ^{o}C	4.83E-10	20.59	3.50E-14	5.31E-15	41.98	50.10
360 ^{o}C	8.01E-10		1.23E-13	1.65E-14		

The predicted values of thickness for both IMC layers at 260, 310, and 360 ^{o}C are displayed

using this modeling approach are compared with experimental results in Figure 2-9, Figure 2-10,

and Figure 2-11.
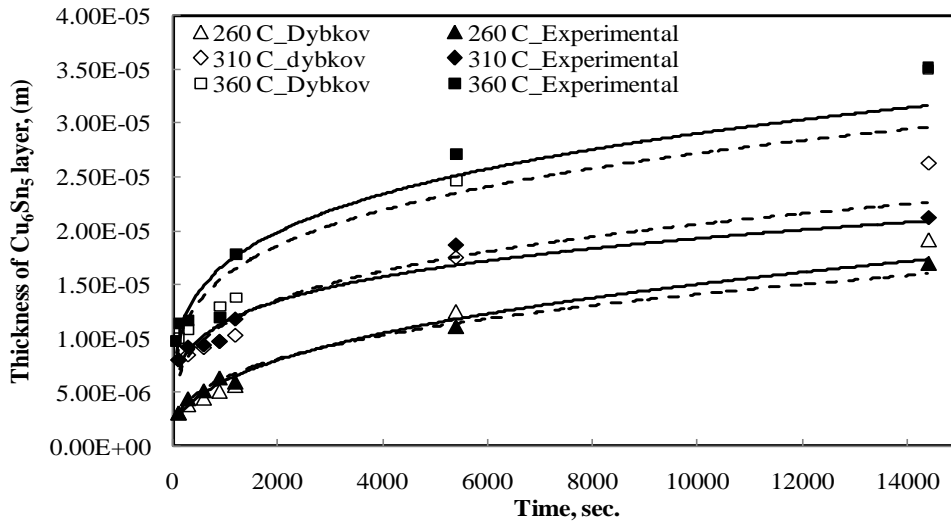
Figure 2-9: Comparison of the thicknesses predicted by Dybkov's model with experimental results of the Cu$_6$Sn$_5$ IMC layer in samples prepared at 260, 310, and 360 ^{o}C.
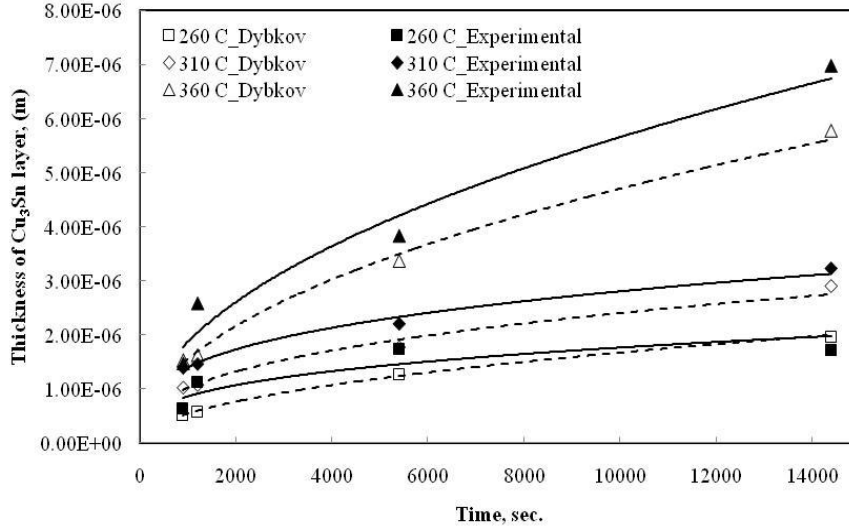
Figure 2-10: Comparison of the thicknesses predicted by Dybkov's model with experimental results of the Cu$_3$Sn IMC layer in samples prepared at 260, 310, and 360 $^{\circ}$C.
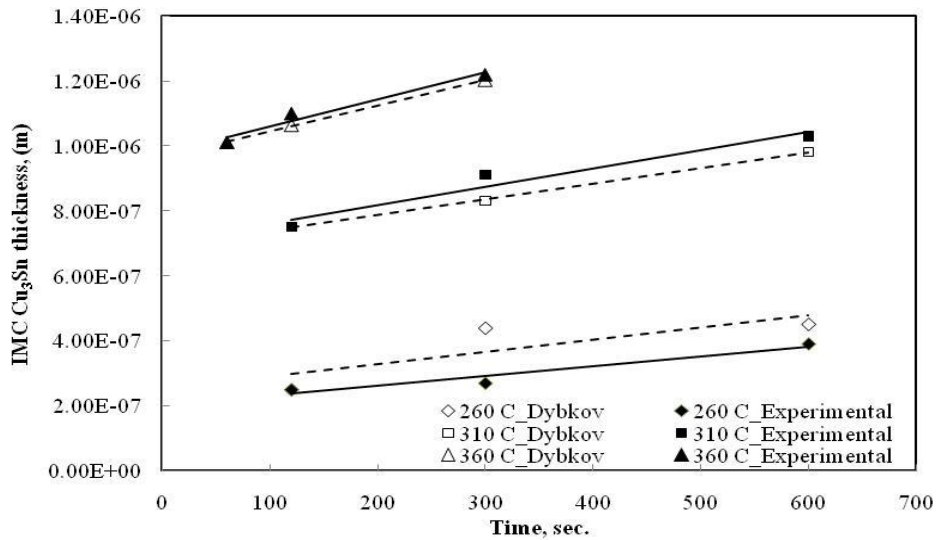
Figure 2-11: Comparison of the thicknesses predicted by Dybkov model with experimental results of the formed Cu$_3$Sn IMC layer.

The temperature dependency of the extracted values of k$^{\text{chem}}$ and k$^{\text{diff}}$ in both growth stages is further exploited using the Arrhenius relationship to determine the activation energies for the growth of Cu$_6$Sn$_5$ and Cu$_3$Sn IMC layers using the following equations:

$$k^{\text{chem}} = k_o^{\text{chem}} \exp\left(-\frac{Q^{\text{chem}}}{RT}\right) \tag{2-29a}$$

$$k^{diff} = k_o^{diff} \exp\left(-\frac{Q^{diff}}{RT}\right) \tag{2-29b}$$

where k_o is the layer growth constant, Q is the activation energy, R is the gas constant (8.314 J/mol-K), and T is the soldering temperature (absolute units). The activation energies were calculated from the slope of the Arrhenius plot using a linear regression model.

Figure 2-12 shows the Arrhenius plots for the growth of IMC layers. Figure 2-12(a) shows the energy plot for Cu_3Sn IMC layer during the chemical reaction-controlled stage while Figure 2-12(b) shows the Arrhenius plot for the growth of Cu_6Sn_5 and Cu_3Sn IMC layers during diffusion-controlled growth stage. The apparent activation energies calculated for the growth of Cu_3Sn IMC layer during the chemical reaction stage and for the growth of Cu_6Sn_5 and Cu_3Sn IMC layers during the diffusion stage are listed in Table 2-3 and also compared with the data from previous works in Table 2-4. Table 2-3 lists for the first time the activation energy for the growth of Cu_3Sn IMC layer, which is 20.59 (kJ/mol), during the chemical reaction-controlled growth stage in Sn-3.5Ag/Cu soldering system.
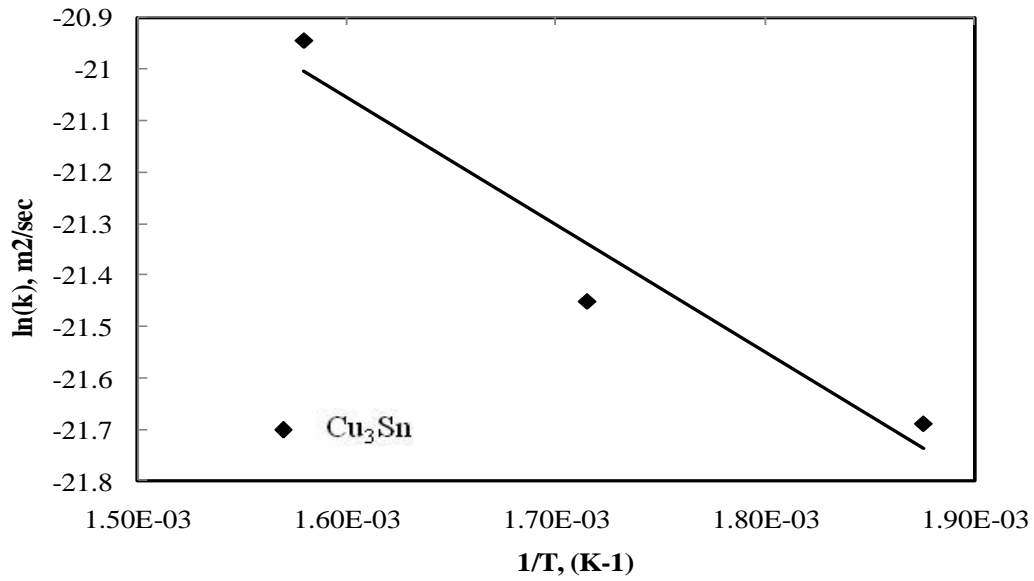
(a)
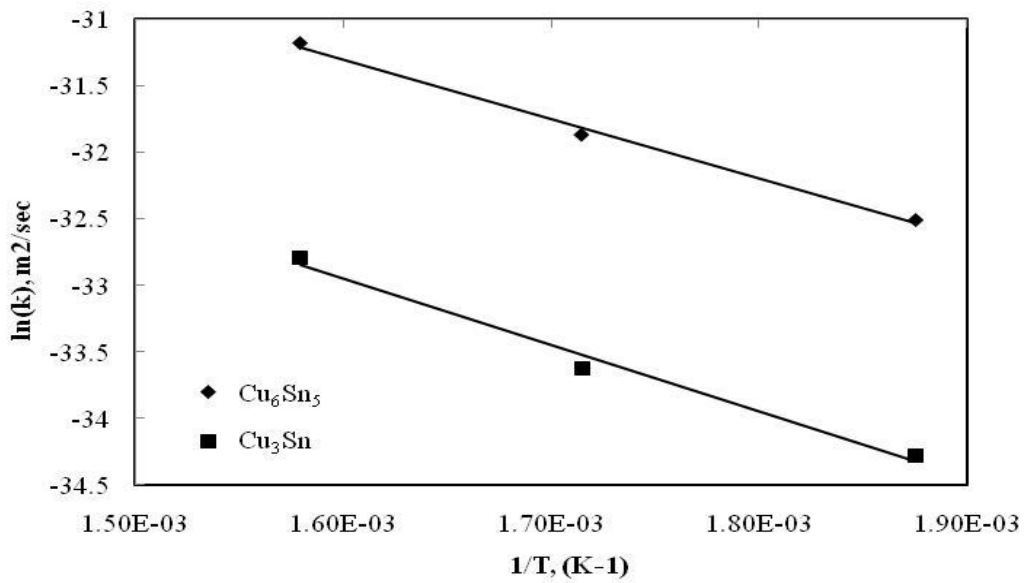
(b)

Figure 2-12: Arrhenius plot of growth rate constants (a) for Cu_3Sn IMC layer during chemical reaction-controlled growth and (b) for Cu_6Sn_5 and Cu_3Sn IMC layers during diffusion-controlled growth.

68

Table 2-4: Kinetics rate constants and activation energies of diffusional IMCs growth from different references.

Solder/substrate	Preparation method	Reaction temperature (^{o}C)	Reaction time	IMC layer	Activation energy Q (kJ/mol.)	Reference
Sn-3.5Ag/Cu	Sandwich type	260-360	20-240 min.	Cu_6Sn_5 Cu_3Sn	41.98 50.10	Current study, Dybkov model
Sn-3.5Ag/Cu	Sandwich type	260-360	20-240 min.	Cu_6Sn_5 Cu_3Sn	30.10 68.71	Current study, Curve fit method
Cu/Sn/Cu	Solid-liquid interdiffusion (SoLID)	260-360	Up to 340	Cu_6Sn_5 Cu_3Sn	19.72±13.1 84.59±25.84	Li, et al 2011
Sn-3.5Ag/Cu	Spreading	70-200	0-60 days	Total Cu_6Sn_5 Cu_3Sn	65.4 55.4 75.7	Yoon, et al 2003
SAC(355)/Cu	Dipping method	120-180	Up to 2000 hr.	Total Cu_6Sn_5 Cu_3Sn	79.42 69.42 91.88	Kim, at al 2010
SAC(355)/Cu-Zn				Cu_6Sn_5	96.61	
Sn-3.5Ag/Cu	Sandwich type	110-208	0-32 days	Cu_6Sn_5 Cu_3Sn	107.1 70.41	Flanders, et al 1997
Sn-5Bi/Cu	Spreading	70-200	0-30 days	Total Cu_6Sn_5 Cu_3Sn	107.1 98.35 90.5	Yoon, et al 2003
Sn-Cu	Spreading	150-227		Cu_6Sn_5 Cu_3Sn	102±5.94 50.7±3.59	Mattafirri, et al 2003
Cu-Sn	electroplating	100-225	0.5-5 hr.	Cu_6Sn_5 Cu_3Sn	41.4 90.4	Tang, et al 2010
Sn-Cu	Sandwich type	250-325	0.5-4000 min	Total Cu_6Sn_5 Cu_3Sn	17.5 13.4 29.2	Gagliano, et al 2003

The activation energy for the growth of Cu_6Sn_5 during diffusion-controlled growth stage is 41.98 (kJ/mol). It is clearly different from 30.25 (kJ/mol) which was obtained by curve fitting method for the current experimental data because power law method does not account for the interaction between the growth of Cu_6Sn_5 and Cu_3Sn. However, it is in agreement with values reported in

literature [17, 57]. The activation energy for the growth of Cu_3Sn during diffusion-controlled growth stage is 50.10 (kJ/mol). It is clear that the value is lower than 68.71 (kJ/mol) which is obtained by curve fitting method in the current study. The main reason is the curve fitting method models each IMC's growth independent of the others, but it is within the range of values reported in literature [58].

The discrepancy among the activation energies, as shown in Table 4, is due to the differences in the type of soldering alloy, diffusion couple method, soldering temperature and time ranges, and the analytical approach used in extracting the kinetics constants.

2.7 Conclusions

The growth kinetics of IMC compound layers formed between Sn-3.5Ag/Cu soldering system were examined at temperatures between 260-360 ^{o}C and different bonding times from 1 to 240 minutes. The results reveal the following conclusions:

- The IMC compound layer was composed of two phases: η-phase (Cu_6Sn_5) adjacent to the solder matrix and ε-phase (Cu_3Sn) adjacent to the Cu substrate.

- The thicknesses of the η and ε IMC phases increase with increasing the bonding time and temperature. The effect of temperature is found to be more pronounced for longer bonding times. The increase in IMC layer thickness during the soldering process was found to obey a parabolic relationship with time. This indicates that the formation of the IMC compound layer is mainly controlled by the volume diffusion mechanism.

- For the first time, the apparent activation energy for the growth of ε-(Cu_3Sn) IMC phase during chemical reaction-controlled growth stage is reported in this study as 20.59 (KJ/mol). The apparent activation energies calculated for the growth of η- (Cu_6Sn_5) and ε-(Cu_3Sn) IMC phases

during diffusion-controlled growth stage are 41.98 and 50.10 (kJ/mol), respectively. The values

slightly differ from literature where a simple power-law fit is used in extracting those quantities

which do not explicitly incorporate the interaction between the different IMCs growth behavior.

In the current study, the activation energies are calculated based on Dybkov's model in which the

net growth rate of any IMC phase is a result of its net growth due in particular to the chemical

reaction and the consumption of one IMC phase in forming the other IMC phase. The values

obtained in the current study are still within the scope of the literature values.

References

[1]. Puttlitz, K. J., Stalter, K. A., "Handbook of Lead-Free Solder Technology for Microelectronic Assemblies," Marcel Dekker AG, Basel, Switzerland, 2004.

[2]. Blackwell, G. R., "The Electronic Packaging Handbook Ed. Blackwell", G.R. Boca Raton: CRC Press LLC, 2000.

[3]. Tu, K. N., Zeng, K., "Tin-lead (SnPb) solder reaction in flip chip technology", Material science and engineering, Vol. R34, No. 1, pp. 1-58, 2001.

[4]. Quan L., Frear D., Grivas D., Morris Jr J. W., "Tensile behavior of Pb-Sn solder/Cu joints," Journal of Electronic Materials, Vol. 16, No. 3, pp.203-208 , 1987.

[5]. Skipor AF., Harren S. V., and Botsis J., "The effect of mechanical constraint on the flow and fracture of 63/37 Sn/Pb eutectic alloy", Journal of Engineering Fracture Mechanics, Vol. 52, No. 4, pp. 647-669, 1995.

[6]. Qi Y., Ghorbani H. R., and Spelt J. K., "Thermal fatigue of SnPb and SAC resistor joints: analysis of stress-strain as a function of cycle parameters", IEEE Transaction Advanced Packaging, Vol. 29, No. 4, pp.690-700, 2006.

[7]. Vianco P., and Arbor A., "Development of alternatives to lead-bearing solders", Center for Solder Science and Technology, Sandia National Laboratories, 1993. http://www.osti.gov/energycitations/product.biblio.jsp?osti_id=10169303. Visited in 04/15/2011.

[8]. Melton C., "Alternatives of lead bearing solder alloys Electronics and the Environment, 1993, Proceedings of the 1993 IEEE International Symposium on, pp. 94-97, 10-12 May 1993, Arlington, VA , USA.

[9]. Abtew M., and Selvaduray G., "Lead-free solders in microelectronics", Journal of Materials Science and engineering, Vol. 27, No. 5-6, pp. 95-141, 2000.

[10]. Wood E. P., and Nimmo K. L., "In search of new lead-free electronic solders", Journal of Electronic Materials, Vol. 23, No. 8, pp. 709-713, 1994.

[11]. U.S. Congress, Office of Technology Assessment, Miniaturization Technologies, OTA-TCT-514 (Washington, DC: U.S. Government Printing Office, November 1991). http://www.fas.org/ota/reports/9129.pdf. Visited in 04/11/2011.

[12]. Sienski K., Eden R., and Schaefer D., "3-D electronic interconnect packaging", IEEE Transaction on Aerospace Applications Conference, pp. 363-373, 3-10 Feb 1996, Aspen, CO, USA .

[13]. Chew K. H., "Drop in replacement of tin/lead solder alloy in wave soldering process-lead free solders", Quantum Chemical Technologies (S) Pte Ltd. http://www.asahisolder.com/publication.html. Visited in 04/17/2011.

[14]. Zeng G., Xue S., Zhang L., Gao L., Dai W., and Luo J., "A review on the interfacial intermetallic compounds between Sn-Ag-Cu based solders and substrates," Journal of Material Science, Vol. 21, No. 5, pp. 421-440, 2010.

[15]. Huang Z., Conway P. P., and Qin R., " Modeling of interfacial intermetallic compounds in the application of very fine lead-free solder interconnections," Journal of Micro-system Technologies-Special Issue on micro-nano-Reliability, Vol. 15, No. 1, pp. 101-107, 2009.

[16]. Li J. F., Agyakwa P. A., and Johnson C M, "Interfacial reaction in Cu/Sn/Cu system during the transient liquid phase soldering process," Acta Materialia, Vol. 59, No. 3, pp. 1198-1211, 2011.

[17]. Yoon J. W. and Jung S. B., "Investigation of interfacial reactions between Sn-5Bi solder and Cu substrate," Journal of Alloys and Compounds, Vol. 359, No. 1-2, pp. 202-208, 2003.

[18]. Ma D., Wang W. D., and Lahiri S. K., "Scallop formation and dissolution of Cu-Sn intermetallic compound during solder flow," Journal of Applied Physics, Vol. 91, No. 5, pp. 3312-3317, 2002.

[19]. Kim Y. M., Roh H.R., and Kim S., "Kinetics of intermetallic compound formation at the interface between Sn-3.0Ag-0.5Cu solder and Cu-Zn alloy substrates," Journal of Electronic Materials, Vol. 39, No. 12, pp. 2504-2512, 2010.

[20]. Li J. F., Agyakwa P. A., and Johnson C. M., "Kinetics of Ag3Sn growth in Ag-Sn-Ag system during transient liquid phase soldering process," Acta Materialia, Vol. 58, No. 9, pp. 3429-3443, 2010.

[21]. Flanders D. R., Jacobs E. G., and Pinizzotto R. F., " Activation energies of intermetallic growth of Sn-Ag eutectic solder on copper substrates," Journal of Electronic Materials, Vol. 26, No. 7, pp. 883-887, 1997.

[22]. Takenaka T., Kano S., Kajihara M., Kurokawa N., and Sakamoto K., " Growth behavior of compound layers in Sn/Cu/Sn diffusion couples during annealing at 433-473K," Journal of Materials Science and Engineering, Vol. A396, No. 1-2, pp. 115-123, 2005.

[23]. Rizvi M. J., Chan Y. C., Bailey C., Lu H., and Islam M. N., "Effect of adding 1 wt% Bi into the Sn-2.8Ag-0.5Cu solder alloy on the intermetallic formations with Cu-substrate during soldering and isothermal aging," Journal of Alloys and Compounds, Vol. 407, No. 1-2, pp. 208-214, 2006.

[24]. Yoon J. W., Lee C. B., Kim D. U., and Jung S. B., "Reaction diffusions of Cu_6Sn_5 and Cu_3Sn intermetallic compound in the couple of Sn-3.5Ag eutectic solder and copper substrate," Materials and Materials International, Vol. 9, No. 2, pp. 193-199, 2003.

[25]. Yu D. Q., Wu C. M. L., Law C. M. T., Wang L., and Lai J. K. L., "Intermetallic compounds growth between Sn-3.5Ag lead-free solder and Cu substrate by dipping method," Journal of Alloys and Comounds, Vol. 392, No. 1-2, pp. 192-199, 2005.

[26]. Takaku Y., Liu X. J., Ohnuma I., Kainuma R., and Ishida K., "Interfacial reaction and morphology between molten Sn base solders and Cu substrate," Material Transactions, Vol. 45, No. 3, pp. 646-651, 2004.

[27]. Bader S., Gust W., and Hieber H., "Rapid formation of intermetallic compounds by interdiffusion in the Cu-Sn and Ni-Sn systems," Acta Metallurgica et Materialia, Vol. 43, No. 1, pp. 329-337, 1995.

[28]. Li J. F., Mannan S. H., Clode M. P., Whalley D. C., and Hutt D. A., " Interfacial reaction between molten Sn-Bi-X solders and Cu substrates for liquid solder interconnects," Acta Materialia, Vol. 54, No. 11, pp. 2907-2922, 2006.

[29]. Li G. Y. and Chen B. L., "Formation and growth kinetics of interfacial intermetallics in Pb-free solder joint," IEEE Transactions on Components and Packaging Technologies, Vol. 26, No. 3, pp. 651-658, 2003.

[30]. Ladani L. and Razmi J., "IMC growth in solid-liquid interdiffusion bonds," Thermal and Thermomechanical Phenomena in Electronic Systems (ITherm), 2010 12th IEEE Intersociety Conference on 2-5 June 2010 Las Vegas, NV.

[31]. Chen J. K., Beraun J. E., and Tzou D. Y., "A dual-phase-lag diffusion model for predicting intermetallic compound layer growth in solder joints," Journal of Electronic Packaging, Vol. 123, No. 1, pp. 52-57, 2001.

[32]. Chen J. K., Beraun J. E., and Tzou D. Y., "A dual-phase-lag diffusion model for predicting thin film growth," Journal of Semiconductor Science and Technology, Vol. 15, No. 3, pp. 235-241, 2000.

[33]. Chen J. K., Beraun J. E., and Tzou D. Y., "A dual-phase-lag diffusion model for interfacial layer growth in metal matrix composites," Journal of Materials Science, Vol. 34, No. 24, pp. 235-241, 1999.

[34]. Tzou D. Y., "Macro- to micro-scale heat transfer: The lagging behavior," Taylor and Francis, New York, 1997.

[35]. Dybkov, "Reaction diffusion in heterogeneous binary systems. Part 2. Growth of the chemical compound layers at the interface between two elementary substances: two compound layers," Journal of Materials Science, Vol. 21, No. 9, pp. 3085-3090, 1986.

[36]. Dybkov V. I., "Reaction diffusion and solid state chemical kinetics," the IPMS Publication, Kyiv 2002.

[37]. Dybkov V. I., "Reaction diffusion in binary solid-solid, solid-liquid and solid-gas systems: common and distinctive features," Defect and Diffusion Forum, Vols. 194-199, pp.1503-1522, 2001.

[38]. Dybkov V. I., Khoruzha V. G., Sidorko V. R., Meleshevich K. A., Samelyuk A. V., Berry D. C., and Barmak K., " Interfacial interaction of solid cobalt with liquid Pb-free Sn-Bi-In-Zn-Sb soldering alloys," Journal of Materials Science, Vol. 44, No. 22, pp. 5960-5979, 2009.

[39]. Dybkov V. I., Khoruzha V. G., Sidorko V. R., Meleshevich K. A., Samelyuk A. V., Berry D. C., and Barmak K., " Interfacial interaction of solid nickel with liquid Pb-free Sn-Bi-In-Zn-Sb soldering alloys," Journal of Alloys and Compounds, Vol. 460, No. 1-2, pp. 337-352, 2008.

[40]. Dybkov V. I., Marmak K., Lengauer W., and Gas P., "Interfacial interaction of solid nickel with liquid bismuth and Bi-base alloys," Journal of Alloys and Compounds, Vol. 389, No. 1-2, pp. 61-74, 2005.

[41]. Dybkov V. I., "Interaction of 18Cr-10Ni stainless-steel with liquid aluminum," Journal of Materials Science, Vol. 25, No. 8, pp. 3615-3633, 1990.

[42]. Barmak K. and Dybkov V. I., "Interaction of iron-chromium alloys containing 10 and 25 mass % chromium with liquid aluminum, Part 2: formation of intermetallic compounds," Journal of Materials Science, Vol. 39, No. 13, pp. 4219-4230, 2004.

[43]. Wang C. H. and Kuo C., "Interfacial reactions between eutectic Sn-Pb solder and Co substrate," Journal of Materials Science, Vol. 46, No. 8, pp. 2654-2661, 2011.

[44]. Chada S., Fournelle R. A., Laub W., and Shangguan D., "Copper substrate dissolution in eutectic Sn-Ag solder and its effect on microstructure," Journal of Electronic Materials, Vol. 29, No. 10, pp. 1214-1221, 2000.

[45]. Barmak K. and Dybkov V. I., "Interaction of iron-chromium alloys containing 10 and 25 mass % chromium with liquid aluminum, Part 1: dissolution kinetics," Journal of Materials Science, Vol. 38, No. 15, pp. 3249-3255, 2003.

[46]. Bernstein L., "Semiconductor joining by the solid-liquid-interdiffusion (SLID) process," Journal of the Electrochemical Society, Vol. 113, No. 12, 1966.

[47]. Bernstein L. and Batholomew, " Application of solid-liquid interdiffusion (SLID) bonding in integrated-circuit fabrication," Transactions of the Metallurgical Society of AIME, Vol. 236, No. 3, pp. 405-412, 1966.

[48]. Lee C. C. and Wanh C. Y., " A low temperature bonding process using deposited gold-tin composites," Journal of Thin Solid Films, Vol. 208, No. 2, pp. 202-209, 1992.

[49]. Lin J. C., Huang L-W., Jang G-Y., and Lee S. L., "Solid-liquid interdiffusion bonding between In-coated silver thick films," Journal of Thin Solid Films, Vol. 410, No. 1, pp. 212-221, 2002.

[50]. Bosco N. S. and Zok F. W., "Strength of joints produced by transient liquid phase bonding in the Cu-Sn system," Acta Materialia, Vol. 53, No. 7, pp. 2019-2027, 2005.

[51]. Bobzin K., Lugscheider E., Zhuang H., Ernst F., Bagcivan N., Maes M., Rosing J., Ferrara S., Erdle A., and Kramer A., " New soldering processes and solder systems for hybrid

microsystems: developments and applications," Microsystem Technology, Vol. 12, No. 7, pp. 620-625, 2006.

[52]. Zou H. F. and Zhang Z. F., "Solid-liquid and liquid-state interfacial reactions between Sn-based solders and single crystal Ag substrate," Journal of Alloys and Compounds, Vol. 469, No. 1-2, pp. 207-214, 2009.

[53]. Ladani L. J., Razmi J., and Bentley J., " Microstructural and mechanical strength of snag-based solid liquid inter-diffusion bonds for 3 dimensional integrated circuits," Journal of Thin Solid Films, Vol. 518, No 17, pp. 4948-4954, 2010.

[54]. Ladani L. J. and Razmi J., " Bonding strength and microstructure of SnAg-based solid liquid inter-diffusion bonds," Proceeding of the ASME 2009 International Engineering Congress and Exposition, IMCE2009, November 13-19, Lake Buena Vista, Florida, USA.

[55]. ImageJ website "http://rsb.info.nih.gov/ij/index.html", visited in 05/23/2011.

[56]. Mattafirri S., Barzi E., Finsechi F., and Rey J. M., "Kinetics of phase growth in the Cu-Sn system and application to composite Nb_3Sn strands," IEEE Transaction on Applied Superconductivity, Vol. 13, No. 2, pp. 3418-3421, 2003.

[57]. Tang W. M., He A. Q., Liu Q., and Ivey D. G., "Solid state interfacial reactions in electrodeposited Cu/Sn couples," Transactions of Nonferrous Metals Society of China, Vol. 20, No. 1, pp. 90-96, 2010.

[58]. Gagliano R. A. and Fine M. E., "Thickening kinetics of interfacial Cu_6Sn_5 and Cu_3Sn layers during reaction of liquid tin with solid copper," Journal of Electronic Materials, Vol. 32, No. 12, pp. 1441-1447, 2003.

Chapter 3 : Effect of Joint Size on Microstructure and Growth Kinetics of Intermetallic Compounds in Solid-Liquid Interdiffusion Sn-3.5Ag/Cu-Substrate Solder Joints

Abstract

The effect of joint size on the interfacial reaction in Sn3.5Ag/Cu-substrate soldering system was examined. An experiment was conducted in which parameters such as bonding time, temperature, and pressure were varied at multiple levels. Morphology and thickness of all intermetallic compounds were analyzed using scanning electron microscopy (SEM) and energy-dispersive x-ray spectroscopy (EDX) techniques. Examination of microstructures of solder joints of different sizes revealed that the size of the solder joint has no effect on the type of intermetallic compounds formed during the process. It was found that joint size affected the thickness of intermetallic layers significantly. Cu_3Sn Intermetallic layers formed in the solder joints of smaller size were found to be thicker than those in the solder joints of larger size. In all specimen sizes, the increase in the thickness of Cu_3Sn intermetallic layers with soldering time was found to obey a parabolic relationship. Also, for the cases when eutectic solder is available in the joints similar soldering time and temperature dependency were found for Cu_6Sn_5 IMC phase. The intermetallic growth of Cu_3Sn phase was under volume-diffusion controlled mechanism. Growth rate constants and activation energies of intermetallic layers were also reported for different joint thicknesses. Furthermore, the growth rate constants and activation energies of Cu_3Sn intermetallic layer were found to increase with the reduction in the size of the joints.

3.1 Introduction

Solder alloys and soldering processes are used extensively in electronic assemblies. Traditionally, eutectic or near-eutectic Sn-Pb alloys have been the most widely-used solders for electronic packaging [1-2]. However, due to legal and technological factors that press for alternative soldering materials, Pb-free solder material is replacing the traditional Sn-Pb solders. The binary and ternary alloys based on the Sn-Cu and Sn-Ag alloy systems are leading candidates in near-eutectic and alloyed forms.

The demand for higher and faster functionality in electronic products has pushed the electronic industry sector towards developing more advanced types of packaging such as three-dimensional integrated circuits (3D-ICs) and wafer-level packaging (WLP). This has resulted in miniaturized interconnects and new processes proposed to fabricate these interconnects. It is well-known that when one of the components' dimensions approaches a characteristic size of the material's microstructure, mechanical size effects occur [3]. Interconnects are considered examples of components which have three small dimensions on the same order of magnitude as the microstructural length scales of their respective materials. The microstructural and structural size effects are expected to have significant impact on the mechanical behavior of such interconnects. Furthermore, new joining technologies are required to fabricate these miniaturized interconnects. One method is solid-liquid interdiffusion (SoLID) technique. SoLID soldering method is one of the potential bonding techniques that are compatible with modern advanced packages such as 3D-ICs and WLP. In this technique, a small amount of low melting temperature material such as solder alloy is deposited on a high melting temperature material such as Cu. During the bonding process, a pair of doubly-deposited materials are placed in contact and heated to a temperature above the melting point of the low-melting material. Pressure may be used to achieve a smoother

78

bond, improve the contact surface, and remove defects such as voids. Upon melting, phase transformation of the liquid component to a high-melting material intermetallic (IMC) compound takes place at the contact interface. IMC is required for successful bonding and possesses the desired high temperature and mechanical stabilities. The formation, growth, morphology, and thickness of an IMC layer is a critical issue for the reliability of solder joints and, therefore, the integrity of the entire electronic package [4]. In a case of a very small joint, the whole joint may consist of only IMCs [5].

A number of studies have been conducted to explore the SoLID process. Bernstein [6] and Bernstein and Batholomew [7] demonstrated the feasibility of using SoLID bonding at low-temperature processing conditions to produce high-temperature bonds which can be used in semiconductor and non-semiconductor brazing and bonding applications. Roman and Eager [8] investigated SoLID bonding of Ag, Au, and Cu base materials using a variety of commercial solder alloys. Bonds as strong as or stronger than the ones obtained by conventional soldering techniques were formed. Li et. al [9-11] investigated the kinetics of the interfacial reaction in a variety of SoLID solder alloy/substrate systems at different bonding temperatures and times. They found that microstructural features and growth kinetics of IMCs formed by SoLID were significantly different from those formed by conventional soldering process.

Other studies were carried out to address the effect of process parameters on the reliability and integrity of the solder joints. Ladani and Razmi [12-13] implemented a full-factorial experiment on the SoLID soldering process to investigate the effect of process parameters such as time, temperature, and pressure on the bond strength and microstructure of Sn-3.5Ag/Cu solder system. It was found that bonding temperature was the most influential factor on the bond strength. Bartels et. al [14] investigated IMC phase formation in Sn/Cu SoLID joints.

79

Microstructural and mechanical characterizations of IMC bonds were performed. It was found that at longer times and higher temperatures, the IMC formation rate increased.

Despite the extensive literature which addresses the growth kinetics of IMCs in SoLID used to join a variety of solder alloy/substrate material systems, there is limited focus on the effect of joint size and geometry on growth kinetics and morphology of the interfacial IMCs presented in small SoLID lead-free solder interconnects. Wu et. al [15] studied the effect of joint thickness on microstructure and tensile properties of Sn-9wt.% Zn/Cu-substrate joint system. It was found that the IMC volume fraction in the joints increased upon decreasing the joint thickness. This was because of the rapid increase of Cu which diffused from substrate into molten solder, within the bulk solder due to decreasing joint thickness. Wiese and Wolter [16] and Wiese et. al [17] analyzed the microstructure of SnAgCu/Cu and Sn-3.5Ag/Cu solder systems. It was found that the microstructure consisted of larger β-Sn dendrites surrounded by a quasi-eutectic phase when Sn-Ag-Cu solder alloy was used in bulk solder specimen. When the same solder alloy was used in a bond configuration, meaning a smaller amount of solder, smaller grains with a columnar structure were formed [16]. The change in grain size and microstructure morphology was attributed to the size effect which was introduced when the solder was used in bond configuration. Zimprich et. al [18-20] compared the microstructure of solder joints with different sizes. Specimens with gap sizes adjusted between 25 and 850 μm were reflow soldered using Sn-3.5wt.% Ag solder alloy. Larger joints showed coarser microstructures compared to small ones. No quantitative information about the grain size was reported.

Huang et al. [21-22], Kinyanjui et. al [23], and Cho et al. [24], demonstrated the dependency of the solidification process on specimen size and under bump metallurgies (UBM) of Pb-free solder alloys. Decreasing specimen size resulted in rapid solidification of molten alloys because

of the under-cooling phenomenon.   Under-cooling has a direct influence on the resulting microstructure of solder joints as well as their mechanical properties. Therefore, the microstructure is directly affected by the joint size. Castro et. al [25] observed a substantial change in the morphology with joint size of three systems of Sn-Pb solder alloys: hypoeutectic, eutectic, and hypereutectic compositions. There was a critical degree of under-cooling at which a transition from lamellar eutectic to anomalous eutectic occurred in Sn-Pb system. The former morphology was a result of rapid solidification, which occurred in small solder joints, while the latter formed due to slow solidification conditions which were associated with large solder joints. Yang et. al [26] addressed the effect of joint size on Sn grain features of Pb-free solder alloy such as number of Sn grains across the joint thickness and grain orientation and distribution. It was found that the number of grains is independent of joint size, aging time, and number of reflows. It was also reported that the Sn grains show highly preferred orientation angles in which the c-axis of the Sn grains tended to be at a small angle with the Cu pads. However, Cong et. al [27] arrived at an opposite conclusion in terms of number of grains across the solder joint thickness. They found that the number of Sn grains across the joint thickness diminished as the joint size decreased.

In the present work, the effect of joint size on the interfacial reaction of Sn-3.5Ag/Cu solder system fabricated using SoLID soldering technique is addressed. In particular, the study compares the effect of size on the resulting interfacial microstructure and morphology. It also carries out a comparison on the growth kinetics of solder joints under the effect of size.

3.2 Experimental Procedure

3.2.1 Specimen Fabrication

Figure 3-1 shows actual images and schematic drawings of the specimens used in this study. Two configurations of specimen design were used. One is a "small-scale specimen" (SS) as shown in Figure 3-1(a). The other configuration is a "large-scale specimen" (LS) and is shown in Figure 3-1(b). As seen in this figure, SS specimen was made of a pair of silicon layers. On the top of each Si-layer, two Cu layers of 15 μm-thick and 1.5 mm-wide were deposited on opposite sides using electron-beam deposition technique. 5 μm-thick Sn-3.5wt.%Ag was then deposited on Cu layers using lift-off procedure. Lift-off technique requires the deposited film thickness to be at least less than one-third of resist depth in order to ensure discontinuity of film, and therefore, a successful lift-off [28]. The LS specimen was made of a pair of (15x5x1) mm Cu layers. A layer of Sn-3.5wt.%Ag solder alloy was manually deposited on Cu layers and sandwiched between the Cu layers during the specimen fabrication. Due to the limited suitability of lift-off technique in producing high-aspect-ratio pattern structures, configuration of LS specimen is different from that for SS specimen. The noticeable difference is the Cu thickness which should not influence the IMC formation during fabrication process as long as Cu layer still has not been consumed totally. The LS fabrication started with polishing the Cu surfaces up to 1200 grit SiC using standard methods followed by cleaning with isopropyl alcohol. Solder paste was then deposited on the cleaned surface. An activation agent was used to activate the chemical reaction during the soldering process. The two Cu surfaces were then placed in intimate contact in the thermal chamber. Bonding temperature and time were varied, and specimens were cooled to room temperature after fabrication.

82
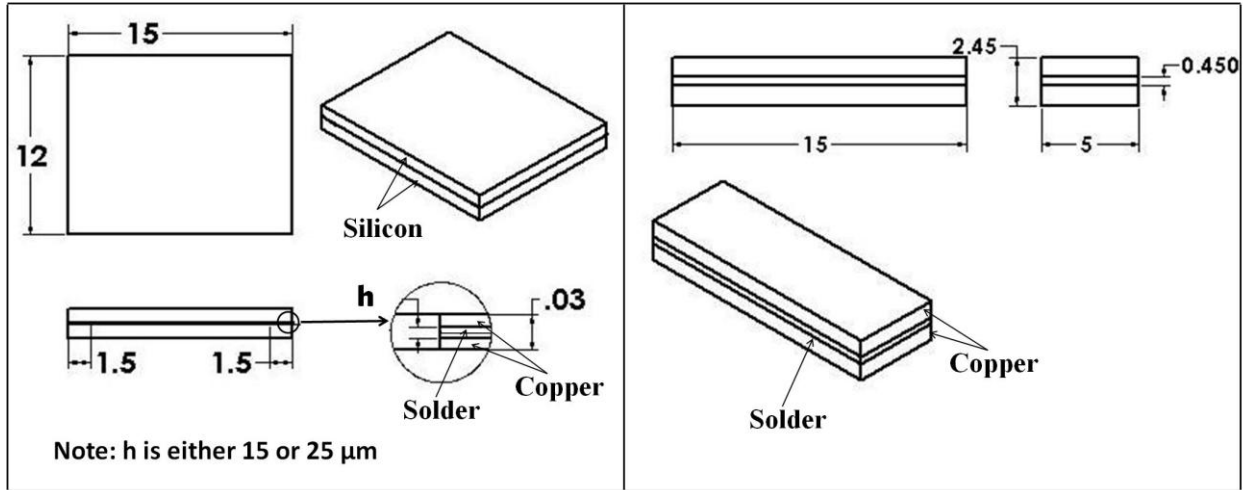
Figure 3-1: (a) Schematic drawing of SS specimen. (**b**) Schematic drawing of LS specimen. Dimensions are in mms.

The joint thicknesses of SS specimens were controlled by applying pressure and are on average about 15 μm (0.55 MPa pressure) and 25μm (0 MPa pressure) in SS configuration and 450 μm in LS configuration. Table 3-1 summarizes the process parameters and their levels.

As identified in many studies, most solder joints (in particular the Sn3.5Ag/Cu-substrate system considered in this study) have two distinctive microstructural features. The first is a eutectic bulk structure consisting of IMC particles such as Ag_3Sn or Cu_6Sn_5. The second is Cu-Sn IMC layer which consists of Cu_6Sn_5 layer at the solder/Cu interface. Under particular conditions, Cu_3Sn could co-exist at the Cu_6Sn_5-Cu interface. To fabricate solder joints containing all possible microstructural features, the process time and temperature were varied in a wide range as shown in Table 3-1. Four replicas were tested in each run of the experiment. This experiment was conducted on all three specimen sizes.

Table 3-1: Process parameters and their levels used during the fabrication process of specimens.

Experiment Run	Temperature, (^{o}C)	Time, (min)
1	260	20
2	260	90
3	260	240
4	310	20
5	310	90
6	310	240
7	360	20
8	360	90
9	360	240

3.2.2 Microstructure Characterization

Microstructural characterization followed the specimen fabrication. A JEOL JSM 7000F scanning electron microscope (SEM) using a backscatter electron signal was used for microstructural characterization. The IMC layers formed between the bulk solder and the Cu substrates were identified using energy-dispersive X-ray spectroscopy (EDX) microanalysis system installed on the SEM. An image analysis method was used to post process the SEM images and measure the IMC layers and bond thicknesses. A detailed description of how the IMC thickness was determined can be found elsewhere [29].

3.3   Results

3.3.1 Interfacial Microstructure

A continuous bilayer of scalloped η-phase Cu_6Sn_5 (adjacent to the solder) and ε-phase Cu_3Sn (adjacent to the Cu substrate) was observed in all the SEM micrographs as shown in Figures 3-2 and 3-3. Figure 3-2 shows SEM micrographs of 25μm-thick (SS2) Sn-3.5Ag solder joints fabricated at three different temperatures and three different soldering times. Similarly, Figure 3-3 shows SEM micrographs of 450μm-thick (LS) Sn-3.5Ag solder joints. The SEM micrographs

of the Sn-3.5Ag solder joints of 15μm-thick (SS1) were similar to those of 25μm-thick (SS2) solder joints and, therefore, were omitted for the sake of brevity.
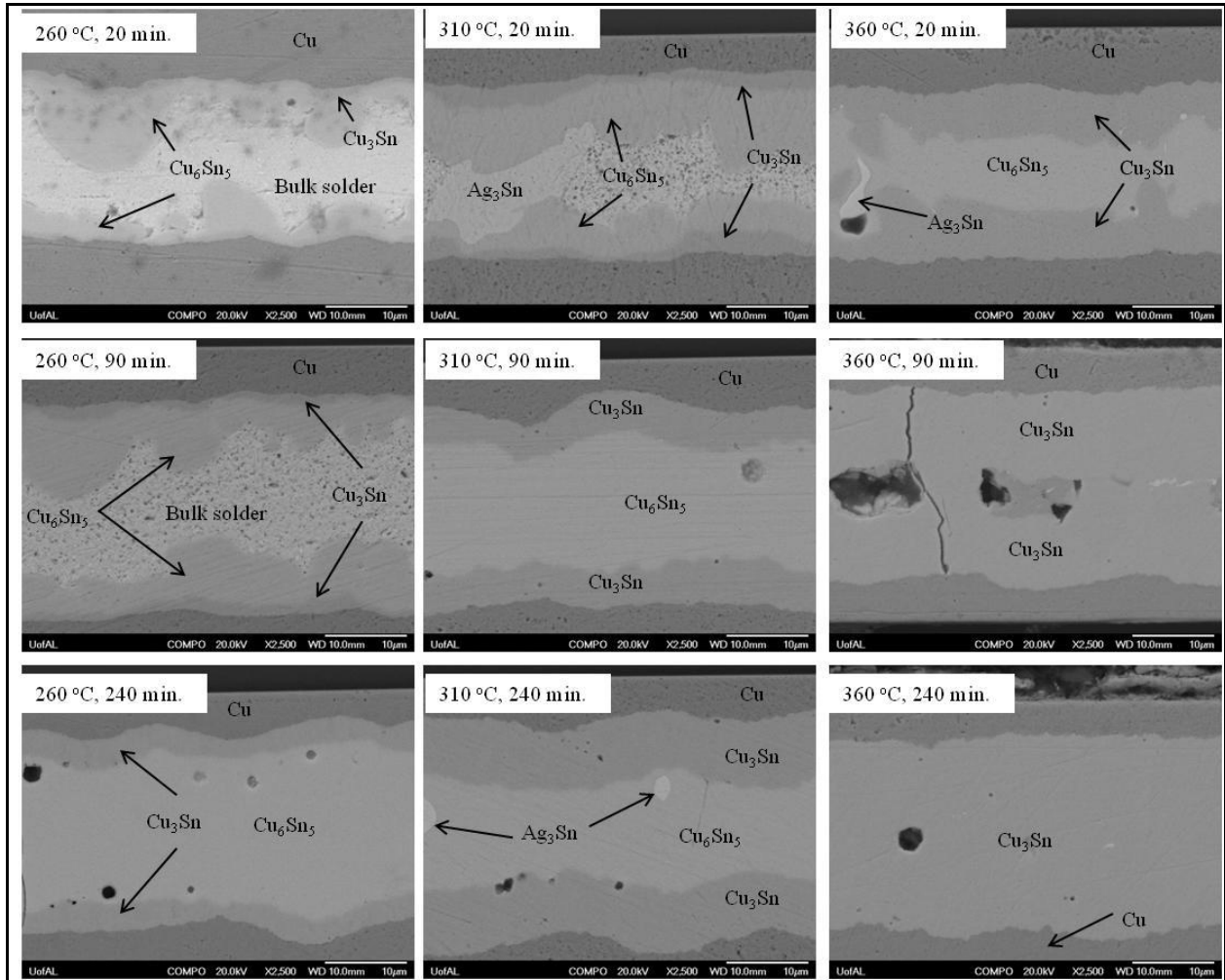
Figure 3-2: SEM backscattered electron images illustrating the microstructure of Sn-3.5Ag/Cu solder joints of SS2 specimen (25 μm-thick) fabricated at different temperatures for various soldering times.

The two IMC phases, η- and ε-IMC phases, are common in all specimens soldered for the designated soldering time and temperatures applied in this study. In addition to the η- and ε-IMC layers located at solder/substrate interface, isolated IMC phase precipitates such as Cu_6Sn_5 and Ag_3Sn were observed inside the solder bulk.
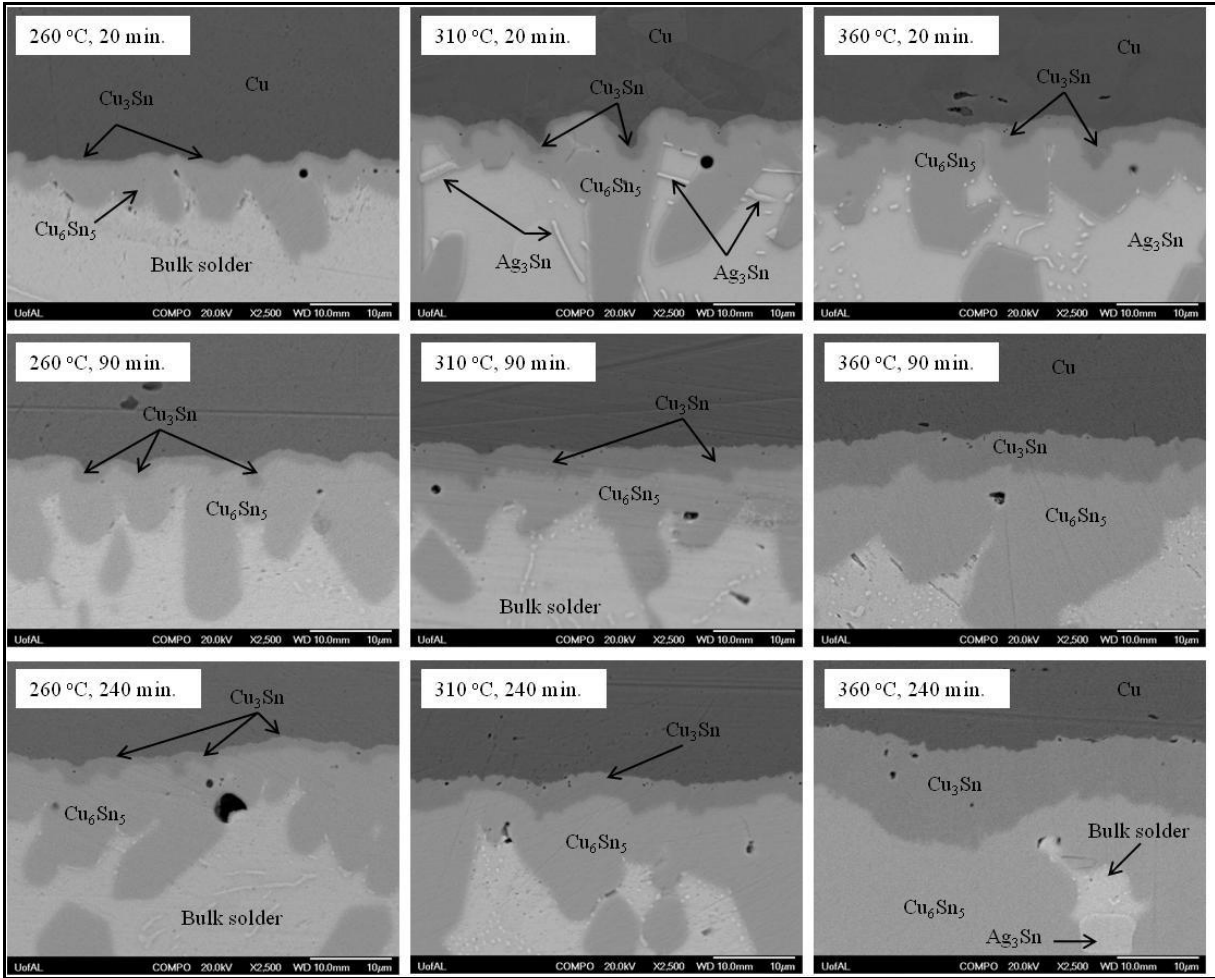
Figure 3-3: SEM backscattered electron images illustrating the microstructure of Sn-3.5Ag/Cu solder joints of LS specimen (450 µm-thick) fabricated at different temperatures for various times.

The chemical compositions of the IMC phases are presented in Figure 3-4. Figure 3-4(a-bottom) shows the chemical composition of the IMC layer adjacent to the Cu layer that was collected at position (a) in Figure 3-4(a-top). EDX data was used in calculating the mass percentage of each element presented in the layer. It confirms that the IMC layer adjacent to Cu substrate is indeed Cu_3Sn IMC which was distinguished from the other IMC by its gray level. Similarly, Figure 3-4(b-bottom) shows the chemical composition of the IMC layer adjacent to the bulk solder which was collected at position (b) in Figure 3-4(b-top). When mass percentage of each element was calculated using EDX data, it was confirmed that this IMC layer was Cu_6Sn_5 IMC. Figure 3-4(c-

bottom) shows the composition of Ag₃Sn IMC which randomly forms in the bulk solder or within the Cu-Sn IMCs. As seen in Figure 3-4(c-top), the EDX data was collected at position (c). Examination of microstructures of solder joints of different sizes revealed that the size of solder joint has no effect on the types of IMC layers present in the joint.

Cu_3Sn			Cu_6Sn_5			Ag_3Sn		
Element	wt.%	at.%	Element	wt.%	at.%	Element	wt.%	at.%
CuK	66.38	78.67	CuK	45.58	61.00	AgK	73.37	75.21
SnL	33.62	21.33	SnL	54.42	38.99	SnL	26.63	24.79
Total	100	100	Total	100	100	Total	100	100
(a)			**(b)**			**(c)**		
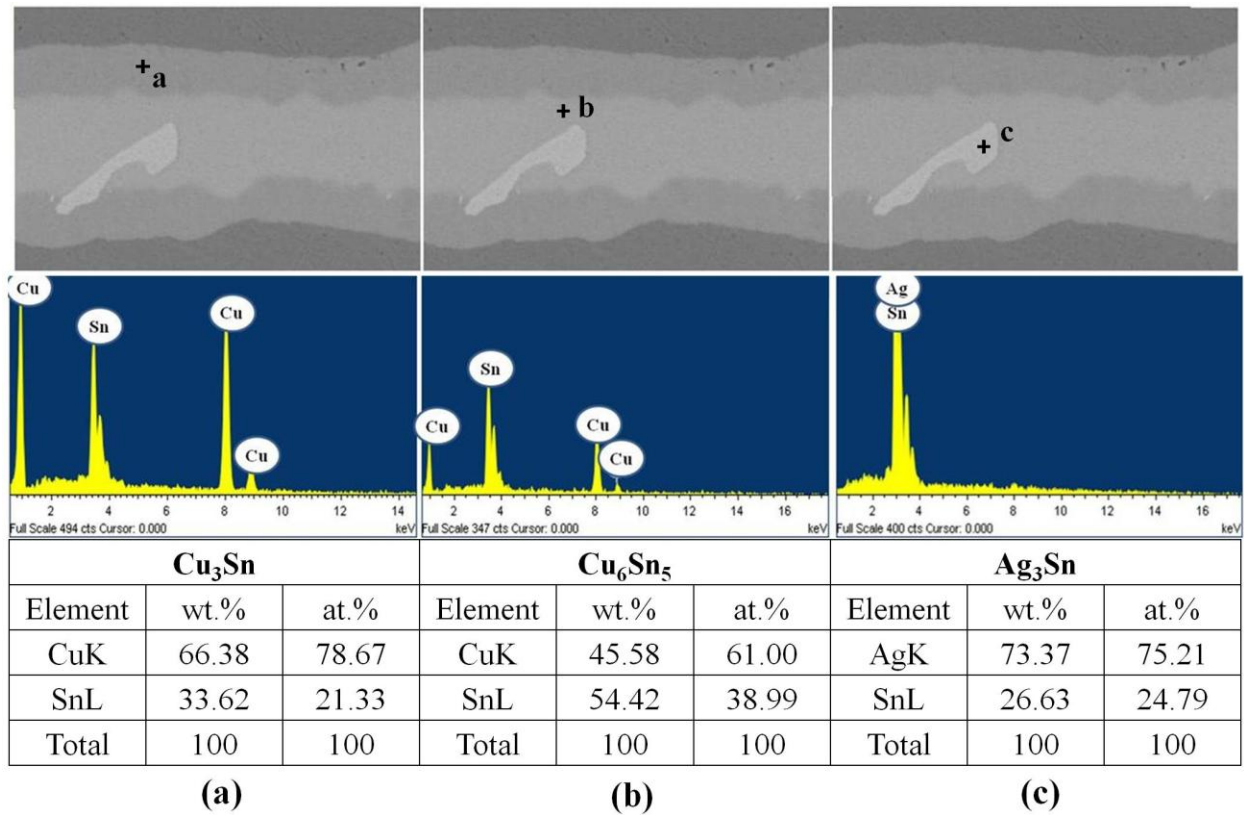
Figure 3-4: EDX analysis indicating the presence of (a) Cu_3Sn, (b) Cu_6Sn_5, and (c) Ag_3Sn IMCs in Sn-3.5Ag/Cu solder joints.

3.3.2 IMC Growth

Figure 3-5 shows the dependence of growth behavior of IMC layers at different temperatures in different specimens. Figure 3-5(a-c) shows the thickness-time relationship of IMC growth for Cu_6Sn_5 IMC layer while Figure 3-5(d-f) shows the thickness-time relationship of growth of Cu_3Sn IMC layer at three different temperatures in SS1, SS2, and LS specimens. As seen in Figure 3-5(a-c), due to the limited amount of bulk solder in the joint of SS1 specimen, the

thickness of Cu_6Sn_5 IMC layer initially increases to the point when all the bulk solder is consumed and then decreases as time increases.
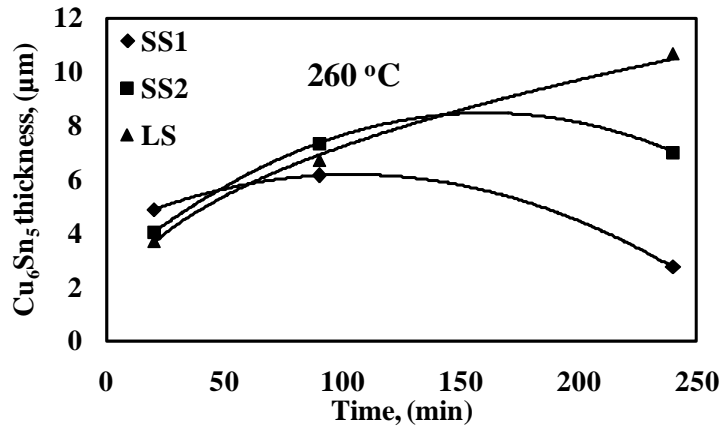
Figure 3-5a: Comparison of Cu_6Sn_5 IMC growth behavior in different specimen sizes at soldering temperature of 260^oC.
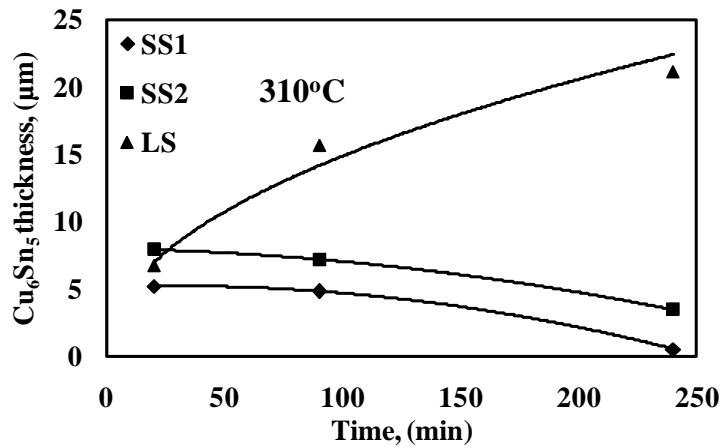
Figure 3-5b: Comparison of Cu_6Sn_5 IMC growth behavior in different specimen sizes at soldering temperature of 310^oC.
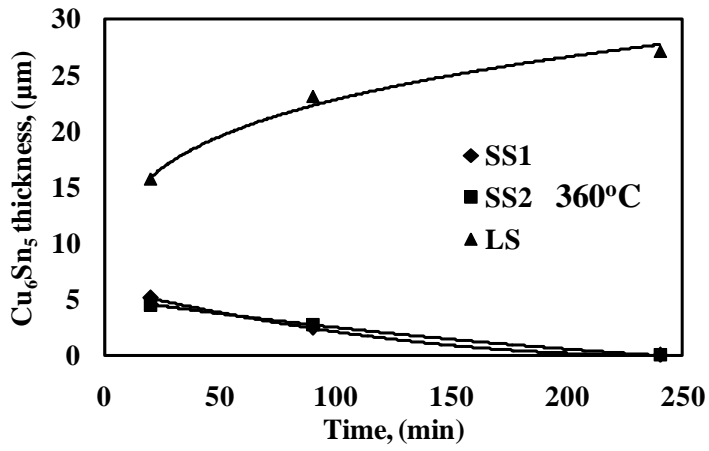
Figure 3-5c: Comparison of Cu_6Sn_5 IMC growth behavior in different specimen sizes at soldering temperature of 360^oC.
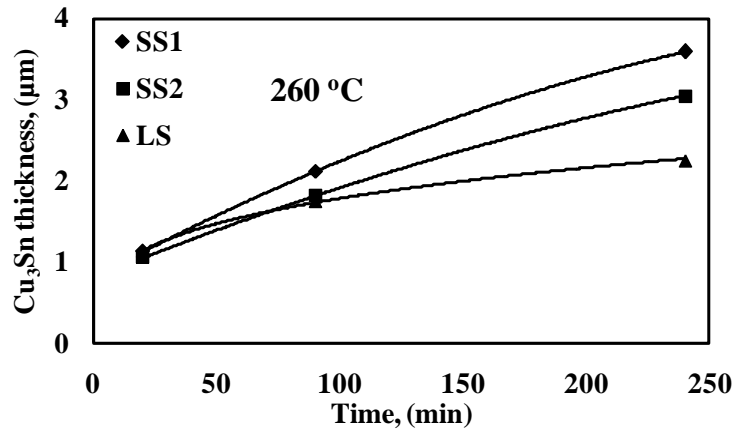
Figure 3-5d: Comparison of Cu_3Sn IMC growth behavior in different specimen sizes at soldering temperature of 260^oC.
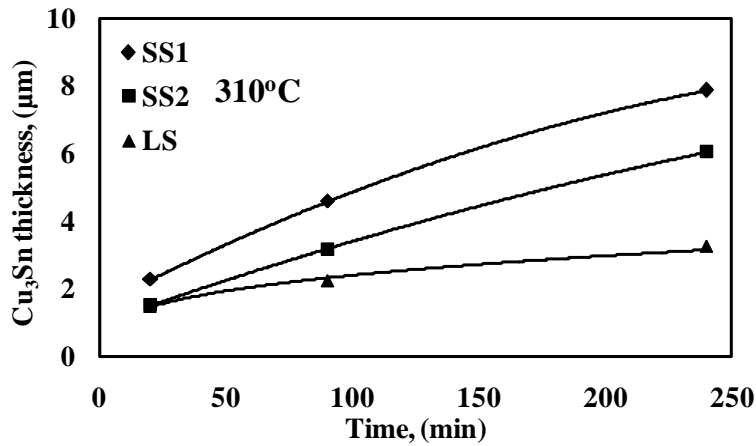
Figure 3-5e: Comparison of Cu_3Sn IMC growth behavior in different specimen sizes at soldering temperature of 310^oC.
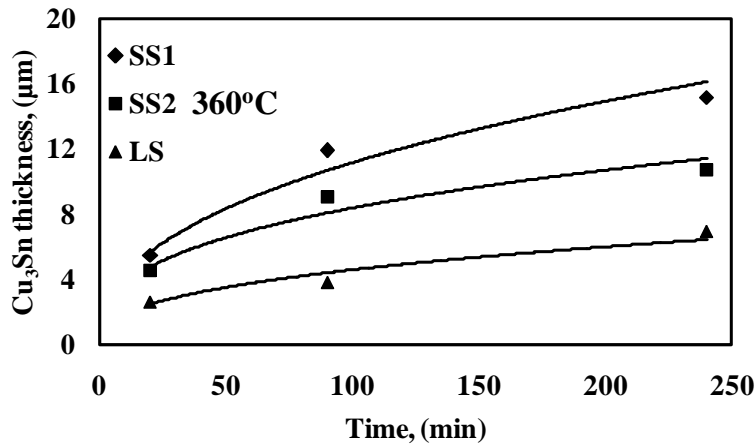
Figure 3-5(f): Comparison of Cu_3Sn IMC growth behavior in different specimen sizes at soldering temperature of 360^oC.

This non-monotonic behavior is observed at temperatures of 260^oC. However, at higher temperature of 310^oC even though the bond contains some bulk solder after it was soldered for 20 min, Cu_6Sn_5 IMC shows decreasing behavior after 90 min soldering time. It is believed that the thickness of Cu_6Sn_5 IMC increases first by consuming the remaining bulk solder and then it decreases due to its consumption in forming Cu_3Sn IMC. Over all, Cu_6Sn_5 IMC shows decreasing trend due to the limited availability of bulk solder, which limits Cu_6Sn_5 IMC

formation, and the growing of Cu_3Sn by decomposition of Cu_6Sn_5 IMC. During soldering temperature of 360°C, the bond is completely filled with Cu_6Sn_5 even at the shortest time of soldering process. Therefore, the only way that Cu_3Sn can grow is with consumption of Cu_6Sn_5 which results in reduction in thickness of Cu_6Sn_5.

SS2 specimens show similar trends for IMC growth as for SS1 specimens as shown in Figure 3-5(a-c). Due to the availability of larger amount of bulk solder in SS2 specimen, Cu_6Sn_5 thickness increases and then decreases as the soldering time proceeds from 20min to 90 min and then to 240 min, during soldering temperature of 260°C. For solder joints fabricated at 310°C and 360°C, Cu_6Sn_5 IMC thickness only decreases with increasing soldering time. The same figures contain thickness-time relationships for LS specimens. For LS specimens, it has been found that the change in thickness with time nicely fits a power law equation for Cu_6Sn_5 IMC layer at each soldering temperature.

Figure 3-5(d-f) shows the time-thickness relationships for Cu_3Sn IMC layer at different temperatures in different specimens. In all specimens, the thickness of Cu_3Sn IMC layer increases as the soldering time and/or temperature increases.

As seen in Figure 3-5(a) for the solder joints made at 260°C, the thickness of Cu_6Sn_5 IMC layer in the solder joints with thickness of 450 μm increases monotonically with soldering time. At the same temperature, however, the Cu_6Sn_5 IMC trend is non-monotonic for the 15 and 25 μm-thick joints. Cu_6Sn_5 IMC shows two different periods; increasing period and decreasing period. It has been noticed that when eutectic solder is still available in the solder joint, Cu_6Sn_5 IMC shows increasing period. From the other hand, when eutectic solder is missed from the solder joint, Cu_6Sn_5 IMC shows decreasing trend because Cu_5Sn_5 IMC has been consumed in forming Cu_3Sn IMC. During the increasing period of Cu_6Sn_5 IMC, it has been noticed that as the thickness of

91

solder joint decreases, thicker Cu_6Sn_5 IMC was formed. Therefore, the growth behavior of Cu_6Sn_5 IMC layer exhibits strong dependence on the size of the solder joint.

This conclusion is less obvious in the cases where solder joints were fabricated at higher temperatures. During soldering temperatures of 310^oC and 360^oC, the Cu_6Sn_5 thickness in 450µm solder joints monotonically increases as shown in Figure 3-5(b) and Figure 3-5(c). However, Cu_6Sn_5 IMC layer thickness decreases monotonically in 15µm and 25µm solder joints during soldering temperatures of 310^oC and 360^oC. As seen from Figure 3-2, bulk solder still exists in the joint during early soldering times, e.g. 20 min, which supplies the Sn element requires for further formation of Cu_6Sn_5 IMC. When the bulk solder is consumed, there is no further formation of Cu_6Sn_5 IMC. Cu_3Sn continues to form by decomposition of Cu_6Sn_5 IMC layer. Therefore, a net reduction in the thickness of Cu_6Sn_5 IMC was observed as soldering time increases in 15µm and 25µm solder joints. In 450 µm, the bulk solder is essentially infinite and lack of Sn supply is not an issue. Therefore, Cu_6Sn_5 IMC layer showed a monotonic increase with time.

In Figure 3-5(d-f), the thickness-time relationships of IMC growth for Cu_3Sn IMC layer at three different temperatures in SS1, SS2, and LS specimens are shown. Clearly, the average thickness of the Cu_3Sn IMC layer increases as the soldering time and temperature increases. It is evident that the thickness of this IMC layer increases as the bond size decreases. This shows a strong size effect on the Cu_3Sn IMC layer growth.

The excessive growth of the IMC layers in solder joints with small size (small thickness) is mainly due to the large amount of under-cooling and, consequently, the prolonged liquid-solid interfacial reaction between the molten solder alloy and the solid substrate material. As reported by previous studies [21-22, 24], the tendency for nucleation of the primary solidification phase in

92

Sn-Ag-based solder systems is $Ag_3Sn > Cu_6Sn_5 > \beta$-Sn. In other words, Ag_3Sn is most likely to nucleate while β-Sn is the least. In small Sn-3.5Ag solder joints, the absolute amount of Ag is less than that in a large one. Therefore, decreasing solder joint size leads to reduction of the number of nucleation sites for solidification which is favorable to increase the degree of under-cooling of solder alloys.

Furthermore, a decrease in the size (thickness) of the solder joint favors the formation of larger IMC layer because the Cu concentration in liquid solder increases faster in a smaller solder joint than in a larger one. Therefore, smaller solder joints require shorter amounts of time to reach saturation. This theory is proven analytically in Section 4. As a result, the formation of a larger IMC layer at the interface of smaller solder joints would be accelerated because of a longer liquid soaking time during the soldering process which means that a higher growth rate will take place during the liquid-state of soldering.

3.3.3 Analytical Modeling of IMC Growth

The growth kinetics of IMC layers are usually treated using parabolic equations of the type:

$$l_i = k_i t^n \tag{3-1}$$

where k_i is the IMC growth rate constant of the appropriate species in the joint, n is the time exponent, and t is the reaction time. Considerable literature [10, 30-34] is available on the subject of solid-state growth of IMC in solder joints in which Eq.(3-1) has been shown to nicely fit the experimental results when a time exponent of 0.5 is used. In such a growth state, it is assumed that diffusion is the rate controlling process in IMC growth during the aging process. In molten solders, different time exponent values have been obtained (n = 0.21-0.90) from experimental results using regression analysis [11, 12].

However, growth kinetics of two IMC layers are somewhat more complicated. According to Dybkov's model [34-37], the growth of any IMC layer at the interface between two materials A and B at a given temperature is a result of counter-diffusion of components A and B across its bulk followed by partial chemical reactions between diffusing atoms of one component and surface atoms of another component. This model is able to reveal the role of diffusion and chemical reactions in determining the IMC layer growth kinetics. Moreover, it allows for the two sequential growth steps, diffusion and then chemical reaction, to be represented in separate terms, which allows for the possibility of evaluating the diffusion and chemical rate constants separately. It also allows for the effect of dissolution process to be incorporated in the model, especially in early IMC formation. More details about Dybkov's model as applied in this study can be found elsewhere [29].

The mathematical description of the layer-growth rates of A_pB_q and A_rB_s IMC layers under the diffusion-controlled mechanism may be stated as shown below [34]:

$$\frac{dx}{dt} = \frac{k'_{1A2}}{x} - \frac{rg}{p}\frac{k'_{1B2}}{y} \tag{3-2a}$$

$$\frac{dy}{dt} = \frac{k'_{1B2}}{y} - \frac{q}{sg}\frac{k'_{1A2}}{x} \tag{3-2b}$$

If A is Sn and B is Cu, then A_pB_q is Sn_5Cu_6 and A_rB_s is $SnCu_3$. Therefore, p = 5, q = 6, r = 1, and s = 3. Renaming the diffusion rate constant of Cu_6Sn_5 growth k'_{1A2} and the diffusion rate constant of Cu_3Sn growth k'_{1B2} to be $k_{Cu_6Sn_5}$ and k_{Cu_3Sn}, respectively, one can reach the following system of equations:

$$\frac{dx}{dt} = \frac{1}{x}k_{Cu_6Sn_5} - \frac{rg}{p}\frac{1}{y}k_{Cu_3Sn} \tag{3-3a}$$

$$\frac{dy}{dt} = \frac{1}{y}k_{Cu_3Sn} - \frac{q}{sg}\frac{1}{x}k_{Cu_6Sn_5} \tag{3-3b}$$

To successfully use Dybkov's model, a few assumptions are made. One assumption is that the interfacial reactions which occur at the two Sn-3.5Ag solder/Cu boundaries (at the top and bottom Cu layers) are identical. Therefore, half of the sample thickness is considered for IMC growth measurement and modeling. Furthermore, the original thickness of the bulk solder is unknown and is calculated using the remaining thickness of the bulk solder and the thicknesses of Cu_6Sn_5 and Cu_3Sn layers as follows [9]:

$$l_{SnAg\_original} = l_{SnAg\_residual} + l_{Sn\_consumed} \qquad (3\text{-}4)$$

where $l_{SnAg\_original}$ is the half thickness of the original solder layer, $l_{SnAg\_residual}$ is the half thickness of the remaining solder layer, and $l_{Sn\_consumed}$ is the half thickness of the tin consumed in forming the Cu_6Sn_5 and Cu_3Sn layers. This is found by following equation [9]:

$$l_{Sn\_consumed} = \frac{5\rho_{Cu_6Sn_5}M_{Sn}l_{Cu_6Sn_5}}{\rho_{Sn}M_{Cu_6Sn_5}} + \frac{\rho_{Cu_3Sn}M_{Sn}l_{Cu_3Sn}}{\rho_{Sn}M_{Cu_3Sn}} \qquad (3\text{-}5)$$

where $l_{Cu_6Sn_5}$ and l_{Cu_3Sn} are the measured average thicknesses of the Cu_6Sn_5 and Cu_3Sn layers in each sample. ρ and M with subscripts Sn, Cu_6Sn_5, and Cu_3Sn are the corresponding densities and molar weights, respectively.

If the remaining solder layer $l_{SnAg\_residual}$ disappears:

$$l_{SnAg\_original} = l_{Sn\_consumed} \qquad (3\text{-}6)$$

This means that eutectic solder is no longer available; Sn is missed, in the solder joint to be used in forming Cu_6Sn_5 IMC. Therefore, there will be no Cu_6Sn_5 IMC layer is further formed in the solder joint. If the solder joint still has Cu_6Sn_5 IMC ($l_{Cu_6Sn_5} > 0$) then Cu_3Sn IMC layer would grow at the expense of the previously formed Cu_6Sn_5 IMC. Thus, the system of Eq.(3-3) is modified in the following form:

$$\frac{dx}{dt} = -\frac{r_g}{p}\frac{1}{y}k_{Cu_3Sn} \tag{3-7a}$$

$$\frac{dy}{dt} = \frac{1}{y}k_{Cu_3Sn} \tag{3-7b}$$

Once the Cu_6Sn_5 IMC has been completely consumed, e.g. $l_{Cu_6Sn_5} = 0$, the interfacial reaction in

the Sn-3.5Ag/Cu system is assumed to stop. Therefore, Eq.(3-3) is modified as follows:

$$\frac{dx}{dt} = 0 \tag{3-8a}$$

$$\frac{dy}{dt} = 0 \tag{3-8b}$$

The effect of the simultaneous dissolution of Cu_6Sn_5 IMC layer and the change of Cu

concentration in the molten solder on the kinetics of the interfacial reaction is specified based on

Eq.(3-6).

$$c = c_s\left[1 - \exp\left(-\frac{Sk_d}{v}t\right)\right] \tag{3-9}$$

where c is the concentration of the dissolved substance in the bulk of the liquid at time t, c_s is the

solubility of B in A at a given temperature, k_d is the dissolution rate constant, S is the surface

area of the solid in contact with the liquid, and v is the volume of the liquid. The dissolution rate

constants; the solubility of Cu in molten solders at different temperatures; and densities of Cu, Sn

and Cu_6Sn_5 are presented in Table 3-2 [9, 38]. When the right values for the constants from

Table 3-2 are substituted into Eq.(3-9), the time required for the molten solder to saturate with

Cu for each bonding temperature can be determined for each joint thickness.

Table 3-2: Cu dissolution rate, Cu solubility limit, and IMC phase density.

k_d , (m/sec.) [37]			c_s, (wt. %Cu), [37]			ρ, kg/m³ [9]		
260 °C	310 °C	360 °C	260 °C	310 °C	360 °C	Cu	Sn	Cu_6Sn_5
8.21E-6	1.09E-5	1.39E-5	1.60	3.025	5.19	8.94	7.29	8.28

Based on this equation, saturation times were found, for temperatures of 260°C, 310°C, and

360°C and for each specimen size, as shown in Table 3-3.

Table 3-3: Saturation times at different soldering temperatures and bond thicknesses.

Temperature, (^{o}C)	Saturation time, (sec)		
	SS1	SS2	LS
260	16	22	240
310	13	18	180
360	09	15	120

According to the results indicated in Table 3-3, liquid solder in SS1 specimen saturates with Cu within 16 seconds at the lowest soldering temperature, 260°C. Saturation occurs within 22 and 240 seconds at the same lowest soldering temperature in SS2 and LS specimens, respectively. As soldering temperature increases, the saturation time decreases. Since the shortest soldering time used in this study was 1200 seconds (20 min), the dissolution effect on the calculation of IMC growth-rate constants can safely be considered negligible at such a long soldering time.

According to literature [36], the chemical reaction-controlled (linear) growth kinetics are observed with thin compound layers up to about 500-600 nm while diffusion-controlled (parabolic) growth is characteristic of much thicker compound layers (1 µm or more). The smallest thickness of Cu_6Sn_5 and Cu_3Sn IMCs (as seen in Figure 3-5) is beyond 600nm. As a result, we assumed that Cu_6Sn_5 and Cu_3Sn IMC layers must have formed under diffusion-controlled mechanism.

To evaluate the growth-rate constants, the experimental thickness measurements showed in Figure 3-5 were fitted using the systems of Eqs.(3-3), (3-7), and (3-8). The calculated values of growth-rate constants are listed in Table 3-4.

Table 3-4: Growth-rate constants and activation energies of IMC diffusional growth in Sn-3.5Ag/Cu solder system.

Specimen size (µm)	Temperature, (^{o}C)	k, (m^2/sec)		Q, (kJ/mol.)	
		Cu_6Sn_5	Cu_3Sn	Cu_6Sn_5	Cu_3Sn
15 (SS1)	260	-	8.36E-15	-	50.32
	310	-	4.34E-14		
	360	-	1.26E-13		
	260	-	6.19E-15		

25 (SS2)	310	-	2.88E-14	-	53.37
	360	-	5.07E-14		
450 (LS)	260	6.72E-14	1.70E-15	27.89	66.32
	310	1.39E-13	4.32E-15		
	360	1.74E-13	2.69E-14		

The results of a computation performed according to Eqs.3-8, 3-12 and 3-13 showed that the growth-rate constants (k) of the Cu_3Sn IMC layer at the interface of the joints increased with decreasing the joint thickness, as shown in Table 3-4. For example, k values changes from 1.70 x 10^{-15} m^2/sec to 6.19 x 10^{-15} m^2/sec then to 8.36 x 10^{-15} m^2/sec at soldering temperature of 260°C, corresponding to joint thicknesses of 450, 25, and 15 µm, respectively. A similar trend is found in joints fabricated at temperatures of 310°C and 360°C. Values for Cu_6Sn_5 IMC growth-rate constants have not been calculated in SS1 and SS2specimens at any soldering temperatures because the limited supply of bulk solders which affected the formation of Cu_6Sn_5 IMC and resulting into non-monotonic growth behavior. Therefore, values of Cu_6Sn_5 growth-rate constants were obtained in LS specimens at all soldering temperatures. Therefore, comparison of values of Cu_6Sn_5 growth-rate constants in different specimens was not possible.

The temperature dependency of the extracted values of k is further exploited using the Arrhenius relationship to determine the activation energies for the growth of Cu_6Sn_5 and Cu_3Sn IMC layers using the following equation:

$$k = k_o \exp\left(-\frac{Q}{RT}\right) \qquad (3\text{-}10)$$

where k_o is the layer growth constant, Q is the activation energy, R is the gas constant (8.314 J/mol.-K), and T is the soldering temperature (absolute units). The activation energies were calculated from the slope of the Arrhenius plot using a linear regression model.

Figure 3-6 shows the log-log plot of growth rate constant versus reciprocal of temperature for the growth of IMC layers. Figure 3-6(a) shows the log-log plot of growth rate constant versus reciprocal of temperature for Cu_6Sn_5 IMC layer while Figure 3-6(b) shows the log-log plot of

growth rate constant versus reciprocal of temperature for the growth of Cu_3Sn IMC layer during diffusion-controlled growth stage.

The apparent activation energies for the growth of Cu_6Sn_5 and Cu_3Sn IMC layers in different specimen sizes are listed in Table 3-4. The change in activation energy with joint size is also shown in Figure 3-7 for Cu_3Sn IMC layer. As seen from the plot, the activation energy for growth of Cu_3Sn IMC layer increases with increases of solder joint size. Lower activation energy in smaller solder joints means that IMC formation is at higher rates. Therefore, much thicker IMC layer will grow in smaller joints at the same soldering time and temperature.
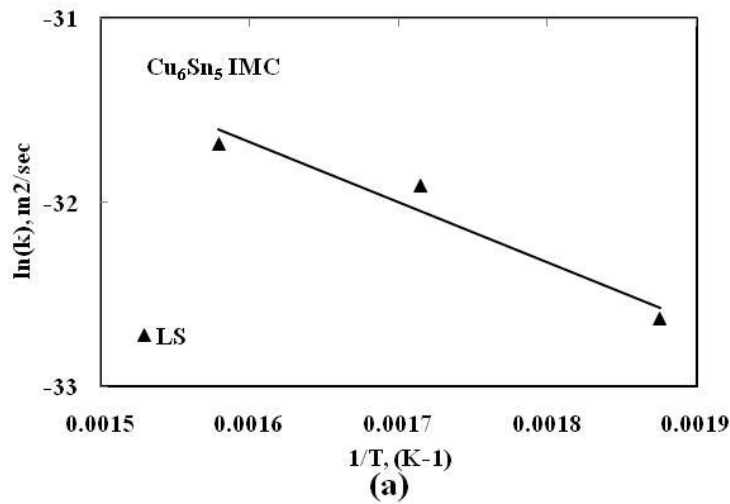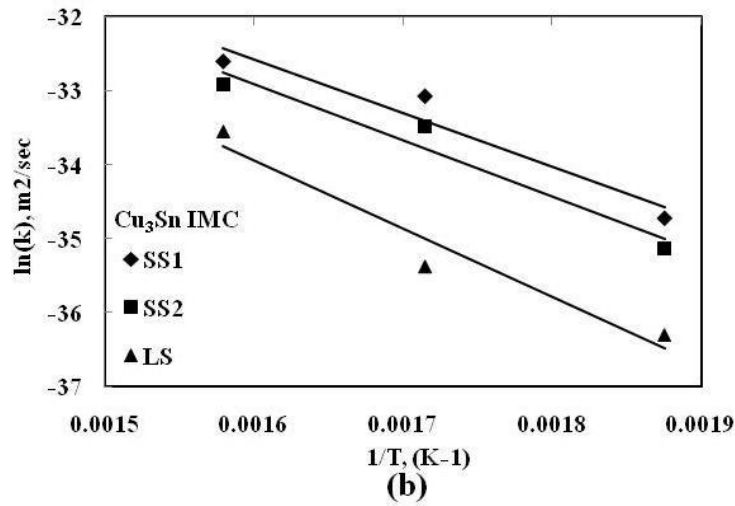
Figure 3-6: Log-log plot of growth rate constant versus reciprocal of temperature (a) for Cu_6Sn_5 IMC layer and (b) for Cu_3Sn IMC layer in different specimen sizes.
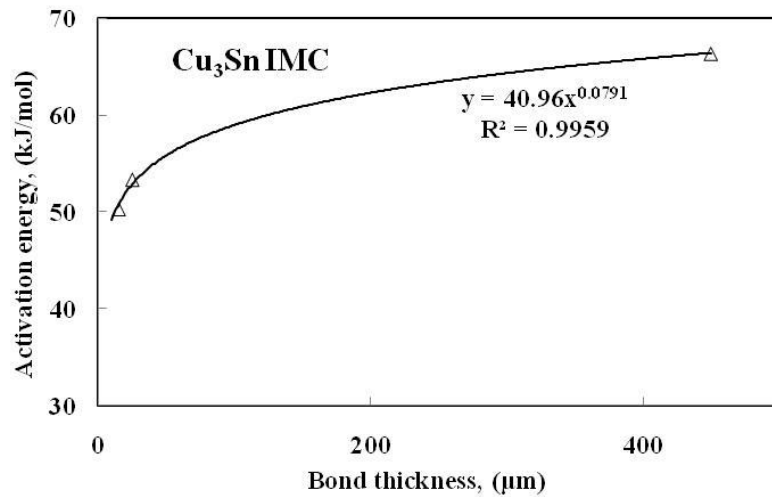
Figure 3-7: Effect of bond thickness on the activation energy of the IMC growth in Sn-3.5Ag/Cu soldering system.

3.4 Conclusions

The effect of solder joint size on the microstructure and growth kinetics of intermetallic compounds in Sn-3.5Ag/Cu-substrate soldering system was investigated through experiment and analytical modeling.

- It was found that the size of solder joint, represented by its thickness, does not introduce any effects on the type of IMCs in the joint microstructure. All specimens of different sizes have shown that the IMC compound layer is composed of two phases: η-phase (Cu_6Sn_5) adjacent to the solder matrix and ε-phase (Cu_3Sn) adjacent to the Cu substrate.

- Thicker Cu_3Sn IMC layers formed in smaller solder joints.

- The thickness of the ε-IMC phase was also found to increase with increasing the soldering time and/or soldering temperature.

- Whenever eutectic solder is available in the joint, η-IMC phase was also found to increase in its thickness with increasing the soldering time and/or soldering temperature.

- The increase in Cu_3Sn IMC layer thickness during the soldering process was found to obey a parabolic relationship with time. This indicates that the formation of the IMC compound layer is mainly controlled by the volume diffusion mechanism.

- Growth rate constants for Cu_3Sn interfacial IMC were found to increase with reduction in the size of solder joint during soldering process.

- The activation energy for the growth of Cu_3Sn IMC layer was found to decrease as the size of solder joint decreases.

References

[1]. Puttlitz K J, Stalter K A, "Handbook of Lead-Free Solder Technology for Microelectronic Assemblies," Marcel Dekker AG, Basel, Switzerland, 2004.

[2]. Blackwell G R, "The Electronic Packaging Handbook Ed. Blackwell", G.R. Boca Raton: CRC Press LLC, 2000.

[3]. Arzt E, " Overview No. 130, Size effects in materials due to microstructural and dimensional constraints: a comparative review," Acta Materialia, Vol. 46, No. 16, pp. 5611-5626, 1998.

[4]. Huang Z, Conway P P, and Qin R, " Modeling of interfacial intermetallic compounds in the application of very fine lead-free solder interconnections," Journal of Micro-system Technologies-Special Issue on micro-nano-Reliability, Vol. 15, No. 1, pp. 101-107, 2008.

[5]. Abdelhadi OM, Ladani L, and Razmi J, "Fracture toughness of bonds using interfacial stresses in four-point bending test," Journal of Mechanics of Materials, Vol. 43, No. 12, pp. 885-900, 2011.

[6]. Bernstein L, "Semiconductor joining by the solid-liquid-interdiffusion (SLID) process," Journal of the Electrochemical Society, Vol. 113, No. 12, 1966.

[7]. Bernstein L and Batholomew, " Application of solid-liquid interdiffusion (SLID) bonding in integrated-circuit fabrication," Transactions of the Metallurgical Society of AIME, Vol. 236, No. 3, pp. 405-412, 1966.

[8]. Roman J W and Eagar T W, "Low stress die attach by low temperature transient liquid phase bonding," Proceeding of the 1992 International symposium on Microelectronics, CA, 19-21, October 1992, pp. 1-6, 1992.

[9]. Li J F, Agyakwa P A, and Johnson C M, "Interfacial reaction in Cu/Sn/Cu system during the transient liquid phase soldering process," Acta Materialia, Vol. 59, pp. 1198-1211, 2011.

[10]. Li J F, Agyakwa P A, and Johnson C M, "Kinetics of Ag_3Sn growth in Ag-Sn-Ag system during transient liquid phase soldering process," Acta Materialia, Vol. 58, pp. 3429-3443, 2010.

[11]. Li J F, Mannan S H, Clode M P, Whalley D C, and Hutt D A, " Interfacial reaction between molten Sn-Bi-X solders and Cu substrates for liquid solder interconnects," Acta Materialia, Vol. 54, pp. 2907-2922, 2006.

[12]. Ladani L J, Razmi J, and Bentley J, "Microstructural and mechanical strength of snag-based solid liquid inter-diffusion bonds for 3 dimensional integrated circuits," Thin Solid Films, Vol. 518, pp. 4948-4954, 2010.

[13]. Ladani L J and Razmi J, " Bonding strength and microstructure of SnAg-based solid liquid inter-diffusion bonds," Proceeding of the ASME 2009 International Engineering Congress and Exposition, IMCE2009, November 13-19, Lake Buena Vista, Florida, USA.

[14]. Bartels F, Morris J W, and Gust W, " Intermetallic phase formation in thin solid-liquid diffusion couples," Journal of Electronic Materials, Vol. 23, No. 8, pp. 787-790, 1994.

[15]. Wu F, Wang B, Du B An B, and Wu Y, " Effect of stand-off height on microstructure and tensile strength of the Cu/Sn9Zn/Cu solder joint," Journal of Electronic Materials, Vol. 38, No. 6, pp. 860-865, 2009.

[16]. Wiese S and Wolter K J, " Microstructure and creep behavior of eutectic SnAg and SnAgCu solders," Microelectronics Reliability, Vol. 44, pp. 1923-1931, 2004.

[17]. Wiese S, Roellig M, and Wolter K J, "The effect of downscaling the dimensions of solder interconnects on their creep properties," Microelectronics Reliability, Vol. 48, pp. 843-850, 2008.

[18]. Zimprich P, Kotas A, Khatibi G, Weiss B, and Ipser H, " Size effects in small scaled lead-free solder joints," Journal of Materials Science: Materials in Electronics, Vol. 19, pp. 383-388, 2008.

[19]. Zimprich P, Saeed U, Betzwar-Kotas A, Weiss B, and Ipser H, " Mechanical size effects in Miniaturized lead-free solder joints," Journal of Electronic Materials, Vol. 37, No. 1, pp. 102-109, 2007.

[20]. Zimprich P, Saeed U, Weiss B, and Ipser H, "Constraining effects of lead-free solder joints during stress relaxation," Journal of Electronic Materials, Vol. 38, No. 3, pp. 392-399, 2009.

[21]. Huang Y C, Wu K S, and Chen S W, "Size and substrate effects upon undercooling of Pb-free solder," Microsystems, Packaging, Assembly and Circuits Technology Conference, IMPACT 2009. 4th International, 21-23 Oct. 2009, pp. 662-665, Taipei, China, 2009.

[22]. Huang Y C and Chen S W, "Co alloying and size effects on solidification and interfacial reactions in the Sn-Zn-(Co)/Cu couples," Materials Research, Vol. 25, No. 12, pp. 2430-2438, 2010.

[23]. Kinyanjui R, Lehman L P, Zavalij L, and Cotts E, " Effect of sample size on the solidification temperature and microstructure of SnAgCu near eutectic alloys," Journal of Materials Research Society, Vol. 20, No. 11, pp. 2914-2918, 2005.

[24]. Cho M G, Kang S K, and Lee H M, " Undercooling and microhardness of Pb-free solders on various under bump metallurgies," Materials Research, Vol. 23, No. 4, pp. 1147-1154, 2008.

[25]. Casrto de W B, Maia M de L, Kiminami C S, and Bolfarini C, "Microstructure of undercooled Pb-Sn alloys," Materials Research, Vol. 4, No. 2, pp. 83-86, 2001.

[26]. Yang S, Rian Y, and Wang C, " Investigation on Sn grain number and crystal orientation in the Sn-Ag-Cu/Cu solder joints of different sizes," Journal of Materials Science: Materials for Electronics, Vol. 21, pp. 1174-1180, 2010.

[27]. Gong J, Liu C, Conway P P and Siberschmidt V V, "Micromechanical modeling of SnAgCu solder joint under cyclic loading: Effect of grain orientation," Journal of Computational Materials Science, Vol. 39, pp. 187-197, 2007.

[28]. Chi Z., "Nanofabrication: Principles, capabilities, and Limits," Springer Press, Didcot, UK, 2008.

[29]. Abdelhadi O.M. and Ladani L., "Intermetallic compound growth of Tin-3.5 wt.% Silver/Copper system: combined chemical reaction and diffusion mechanisms". Journal of Alloys and Compounds, Vol. 537, In Progress (05 Oct. 2012), pp. 87-99, 2012.

[30]. Kim Y. M., Roh H.R., and Kim S., "Kinetics of intermetallic compound formation at the interface between Sn-3.0Ag-0.5Cu solder and Cu-Zn alloy substrates," Journal of Electronic Materials, Vol. 39, No. 12, pp. 2504-2512, 2010.

[31]. Yoon J. W., Lee C. B., Kim D. U., and Jung S. B., "Reaction diffusions of Cu_6Sn_5 and Cu_3Sn intermetallic compound in the couple of Sn-3.5Ag eutectic solder and copper substrate," metals and Materials International, Vol. 9, No. 2, pp. 193-199, 2003.

[32]. Yu D. Q., Wu C. M. L., Law C. M. T., Wang L., and Lai J. K. L., "Intermetallic compounds growth between Sn-3.5Ag lead-free solder and Cu substrate by dipping method," Journal of Alloys and Comounds, Vol. 392, No. 1-2, pp. 192-199, 2005.

[33]. Ladani L. and Razmi J., "IMC growth in solid-liquid interdiffusion bonds," Thermal and Thermomechanical Phenomena in Electronic Systems (ITherm), 2010 12th IEEE Intersociety Conference on 2-5 June 2010 Las Vegas, NV.

[34]. Dybkov V. I., "Reaction diffusion and solid state chemical kinetics," the IPMS Publication, Kyiv 2002.

[35]. Dybkov V. I, "Reaction diffusion in binary solid-solid, solid-liquid and solid-gas systems: common and distinctive features," Defect and Diffusion Forum, Vols. 194-199, pp.1503-1522, 2001.

[36]. Dybkov V. I., Khoruzha V. G., Sidorko V. R., Meleshevich K. A., Samelyuk A. V., Berry D. C., and Barmak K., " Interfacial interaction of solid cobalt with liquid Pb-free Sn-Bi-In-Zn-Sb soldering alloys," Journal of Materials Science, Vol. 44, No. 22, pp. 5960-5979, 2009.

[37]. Wang C. H. and Kuo C., "Interfacial reactions between eutectic Sn-Pb solder and Co substrate," Journal of Materials Science, Vol. 46, No. 8, pp. 2654-2661, 2011.

[38]. Chada S., Fournelle R. A., Laub W., and Shangguan D., "Copper substrate dissolution in eutectic Sn-Ag solder and its effect on microstructure," Journal of Electronic Materials, Vol. 29, No. 10, pp. 1214-1221, 2000.

Chapter 4 : Optimization of Preparation Process Procedure for Successful Electron Backscatter Diffraction (EBSD) of Multi-Layer Specimens: Application to Lead-Free Solder Joints

Abstract

Electron backscatter diffraction (EBSD) is a powerful technique that provides a wide range of analytical data such as crystallographic orientation, phase identification, and grain size information. The quality of diffraction pattern, which influences the quality of the indexing of the diffraction pattern, depends mainly upon the achievement of a very flat and fully distortion-free sample surface. Many studies have reported specimen preparation guidelines for EBSD for a variety of materials such as metals and ceramics. However, limited studies have been documented in literature for optimized preparation of multi-layer specimens.

In this study, a series of mechanical polishing procedures have been developed, which will be adequate for producing damage-free surfaces in multiple-layer specimens for EBSD. The proposed method was used to prepare Sn-3.5%Ag/Cu-substrate solder joints as an example of a multiple-layer specimen which is consists of multiple materials with wide range of stiffness and wear resistance and has produced the best possible surfaces. The results suggested adding vibratory-polishing step for certain amount of time is critical in order to produce EBSD patterns for the microstructure of Sn-3.5Ag/Cu solder system. A poor pattern quality occurred, particularly in Cu and β-tin regions, when the vibratory polishing step was skipped or was conducted shorter than a certain amount of time.

This study also aimed to investigate the effect of the processing parameters of the EBSD software on the EBSD results extracted for the multiple-layer specimen under investigation. It was found that the step size and the minimum number of detected bands are important parameters. It has been found that at least six (6) detected bands necessary for accurate mapping and quality imaging. At this optimum value, the indexing rate was the highest in all phases and the phase identification was the most accurate.

Key words: Electron backscatter diffraction (EBSD), sample preparation, multiple-layer specimen, vibratory polishing, EBSD parameters, step size, Kikuchi bands.

4.1 Introduction

Properties of materials usually are defined by their microstructure. Therefore, microstructure characterization is an essential stage in material characterization. A number of techniques based on chemical composition analysis are used for this purpose such as energy and wavelength dispersive spectroscopy (EDS and WDS), X-ray photoelectron spectroscopy (XPS), etc. [1] Unfortunately, in some investigations the chemical composition information is not sufficient such as when the crystal structure of a phase is needed for its identification or when the accuracy of chemical analysis is too low [2-3]. In such investigation, transmission electron microscopy (TEM) is an alternative [1], especially when phases are to be identified in small regions. Unfortunately, TEM requires a complicated and time consuming sample preparation procedure [4, 5]. Electron Backscatter Diffraction (EBSD) could be a potential alternative because of its relative simplicity in sample preparation [6]. EBSD is a very powerful technique that provides a wide range of analytical data in which the local crystallographic orientation is of interest. It provides qualitative and quantitative information on crystal structure and orientation of local crystallographic regions. It is possible to obtain other information such as phase identification and distribution, grain characterization, and estimation of elastic and plastic strains by this

technique. It can also be used to correlate the crystal structure analysis with the morphological information and local chemical analysis during phase identification in many different multiphase materials [7].

EBSD is a surface-sensitive material characterization technique as the depth below the specimen surface from where EBSD diffraction patterns arise is shallow, on the order of nanometers. Therefore, the effect of decreasing surface quality, such as carbon contamination, relief, or high dislocation density on the sample's surface have a strong influence on the pattern quality and subsequently on the indexing percentage and reliability. Contamination could be introduced by improper specimen handling. Reliefs can be caused by several preparation methods such as electro-polishing, etching, ion milling. Mechanical polishing is known to cause plastic deformation which increases dislocation density. Thus, a relatively clean, flat, and distortion-free sample surface which is essential for successful EBSD analysis can only be obtained by removing all the surface defects or deformation using an appropriate specimen preparation procedure. Optimum specimen preparation is a fundamental requirement for obtaining quality EBSD images. Inadequate specimen preparation will result in degraded diffraction patterns causing loss of data, quality, and reliability.

Different preparation methods for SEM-EBSD applications are recommended in the literature for several metals and their alloys such as Cu, aluminum, titanium, nickel, tungsten, zirconium [8-10], and for ceramics [11]. Unfortunately, preparation techniques that produce plane surfaces are known to cause varying degrees of material damage, and those techniques that minimize damage do not necessarily result in plane surfaces. This is due to the remaining residual distortion at the sample's surface, mainly by deformation introduced during preparation process. Therefore, an

additional preparation step is often required, especially when soft and oxidized metals are under preparation for EBSD analysis.

When diamond paste down to 1 μm-grade was used in mechanical polishing, the method was determined to be inappropriate for material subjected to EBSD investigation due to existence of a residual deformation layer on the sample's surface [8, 12]. However, mechanical polishing with an oxide polishing suspension based on water and colloidal silicon followed by short electro-polishing has been shown to be an ideal way of generating surface suitable for EBSD analysis of metallic materials [12, 13]. Others have claimed that removal of surface damage can be obtained using a slight etching or ion-milling step during the final preparation steps [6, 14-16]. Most of available literature is on pure metals, alloys and ceramics. However, material scientists are often confronted with the task of extracting EBSD data from samples that have complicated structures, and therefore, are not easily prepared, such as electronics, MEMS (micro-electro-mechanical systems), and composite and hybrid specimens. These samples are commonly made of multiple layers and usually of different materials. Therefore, the difficulty may arise due to a variety of reasons: inherent lattice damage due to processing, large differences in hardness and reactivity between phases due to composition, and/or approaching the physical limit of the EBSD technique [17]. Authors have discussed the preparation required for samples containing strongly dissimilar phases, in layer fashion, trying to optimize the preparation procedure as well as the EBSD parameters.

It is well known that optimization of microscopy parameters, such as accelerating voltage, probe size, and specimen tilt, along with good preparation of specimen surface, are essential for good quality results [13, 18]. EBSD data analysis is computer based and to obtain reliable and precise results, particular attention should be paid to certain processing parameters [18-20] such as the

minimum number of detected bands [21] and step size [22] which are believed to be the two

parameters that affect the accuracy of the pattern indexing (phase identification) and grain size

and grain boundary measurements. The effect of these parameters on the quality of image in a

multilayer specimen is investigated and an optimum rage of parameters are recommended for

obtaining a clear pattern in all the existing phases of the system of materials investigated here.

The specimen under investigation was a lead-free solder joint.

4.2 Experimental Procedure

4.2.1 Materials

The analysis was performed on one of the most researched multilayer structures: the lead-free

Sn-3.5%Ag/Cu-substrate solder joints. The specimen configuration, as shown by Figure 2-1, and

preparation process of the solder joints were detailed elsewhere [23]. In all the joints, the

microstructure consists of Cu, β-tin and intermetallic (IMC) layers, namely, Cu_6Sn_5 and Cu_3Sn

IMCs as seen in Figure 4-1. The average thickness of the joints was 450 µm. The average

thickness of the IMC layers was 27 µm and 9 µm, for Cu_6Sn_5 and Cu_3Sn IMCs respectively.
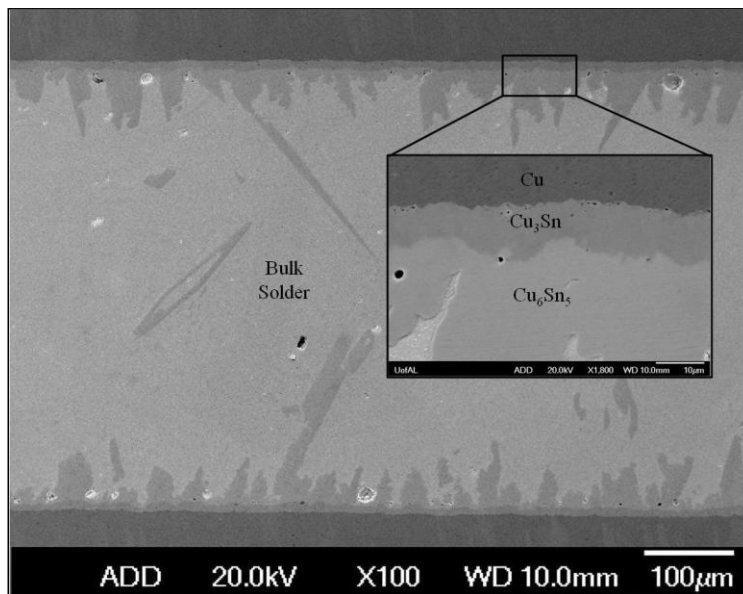
Figure 4-1: Microstructure of solder joint showing different phases present in the joint.

109

4.2.2 Preparation Strategy for EBSD

4.2.2.1 Mechanical Polishing

After the solder joints were fabricated, they were mounted in regular Cu-based conductive mounting resin to facilitate the subsequent preparation steps and for charging release. In order to obtain a flat and distortion-free surface, the standard grinding and polishing procedures for general metallographic investigation have to be adjusted. Such adjustments mainly concern reducing the loads and rotation speeds used for mechanical grinding and polishing for general metallographic investigation purposes. Automated preparation equipment is recommended which allows for the preparation procedure to be performed accurately and reproducibly. Manual preparation should be avoided because it cannot result in a flat and distortion-free surface reproducibly. Mechanical polishing was performed on an automatic polisher equipped with 200 mm diameter wheels and sample mounts of 37 mm (1.25 inches). Grinding and polishing was performed according to the parameters found in Table 4-1, which shows the steps that to be followed during mechanical preparation. This proposed preparation recipe was found to give the optimum surface finishes suitable for EBSD on the specimen configuration adopted in this study if it is followed with vibratory polishing for certain amount of time.

Table 4-1: sample preparation parameters used in mechanical grinding and polishing stages.

Parameters Prep. step	surface	medium	Speed, (rpm)	Time, (min)	Force, (N)	Rotation
	SiC paper	320-grit	300	5 or until flat	25	Contra
Mechanical Grinding (MG)	SiC paper	600-grit	300	5	25	Contra
	SiC paper	800-grit	300	5	25	Contra
	SiC	1200-grit	300	5	25	Contra

110

	paper					
Mechanical	Cloth[1]	1µm Al_2O_3 solution	150	30	20	Contra
Polishing (MP)	Cloth[2]	0.3µm Al_2O_3 solution	150	30	20	Contra

1: Use cloth that is inexpensive and versatile, suitable for intermediate automatic polishing.
2: Use a final polishing cloth that can be used with sub-micron polishing compounds and abrasives of any types.

4.2.2.2 Vibratory Polishing

The final stage of the preparation process can be performed in different ways that would depend on the type of material being prepared. Electro-polishing, etching, and ion-beam milling are very common final polishing methods for pure metals, alloys, and ceramics for EBSD applications. Care should be given to avoid pitting, severe surface roughening, and other surface damages due to utilization of dangerous electrolytes in electro-polishing, etching chemicals, and high-beam energies associated with ion-beam milling. Furthermore, these methods are high-cost and time and effort consuming and electro-polishing works only for homogeneous and electrically conductive materials.

Vibratory polishing with colloidal silica is very often preferred as a final polishing step due to its capability in preparing high quality surfaces on a wide variety of materials and applications. The unique polishing action associated with vibratory polishing produces less deformation, smooth, and distortion-free surfaces very suitable for EBSD measurements. The polishing time varies and can be a few hours [24], but normally this is acceptable as no additional abrasive-polishing medium and no additional manpower are needed. Prolonged polishing is not preferred because a high surface waviness and strong surface relief are usually observed when metals, alloys, and ceramics are vibratory-polished for extended periods [25].

In this study, vibratory polishing was used as a final polishing stage to prepare the solder-joint specimens under consideration. The installation is very simple, consisting of colloidal silica, specimen holder, standard cloth, and vibratory polisher. It was performed according to the

parameters found in Table 4-2. During the vibratory polishing, the cloth was flooded with the

colloidal silica. The polishing time was varied between 0 to 240 min by an increment of 120 min,

to address the development of the surface preparation quality for EBSD analysis in the

investigated specimens. In literature, there is no reliable data of the polishing time because this

depends on many factors. Some materials showed improved results within minutes and other

often require hours or even over night to produce the best possible surface quality [24]. In this

study, four hours of vibratory polishing gave the best possible results when used to prepare the

specimens used in this study.

Table 4-2: Sample preparation parameters used in vibratory polishing

Parameter⟍ Prep. Step	Surface	Medium	Speed, (rpm)
Vibratory polishing (VP)	Cloth³	0.05 µm colloidal silica suspension	60% amplitude

3: Use super finishing cloth that can be used with all materials. It can be used with sub-micron
abrasives.

4.2.2.3 Electron Backscatter Diffraction (EBSD)

EBSD was performed using a JEOL 7000F SEM equipped with a Shottky field emission gun and

high-resolution HKL EBSD-system (Nordlys 2). All measurements were conducted at a tilt of

70°, an acceleration voltage of 20 kV, a range of working distances of 15-17.5 mm, and a range

of magnifications of 1000 – 4000X. All EBSD scans were performed using a fine step size (0.4

to 0.05 µm). For the purpose of optimizing EBSD software parameters, step size and minimum

number of detected bands were varied in multiple levels. All the indexed points were identified

as face centered cubic (FCC) Cu, tetragonal β-tin, hexagonal η-Cu_6Sn_5 IMC, or orthorhombic ε-

Cu_3Sn IMC.

To investigate the influence of the mechanical preparation treatment on surface quality for EBSD

measurements, 20 electron diffraction (Kikuchi) patterns (EBSP) were collected for each present

phase at each preparation step. The average band contrast (BC), band slope (BS), and mean

angular deviation (MAD) values were recorded for each of the acquired EBSPs. BC is an EBSP

quality parameter that describes the average intensity of the Kikuchi bands with respect to the

overall intensity within the measured area of EBSP [7]. Its values are scaled to a byte range from

0 to 255. The higher the value for BC, the better the EBSP quality. Deformed and grain boundary

regions usually exhibit a low BC value. Similarly, BS is EBSP quality-parameter which

describes the maximum intensity gradient at the margins of the Kikuchi bands in an EBSP. Its

values vary between 0 and 255 bytes. The higher the value, the higher is the contrast difference

and the sharper the appearance of Kikuchi bands. Another pattern quality parameter is MAD. It

is also called pattern misfit. It is a number that expresses how well the simulated EBSP overlays

the actual EBSP. A low value is an indication that the simulation is a good match with high-

quality EBSPs. The BC values in conjunction with the BS and MAD values are frequently

considered to determine the reliability of EBSD scan.

4.3   Results and Discussions

4.3.1 Optimization of Preparation Procedure

To assess the influence of the preparation stage on the development of EBSPs, data of Kikuchi

patterns have been collected at the end of the mechanical polishing stage and at different time

increments during the vibratory polishing stage. For further investigation of pattern quality,

parameters such as BC, BS, and MAD were also collected for EBSPs.

Figure 4-2 shows examples of Kikuchi patterns (EBSP) in different phases for different vibratory

polishing times; 0 min, 120 min, and 240 min. Table 4-3 shows a summary of the average and

max/min values of BC, BS, and MAD of EBSPs of different phases at different preparation

steps. Figure 4-2 clearly shows that a very poor pattern quality is obtained in all phases at the end

of mechanical polishing step except in β-tin, which shows somewhat better patterns. In the case of Cu, Cu_6Sn_5, and Cu_3Sn phases, very low-quality Kikuchi bands were obtained for the measurement conditions used.

Overall, the indexing rate was the lowest at this preparation stage in which the non-indexing rate was about 15-25% as seen in Table 4-4. It can be inferred that the distortion-free crystal, surface deformation, and flatness are yet far from what is required for successful EBSD measurements. The values for BS are the lowest ones in all phases in this preparation stage. β-tin shows higher BC and BS, and lower MAD values compared to those for other phases.
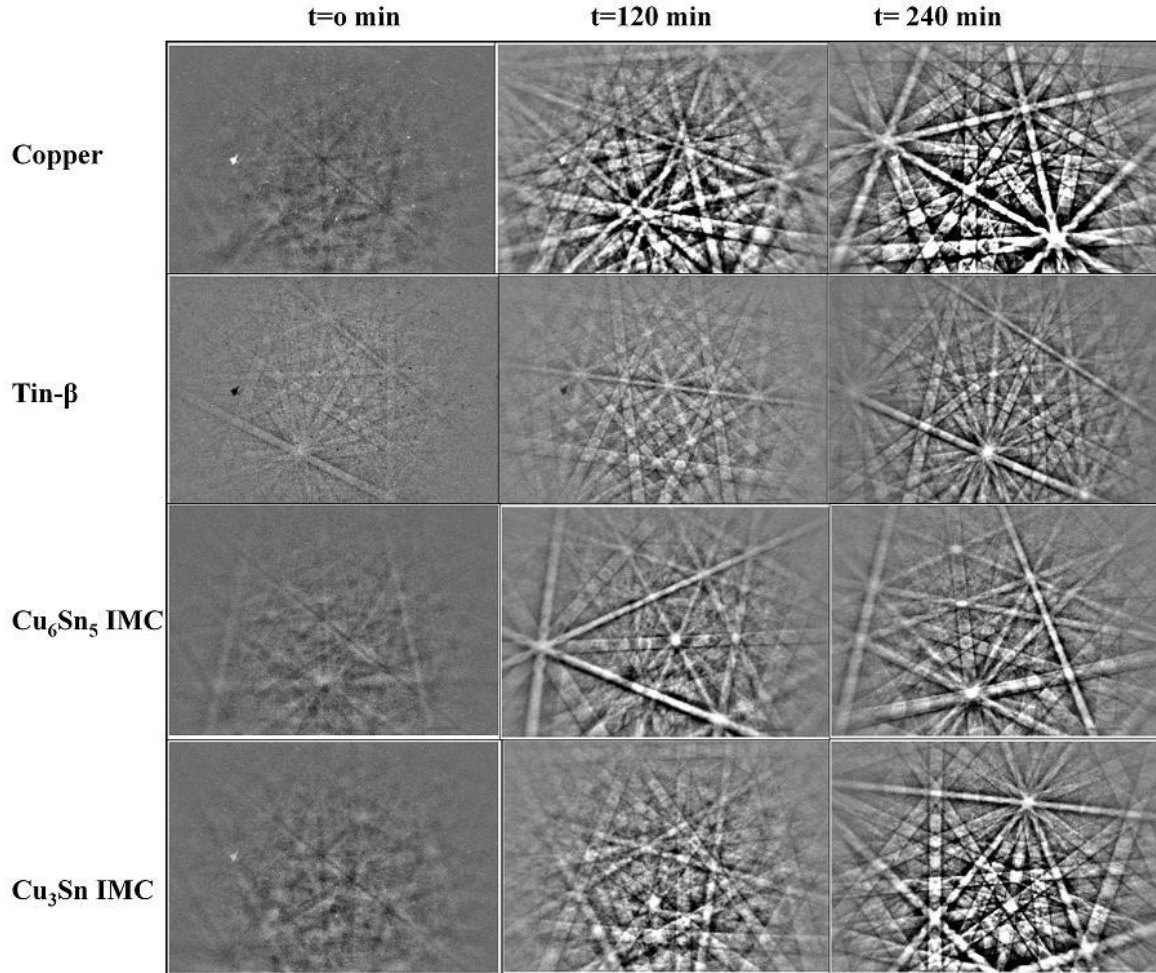
Figure 4-2: Examples of Kikuchi patterns (EBSP) in different phases for different vibratory polishing times.

When vibratory polishing took place, improved surface quality results in noticeably sharper

EBSPs, as seen in Figure 4-2. At 2 hours of VP, substantial improvement in indexing rate

percentage was noticed as shown in Table 4-4. Indexing was possible for all phases. Overall, the

indexing rate ranges between 75 and 80% dependent on the material. BC and BC values also

show significant improvements. All phases exhibit very high values of BS and BC relative to no

VP stage, and MAD decreases significantly. Some phases such as Cu and Cu_6Sn_5 have reached,

while other phases show values that approach, the highest values for BS as seen in Table 4-3.

Table 4-3: Summary of average and max/min values of BC, BS, and MAD parameters of EBSP of different phases at different preparation steps.

	Polishing step	Cu			Tin		
		BC	BS	MAD	BC	BS	MAD
Average	VP(t=0)	95.46±14.72	76.38±7.84	4.91±5.30	188.38±26.59	174.54±55.68	0.84±0.29
	VP (t=120 min)	216±14.42	255±0	0.57±0.24	193.4±21.19	245.5±24.26	0.78±0.97
	VP (t=240 min)	223.4±20.15	255±0	0.6439±0.13	203.5±7.66	247±18.63	0.52±0.10
Min/Max Values	VP(t=0)	70/127	65/91	1.533/18.65	144/243	82/255	0.42/1.36
	VP (t=120 min)	184/243	255/255	0.27/1.27	155/218	177/255	0.32/3.52
	VP (t=240 min)	189/253	255/255	0.39/0.85	191/211	209/255	0.32/0.59
	Polishing step	Cu_6Sn_5			Cu_3Sn		
		BC	BS	MAD	BC	BS	MAD
Average	VP(t=0)	173.92±30.36	123.16±36.62	1.46±0.74	142.25±25.62	125.07±34.98	2.53±3.24
	VP (t=120 min)	250.24±7.50	255±0	0.52±0.24	200.91±31.83	255±0	2.68±5.18
	VP (t=240 min)	237.77±21.07	250.15±17.47	0.47±0.11	215.67±23.38	255±0	0.53±0.13

Min/Max Values	VP(t=0)	117/255	62/200	0.62/3.25	86/181	66/210	0.37/13.38
	VP (t=120 min)	232/255	255/255	0.14/1.29	148/247	255/255	0.177/4.29
	VP (t=240 min)	189/255	192/255	0.31/0.70	190/255	255/255	0.348/0.727

As the time of vibratory polishing extended to 4 hours, pattern quality was enhanced accordingly as seen in the third column of Figure 4-2. At VP times longer than two hours the rate of improvement was slower compared to VP times smaller than two hours. At four hours of VP, further increases in BC and BS, and decrease in MAD values with very small standard deviation were observed. Very strong and sharp Kikuchi bands result in indexing rate ranging between 85 and 95% with slight variation between different phases.

Table 4-4: Indexing rate at each preparation step.

Preparation step	Indexing rate, (%)
VP(t=0)	15-25
VP(t=120 min)	75-80
VP(t=240 min)	85-95
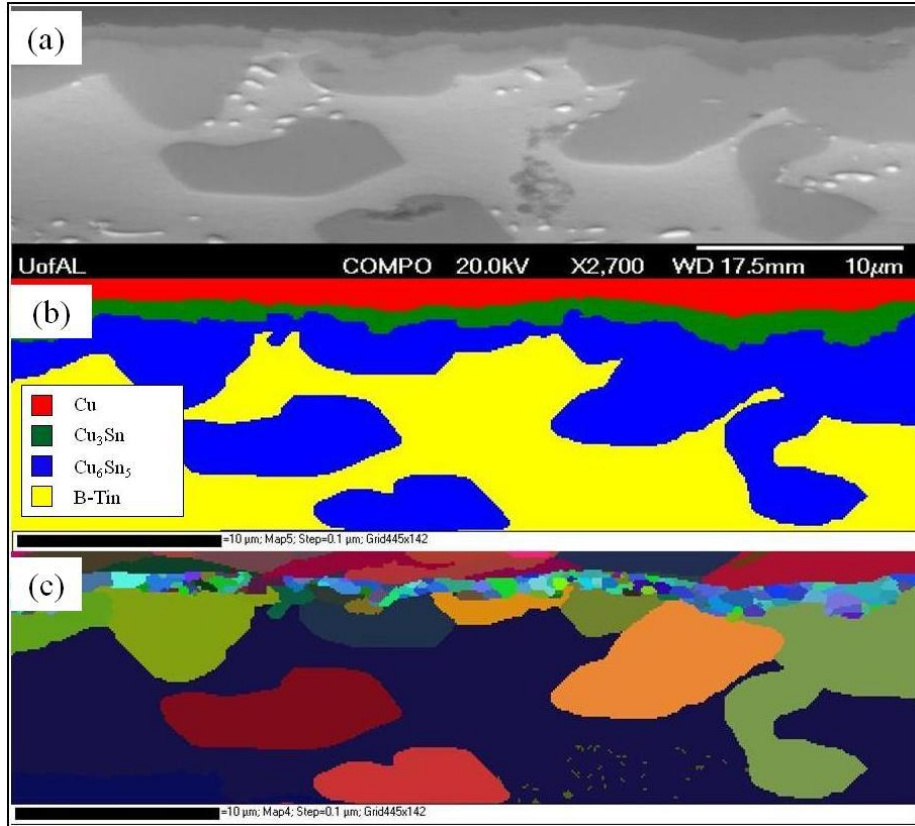
Figure 4-3: (a) a representative SEM image, (b) EBSD phase map, and (c) EBSD orientation map. The minimum number of bands and step size are 6 and 0.1 μm, respectively.

A representative SEM image and EBSD phase and orientation maps are presented in Figure 4-3.

This is the SEM image taken after four hours of VP. This EBSD map was composed of points

representing an analysis of 51,429 separate patterns. The scan quality statistics were as follows:

confidence index (CI) = 0.62 and image quality (IQ) =180, indicating that a quality EBSD map

can be generated using the previously described surface preparation procedure. CI indicates the

degree of confidence that the orientation calculation is correct while IQ is a quality factor that

defines the sharpness of the diffraction pattern. CI may range from 0 to 1. Both are used

frequently to evaluate the overall quality and reliability of EBSD analysis.

4.3.2 Optimization of EBSD Software Parameters

EBSD orientation and phase maps were obtained at different levels of magnification using the default settings for the hkl Channel software and changing the EBSD parameters which are shown in Table 4-5. The variables are the step size and the minimum number of detected bands which are varied between 0.05 and 0.4 μm and between 4 and 7 bands, respectively. The resulting phase maps at different minimum number of detected bands are shown in Figure 4 4(b-f). It also shows band contrast map (Figure 4 4(b)) for the mapped area showed in the SEM back scattered electron image of Figure 4 4(a).

Table 4-5: EBSD parameters and their levels

Parameter	Level
Minimum number of detected bands	4, 5, 6, and 7
step size (μm)	0.05, 0.075, 0.1, 0.2, 0.3, and 0.4
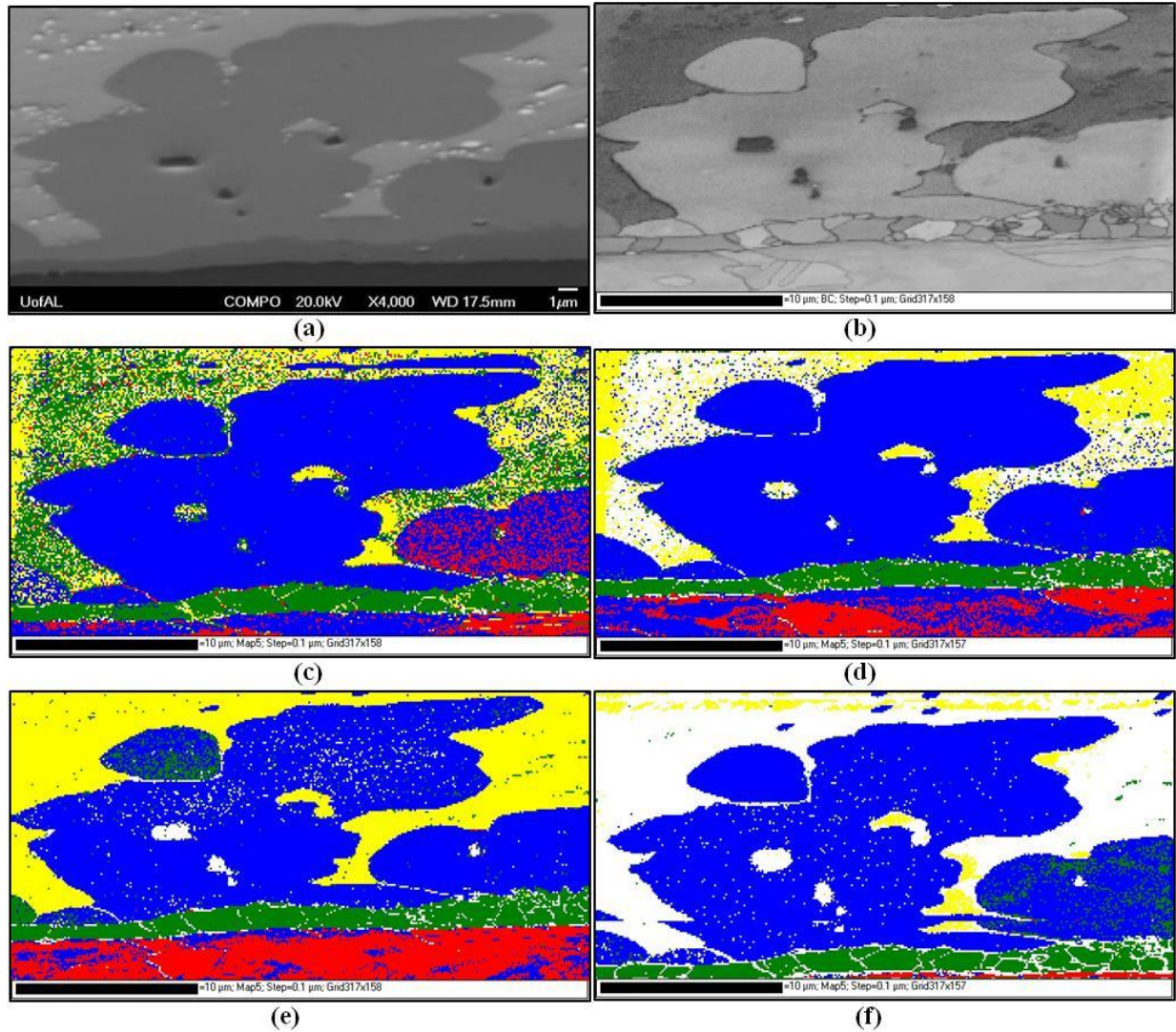
Figure 4-4: Effect of minimum number of detected bands on the quality of EBSD measurements. (a) SEM image, (b) band contrast image, (c), (d), (e), and (f) are phase maps collected using 0.1 µm-step size and 4, 5, 6, and 7 minimum number of detected bands, respectively.

The best match between the obtained phase maps and the SEM image, in terms of identifying each phase region, was the one achieved at 6 detected bands, as shown in Figure 4-4(e). A limited number of points in β-tin region were miss-indexed which can be corrected for using clean up techniques at post processing stage. Therefore, this value is considered to be the optimum minimum number of detected bands one should use when this specimen configuration is under EBSD investigation. Although the percentage of indexed points in Figure 4-4(c) looks

comparable with the one in Figure 4-4(e), as one can confirm from Figure 4-4(d), a large portion of points were miss-indexed. In particular, part of β-tin and Cu_6Sn_5 IMC, in Figure 4-4(c) were unreliably indexed as Cu_3Sn IMC and Cu, respectively, while part of Cu was indexed as Cu_6Sn_5 IMC.

The miss-indexing issues in the β-tin region are most likely related to the low crystal symmetry associated with this phase. β-tin has a body-centered tetragonal structure, which is known to have low symmetry. A low minimum number of detected bands (4 bands) is reasonable for a cubic material, but is probably too low for non-cubic or when trying to discriminate different phases. As the minimum number of detected bands increases, accuracy of the phase identification has improved as in Figure 4-4(d). When the minimum number of band detected was 6, the greatest accuracy was obtained in all regions; especially in β-tin and Cu_6Sn_5 and Cu_3Sn IMCs. Increasing the minimum number of detected bands to 7 (Figure 4-4(f)) resulted in obtaining comparable accuracy of phase identification in Cu and IMC regions. However, poor indexing was achieved in β-tin region. This was attributed to the limited number of sharp and bright bands being detected in this region. The EBSD will not assign a solution for a pattern that has been analyzed with lower number of bands (less than 7 in this case). Similarly, the reliability of indexing in Cu_6Sn_5 IMC region was affected by the minimum number of detected bands. This was attributed to the low crystal symmetry associated with this material. Improved indexing reliability was achieved as the minimum number of detected bands increases. The best results compared to SEM reference image were obtained at 6 bands. It also was observed from Figure 4-4 that Cu_3Sn IMC region was less affected by changing minimum number of detected bands. Comparable indexing rates were achieved regardless of the chosen value for the minimum number of detected bands. In general, it was concluded that if good quality patterns (perfect preparation) and

120

accurate calibration are used, then the miss-indexing problem can be minimized by using a large number of bands for pattern solution.

The effect of minimum number of detected bands on EBSD results was further investigated in terms of BC, BS, MAD, and non-indexing rate, as shown in Figure 4-5.
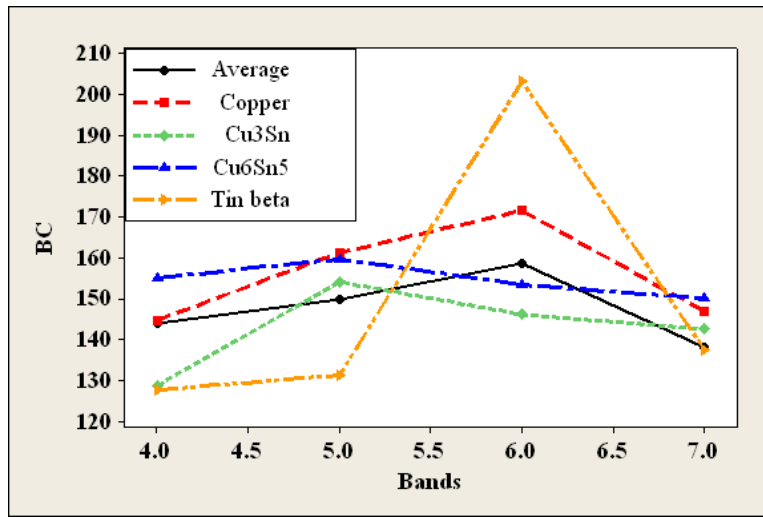
Figure 4-5(a): The effect of minimum number of detected bands on BC. Step size was held constant at 0.1µm.
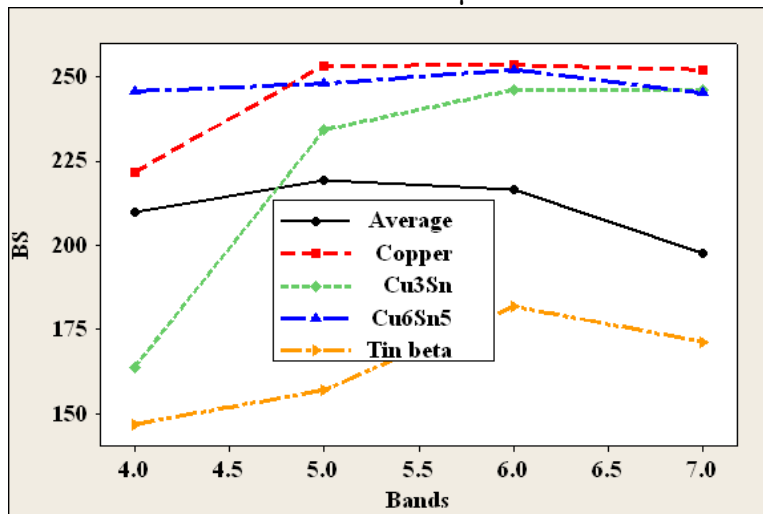
Figure 4-5(b): The effect of minimum number of detected bands on BS. Step size was held constant at 0.1µm.
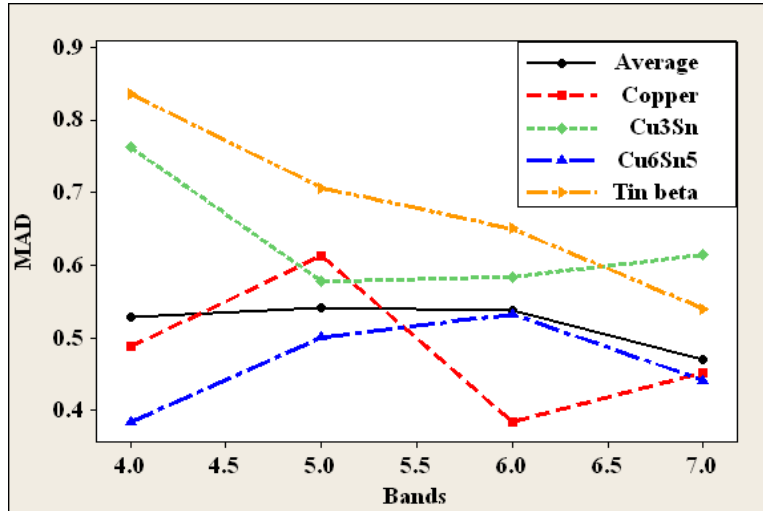
Figure 4-5(c): The effect of minimum number of detected bands on MAD. Step size was held constant at 0.1μm.
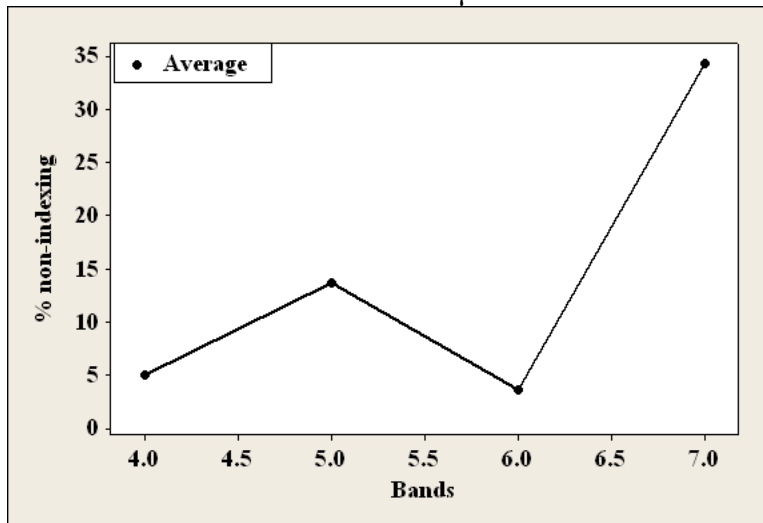
Figure 4-5(d): The effect of minimum number of detected bands on non-indexing rate percentage. Step size was held constant at 0.1μm.

Cu and Cu_6Sn_5 IMC always show higher BC and BS and lower MAD values compared to β-tin

and Cu_3Sn IMC as seen in Figure 4-5(a-c). β-tin has the highest BC and BS, and relatively lower

MAD values at a minimum number of 6 detected bands. This combination of values was behind

the highest accuracy in phase identification achieved at that minimum number of detected bands

as shown in Figure 4-5(d) by achieving a smaller non-indexing percentage. At minimum number

of detected bands of 6, the majority of sampled areas have been indexed as one of the expected

phases and showed the highest accurate indexing percentage. Otherwise, a significant number of data points were either miss-indexed or non-indexed. This implies that minimum number of detected bands of 6 is the optimum value at which reliable EBSD results and avoiding non- or miss-indexing of the data are achieved.

If the grain or sub-grain sizes and shapes are to be determined by EBSD, then close attention must be paid to the step size in relation to the grain size. It has been stated [13] that a step size of one-tenth of the average grain size is a good starting point for general microstructure, grain size, shape, and orientation measurements. A smaller step size would be needed if the grain size distribution is nonhomogeneous, as one might expect in multiple-layer specimen. In such specimens, there is a high possibility of having a nonhomogeneous distribution of grain size due to presence of different materials in the structure. The use of smaller step size allows for all small grains to be captured if the grain size is to be determined from the maps. Similarly, a small step size, relative to the grain size, is also required for high resolution definition of grain boundaries [13].

Figure 4-6 shows the effect of step size on the EBSD results. Figure 4-6 (b) shows grain size distribution for the mapped surface in Figure 4-6 (a) using a step size of 0.1 µm. At this step size and at lower values, it was found that grain size measurements stabilized. When higher values of step size were chosen, variation in grain size measurements was witnessed. Therefore, a step size of 0.1 µm was chosen to be the highest value to reveal accurate and reliable grain size measurements.
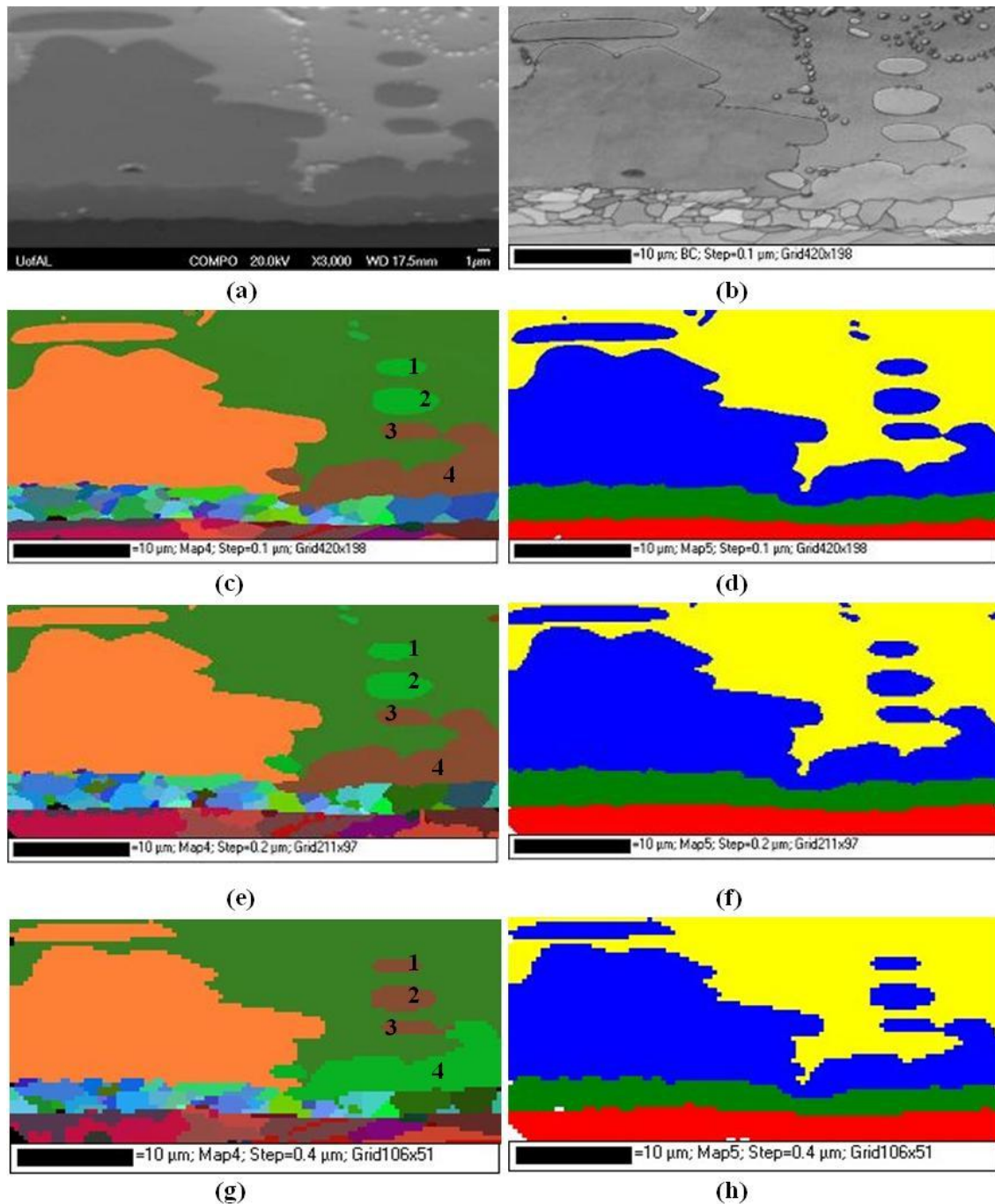
Figure 4-6: (a) SEM image, (b) contrast image of SEM image in (a). (c-h) orientation maps (left) and phase maps (right) at different step sizes; (c, d) 0.1 μm, (e, f) 0.2 μm, and (g, h) 0.4 μm. In this display, Figure 4-6(b), the average grain area measurements were as follows: 29.69 μm², 1.65 μm², 300.24 μm², and 2.98 μm² for Cu_6Sn_5, Cu_3Sn, β-tin, and Cu, respectively. Figure 4-6(c), (e), and (g) show the orientation maps while Figure 4-6(d), (f), and (h) show the phase maps for the same area in Figure 4-6 (a) obtained at different step sizes. As seen, the accuracy of

124

grain size and shape measurements is significantly affected by the step size used during EBSD mapping. Coarser grain shapes and, therefore, rough grain size and grain boundary measurements, were obtained at higher step sizes; see Figure 4-6 (d), (f), and (h). Additionally, it has been observed that there were some changes in grain orientation measurements in some phases as step size changes. This was very obvious by comparing the change in color of similar grains in Figure 4-6 (c), (e), and (g), for instance, see the change in color for grains marked 1, 2, 3, and 4 in the figures. This indicates that step size is an important factor in determining the right orientation for grains as well.

Figure 4-7 shows the grain size measurements at different step size for different Cu-Sn IMCs. Measurements for β-tin and Cu have been omitted for brevity. However, their measurements are summarized in Table 4-6. All materials showed a change in grain size measurements and their frequencies as the step size changes; see also Table 4-6 for quantitative results of grain size measurements of all materials. The grain size measurements obtained at step sizes of 0.075 and 0.05 μm were omitted because they are similar to the results showed for 0.1 μm except for β-tin grain size measurement which showed poor indexing rate especially during 0.075 μm step size. It was found that there is a tradeoff between the time and accuracy at which these images are obtained. As the step size increases the time required to get the pictures decrease. The range of measured grain size and frequency changes in all phases as step size changes. The grain size measurements stabilize as step size gets at or smaller than 0.1 μm. Therefore, this step size was considered the highest possible value to get accurate results in terms of grain size measurements.
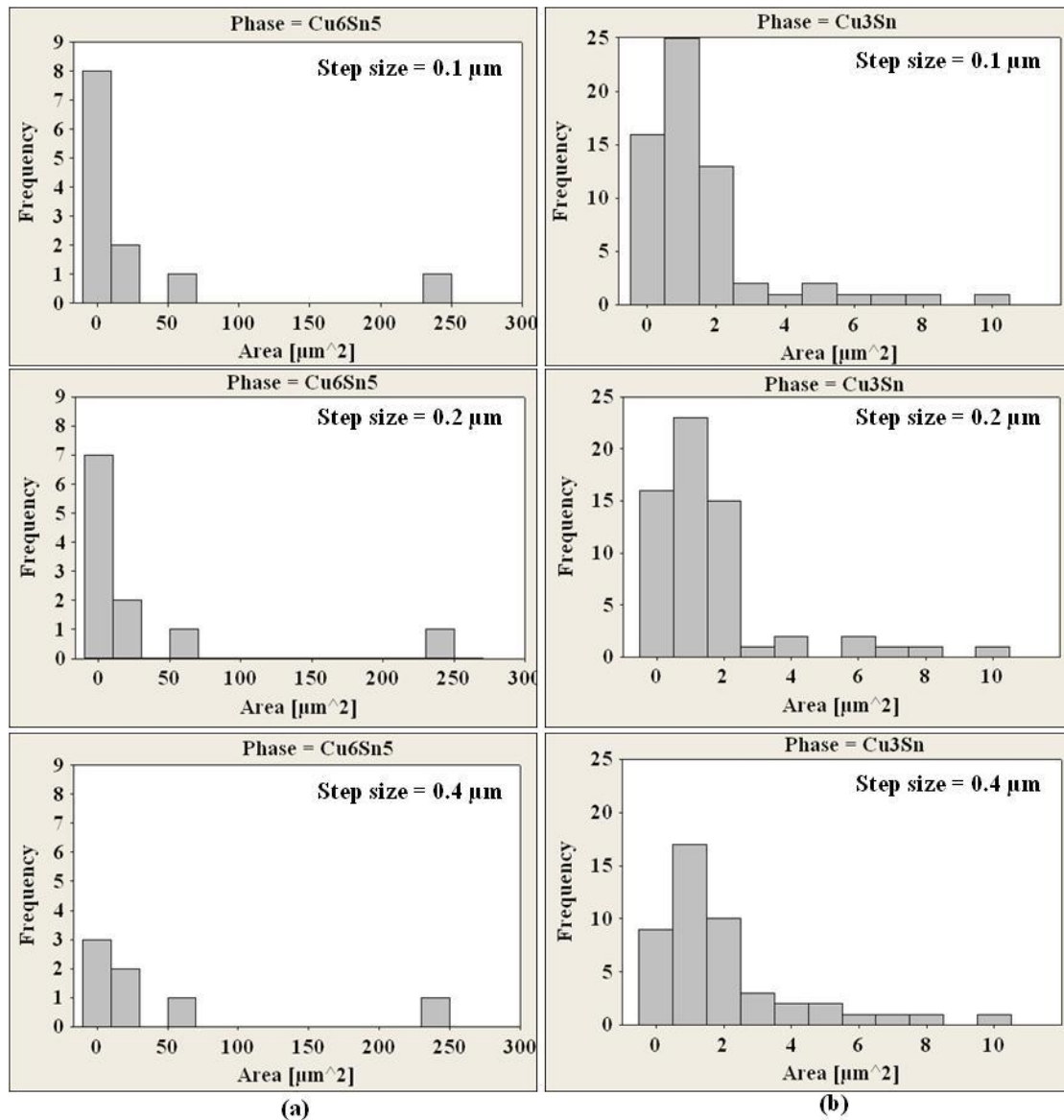
Figure 4-7: Effect of step size on grain size measurements of different Cu-Sn IMCs: (a) Cu_6Sn_5 and (b) Cu_3Sn.

Figure 4-8 shows the change in BC, BS, MAD, and non-indexing rate as step size varies between 0.05 and 0.4 μm. In all phases, BC and BS show higher values while MAD and percent non-indexing show lower values as step sizes vary between 0.1-0.3 μm. At smaller step sizes, e.g. 0.05-0.075 μm, higher MAD and percent non-indexing were depicted. This would be attributed to the fact that these values approach the limits of the EBSD spatial and angular resolutions. At

0.4 μm step size, the non-indexing rate percentage was the lowest. No correlation was extracted

for the possible reasons behind the enhancement in indexing rate at this step size.

Table 4-6: Grain size measurements of different materials obtained at different step sizes

Step size, (μm)	Statistics	Cu_6Sn_5 IMC		Cu_3Sn IMC	
		Area, (μm^2)	Diameter, (μm)	Area, (μm^2)	Diameter, (μm)
0.1	average	29.69	3.74	1.65	1.01
	Std. Dev.	70.71	5.09	2.01	0.87
	Min	0.12	0.39	0.13	0.11
	Max	245.67	17.69	10.29	3.62
	# of grains	12	-	63	-
0.2	average	31.67	3.93	1.68	1.07
	Std. Dev.	53.14	3.97	1.96	0.83
	Min	0.24	0.50	0.12	0.23
	Max	242	17.55	10	3.57
	# of grains	11	-	62	-
0.4	average	51.38	5.83	2.10	1.41
	Std. Dev.	90.38	6.01	2.13	0.78
	Min	2.4	0.45	0.32	0.45
	Max	249.12	17.81	9.76	3.53
	# of grains	7	-	47	-
		β-tin		Cu	
0.1	average	300.24	19.55	2.98	0.92
	Std. Dev.	#	#	3.76	1.28
	Min	300.24	19.55	0.14	0.11
	Max	300.24	19.55	16.2	0.54
	# of grains	1	-	23	-
0.2	average	263.32	18.31	4.49	1.55
	Std. Dev.	#	#	6.80	1.51
	Min	263.32	18.31	0.32	0.23
	Max	263.32	18.31	30.84	6.27
	# of grains	1	-	22	-
0.4	average	141.04	10.76	3.93	1.42
	Std. Dev.	190.86	11.29	5.06	1.34
	Min	6.08	2.78	0.48	0.45
	Max	276	18.75	20.16	5.07
	# of grains	2	-	29	-
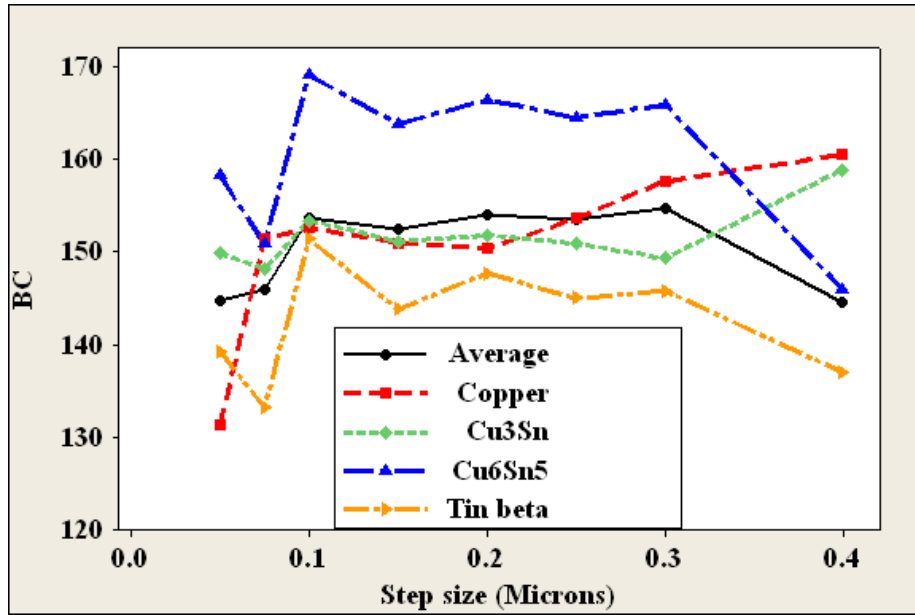
Figure 4-8(a): Effect of step size on BC.
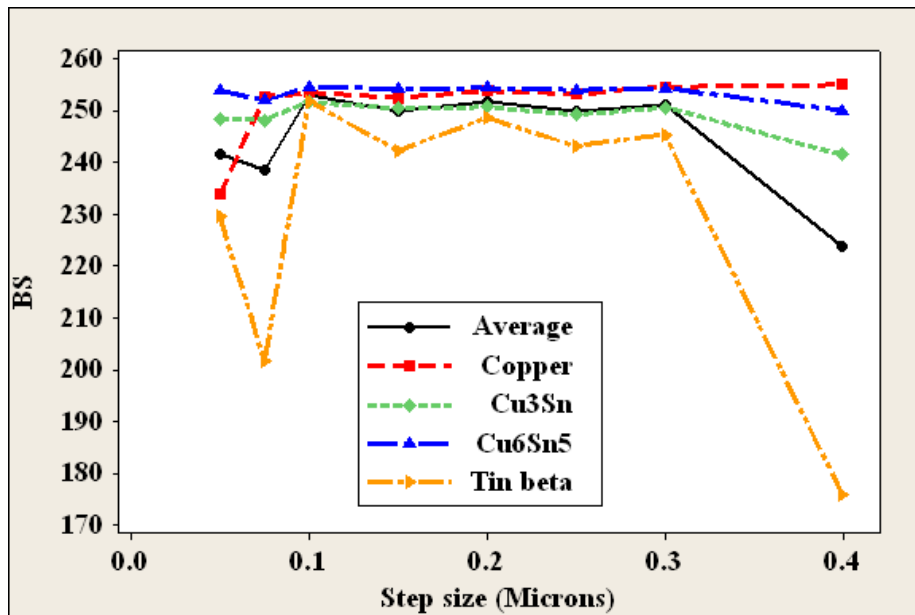
Figure 4-8(b): Effect of step size on BS.
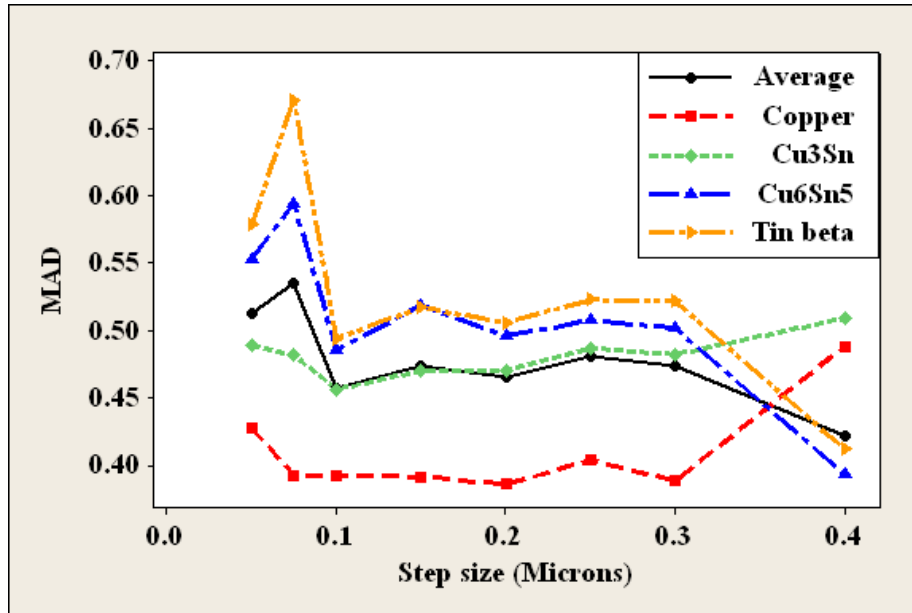
Figure 4-8(c): Effect of step size on MAD.
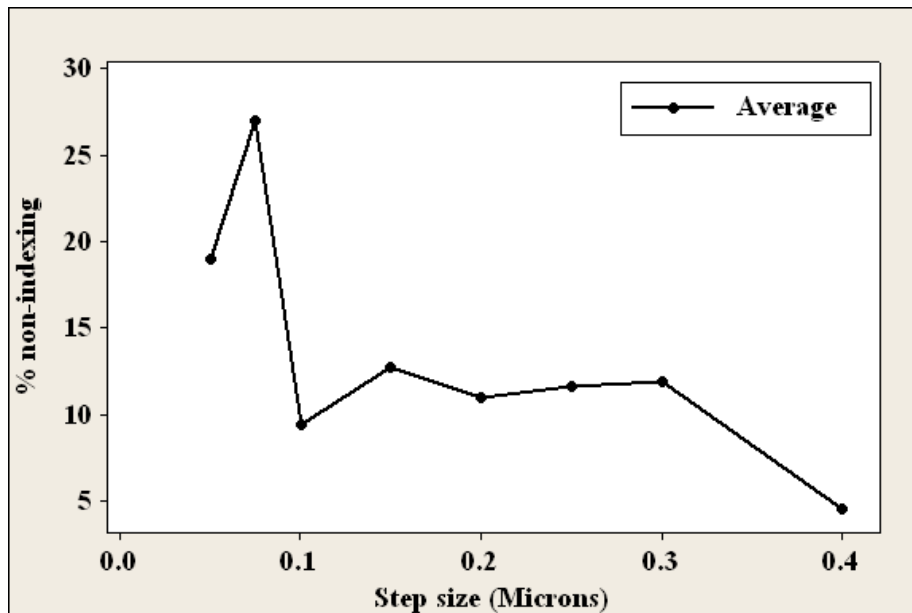
Figure 4-8(d): Effect of step size on percentage of non-indexing rate.

4.4 Conclusions

In this study, a preparation procedure that is adequate for surface preparation of multiple-layer specimens has been developed and optimized. The effect of EBSD parameters on EBSD results

extracted from multiple-layer specimens is investigated and optimized. The proposed surface preparation technique for EBSD analysis was used to finish lead-free solder joint (Sn-3.5%Ag/Cu soldering system).

- It has been found that the best possible surface finish is obtained when automatic grinding-polishing is followed by vibratory-polishing with standard consumable products for certain number of hours.

- High quality EBSD patterns were obtained in a reasonable amount of time and at low cost.

- If the vibratory-polishing step was skipped or shortened, very poor quality EBSD patterns were resulted.

- In this study, four hours of vibratory polishing gave the best possible results when used to prepare the specimens used in this study.

- For other materials, the time range specified here may or may not be the optimum and, therefore, a new time range has to be set by running a parametric study on this factor for the particular set of specimens.

- For valid and reliable phase discrimination and grain size and grain orientation measurement, certain EBSD analysis setting parameters must be optimized. In particular the optimum values for step size and minimum number of detected bands were determined.

- High quality EBSD phase discrimination is obtained in all phases when an optimum value of the minimum number of detected bands of 6 bands is used. As the minimum number of detected bands deviates from this value, some phases were miss-indexed.

References

[1].   Brandon D. and Kaplan W. D., "Microstructural characterization of materials," Wiley Press, England, 1999.

[2].   Kane P. F. and Larrabee G. B., "Characterization of Solid Surfaces," Plenum Press, New York, 1978.

[3].   Klimek L. and Pietrzyk B., "Electron backscatter diffraction as a useful method for alloys microstructure characterization," Journal of Alloys and Compounds, Vol. 382, pp. 17-23, 2004.

[4].   Nakahara S., "Recent development in a TEM specimen preparation technique using FIB for semiconductor devices," Surface and Coating Technology, Vol. 169-170, pp. 721-727, 2003.

[5].   Li J., Malis T., and Dionne S., "Recent advances in FIB-TEM specimen preparation techniques," Materials Characterization, Vol. 57, pp. 64-70, 2006.

[6].   Tkachenko A., Mueller M., Zerna T., and Wolter K. J., "Influence of metallographic preparation on electron backscatter diffraction characterization of copper wire bonds," 33rd International Spring Seminar on Electronics Technology (ISSE), 12-16 May 2010, pp. 50-54.

[7].   Zhou W. and Wang Z. L., "Scanning microscopy for nanotechnology: techniques and application, Springer Press, New York, 2006.

[8].   Katrakova D. and Mucklick F., "Specimen preparation for electronic backscatter diffraction-part I: metals," Praktische Metallographie, Vol. 38, No. 10, pp. 547-565, 2001.

[9].   Voort V. G., "Metallographic specimen preparation for electron backscattered diffraction-Part I," Praktische Metallographie, Vol. 48, No. 9, pp. 454-473, 2011.

[10]. Voort V. G., "Metallographic specimen preparation for electron backscattered diffraction-Part II," Praktische Metallographie, Vol. 48, No. 10, pp. 527-543, 2011.

[11]. Katrakova D. and Mucklick F., "Specimen preparation for electronic backscatter diffraction-part II: ceramics," Praktische Metallographie, Vol. 39, No. 12, pp. 644-662, 2002.

[12]. Koll L., Tsipouridis P., and Werner E. A., "Preparation of metallic samples for electronic backscatter diffraction and its influence on measured misorienation," Journal of Microscopy, Vol. 243, No. 2, pp. 206-219, 2011.

[13]. Randle V., "Electron backscatter diffraction: strategies for reliable data acquisition and processing," Materials characterization, Vol. 60, pp. 913-922, 2009.

[14]. Eicke A., "Enhancements in specimen preparation of Cu(In, Ga)(S, Se)2 thin films," Micron, Vol. 43, pp. 470-474, 2012.

[15]. Wynick G. L. and Boehlert C. J., "Electron backscattered diffraction characterization technique for analysis of Ti2AlNb intermetallic alloy," Journal of Microscopy, Vol. 219, No. 3, pp. 115-121, 2005.

[16]. Wynick G. L. and Boehlert C. J., "Use of electropolishing for enhanced metallic specimen preparation for electron backscatter diffraction analysis," Materials Characterization, Vol. 55, pp. 190-202, 2005.

[17]. Sullivan A. P., "Preparation of difficult samples for EBSD," Microscopy and Microanalysis, Vol. 16, No. S2, pp. 694-695, 2010.

[18]. Humphreys F. J., "Review grain and subgrain characterization by electron backscatter diffraction," Journal of Materials Science, Vol. 36, pp. 3833-3854, 2001.

[19]. Humpherys F. J., "Quantitative metallography by electron backscattered diffraction," Journal of Microscopy, Vol. 195, No. 3, pp. 170-185, 1999.

[20]. Humphreys F. J., "Characterization of fine-scale microstructures by electron backscatter diffraction (EBSD)," Scripta Materialia, Vol. 51, pp. 771-776, 2004.

[21]. Palidar Y., Cochrane R. C., Brydson R., Leary R., and Scott A. J., "Accurate analysis of EBSD data for phase identification," Journal of Physics-Conference Series, Vol. 241, No. 1, pp. 121-124, 2009.

[22]. Chen Y., Hjelen J., Gireesh S. S., and Roven A. J., "Optimization of EBSD parameters for ultra-fast characterization," Journal of Microscopy, Vol. 245, No. 2, pp. 111-118, 2012.

[23]. Abdelhadi O. M. and Ladani L., "IMC growth of Sn-3.5%Ag/Cu system: combined chemical reaction and diffusion mechanisms," Journal of Alloys and Compounds, In Press, Accepted Manuscript, Available online in 54 May 2012.

[24]. Voos P., "Metallographic preparation for electron backscattered diffraction," Materials Science Forum, Vol. 702-703, pp. 578-581, 2012.

[25]. Katrakova D., Damgaard M. J., and Mucklick F., "Preparation for electron backscatter diffraction with LaboPol-4/LaboForce-1," Struers Resources, http://www.struers.com/resourses/elements/12/2435/38art5.pdf, visited in 30 May 2012.

Chapter 5 : Mechanical Characterization of Intermetallic Compounds in Sn-3.5Ag/Cu-Substrate Soldering Systems

Abstract

Elastic and plastic mechanical properties of intermetallic compound (IMC) phases of lead-free Sn3.5Ag/Cu-substrate soldering system are investigated in joints with different sizes using nanoindentation technique. The specimens of different solder joint thicknesses (ranging from 15 µm to 450 µm) were prepared using solid-liquid interdiffusion (SoLID) soldering process. Solder joints were subjected to $360^{o}C$ soldering temperature for 20 min, and then air cooled to room temperature. Nanoindentation technique was used to extract the elastic and plastic properties of Cu_6Sn_5, Cu_3Sn and Ag_3Sn IMCs and β-tin and copper materials. Cu-Sn IMCs formed in specimens with smaller joint thickness show higher elastic modulus, hardness, and yield strength and lower work hardening exponent. This was attributed to the dimensional constraints associated with decreasing joint thickness. Local elastic modulus and hardness of different Cu_6Sn_5 IMC grains were obtained using a combination of nanoindentation and electron backscatter diffraction (EBSD) techniques. Grains with perpendicular orientation to the loading direction show higher elastic modulus and hardness compared to the ones with c-axis parallel to the loading direction.

Key words: Size Effects, Sn-3.5Ag Solders, Nanoindentation, Elastic modulus, Plastic Properties, Intermetallic Compounds.

5.1 Introduction

The mechanical properties of a material determine the limit of applications in which the material can be effectively used. Solder alloy as a joining material provides electrical, thermal, and mechanical functions in electronic assemblies. When an electronic device is in service, the solder connections are subjected to a variety of thermal, mechanical, and thermo-mechanical loads, including shear and axial loads. Creep, stress relaxation, and thermal fatigue are primarily consequences of long term and repeated cycles of loads. Problems of creep, fatigue, crack, and failure of solder joints has been given large amount of attention over many decades [1-11]. Depending on the type of solder and device deformation mechanisms in different types of loading, various constitutive equations have been developed and reported in literature. These constitutive equations are often used in finite element simulation to predict the mechanical behavior of the solder joints in different geometrical configurations and loading conditions. The accuracy of the modeling activities, such as finite element analysis, in probing the solder behavior is inherently affected by the accuracy of the mechanical properties (e.g. elastic modulus, yield stress, work hardening, creep exponent, and fatigue constants, etc.). However, the reported values of mechanical properties for solder materials show a wide range of scatter. This scatter in reported values could be attributed to the differences in the fabrication methods, the testing methods and conditions, and the specimen size and geometry.

Theoretical and/or numerical predictions of the properties of materials are very important not only to analyze and optimize their performance, but also to design new materials. For these reasons, variety of models to predict the effective properties of materials has been reported in literature. One of these models is 2D/3D microstructure-based finite element modeling which strongly depend on accurately knowing the local mechanical properties of different grains and

phases [12-14]. It has been introduced to account for the microstructural factors that influence the mechanical behavior of the materials. Design and development of high performance materials requires a thorough understanding and careful control of microstructure and its effect on the physical and mechanical properties of a material. Therefore, the need to incorporate real, experimentally measured microstructural data such as grain size and distribution, local crystallography of the grains, and local elastic and plastic properties into the property simulations has come to the forefront in recent years.

A review of literature shows that conventional analytical and numerical modeling techniques simplify the heterogeneous microstructure of multiphase solder materials to make analysis more efficient and straightforward. Microstructural complexities, such as spatial distribution of IMC particles, irregular morphology of the IMC particles, and anisotropy in IMC particle orientation and local mechanical response are often simplified because of lack of this information from literature. In order to accurately predict the effective macroscopic material behavior and understand the localized damage mechanism, local (nano- and/or micro-scale) mechanical properties such as Young's modulus and hardness of the different phases formed in solder joints are in need. The local properties of any material can be obtained using nanoindentation which has been proven to be a reliable technique in obtaining elastic properties and has shown fairly accurate results in providing information about plastic behavior of materials. However, the disadvantage of nanoindentation is the absence of any imaging ability which is an issue for heterogeneous materials such as solder joints. Consequently, it is not possible to infer from nanoindentation alone the specific phase or composition under the indent being tested. Some studies have coupled nanoindentation with atomic force microscopy (AFM) while others combined it with scanning electron microscopy (SEM) to overcome this issue. Both techniques

have their limitations. AFM has poor resolution capabilities and SEM does not provide grain

structure and orientation data. Our proposed solution is to combine nanoindentation with electron

backscatter diffraction (EBSD). Nanoindentation is utilized to mechanically probe small volume

of a material within individual grains for which local crystallographic information are obtained

from post EBSD mapping.

5.2   Fundamentals of Nanoindentation

Nanoindentation is an important tool for probing the local mechanical properties of materials.

The main information that one obtains from a nanoindentation test is the load versus depth of

penetration. A typical load versus depth curve is shown in Figure 5-1.
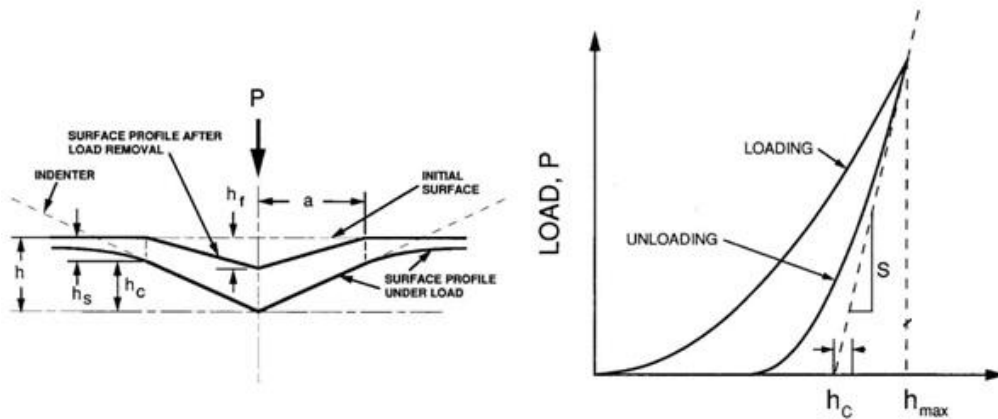
Figure 5-1: (a) A schematic representation of indenter and specimen surface geometry at full
load and full unload for conical indenter showing the relevant quantities, (b) A Schematic
representation of typical Load versus indentation depth curve showing relevant quantities used in
nanoindentation data analysis [16].

The key points of interest in this curve are the maximum applied load, P_{max}; the maximum depth

of penetration, h_{max}, the vertical distance along which contact is made (contact depth after load

removal), h_c; and the unloading slope (contact stiffness) measured at maximum load, S. This data

can be used in calculating the mechanical properties such as elastic modulus and hardness as

well as plastic properties. One of the more commonly used procedures for analyzing

136

nanoindentation load-penetration depth data is the one developed by Oliver and Pharr [16]. In this regard, it is useful to summarize the salient features and the approach taken in this procedure.

The hardness and the reduced Young's modulus are derived as follows [16]:

$$H=\frac{P_{max}}{A} \qquad\qquad (5\text{-}1)$$

and

$$E_r=\frac{\sqrt{\pi}}{2\beta\sqrt{A}} \quad S=\left[\frac{1-v_s^2}{E_s}+\frac{1-v_i^2}{E_i}\right]^{-1} \qquad\qquad (5\text{-}2)$$

where A is the projected area, E_r the reduced modulus, and β is a dimensionless constant. E_s, v_s and E_i, v_i are elastic modulus and Poisson's ratios of the specimen and the indenter, respectively. As seen from Eq.(5-1) and Eq.(5-2), the key to measuring the mechanical properties of a material would be evaluating the contact area (A) at the peak load. This is the single most important factor in analyzing nanoindentation data since most errors in the analysis come from improper assumptions about how the contact area is estimated [16, 17]. Oliver and Pharr found a function that relates the contact area to the contact depth (h_c) for a Berkovich tip; which is three-sided pyramids commonly used in nanoindentation tests, as shown below

$$A(h_c)=24.5h_c^2+f(h_c) \qquad\qquad (5\text{-}3)$$

where $f(h_c)$ is a correction function that takes into account the finite truncation of real tips. The last step in the analysis to calculate the contact area is finding the contact depth, h_c. Experimental determination of the contact stiffness S between the specimen and the indenter tip as the initial slope of the unloading curve allows for the contact depth to be obtained as follows [16]

$$h_c=h_{max}-\varepsilon\frac{P_{max}}{S} \qquad\qquad (5\text{-}4)$$

where ε is a geometry dependent factor that depends on type of indenter.

5.3 Extracting Plastic Properties from Nanoindentation Data

While Young's modulus and hardness of a variety of solder alloys, measured by nanoindentation, have been reported in some studies, the plastic properties such as yield strength and work hardening exponent are not well known. Some studies proposed models for extracting these properties from nanoindentation load-penetration depth data [18-21].

Very few studies characterize the plastic properties of solder joints [22, 23]. In those studies, nanoindentation data were used to extract the hardness and elastic and plastic properties of Sn-3.5Ag and Sn-Ag-Cu solder joints and their associated IMCs. In Deng et al. [22] work, solder joints of 0.5 mm in thickness and 6.35 mm in diameter were used. This size is relatively large when it is compared to current sizes of solder interconnects which are typically in the scale of microns. In his results reported in Table 5-1, the predicated yield strengths of Cu_6Sn_5 and Cu_3Sn IMCs were quite high compared to the values obtained by Song et al. [23]. Work hardening exponents for Cu_6Sn_5 and Cu_3Sn IMCs were shown to be zero in Deng's study while non-zero positive values were obtained in Song's study. The differences in the reported values could be due to the difference in the experimental procedure applied to prepare the solder joints. Although both studies used very close soldering temperatures; $240^{o}c$ and $250\ ^{o}C$ in Deng et al. and Song et al. study, respectively, the solder alloy and the subsequent fabrication steps such as soldering time, number of reflows, aging time and temperature are different. Solder alloy of 3.5wt%Ag reflowed on Cu substrate was used in Deng's study while Sn-3wt.%-0.5wt.%Cu reflowed on Cu substrate was used by Song et al. both studies have not reported the thickness of the resulting joints and therefore, no correlation on possible size effects was possible to be made. Thus, further studies should be conducted to elucidate these contradicting results of plastic properties of solder joints.

Table 5-1: Comparison of two different results of plastic properties of different IMC phases calculated following Dao's model obtained

phase	Deng et al. [22]		Song et al. [23]	
	Yield strength, (MPa)	Work-hardening exponent	Yield strength, (MPa)	Work-hardening exponent
Cu_6Sn_5 IMC	2009±63	0	1850.6±123.9	0.105±0.010
Cu_3Sn IMC	1787±108	0	1440.3±260.4	0.075±0.001
Ag_3Sn IMC	794±92	0.072±0.027	334.1±39.1	0.056±0.002

The size effects on elastic and plastic properties have not been done which motivates this current study to consider its possible influence on the resulting plastic properties of micro-scale solder joints. Dao et al. developed a method to extract the plastic constitutive properties of materials using nanoindentation test [20]. Their technique was further modified by researchers in different aspects [18, 19, and 21]. However, comparing the original model with a modified version actually showed no significant difference and in some ranges of materials, Dao's model showed more accurate results [15]. Dao's model uses the constant, C, in the load-displacement relationship developed by Kick's law as follows:

$$P=Ch^2$$
(5-5)

where P, is the indentation load, h, is the indentation depth, and C, a constant given by

$$C=\sigma_{0.033}\Pi_1(\frac{E_r}{\sigma_{0.033}})$$
(5-6)

where $\sigma_{0.033}$ is the representative stress at a plastic strain of 0.033 determined by the indenter geometry, E_r is the reduced elastic modulus, and Π_1 is a dimensionless function given by the following equation

$$\pi_1 = -1.131\left[\ln\left(\frac{E_r}{\sigma_{0.033}}\right)\right]^3 +13.635\left[\ln\left(\frac{E_r}{\sigma_{0.033}}\right)\right]^2 - 30.594\left[\ln\left(\frac{E_r}{\sigma_{0.033}}\right)\right]+29.267$$
(5-7)

The representative stress is theoretically related to the yield stress as follows:

$$\sigma_{0.033}=\sigma_y(1+\frac{E}{\sigma_{0.033}}0.033)^n$$
(5-8)

139

where E is the elastic modulus of indented material, and n is work hardening exponent of the same material. The work hardening exponent can be calculated using another dimensionless function as follows:

$$\frac{1}{E_r h_{max}} \frac{dP}{dh} \Big|_{h_{max}} = \Pi_2 \left(\frac{E_r}{\sigma_r}, n\right) \tag{5-9}$$

where h_{max} is the maximum indentation depth, $\frac{dP}{dh} \big|_{h_{max}}$ is the slope of the unloading segment evaluated at maximum depth, and Π_2 is the second dimensionless function given in Eq.(5-10).

$$\pi_2 = (-1.40557n^3 + 0.77526n^2 + 0.15830n - 0.06831)\left[\ln\left(\frac{E_r}{\sigma_{0.033}}\right)\right]^3$$

$$+ (17.93006n^3 - 9.22091n^2 - 2.37733n + 0.86295)\left[\ln\left(\frac{E_r}{\sigma_{0.033}}\right)\right]^2 \tag{5-10}$$

$$+ (-79.99715n^3 + 40.55620n^2 + 9.00157n - 2.54543)\left[\ln\left(\frac{E_r}{\sigma_{0.033}}\right)\right]$$

The determination of the plastic properties starts with identifying a complete nanoindentation (i.e., loading-unloading) load-displacement curve. From this curve the representative stress is determined by Eq.(5-6) which involves utilization of a dimensionless function of the form given in Eq.(5-7). After the representative stress has been determined, the value of work hardening exponent, n, is determined using Eq.(5-9) which incorporates a second dimensionless function of the form given in Eq.(5-10). Once both the representative stress and work hardening exponent are determined and a point in the plastic region of the material's stress strain curve is known, a value for yield stress can be evaluated by using Eq.(5-8).

5.4 Experimental Procedure

In the present work, the Pb-Free Sn-3.5%Ag/Cu-substrate solder joints were investigated. To evaluate the effect of size on the local mechanical properties, two different joint configurations with different sizes were fabricated [24]. Figure 3-1shows actual images and schematic drawings

of the two configurations used in this study. One is called "small-scale specimen" (SS) as shown in Figure 3-1(a). The other configuration is called "large-scale specimen" (LS) and is shown in Figure 3-1(b). To obtain all different possible phases of IMCs, higher temperature of 360 $^{\circ}$C and longer time or 20 min were used for fabrication. The joint thickness in SS specimens were controlled by applying pressure and are on average about 15 μm and 25μm when 0.55 and zero MPa pressure were applied, respectively. The two thicknesses obtained from SS configuration were differentiated by two different names; SS1 is used for specimen with 15 μm and SS2 is used for 25 μm-thick specimen. A joint thickness of 450 μm was achieved in LS configuration without applying any pressure. After fabrication, microstructural analysis was used and it was shown that all the joints consist of Cu, β-tin and intermetallic (IMC) layers, namely, Cu_6Sn_5 and Cu_3Sn IMCs. IMC particles such as Ag_3Sn or Cu_6Sn_5a were also observed, and most clearly in LS specimens. Mechanical polishing procedures followed by vibratory polishing, as described elsewhere [25], were used for the joint preparation for nanoindentation testing as well as for subsequent EBSD mapping.

Nanoindentation tests were conducted at room temperature using a Hysitron TriboIndenter with force and displacement resolutions of 50nN and 0.1 nm, respectively. The machine was equipped with an indenter tip with standard diamond Berkovich geometry. The indenter was pressed into the specimen up to 5000 μN maximum load with loading rate of 1000 μN /sec, and then it was held at the maximum load for 5 sec [26], to avoid the influence of creep on unloading characteristics, before it was completely withdrawn at unloading rate of 1000 μN /sec. At least 5 indents were collected from each material. The indents were separated by 5μm which was enough distance to avoid interaction between the sites. The results from the nanoindentation

experiments, mainly the force-displacement curve, were used in Eqs.(5-1) to (5-10), to determine the elastic and plastic properties for each material.

For evaluation of local properties of individual Cu_6Sn_5 IMC grains, nanoindentation tests were conducted on Cu_6Sn_5 IMC regions. Therefore, nanoindentation impressions were located within the individual grains of IMC phase. The 15x7 array of indentations gave a total of 105 indents. When indentation tests were done, specimens were transferred to a SEM equipped with EBSD system to allow for the areas with indents to be EBSD mapped. This step allows the extraction of local crystallographic information, such as grain size and orientation and relates them to the local mechanical properties obtained from nanoindentation test.

5.5   Results and Discussions

Average representative nanoindentation load versus displacement curves in Cu_6Sn_5, Cu_3Sn, Ag_3Sn, β-tin, and Cu regions are shown in Figure 5-2.
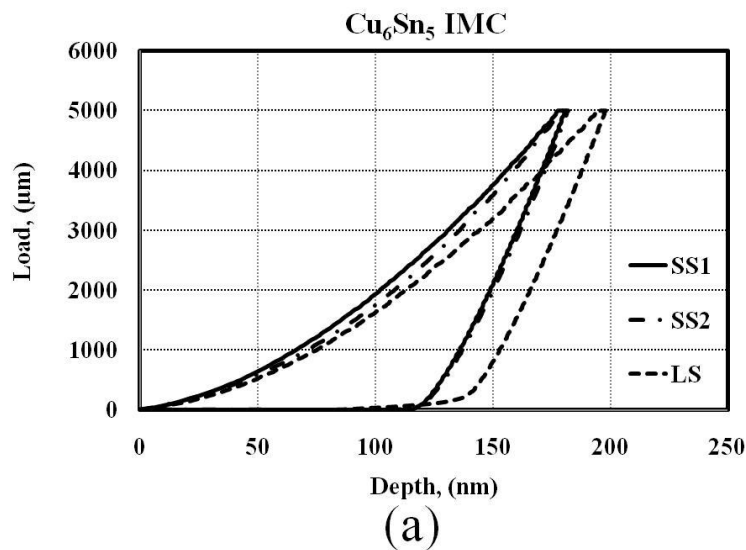
Figure 5-2(a): Nanoindentation load versus displacement curves of Cu_6Sn_5 IMC.

(b)
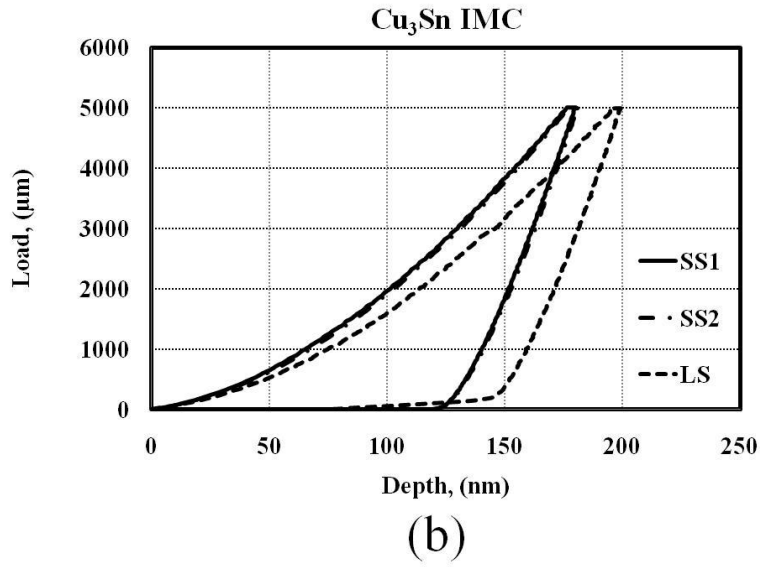
Figure 5-2(b): Nanoindentation load versus displacement curves of Cu$_3$Sn IMC.

(c)
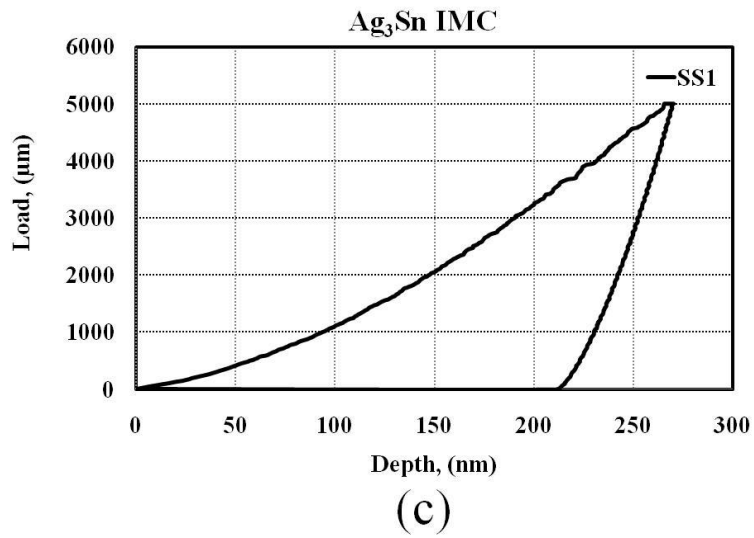
Figure 5-2(c): Nanoindentation load versus displacement curves of Ag$_3$Sn IMC.
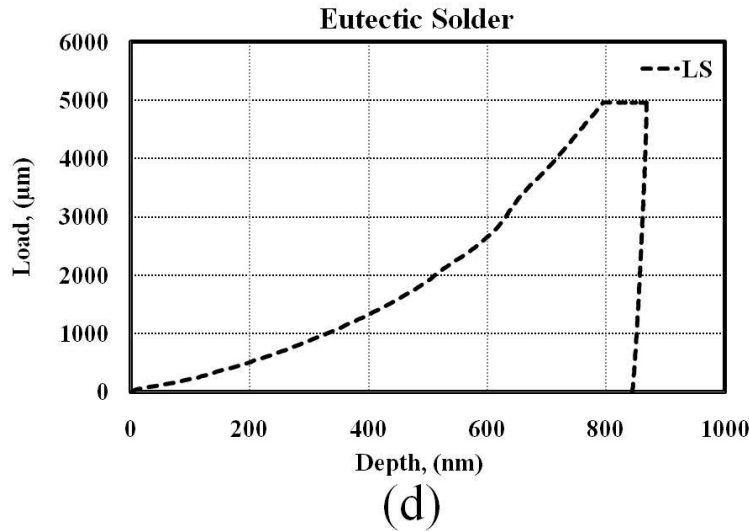
Figure 5-2(d): Nanoindentation load versus displacement curves of eutectic solder.
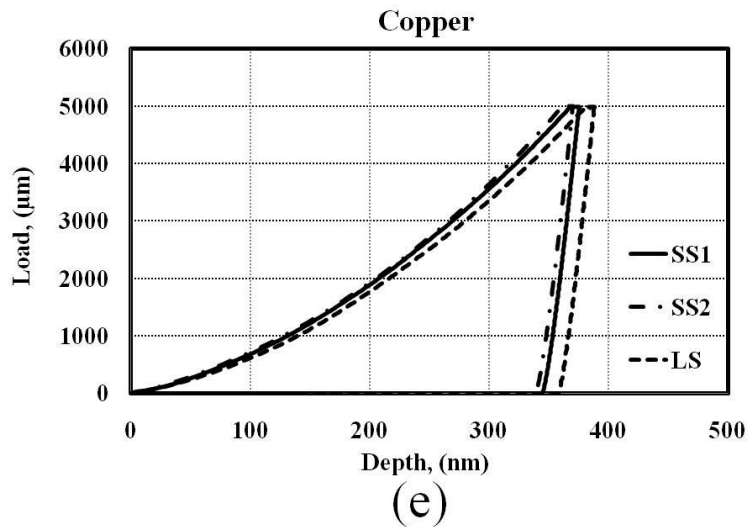
Figure 5-2(e): Nanoindentation load versus displacement curves of Cu.

The curve data was collected for each material from each specimen except for eutectic solder and

Ag_3Sn. Nanoindentation data curves for eutectic solder were available only from LS specimens

because much eutectic solder is available for testing in this specimen when comparing with other

two specimens nanoindentation curves for Ag_3Sn IMC were only obtained from SS1 specimens

because under the condition of fabrication the SS1 specimen had completely transformed to

IMCs and large Ag_3Sn IMC was available for evaluation. Ag_3Sn IMC formed in LS specimens

was relatively in small grains and not suitable for nanoindentation testing. The curves exhibit

144

different shapes from one material to another, primarily due to the difference between the mechanical properties of the materials involved in the soldered joint structure. This is confirmed by Figure 5-3 which shows SEM micrographs indicating representative nanoindentation impressions in different materials.

As can be seen from Figure 5-2(a), (b), and (e), the load-displacement curves at the same peak load obtained from SS1 and SS2 are almost identical and coincident on each other, while they differ from that obtained from LS specimen for the same material/phase. This is attributed to the greater size difference between SS and LS specimens. LS specimens show larger indentation depth at maximum load. The elastic and plastic properties are extracted directly from the curves. Therefore, these properties vary for different size of specimens for the same phase. For the Cu material shown in Figure 5-2(e), the load-displacement curves obtained from different specimens are almost identical with nearly parallel unloading segments.   Therefore, less variation in the mechanical response of Cu is expected.
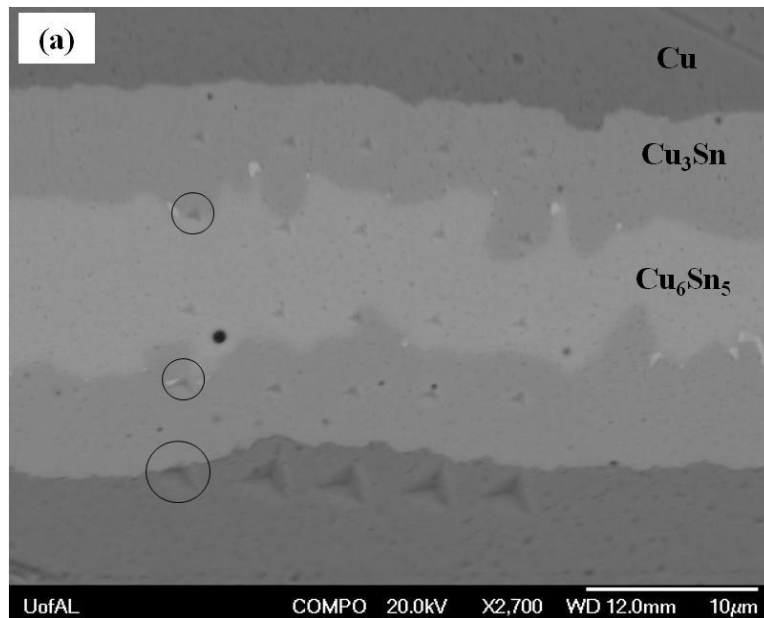
Figure 5-3(a): SEM micrograph shows representative nanoindentation tests in SS1 specimen.
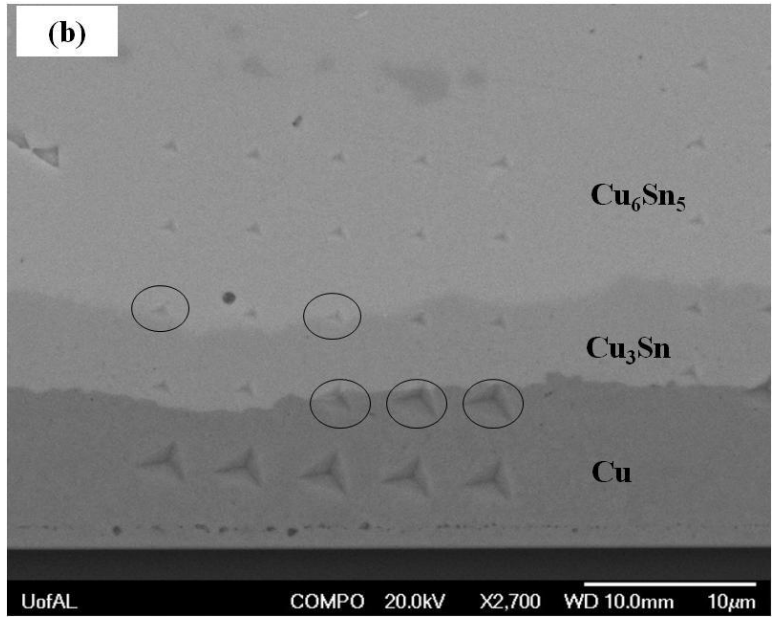
Figure 5-3(b): SEM micrographs show representative nanoindentation tests in SS2 specimen.
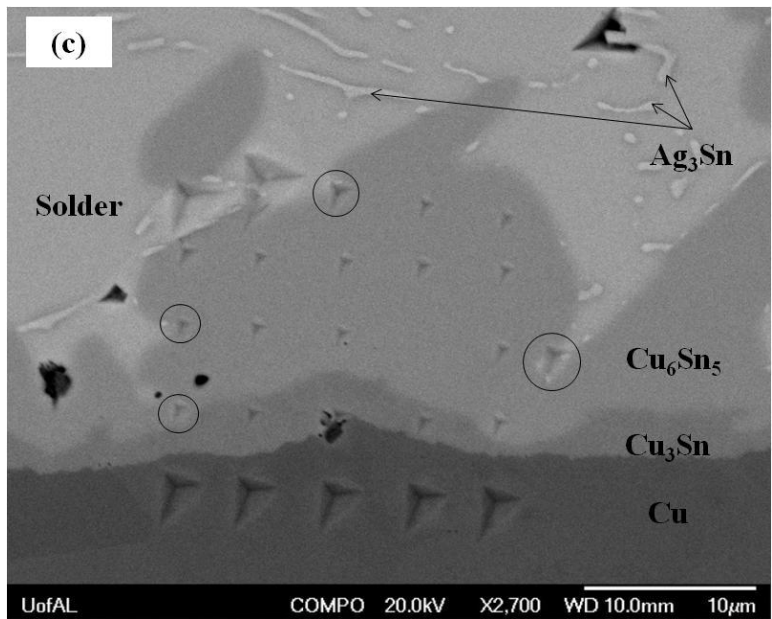
Figure 5-3(c): SEM micrograph shows representative nanoindentation tests in LS specimen.
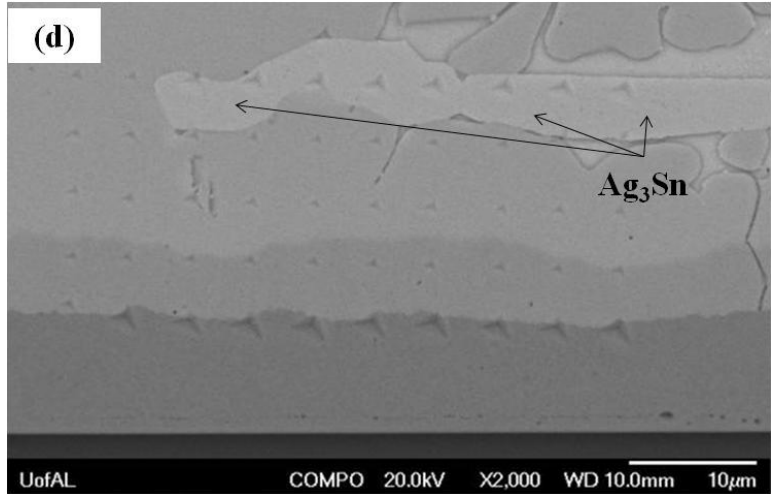
Figure 5-3(d): SEM micrograph shows representative nanoindentation tests in Ag$_3$Sn region.
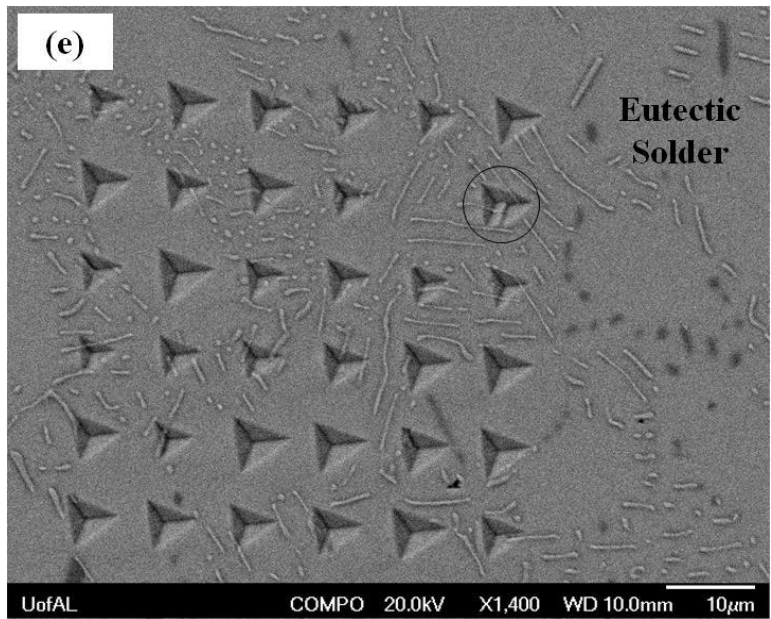
Figure 5-3(e): SEM micrograph shows representative nanoindentation tests in in eutectic solder region.

At least 10 indentation load-displacement curves were collected from each material to obtain statistically significant data. Indentation impressions that were within or near the interfaces between materials and close to defect sites were avoided in this study. In Figure 5-3, circled impressions were excluded from data analysis. Using the method of Oliver and Pharr [16] summarized by Eqs.(5-1) to (5-4) in Section 5.2, the elastic modulus and hardness were

determined from the load-displacement curve of each material in different specimens. For a diamond indenter tip, E_i = 1140 Gpa and v_i = 0.07 [16] while v_s was assumed to be 0.309 for Cu_6Sn_5, 0.299 for Cu_3Sn, 0.30 for Ag_3Sn, 0.30 for eutectic solder, and 0.33 for Cu [21-22, 27]. Results of elastic properties are summarized in Table 5-2.

Table 5-2: Elastic properties (elastic modulus and hardness) of Cu_6Sn_5, Cu_3Sn, Ag_3Sn, Eutectic Solder, and Cu materials.

Joint Thickness (µm)	Cu_6Sn_5 IMC		Ag_3Sn IMC	
	E (GPa)	H (GPa)	E (GPa)	H (GPa)
15	112.32±1.21	7.73±0.18	88.69±4.18	3.38±0.25
25	117.63±3.26	8.09±0.37	-	-
450	104.07±3.35	6.73±0.51	-	-
	Cu_3Sn IMC		Bulk Solder	
	E (GPa)	H (GPa)	E (GPa)	H (GPa)
15	130.08±2.69	7.57±0.21	-	-
25	131.71±3.27	7.49±0.27	-	-
450	118.65±2.18	6.19±0.56	58.35±2.27	0.30±0.025

Joint Thickness (µm)	Cu	
	E (GPa)	H (GPa)
15	100.83±4.65	1.65±0.081
25	103.16±1.63	1.67±0.13
450	102.67±4.80	1.57±0.038

Figure 5-4 shows the size effect of joint thickness on elastic properties for Cu_6Sn_5, Cu_3Sn, and Cu materials. Overall, the experimental results of elastic properties for the different materials were found within the range of literature [22-23, 26, 28-29].

It can be seen from Table 5-2 and Figure 5-4 that the elastic modulus and hardness show noticeable changes as the specimen size changes.

(a)   (b)
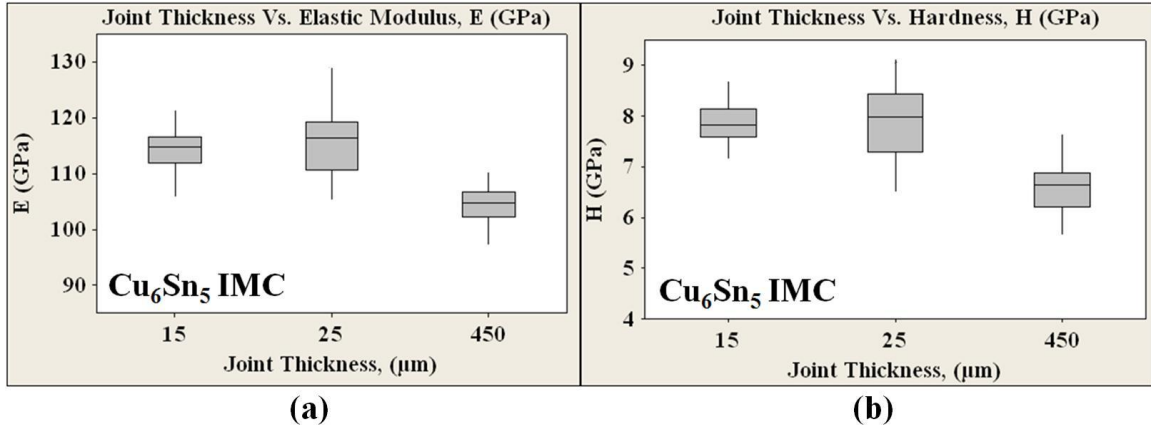
Figure 5-4(a, b): Elastic modulus and hardness versus joint thickness for Cu_6Sn_5 IMC

(c)   (d)
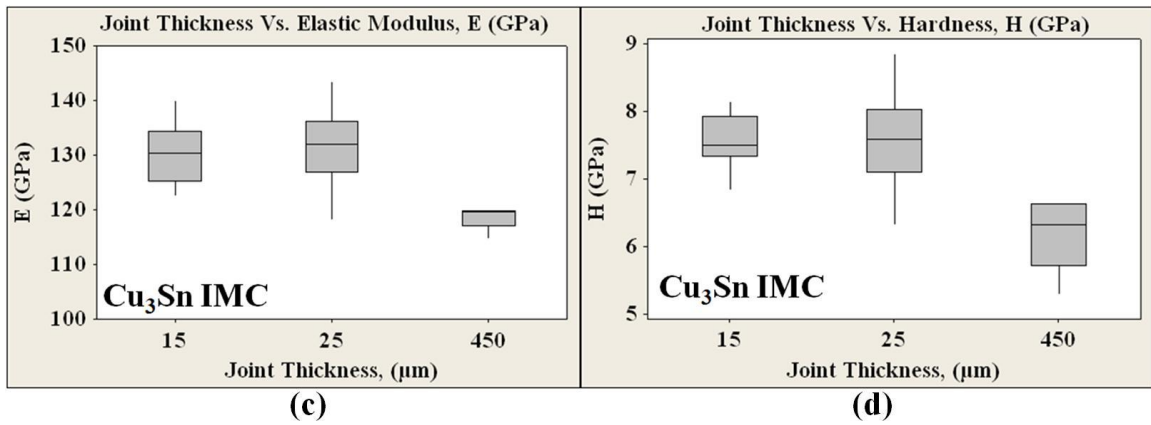
Figure 5-4(c, d): Elastic modulus and hardness versus joint thickness for Cu_3Sn IMC

(e)   (f)
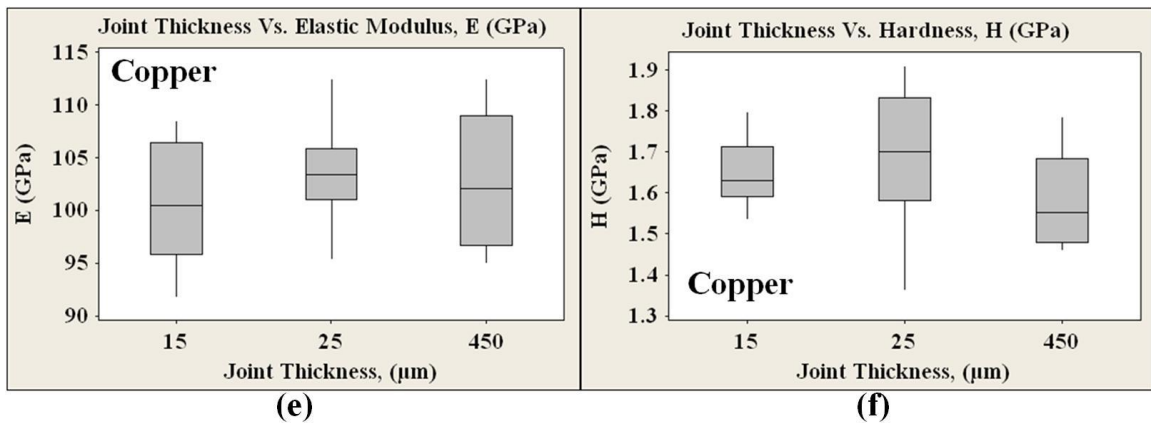
Figure 5-4(e, f): Elastic modulus and hardness versus joint thickness for Cu.

The elastic modulus and hardness of Cu_6Sn_5 IMC first increases and then decreases as joint

thickness changes from 450 to 25 and then to 15 µm. Overall, the SS specimens show higher

average elastic modulus and hardness compared to LS specimen. This can be considered a sign

of size effects playing a role in this IMC. Similarly, the elastic modulus for Cu_3Sn IMC shows

similar behavior as in Cu_6Sn_5 IMC while hardness shows monotonic increase as the joint

thickness decreases. Cu results show similar values for elastic modulus in all specimens.

Therefore, this property was found to be independent of joint thickness. Hardness results for Cu

show increase in values obtained for SS specimens. For Ag_3Sn IMC and eutectic solder,

comparison of elastic properties with respect to joint thickness was not possible. This was

because of the limited size and limited availability of these phases in the respected specimens.

Phases were either missed or very small and therefore, it was extremely difficult to locate

nanoindentation tests on them.

Table 5-3: Plastic properties (yield strength and work hardening exponent) of Cu_6Sn_5 IMC, Cu_3Sn IMC, Ag_3Sn IMC, Eutectic Solder, and Cu.

Joint Thickness (µm)	Cu_6Sn_5 IMC		Ag_3Sn IMC	
	σ_y,(MPa)	n	σ_y,(MPa)	n
15	2382.38±149.41	0.19±0.021	254.76±54.57	0.47±0.014
25	3264.99±507.77	0.11±0.009	-	-
450	2000.02±403.93	0.23±0.054	-	-
	Cu_3Sn IMC		Bulk Solder	
	σ_y,(MPa)	n	σ_y,(MPa)	n
15	2200.32±138.02	0.20±0.014	-	-
25	2361.96±63.02	0.16±0.009	-	-
450	1481.59±358.72	0.28±0.045	0.37±0.069	0.61±0.001
Joint Thickness (µm)	Cu			
	σ_y,(MPa)	n		
15	17.89±1.30	0.56±0.002		
25	18.59±2.68	0.55±0.004		
450	11.78±0.78	0.58±0.002		

Eqs.(5-5) to (5-8) were used to extract the yield strength and work hardening exponent from the

load-displacement curves for each phase. The results in different specimens are listed in Table 5-

3 and are visualized in Figure 5-5, for all different materials tested in this study.

Cu_6Sn_5 IMC shows an increase in yield strength as the joint thickness increases from 15 µm to

25 µm, and yield strength decreases as the joint thickness experiences a further increase from 25

µm to 450 µm. For the same material, work hardening exponent decreases and then increases as

the joint thickness increases from 15 µm to 25 µm and then to 450 µm. Therefore, similar non-

monotonic behavior in the values of yield strength and work hardening exponent is observed.

When values of yield strength and working hardening exponents extracted for Cu_6Sn_5 IMC are

compared in SS and LS specimens, SS specimens show higher yield strength and lower work

hardening exponents compared to the values of LS specimen. This was attributed to the size

effect. Our plastic properties of Cu_6Sn_5 IMC were also compared to the reported values from

literature. The yield strength from our study was within the range of the reported values by Deng

et al. and Song et al. [22, 23]. However, the current value of work hardening exponent correlates

well with the value obtained in Song's work [23].

Similarly, Cu_3Sn IMC has shown an identical behavior as that associated with Cu_6Sn_5 IMC.

Yield strength slightly increases and then decreases while work hardening exponent decreases

and then increases as the joint thickness increases from 15 µm to 25 µm and then to 450 µm.

Overall, the SS specimens show higher yield strength and lower work hardening exponents

compared to the values extracted from LS specimens. Therefore, this was attributed to the size

effects. The reported values for the yield strength for Cu_3Sn IMC, from this study, are reasonable

compared to the documented literature values summarized in Table 5-1 [22, 23]. However, our

values for the work hardening exponent are much higher compared to the values in the literature [22, 23] as summarized in Table 5-1.
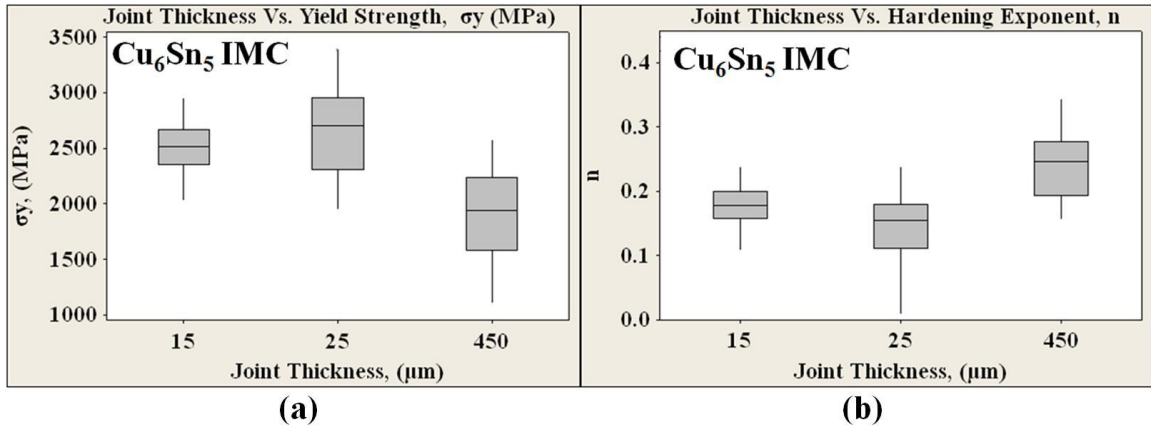
Figure 5-5(a, b): Yield strength and work hardening exponent versus joint thicknessCu_6Sn_5 IMC.
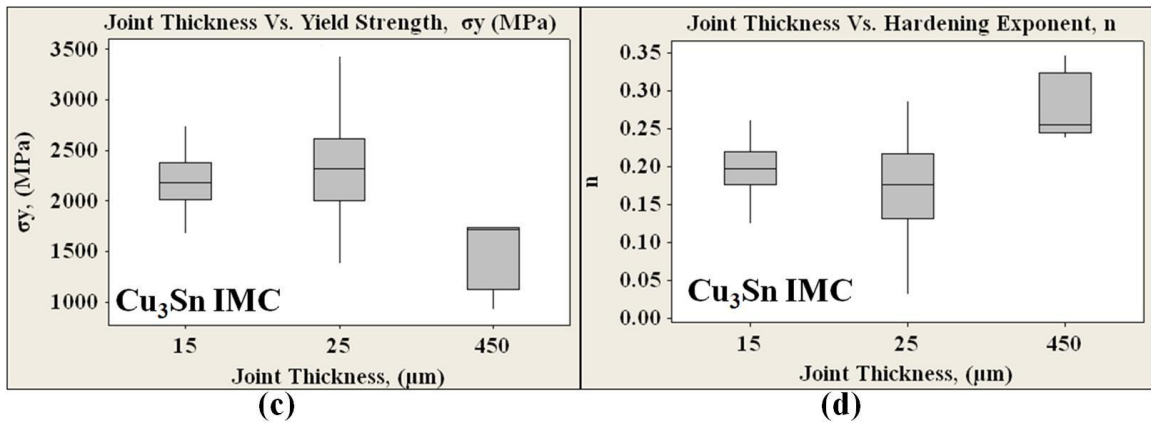
Figure 5-5(c, d): Yield strength and work hardening exponent versus joint thickness Cu_3Sn IMC.
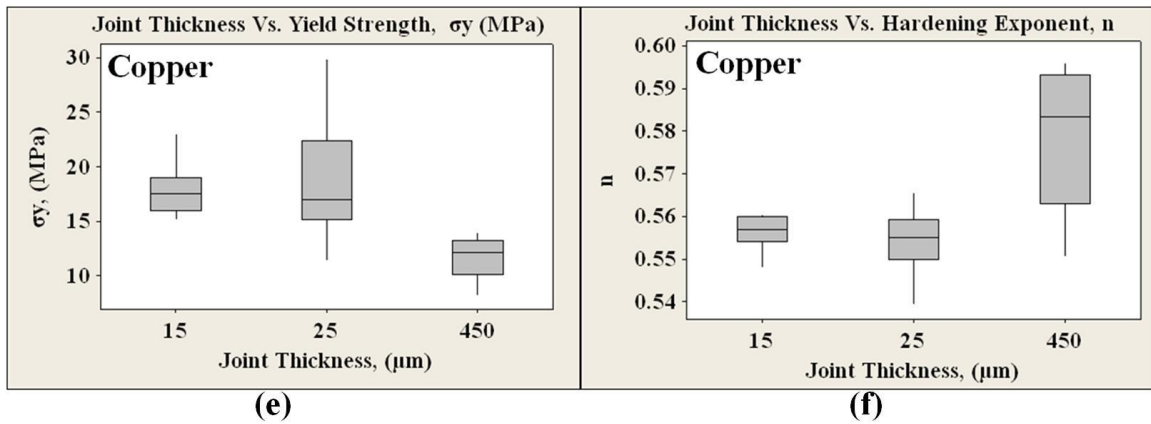
Figure 5-5(e, f): Yield strength and work hardening exponent versus joint thickness Cu.

152

The values obtained for Ag$_3$Sn were compared with the values reported in the literature, see Table 5-4. Our value of yield strength for Ag$_3$Sn, 254.76±54.57 MPa, is lower than but close to the value reported by Song et al. [23], 334.1±39.1 MPa. However, it is significantly lower than that reported by Deng et al. [22], 794±92 MPa.

Table 5-4: Comparison of plastic properties of different materials in the current study with those reported in the literature.

	Current study			Reference 22			Reference 23		
Cu$_6$Sn$_5$ IMC	Joint Thickness (µm)	σ$_y$,(MPa)	n	Joint Thickness (µm)	σ$_y$,(MPa)	n	Joint Thickness (µm)	σ$_y$,(MPa)	n
	15	2382.38±149.41	0.19±0.021	500	2009±63	0	Not indicated	1850.6±123.9	0.105±0.010
	25	3264.99±507.77	0.11±0.009						
	450	2000.024 03.93	0.23±0.054						
Cu$_3$Sn IMC		σ$_y$,(MPa)	n		σ$_y$,(MPa)	n		σ$_y$,(MPa)	n
	15	2200.32±138.02	0.20±0.014	500	1787±108	0	Not indicated	1440±260.4	0.075±0.001
	25	2361.96±63.02	0.16±0.009						
	450	1481.593 58.72	0.28±0.045						
Ag$_3$Sn IMC		σ$_y$,(MPa)	n		σ$_y$,(MPa)	n		σ$_y$,(MPa)	n
	15	254.76±54.57	0.47±0.014	Not indicated	794±92	0.072±0.027	Not indicated	334.1±39.1	0.056±0.002
	25	-	-						
	450	-	-						
	Current study			Reference 22					
Eutectic Solder		σ$_y$,(MPa)	n		σ$_y$,(MPa)	n			
	15	-	-	500	50±20	0.077±0.003			
	25	-	-						
	450	0.37±0.069	0.61±0.001						
	Current study			Reference 22			Reference 21		
Cu	Joint Thickness (µm)	σ$_y$,(MPa)	n	Joint Thickness (µm)	σ$_y$,(MPa)	n	Joint Thickness (µm)	σ$_y$,(MPa)	n
	15	17.89±1.30	0.56±0.002	Not indicated	180±9	0.11±0.003	Not indicated	10	0.5
	25	18.59±2.68	0.55±0.004						
	450	11.78±0.78	0.58±0.002						

The work hardening exponent of 0.47±0.014 MPa was found to be much higher than the values reported in literature [22, 23]. Cu has shown similar values for yield strength and work hardening exponent in SS specimens. When these values compared with those obtained from LS specimen, higher yield strength is found in SS specimens while comparable value was obtained for the work hardening exponent in all specimens. Overall, the plastic properties for the Cu, obtained in our study, are reasonable compared to the values reported in the literature [21], as seen in Table 5-4. However, they show significant difference with those reported by Deng et al. [22].

5.6 Local Mechanical Properties of Cu_6Sn_5 IMC

Of the 105 indents in the array, an average of 10 to 30 indents were located within individual grains and were used to compare the variation of the mechanical properties from one grain to another. Some of the indents were excluded either if they were not successfully made, were within a grain boundary region, or were on inclusions. Figure 5-6 shows SEM images and EBSD maps of two different pre-indented Cu_6Sn_5 IMC grains. 10 indents were located within grain #1 and 28 indents were located within grain #2.
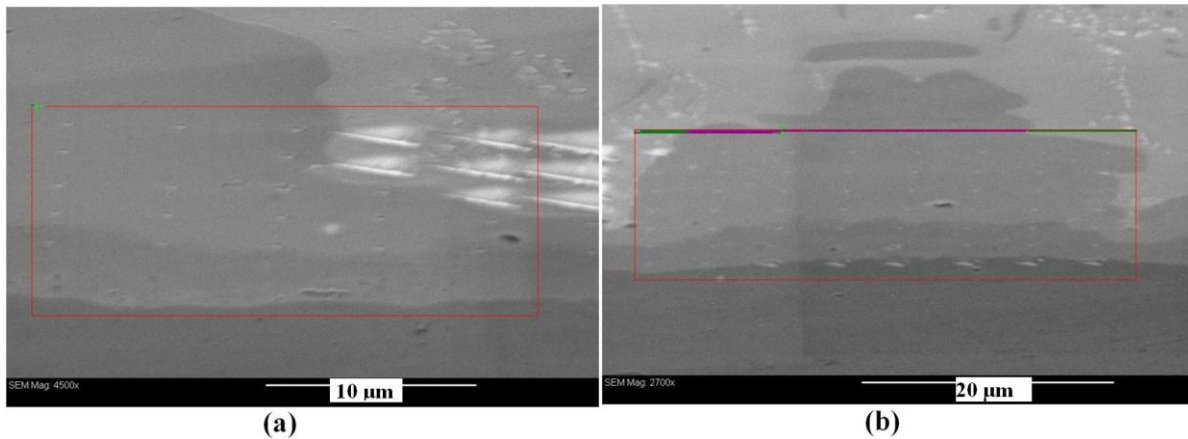
Figure 5-6(a, b): SEM images of two different Cu_6Sn_5 grains.

154
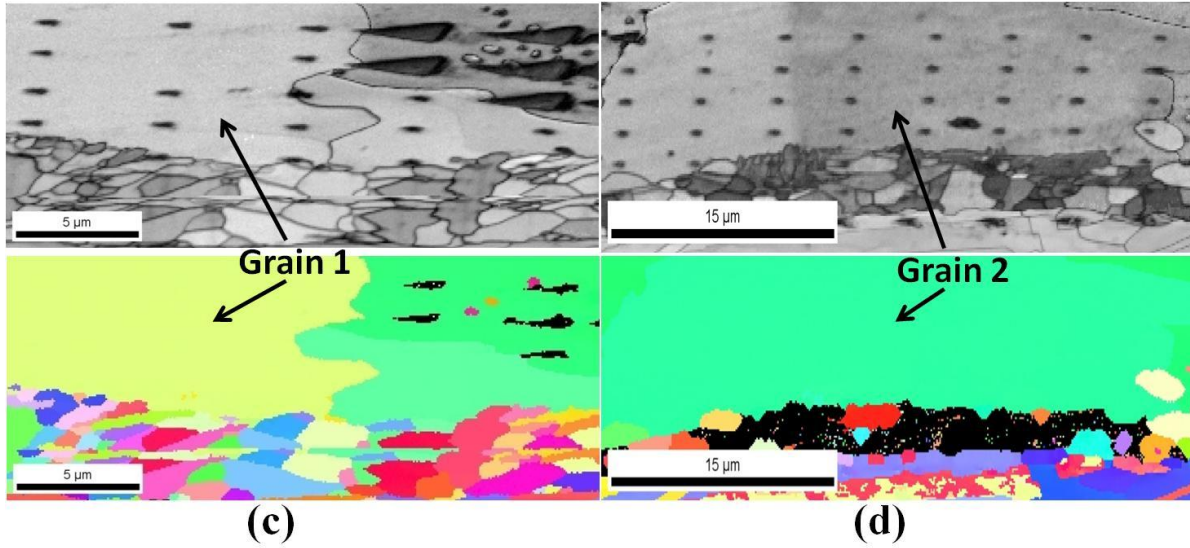
Figure 5-6(c, d): Band contrast (top) and orientation maps for Cu_6Sn_5 grains in a and b.
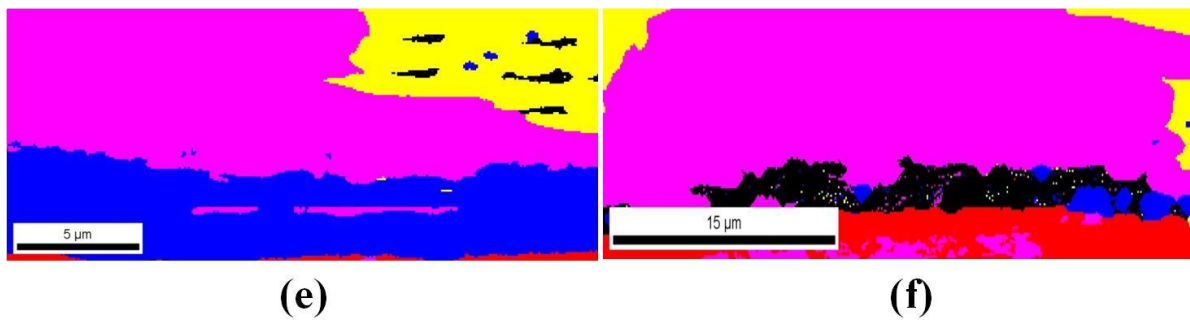
Figure 5-6(e, f): Phase maps for Cu_6Sn_5 grains in a and b.

Figure 5-6(g, h): (g) shows the inverse pole figures for orientation maps in c and d. (h) shows the color code in e and f.

Grains #1 and 2 are selected as they have shown distinctive local orientations as one could

distinguish based on the difference in color of each grain using the orientation maps in Figure 4-

6(c and d), color interpretation of figure 5-6(g) as well as the EBSD local orientation data

155

provided in Table 5-5. When the local orientation of each Cu_6Sn_5 grain, given in Table 5-5, is

related to the indentation loading direction, grain #1 was found to have its c-axis is almost

perpendicular to the loading direction and grain #2 to have its c-axis is nearly parallel to the

loading direction. These local orientations corresponded to the following Burge Euler angles

(phi1, PHI, phi2) = (189.3º, 55.4º, 54.4º) and (358.8º, 881º, 36.1º) for grain #1 and #2,

respectively as summarized in Table 5-5.
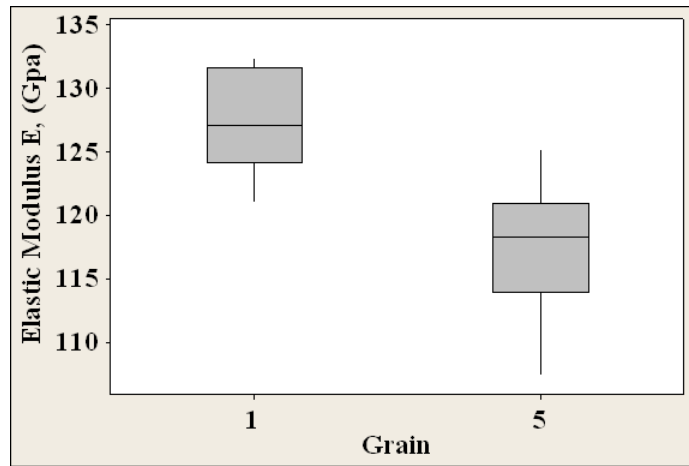
Figure 5-7(a): Comparison of Elastic modulus in two different Cu_6Sn_5 IMC grains.
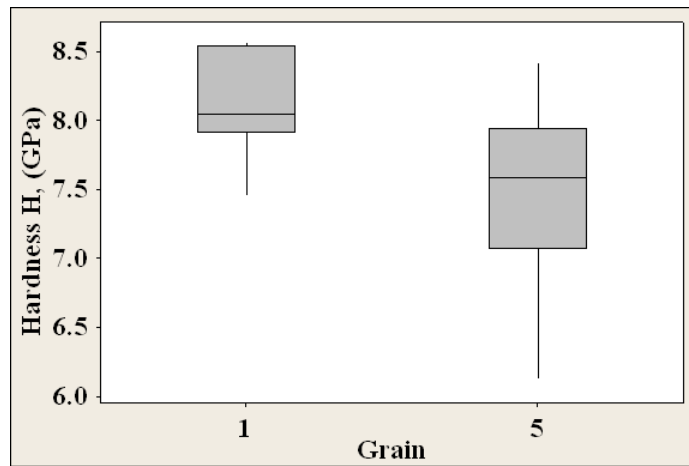
Figure 5-7(b): Comparison of Hardness in two different Cu_6Sn_5 IMC grains

Using nanoindentation load-displacement curves associated with these indents, elastic modulus

and hardness for each of the indents were calculated. For each Cu_6Sn_5 IMC grain, these local

mechanical properties were then averaged and the final results are displayed and summarized in Figure 5-7 and Table 5-5, respectively. Figure 5-7 and Table 5-5 show that both the elastic modulus and hardness are different in one grain from the other. Grain #1 show higher elastic modulus and hardness compared to grain #2. Higher elastic modulus in specific direction of Cu_6Sn_5 IMC crystal was attributed to the elastic anisotropy associated with Cu_6Sn_5 hexagonal structure [31]. The origin of elastic isotropy was attributed to the difference in bonding strength along some directions compared to the others [31]. Higher hardness was attributed to the limited slip systems present in the hexagonal structure.

Table 5-5: Summary of elastic properties of two different Cu_6Sn_5 IMC grains.

Variable	Grain	Mean	Standard Deviation	Minimum	Maximum	Average Orientation		
						Phi1	Phi	Phi 2
E (Gpa)	1	127.57	3.99	120.99	132.4	189.3	55.4	54.4
	2	117.39	5.3	107.36	125.16	358.8	88.1	36.7
H(GPa)	1	8.137	0.373	7.456	8.57	189.3	55.4	54.4
	2	7.475	0.631	6.123	8.425	358.8	88.1	36.7

5.7 Conclusions

The following conclusions can be drawn from our study on the size effects on the mechanical properties of as-soldered Sn-3.5Ag/Cu-substrate joints.

- The results of elastic properties for IMCs and eutectic solder show significant size effects. Values of elastic modulus increase as the joint size decreases.
- Plastic properties show a correlation with the joint size. As the joint size decreases, the yield strength of Sn-Cu IMCs increases while the work hardening exponent decreases.
- Local elastic properties of cu_6Sn_5 IMC grains show strong correlation with the local crystallographic characteristics of the grains.

-       Lower elastic modulus and hardness are obtained in grains that have their c-axis of the Cu_6Sn_5 IMC hexagonal structure deviates from being perpendicular to the nanoindentation loading direction.

References

[1]. Yin L.M., Zhang X.P., and Lu C., " Size and volume effects on the strength of microscale lead-free solder joints," Journal of Electronic Materials, Vol. 38, No. 10, pp. 2179-2183, 2009.

[2]. Huijun J.W., Hoe C., and Hua W.E., " Modeling solder joint reliability of BGA packages subject to drop impact loading using sub-modeling," in proceedings of ABAQUS User's Conference, pp. 1-11, 2002.

[3]. Chaparala S., Pitarresi J.M., Parupalli S., Mandepudi S., and Meilunas M., "Experimental and numerical investigation of the reliability of double-sided area array assemblies," Journal of Electronic Packaging, Vol. 128, pp. 441-448, 2006.

[4]. Chung S., and Park S.B., " Numerical investigation of underfill failure due to phase change of Pb-free flip chip solders during board-level reflow," IEEE Transactions on Components and Packaging Technology, Vol. 31, No. 3, pp. 661-669, 2008.

[5]. Wippler S. and Kuna M., "Experimental and numerical investigation on the reliability of lead-free solders," Journal of Engineering Fracture Mechanics, Vol. 75, pp. 3534-3544, 2008.

[6]. Yang P. and Li W., "Numerical analysis on thermal characteristics for chip scale packaging by integrating 2D/3D models," International Journal of Numerical Modeling: Electronic Networks, Devices and Fields, Vol. 22, pp. 43-55, 2009.

[7]. Liu De S., Yeh S.S., Kao C.T., Huang P.Y., Tsai C.I., Liu A.H., and Ho S.C., " An experimental and numerical investigation into the effects of the chip-on-film (COF) processing parameters on the Au-Sn bonding temperatures," Soldering and Surface Mount Technology, Vol. 22, No. 4, pp. 31-41, 2010.

[8]. Ladani L., "Numerical analysis of thermo-mechanical reliability of through silicon vias (TSVa) and solder interconnects in 3-dimensional integrated circuits," Journal of Microelectronic Engineering, Vol. 87, pp. 208-215, 2010.

[9]. Jen Y.M., Chiou Y.C., and Yu C.L., "Fracture mechanics study on the intermetallic compound cracks for the solder joints of electronic packages," Journal of Engineering Failure Analysis, Vol. 18, pp. 797-810, 2011.

[10]. Tu K.N., "Reliability challenges in 3D IC packaging technology," Journal of Microelectronics Reliability, Vol. 51, pp. 517-523, 2011.

[11]. Zhang C. and Li L., " Characterization and design of through-silicon via arrays in three-dimensional ICs based on thermo-dynamical modeling," IEEE Transactions on Electron Devices, Vol. 58, No. 2, pp. 279-287, 2011.

[12]. Chawla N. Patel B.V., Koopman M., Chawla K.K., Saha R., Patterson B.R., Fuller E.R., and Langer S.A., "Microstructure-based simulation of thermomechanical behavior of composite materials by object-oriented finite element analysis," Materials Characterization, Vol. 49, No. 5, pp. 395-407, 2003.

[13]. Chawla N. and Sidha R.S., "Microstructure-based modeling of deformation in Sn-rich (Pb-free) solder alloys," Journal of Materials Science: Materials for Electronics, Vol. 18, No. 1-3, pp. 175-189, 2007.

[14]. Lewis A.C., Qidwai S.M., Jackson M., and Geltmacher A.B., "Strategies for integration of 3-D experimental data with modeling and simulation," Journal of the Minerals, Metals, and Materials Society, Vol. 63, No. 3, pp. 35-39, 2011.

[15]. Harvey E., Ladani L., and Weaver M., "Complete mechanical characterization of nanocrystalline Al-Mg alloy using Nanoindentation," Mechanics of Materials, pp. 1-11, 2012.

[16]. Oliver W.C., Pharr G.M., " An improved technique for determining hardness and elastic modulus using load and displacement sensing indentation experiments," Journal of Materials Research Society, Vol. 7, No. 6, pp. 1564-1583, 1992.

[17]. Bhushan B., "Handbook of nanotechnology," Springer Berlin Heidelberg, New York, Ch. 37, pp. 1137-1161, 2007.

[18]. Giannakopoulos A.E. and Suresh S., " Determination of elastoplastic properties by instrumented sharp indentation," Journal of Scripta Materialia, Vol. 40, No. 10, pp. 1191-1198, 1999.

[19]. Venkatech T.A., Vliet K.J.V., Giannakopoulos A.E., and Suresh S., "Determination of elasto-plastic properties by instrumented sharp indentation: Guidelines for property extraction," Journal of Scripta Materialia, Vol. 42, pp. 833-839, 2000.

[20]. Dao, M., Chollacoop N., Vliet K.J.V., Venkatesh T.A., and Suresh S., " Computational modeling of the forward and reverse problems in instrumented sharp indentation," Journal of Acta Materialia, Vol. 49, pp. 3899-3918, 2001.

[21]. Bucaille J L, Stauss S, Felder E, and Michler J, " Determination of plastic properties of metals by instrumented indentation using different sharp indenters," Journal of Acta Materialia, Vol. 51, pp. 1663-1678, 2003.

[22]. Deng X., Chawla N., Chawla K.K., and Koopman M., "Deformation behavior of (Cu, Ag)-Sn intermetallics by nanoindentation," Acta Materialia, Vol. 52, pp. 4219-4303, 2004.

[23]. Song J.M. and Su C.W., "Time-dependent deformation behavior of interfacial intermetallic compound layers in electronic solder joints," Journal of Materials Research, Vol. 25, No. 4, pp. 629-632, 2010.

[24]. Abdelhadi O.M. and Ladani L., "Effect of joint size on microstructure and growth kinetics of intermetallic compounds in solid-liquid interdiffusion Sn-3.5Ag/Cu-substrate solder joints," unpublished work.

[25]. Abdelhadi O.M. and Ladani L. "Optimization of preparation procedure for successful electronic backscatter diffraction (EBSD) of multi-layer specimen-application to lead-free solder joints," submitted to Microscopy and Microanalysis.

[26]. Sun Y., Liang J., Xu Z.H., Wang G., and Li X., "Nanoindentation for measuring individual phase mechanical properties of lead free solder alloy," Journal of Materials Science, Vol. 19, pp. 514-521, 2008.

[27]. Yang P.F., Lai Y.S., Jian S.R., Chen J., and Chen R.S., "Nanoindentation identifications of mechanical properties of Cu_6Sn_5, Cu_3Sn, and Ni_3Sn_4 intermetallic compounds derived by diffusion couples," Materials Science and Engineering A, Vol. 485, pp. 305-310, 2008.

[28]. Rosenthal Y., "Nanoindentation measurements and mechanical testing of as-soldered and aged Sn-0.7 Cu lead-free miniature joints," Material Science and Engineering A, Vol. 527, pp. 4014-4020, 2010.

[29]. Jang G.Y., Lce J.W., and Duh J.G., "The nanoindentation characteristics of Cu_6Sn_5, Cu_3Sn, and Ni3Sn4 intermetallic compounds in the solder bump," Journal of Electronic materials," Vol. 33, No. 10, pp. 1103-1110, 2004.

[30]. Yang P.F., Lai Y.S., Jian S.R., and Chen J., "Mechanical properties of Cu_6Sn_5, Cu_3Sn, and Ni3Sn4 intermetallic compounds measured by nanoindentation," In proceeding of 8th International Conference on: Electronic Packaging Technology, ICEPT 2007, 14-17 Aug. 2007, pp. 1-5.

[31]. Zhou W., Liu L., and Wu P., "Structural, electronic, and thermo-elastic properties of Cu_6Sn_5 and Cu_5Zn_8 intermetallic compounds: first-principles investigation," Intermetallics, Vol. 18, pp. 922-928, 2010.

Chapter 6 : Fracture Toughness of Bonds Using Interfacial Stresses in Four-Point Bending Tests

Abstract

Bond strength is an important factor in electronic and photonic packaging. Measuring bond characteristics, strength, and fracture toughness is particularly difficult in microelectronic devices where miniaturized bonds are used (e.g., wafer bonding and 3 dimensional integrated circuits). Since applying load directly to the bonds is proven difficult, four-point bending test with notched specimen has been typically used to facilitate fracture toughness measurements at small scale. This method is based on experiencing large peeling and shear stresses at the interface of two layers of different materials at the notch. However, there is a lack of analytical solution that can be used to determine the peeling and shear stresses at the interface of four-point bend specimen. This manuscript presents analytical modeling of peeling and shear stresses in tri-layer four-point bend specimens. Strength of materials approach with the assumption of small strains, within elastic region, is adopted in this study for evaluation of stresses and displacements. Furthermore, beam theory is utilized to develop equations that describe the moments and shear forces in the assembly due to the four-point bending loads. Second and fourth order differential equations are derived for shear and peeling stresses respectively at the interfaces of the assembly. Boundary conditions are determined based on load, supports and shear force and moment diagrams of the assembly. The problem solution is obtained by solving the governing differential equations instantaneously using standard methods. Finite-Element-based simulation is used to compare with and verify the analytical

solution. This work also presents an alternative approach where the stresses at the notch are used to determine the fracture toughness. An experiment is conducted on a specimen with intermetallic material as bond material. The analytical approach is then verified with the results of four-point bending experiment and is validated using the conventional technique (which is based on energy equilibrium and presented by equation 60).

Key words: Interfacial shear and peeling stresses; four-point bending; stress intensity factor; fracture toughness.

6.1 Introduction

Electronic devices are used in almost every daily activity as well as in applications such as health care, aerospace, military, and numerous others. Failure may have severe consequences and result in large economical loss or loss of human lives. Therefore, reliability is a critical parameter that electronic manufacturers need to investigate during the design phase. Electronic packages usually consist of multilayered structures connected together by different means. Different types of bonding may be used in miniaturized packages such as solid-liquid-inter-diffusion bonds, thermo-compression bonds, or adhesive bonds. The strength of the bond to sustain mechanical and thermo-mechanical stresses during the manufacturing and service life is a key consideration. The ability to predict and possibly minimize the causes of failure in microelectronic and photonic devices is of obvious practical importance. One of the major contributors to the failure in such assemblies is interfacial brittle fracture which is considered a critical problem in design and manufacture of electronic and composite packages [1-2]. Fracture and failure at the interface can happen due to stresses caused by mechanical or thermal mismatch, or a combination of both. The fracture in such assemblies could be

163

quantified by specifying the bond fracture toughness according to the type of loading condition. In most fabrication and operation conditions, the components are subjected to tension (mode I), shear (mode II), out-of-plane shear (mode III), or mixed-mode (modes I+II) loading [3]. Depending on the loading conditions, several experimental techniques are available to evaluate bond strength. For example, four-point bend test, double-cantilever beam and Chevron tests are commonly used to address and measure the strength and fracture toughness of interfacial bonds when mixed mode loading conditions exist [4-5]. Four-point bending test in particular is based on stresses developed at the interface of multilayer notched specimen and is used to determine the fracture toughness of interface or bond layer. Failure occurrence at interface of bi- or multi-layer assemblies is usually attributed to the stresses at that region. Conventional four-point bending techniques use the bending moment to determine the fracture toughness of the bond without attempting to determine the stresses at the tip of the crack or at the interface material. Although this technique has several advantages such as ease of use and applicability to cases that initial crack length is not known, understanding the stresses developed at the interface, and relating these stresses to fracture toughness is scientifically significant. Closed-form solutions of interfacial shear and peeling stresses under thermal loading have been obtained based on either strength of materials, theory of elasticity, or classical beam theory. One of the earlier solutions was developed by Timoshenko [6] who found the interfacial forces in bi-layer material due to thermal loading and based on theory of bending. He concluded that the interfacial forces are concentrated at the free edges and consisted of shear and peeling forces. His model leads to simple and sufficiently accurate solutions to evaluate deflection and forces at the interface of bi-material thermo-sets.

164

However, the solution does not provide formulas for the distribution of interfacial shear and peeling stresses at the interface.

Since the conception of Timoshenko's solution [6], considerable attention has been devoted to the analysis of the interfacial stresses under thermal loading [7-15]. Suhir [7] expanded upon Timoshenko's beam theory model and based his model on the assumption that the deviation of the longitudinal interfacial displacement at an interfacial point is proportional to the interfacial shear stress at that point. He obtained a remarkably simple solution and has extended the model to multilayered structures [8]. Suhir's hypothesis showed that the axial interfacial displacement is proportional to the shear stress at a particular point. Ru [9] introduced an amendment to Suhir's hypothesis in which the axial interfacial displacement is also proportional to the second derivative of shear stress at the same point. Several other studies have modified Suhir's and Timoshenko's studies on thermal loading [11-13].

Despite the need for a closed form analytical solution for quantitative calculation of stresses due to mechanical loading at the interface, very few studies have been conducted. Suhir [16] derived a solution based on his previous works [7-8, 14-15], considering a bi-material structure in which a tensile force or moment is applied to one layer. He obtained two separate equations to calculate interfacial shear and peeling stresses between the layers. Other studies [18-20], based on Taljstens approach [17], have been conducted to develop a closed-form solution of interfacial stresses in beams strengthened by adhesively bonded plates. The solution proposed by Taljsten related the interfacial displacements and structure deflection to the interfacial shear and peeling stresses respectively. However, the solution neglected the stiffness of the strengthening plate. Smith and Teng [18] developed an analytical model based on theory of elasticity to calculate the interfacial shear and normal stresses between a plate and retrofit

165

beam. Unlike Taljstens approach, Smith and Teng considered the stiffness of the strengthening plate in their solution.

Abdelouahed et al. [19-20] revised Smith and Teng's [18] method to incorporate the interfacial shear deformations using linear and parabolic formulas to express the interfacial shear deformation effect. Their methods are applied to large structures and components where the elastic and geometric features of the beam determine the order of magnitude of the stresses at the interface. Despite the extensive use of four-point bending test specimens for quantifying bond strength, no analytical solution is available to determine the interfacial stresses at the notch. This makes verifying the technique with a conventional fracture mechanics approach impossible.

We have developed a simple predictive analytical model that enables the assessment of the interfacial shearing and peeling stresses and strains in multilayered assemblies due to four-point loading in notched specimens. The model is validated using pre-existing formula for fracture toughness measurements in four-point bending tests.

6.2 Analysis

Let a bi-material assembly with a continuous bonding layer be manufactured with four-point bending geometry as shown in figure 6-1(a). The present model has been built on the following assumptions.

- All stresses and strains are low enough to allow a linear elastic approach to be applied.

- Stresses and strains are evaluated using strength of material equations.

- The interfacial layer is very thin compared to the thicknesses of the adherends resulting in the interfacial shear and normal stresses being unchanged through the thickness.

166

- The interface material is brittle that only experiences elastic deformation up to the point of fracture.

- The bonding layer does not carry bending moments.

- The interfacial shear stresses can be determined without considering the effect of peeling stresses.

- When interfacial shear stress is considered, the curvatures of layers are equal. This assumption is disregarded when normal stress is derived.

- The interfacial shear stresses are calculated based on the compatibility conditions of the displacements.

- When the interfacial peeling stress is calculated, the layers will deform differently which allow them to have different curvatures.

- The peeling stresses are proportional to the difference between the deflections of the layers.

6.2.1 Free-Body Diagram and Equilibrium Equations

Figure 6-1(b) shows the free-body diagram for a differential segment of the tri-layer assembly with a length dx. To simplify the derivation, it is assumed that the segment is loaded by a uniformly distributed load, q (N/m). The distance from the centerline of the assembly to the free edges is (L/2). The Poisson ratio, elastic modulus, width, and the thickness of each layer are, v_i, E_i, b_i and h_i respectively. $i = 1$ and 2 denotes top and bottom layers, and $i = a$ denotes the interfacial layer. The free-body diagram also shows the interfacial shear and peeling stresses, $\tau(x)$ and $\sigma_p(x)$ as well as the cross-sectional loads and moments, $N_i(x)$, $M_i(x)$, and $V_i(x)$. The forces and moments equilibrium at each cross section implies that:

From equilibrium of forces in x-direction, one gets

$$\frac{dN_1(x)}{dx} = -b_1 \tau(x) \tag{6-1}$$

$$\frac{dN_2(x)}{dx} = b_2 \tau(x) \tag{6-2}$$

From equilibrium of forces in y-direction, one gets

$$\frac{dV_1(x)}{dx} = -q - b_1 \sigma_p(x) \tag{6-3}$$

$$\frac{dV_2(x)}{dx} = b_2 \sigma_p(x) \tag{6-4}$$

From equilibrium of moments about z-axis, one gets

$$\frac{dM_1(x)}{dx} = V_1(x) - \frac{b_1 h_1 \tau(x)}{2} \tag{6-5}$$

$$\frac{dM_2(x)}{dx} = V_2(x) - \frac{b_2 h_2 \tau(x)}{2} \tag{6-6}$$

6.2.2 Derivation of Interfacial Shear Stresses

According to aforementioned assumptions, strains in the top and bottom adherends can be

expressed as:

$$\varepsilon_1(x) = \frac{du_1(x)}{dx} = \varepsilon_1^M(x) + \varepsilon_1^N(x) \tag{6-7}$$

$$\varepsilon_2(x) = \frac{du_2(x)}{dx} = \varepsilon_2^M(x) + \varepsilon_2^N(x) \tag{6-8}$$

$u_1(x)$ and $u_2(x)$ are the longitudinal interfacial displacement at the bottom of layer 1 and top

of layer 2 respectively. $\varepsilon_1^M(x)$ and $\varepsilon_2^M(x)$ are strains induced by the bending moment at layer 1

and 2 respectively and are as follows:
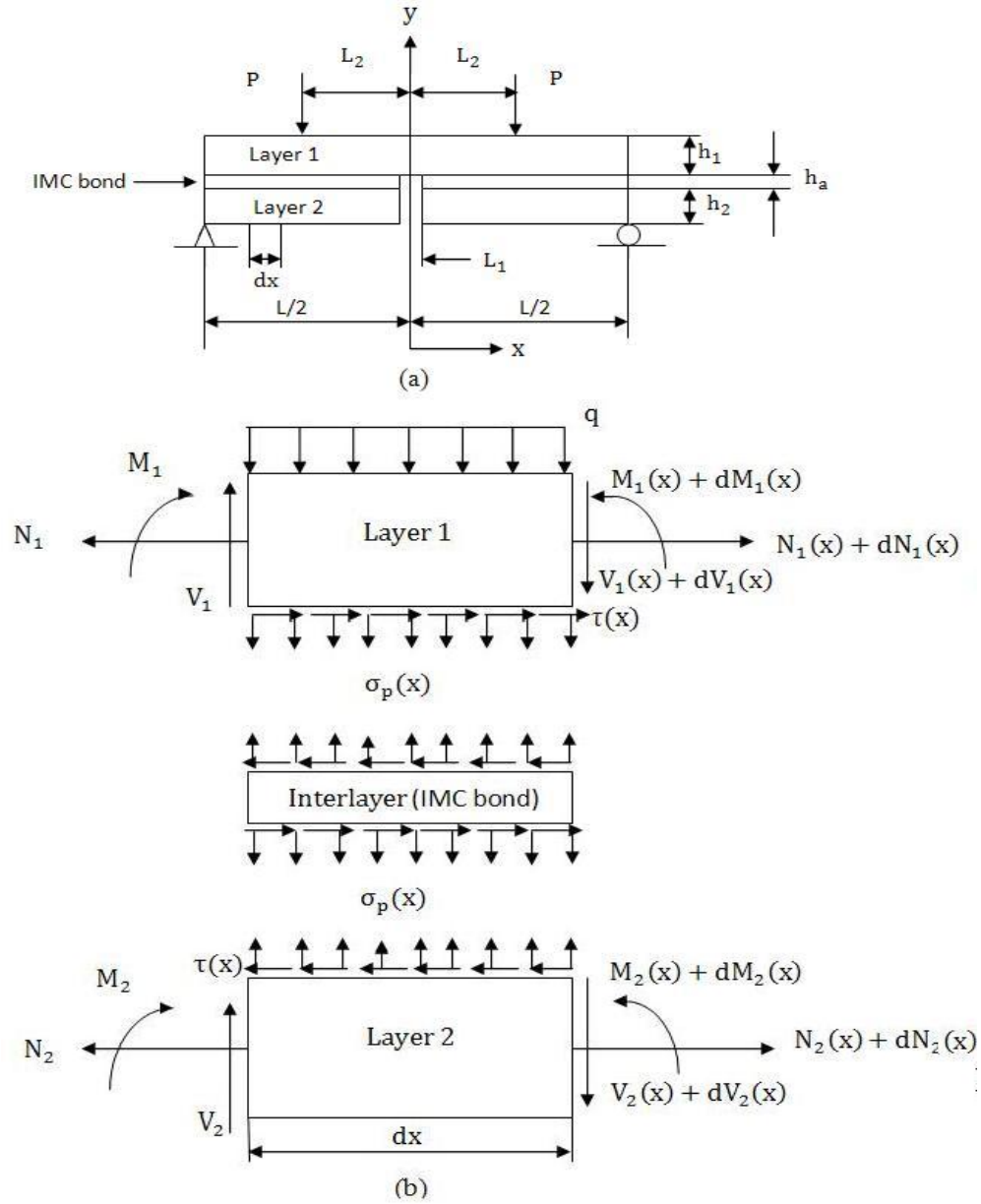
Figure 6-1: (a) General notched tri-layer four-point bend assembly. (b) Free body diagram of segment (dx).

$$\varepsilon_1^M(x) = \frac{h_1}{2E_1 I_1} M_1(x), \text{ and} \tag{6-9a}$$

$$\varepsilon_2^M(x) = -\frac{h_2}{2E_2 I_2} M_2(x) \tag{6-9b}$$

$$I_1 = \frac{b_1 h_1^3}{12} \tag{6-9c}$$

$$I_2=\frac{b_2 h_2^3}{12} \tag{6-9d}$$

I_1 and I_2 are the moment of inertia for layer 1 and 2 respectively. $\varepsilon_1^N(x)$ and $\varepsilon_2^N(x)$ are the

longitudinal strains due to the longitudinal forces and given as:

$$\varepsilon_1^N(x)=\frac{N_1(x)}{E_1 A_1}, \text{ and} \tag{6-10a}$$

$$\varepsilon_2^N(x)=\frac{N_2(x)}{E_2 A_2} \tag{6-10b}$$

N_i and A_i are the axial forces and cross sectional areas, respectively. Assuming equal

curvature in the top and bottom adherends, the relationship between the flexural rigidities and

the moments in the two adherends can be expressed as:

$$R=\frac{E_1 I_1}{E_2 I_2} \tag{6-11}$$

$$M_1(x)=RM_2(x) \tag{6-12}$$

Considering the horizontal and moment equilibria, the total bending moment and the bending

moment in each layer are obtained in the following forms:

$$M_T(x)=M_1(x)+M_2(x)+N_1(x)(y_1+h_a)+N_2(x)(y_2+h_a) \tag{6-13}$$

$$M_1(x)=\frac{R}{R+1}\left[M_T(x)-b_2\int_0^x \tau(\xi)(y_1+y_2+h_a)d\xi\right] \tag{6-14}$$

$$\frac{dM_1(x)}{dx}=\frac{R}{R+1}\left[V_T(x)-b_2\tau(x)(y_1+y_2+h_a)\right] \tag{6-15}$$

$$M_2(x)=\frac{1}{R+1}\left[M_T(x)-b_2\int_0^x \tau(\xi)(y_1+y_2+h_a)d\xi\right] \tag{6-16}$$

$$\frac{dM_2(x)}{dx}=\frac{1}{R+1}\left[V_T(x)-b_2\tau(x)(y_1+y_2+h_a)\right] \tag{6-17}$$

where y_1 and y_2 are distances from the bottom of layer 1 and the top of layer 2 to their

respective neutral axis. The interfacial shear stress can be related to displacements at the

interface using Hook's law which allows for the compatibility condition of displacements at

the interface to be expressed in the following form

$$\tau(x) = K_s \left[u_2(x) - u_1(x) \right] \tag{6-18}$$

where K_s is shear stiffness and is approximated as follows [17-20]

$$K_s = \frac{G_a}{h_a} \tag{6-19}$$

G_a and h_a are the shear modulus and the thickness of the interlayer (bond) respectively.

Differentiating the above expression results in:

$$\frac{d\tau(x)}{dx} = K_s \left[\frac{du_2(x)}{dx} - \frac{du_1(x)}{dx} \right] \tag{6-20}$$

Substituting Eqs.(6-9) and (6-10) into Eqs.(6-7) and (6-8) and the resulting expression into Eq.(6-22), the following equation is obtained:

$$\frac{d\tau(x)}{dx} = K_s \left[\left(-\frac{h_2}{2E_2 I_2} M_2(x) + \frac{N_2(x)}{E_2 A_2} \right) - \left(\frac{h_1}{2E_1 I_1} M_1(x) + \frac{N_1(x)}{E_1 A_1} \right) \right] \tag{6-21}$$

Differentiating Eq.(6-21) and substituting shear (Eqs.(6-15) and (6-17)) and axial (Eqs.(6-1) and (6-2)) forces into Eq.(6-21) provide the following governing second-order differential equation:

$$\frac{d^2\tau(x)}{dx^2} - K_s b_2 \left[\frac{1}{E_1 A_1} + \frac{1}{E_2 A_2} + \frac{(y_1+y_2)(y_1+y_2+h_a)}{E_1 I_1 + E_2 I_2} \right] \tau(x) + K_s \left[\frac{(y_1+y_2)}{E_1 I_1 + E_2 I_2} \right] V_T(x) = 0 \tag{6-22}$$

The general solution presented below is limited to either concentrated or uniformly distributed loading over a finite section or the entire length of the assembly. For such loading $\frac{d^2 V(x)}{dx^2} = 0$, and the general solution is given by:

$$\tau(x) = B_1 \exp(-\lambda x) + B_2 \exp(\lambda x) + m_1 V_T(x) \tag{6-23}$$

where:

$$m_1 = \frac{K_s}{\lambda^2} \left[\frac{(y_1+y_2)}{E_1 I_1 + E_2 I_2} \right] \tag{6-24}$$

$$\lambda^2 = K_s b_2 \left[\frac{1}{E_1 A_1} + \frac{1}{E_2 A_2} + \frac{(y_1+y_2)(y_1+y_2+h_a)}{E_1 I_1 + E_2 I_2} \right] \tag{6-25}$$

6.2.3 Derivation of Interfacial Peeling Stresses

The interfacial peeling stress is proportional to the difference of the deflections expressed as follows:

$$\sigma_p(x) = \delta_{12}\left[w_2(x) - w_1(x)\right] \tag{6-26}$$

$$\delta_{12} = \frac{E_a}{h_a} \tag{6-27}$$

δ_{12} is the normal stiffness of the interface layer and $w_1(x)$ and $w_2(x)$ are the vertical deflections of layer1 and 2 respectively.

Beam theory gives the relation between the moments and curvatures as follows:

$$\frac{d^2 w_2(x)}{dx^2} = -\frac{M_2(x)}{E_2 I_2}, \text{ and} \tag{6-28a}$$

$$\frac{d^2 w_1(x)}{dx^2} = -\frac{M_1(x)}{E_1 I_1} \tag{6-28b}$$

Differentiating Eqs.(6-28a) and (6-28b) twice, substituting Eqs.(6-3) to (6-6) into the resulting expression, and plugging the final results into Eq.(6-26) after it is differentiated four times, the governing differential equation for interfacial peeling stress is given as follows.

$$\frac{d^4 \sigma_p(x)}{dx^2} + \delta_{12}\left(\frac{b_1}{E_1 I_1} + \frac{b_2}{E_2 I_2}\right)\sigma_p(x) + \delta_{12}\left(\frac{b_1 h_1}{2 E_1 I_1} - \frac{b_2 h_2}{2 E_2 I_2}\right)\frac{d\tau(x)}{dx} + \delta_{12}\frac{q}{E_1 I_1} = 0 \tag{6-29}$$

The general solution to this fourth-order differential equation is:

$$\sigma_p(x) = e^{-\beta x}\left[D_1 \cos(\beta x) + D_2 \sin(\beta x)\right] + e^{\beta x}\left[D_3 \cos(\beta x) + D_4 \sin(\beta x)\right] - n_1 \frac{d\tau(x)}{dx} - n_2 q \tag{6-30}$$

$$\beta^4 = \frac{E_a b_2}{4 h_a}\left(\frac{1}{E_1 I_1} + \frac{1}{E_2 I_2}\right), \tag{6-31a}$$

$$n_1 = \left(\frac{y_1 E_2 I_2 - y_2 E_1 I_1}{E_1 I_1 + E_2 I_2}\right), \text{ and} \tag{6-31b}$$

$$n_2 = \frac{E_2 I_2}{b_2(E_1 I_1 + E_2 I_2)} \tag{6-31c}$$

Since the assembly is subjected to point loads applied in a symmetrical manner, the interfacial peeling stress is symmetric with respect to the mid-cross section. This enables the elimination of the asymmetric terms as well as the last term from the solution as follows:

$$D_2=D_4=0, \text{ and } q=0 \tag{6-32}$$

$$\sigma_p(x)=e^{-\beta x}[D_1 \cos(\beta x)]+e^{\beta x}[D_3 \cos(\beta x)]-n_1 \frac{d\tau(x)}{dx} \tag{6-33}$$

6.2.4 Application of Boundary Conditions

In order to use the expressions of interfacial peeling and shearing stresses, appropriate boundary conditions must be used to solve for the coefficients. A simply supported composite beam as shown in Figure 6-1(a) is investigated which is subjected to an arbitrary four-point bending load. The specimen has a notch which is located at specimen's mid-span and it deepens into the bottom and intermediate layers.

6.2.4.1 Interfacial Shear Stress

The geometry is symmetric with respect to mid span notch as it is shown in figure 6-1(a). In the following analysis, the right portion of the specimen is considered. Since the last term in Eq.(6-23) represents the contribution of the shear force in the interfacial shear stress, the general solution must be written according to the shear force value as it varies with distance from mid-cross section towards the right edge. Substituting the appropriate expression for the shear force results in the general solution for the interfacial shear stress as follows:

$$\tau_1(x)=B_1\exp(-\lambda x)+B_2\exp(\lambda x), \qquad 0\leq x\leq L_2 \tag{6-34}$$

$$\tau_2(x)=B_3\exp(-\lambda x)+B_4\exp(\lambda x)-m_1 P, \qquad L_2\leq x\leq \frac{L}{2} \tag{6-35}$$

Applying the following boundary conditions makes it possible to solve for the unknown constants in Eqs.(6-34) and (6-35).

1-   At the notch, the total moment and the sheer force are carried by the top layer.

$$M_2(L_1)=0,$$ (6-36a)

$$N_1(L_1)=N_2(L_1)=0, \text{ and}$$ (6-36b)

$$M_1(L_1)=M_T(L_1)=\frac{PL}{4}$$ (6-36c)

Substituting Eqs.(6-9) and (6-10) into Eq.(6-20) and simplifying the resulting expression using the above boundary conditions gives;

$$\frac{d\tau_1(L_1)}{dx}=-m_2 M_T(L_1)$$ (6-37a)

Where $m_2=\frac{y_1 G_a}{E_1 I_1 t_a}$ (6-37b)

2-   The interfacial shear stress is continuous under the point load [18-20].

$$\tau_1(L_2)=\tau_2(L_2)$$ 6-38

3-   The first derivative of interfacial shear stress is continuous under the point load [18-20].

$$\frac{d\tau_1(L_2)}{dx}=\frac{d\tau_2(L_2)}{dx}$$ (6-39)

4-   It is assumed that a local maximum value of interfacial shear stress occurs at the ends resulting in the first derivative of the interfacial shear stress dropping out of the equation. This assumption is based on the fact that the interfacial displacement increases as we approach further from the mid-point and it reaches maximum values at the free edges [16].

$$\frac{d\tau_2\left(\frac{L}{2}\right)}{dx}=0$$ (6-40)

Substituting Eqs.(6-34) and (6-35) into Eqs.(6-37) to (6-40), the coefficients of the interfacial shear stresses are found as:

$$B_1=-\frac{1}{2}\frac{\left[m_1\lambda P\left(e^{\lambda L_2}e^{\frac{-\lambda L}{2}}-e^{-\lambda L_2}e^{\frac{\lambda L}{2}}\right)+2m_2 M_T(L_1)e^{\frac{\lambda L}{2}}\right]}{\lambda\left(e^{\frac{-\lambda L}{2}}-e^{\frac{\lambda L}{2}}\right)}$$ (6-41)

$$B_2 = -\frac{1}{2} \frac{\left[m_1 \lambda P \left(e^{\lambda L_2} e^{\frac{-\lambda L}{2}} - e^{-\lambda L_2} e^{\frac{\lambda L}{2}} \right) + 2m_2 M_T(L_1) e^{\frac{-\lambda L}{2}} \right]}{\lambda \left(e^{\frac{-\lambda L}{2}} - e^{\frac{\lambda L}{2}} \right)} \tag{6-42}$$

$$B_3 = -\frac{1}{2} e^{\frac{\lambda L}{2}} \frac{\left[(m_1 \lambda P \left(e^{\lambda L_2} - e^{-\lambda L_2} \right) + 2m_2 M_T(L_1) \right]}{\lambda \left(e^{\frac{-\lambda L}{2}} - e^{\frac{\lambda L}{2}} \right)} \tag{6-43}$$

$$B_3 = -\frac{1}{2} e^{\frac{-\lambda L}{2}} \frac{\left[(m_1 \lambda P \left(e^{\lambda L_2} - e^{-\lambda L_2} \right) + 2m_2 M_T(L_1) \right]}{\lambda \left(e^{\frac{-\lambda L}{2}} - e^{\frac{\lambda L}{2}} \right)} \tag{6-44}$$

6.2.4.2 Interfacial Peeling Stress

Since the interfacial shear stress is expressed in two regions by Eqs.6-34 and 6-35, and the last term in Eq.6-33 shows the contribution of interfacial shear stress in the normal stress, the normal stress must be expressed in these corresponding regions by the two expressions that follow:

$$\sigma_p(x) = R_1 e^{-\beta x} \cos(\beta x) + R_2 e^{\beta x} \cos(\beta x) - n_1 \frac{d\tau_1(x)}{dx}, \quad 0 \leq x \leq L_2 \tag{6-45}$$

$$\sigma_p(x) = R_3 e^{-\beta x} \cos(\beta x) + R_4 e^{\beta x} \cos(\beta x) - n_1 \frac{d\tau_2(x)}{dx}, \quad L_2 \leq x \leq \frac{L}{2} \tag{6-46}$$

Appropriate boundary conditions are developed below.

1- The total moment and total shear force are carried by the top layer at the notch.

$$M_1(L_1) = M_T(L_1) = \frac{PL}{4} \text{ and } V_1(L_1) = V_T(L_1) = 0 \tag{6-47}$$

Differentiating Eq.(6-27) two times and substituting Eqs.(6-5) and (6-6) into the resulting expression lead to the following relationship at the notch:

$$\frac{d^2 \sigma_p(x)}{dx^2} = \frac{E_a M_T(L_1)}{E_1 I_1 h_a} \tag{6-48}$$

2- The peeling stress is continuous at the point load which is expressed in the following equality [18]:

$$\sigma_{p_1}(L_2)=\sigma_{p_2}(L_2) \tag{6-49}$$

3-   The first derivative of the interfacial peeling stress is a continuous function written as follows [18]:

$$\frac{d\sigma_{p_1}(L_2)}{dx}=\frac{d\sigma_{p_2}(L_2)}{dx} \tag{6-50}$$

4-   It is assumed that a local maximum value of interfacial peeling stress occurs at the free edge. So the first derivative of interfacial peeling stress vanishes at that end [16]:

$$\frac{d\sigma_{p_2}\left(\frac{L}{2}\right)}{dx}=0 \tag{6-51}$$

Application of the above boundary conditions to Eqs.(6-45), and (6-46), defines the coefficients of the solution thus giving an expression to the interfacial peeling at any point along the structure interface. For complete version of the solution, expressions for coefficients $R_1, R_2, R_3,$ and R_4 are listed in the appendix A.

6.2.4.3 Numerical Example and Discussion

The formulation developed in the previous sections will be used to determine the shear and peeling stresses at the interface for a typical example used in electronic materials testing. In the electronic industry, inter-diffusion bonding is a popular method used to fabricate integrated circuit components. Table 6-1 summarizes the geometry and material properties of an arbitrary example of a three-layered specimen in which the layers are bonded to each other by creating an Intermetallic Compound (IMC).

Table 6-1: Dimension and material properties used in the current example.

Component	Material	Young's Modulus (Gpa)	Poisson ratio	Width (mm)	Thickness (mm)
Top and bottom adherent layers	Cu	117.215	0.34	5	1
Bonding layer	IMC	85	0.309	5	0.35

Specimen's length is 26 mm and the spans of the supports and the inner loading points are 16 and 26 mm, respectively. A critical load of 42.5N four-point load is symmetrically applied at a distance of 8mm from the center of the notch. Figures 6-2 and 6-3 show the interfacial shear and peeling stresses as a function of the distance from the mid-span.
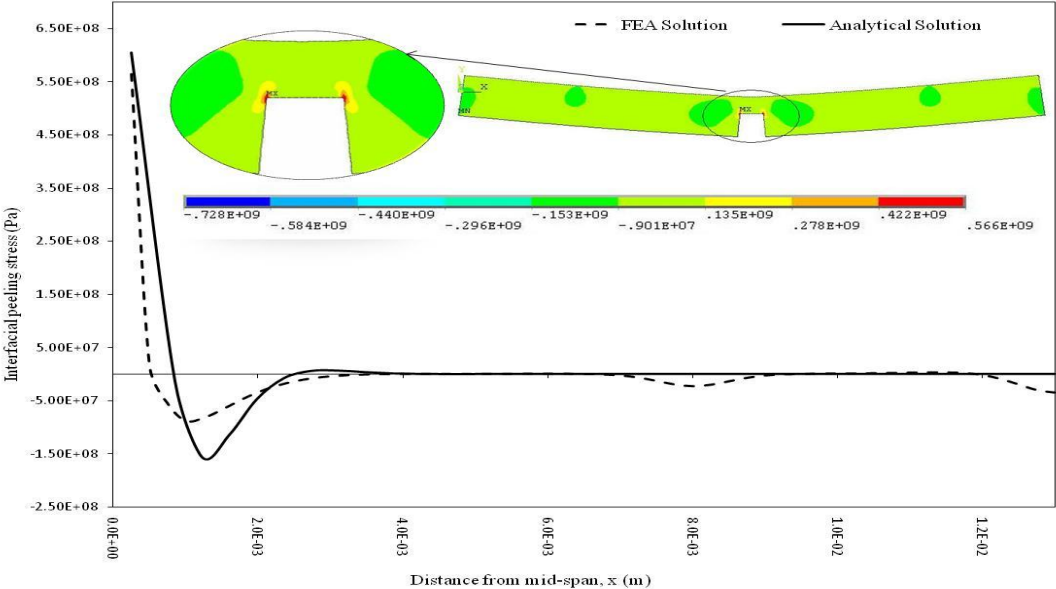
Figure 6-2: Comparison of theoretical interfacial peeling stress versus FEA results
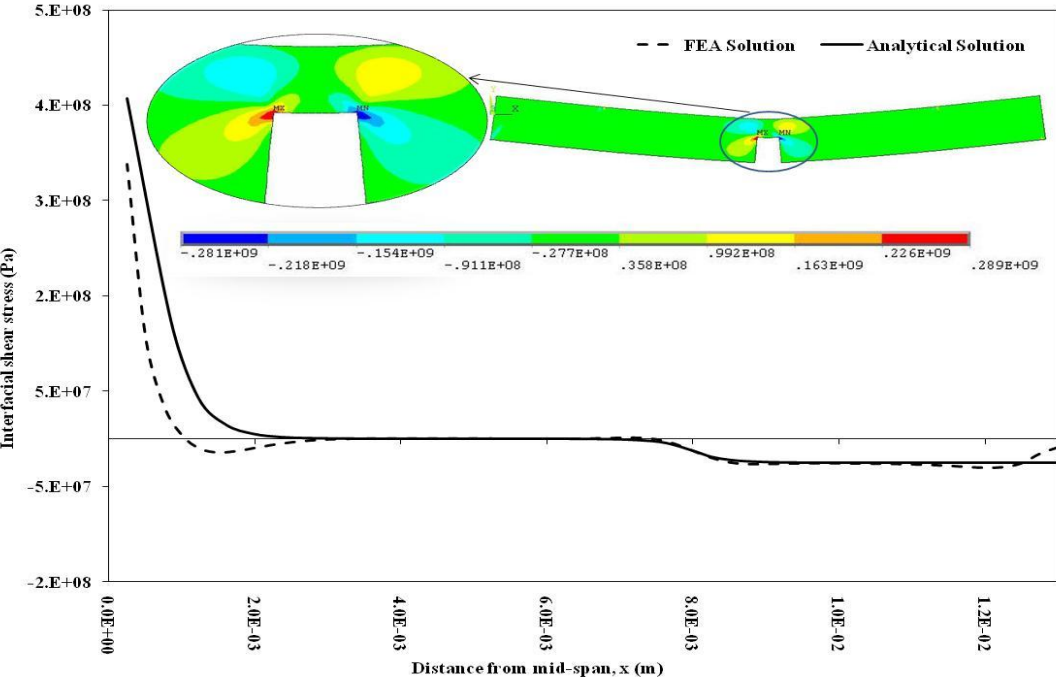
Figure 6-3: Comparison of theoretical interfacial shear stress with FEA results.

In order to verify the predictions of the present model, they were compared to those obtained from finite element models. For the given example, 2D FEA model has been generated using commercial finite-element software. The assembly was meshed using the PLANE42 element having 4 nodes and 2 degrees of freedom at each node. Progressive refinements in mesh density were examined under plane stress conditions. It was found that a minimum mesh density of 1239 nodes and 1116 elements produce results that are mesh-insensitive. The results of interfacial shear and peeling stresses calculated in Eqs.6-34 to 6-35 and Eqs. 6-45 to 6-46 are plotted in Figures 6-2 and 6-3 along with the ones obtained from FEA model. It is clear from these figures that the derived expressions for the interfacial shear and peeling stresses give values that agree well with the ones obtained using the FEA program as the two values are hardly indistinguishable in most regions. From these comparisons, it is evident that Eqs.34-35 and 45-46 provide reasonably accurate maximum interfacial shear and peeling stresses at the notch.

The interfacial stresses are very critical in design, fabrication, and service of electronic packages due to the functional failures they could cause. Notched specimens can help in understanding the state of stresses in real applications. A parametric study has been conducted to gain additional understanding of how the stresses at the notch can be maximized. This knowledge helps in optimizing four-point bend test specimens and processes. In Figure 6-4, the interfacial stresses at the notch linearly increase as the load increases while all other parameters are fixed. One cause of the interfacial shear stress increase is the direct relationship between the moment and the applied load. The interfacial strains induced by the bending moments increase due to the increase in moment according to Eq.6-9. Their net increase adds up when Eqs.6-7 and 6-8 are substituted into Eq.6-18 which results in the

interfacial shear stress increase. The increase of the bending moment due to the increase in the applied load is also shown to have the same influence on the interfacial peeling stresses. Beam theory, Eq.6-29, shows the relationships between the moments and the curvatures in each layer of the beam. When Eq.6-29 is substituted into the compatibility equation (Eq.6-27), it causes the peeling stress to increase. The effect of beam length is also addressed. Figure 6-5 shows the change of interfacial stresses versus the change in specimen length while the inner loading points were kept half way between the mid-span and the free edges.
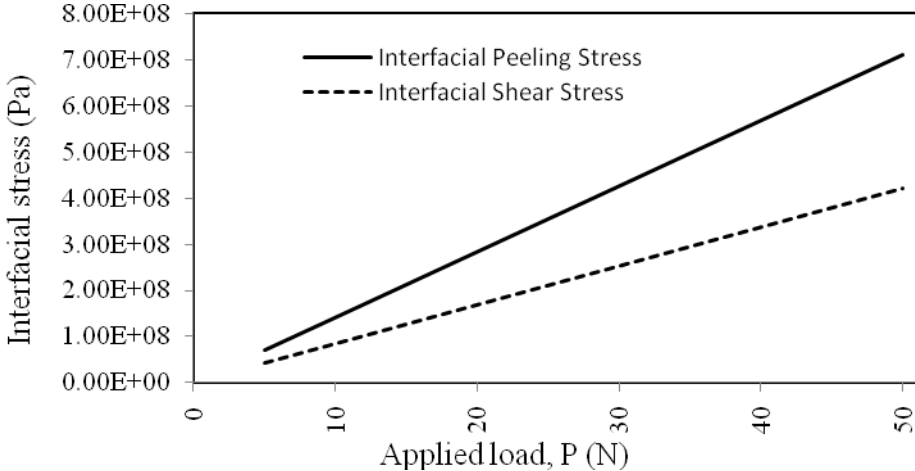
Figure 6-4: Applied load versus maximum interfacial stresses.
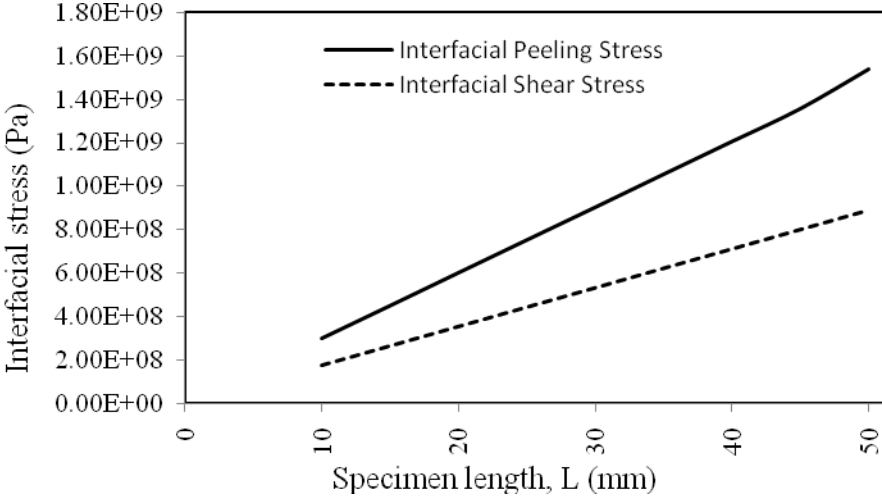
Figure 6-5: Specimen length versus maximum interfacial stresses.

Both stresses increase linearly due to increase in total moment which is proportional to the

specimen length as stated in Eq.6-36. The plot of interface modulus versus the interfacial

stresses (Figure 6-6), shows that the interfacial shear stresses increase when the modulus of

the interface layer increases. Eqs.6-19 and 6-27 show linear proportionality of the interfacial

stresses to the interface modulus. Figure 6-6 also shows that the peeling stresses are less

affected by the net increase of interfacial young's modulus comparing to the obvious

influence of the same factor on the interfacial shear stresses. Figure 6-7 shows inverse

proportionality between the interfacial stresses and the thickness of the interface layer. The

interaction between the interfacial stresses and the thickness of interface layer is shown

symbolically in Eqs.6-18 and 6-27.
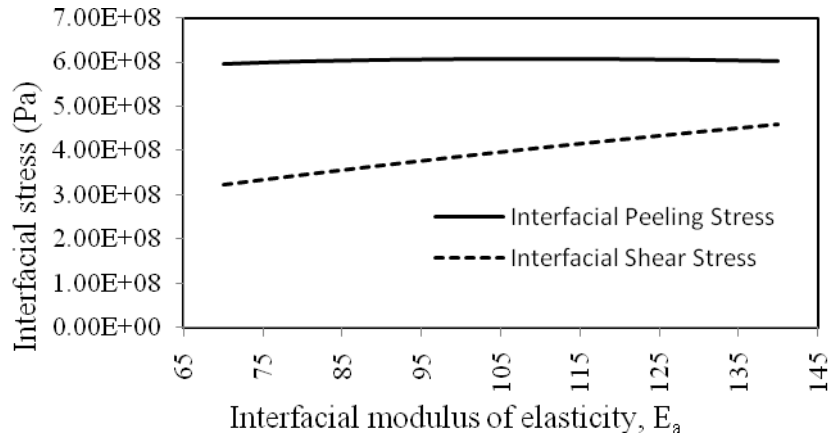
Figure 6-6: The Change in maximum interfacial stresses when elastic modulus of the interface
material is varied
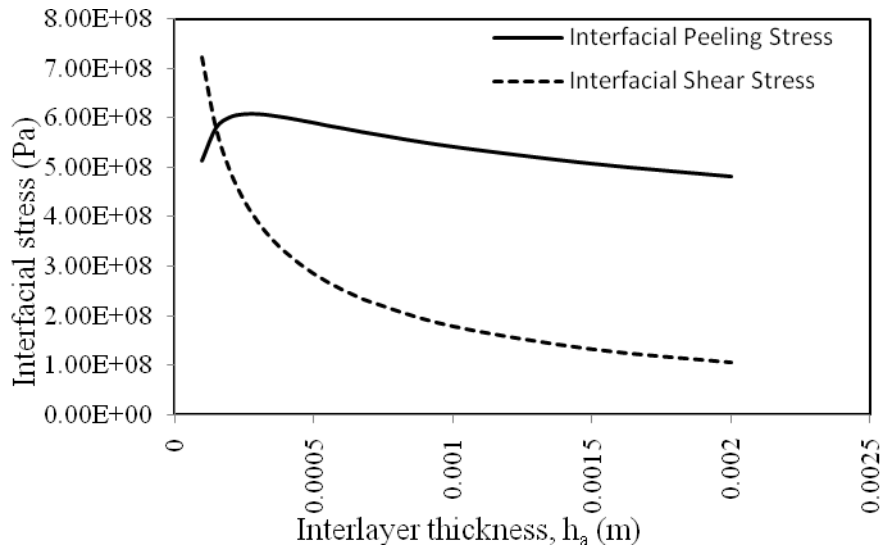
Figure 6-7: The Change in interfacial thickness vs. maximum interfacial stresses.

6.2.5 Calculation of Interfacial Stress Intensity Factor

Fracture of the interface bond is one important aspect which needs to be taken into account because of its ability to affect the overall reliability of the package. Fracture mechanics has introduced two approaches for evaluating behavior of cracked structures under different remote loading conditions. The first approach, based on the first law of thermodynamics, is called the Energy Release Rate (ERR). It is the energy dissipated during fracture per unit of newly created fracture surface area. ERR states that crack extension occurs when the energy available for crack growth is sufficient to overcome the resistance of the material that prevents the crack to propagate through the material's crystal structure. The second approach is called the Stress Intensity Factor (SIF) approach. It is a measure of the stress-field intensity near the tip of the crack caused by remote loading, and plays a major role in Linear Elastic Fracture Mechanics (LEFM) analysis.

Loading mode, crack length, and specimen geometries are the major parameters that affect the chosen technique of evaluating SIFs. One technique to evaluate the SIFs consists of

181

calculating the ERR and then using that value to calculate the SIFs based on the relationship between these two parameters. It is a straightforward technique commonly applied to problems involving pure loading modes in isotropic materials [21]. Complications arise in mixed-mode problems involving anisotropic materials, which make the above mentioned technique virtually unusable. The first issue in mixed-mode problems is mode partitioning in which the ERR must be separated into two or three components according to the number of modes that exist [22-23]. The second issue is the discontinuity of material properties through the specimen's thickness [24-26] in multilayered or composite materials. Discontinuity of the stress field around the crack can occur resulting in the SIF no longer relating directly to the remote stress fields applied to the specimen.

Morias [21] overcame some of these issues using a technique which applies the force method in calculating the SIF from finite element (FE) models. Basically, SIFs are estimated from forces acting on nodes along a certain ligament at a specified distance from the crack tip. Linear regression analysis is performed on the obtained data and extrapolated to zero (crack tip) to give the SIF values [27]. The technique does not require paying close attention to the stress field around the crack. Isotropic and orthotropic specimens under mode-I, mode-II, and mixed-mode I+II loading can be handled under this approach. Layered structures have been shown to suffer from both mode mixity and material discontinuity issues [28]. Previous works have introduced the complex stress intensity factor concept [28-31]. The interfacial SIFs are calculated at the interface of a multilayered specimen taking into account the discontinuity of material properties, loading, and mode mixity.

In this section, an analytical equation to determine the stress intensity factor is developed making it possible to find the fracture toughness of interfacial bonds by evaluating the stresses

at the interface. A symmetric four-point bend test is commonly used to study the fracture

behavior of multi-layered structures because of its capability of developing mixed-mode

loading conditions [32-34]. Furthermore, for a crack located between the inner loading lines,

the cracked ligament is under a constant moment condition [34-35]. This constant-moment

region exhibits steady-state behavior of the ERR and allows for the calculation of the critical

ERR based on the energy difference between cracked and un-cracked beams.

In obtaining interfacial measurements of layered specimens, the materials are assumed to act

elastically and the effect of the residual stresses is ignored. The interface can be modeled as a

semi-infinite layer which includes a crack. Crack length and thickness are assumed to be very

small compared to the interface layer dimensions (Figure 6-8(a)). The interfacial stresses can

then be treated as far-field tensile and shear stresses, Figure 6-8(b).
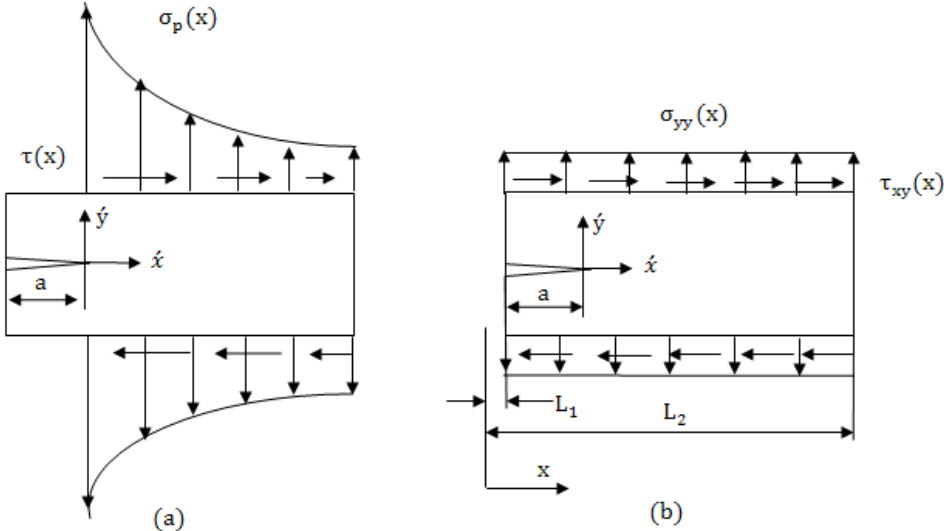
Figure 6-8: (a) Interfacial stresses and crack geometry. (b) Averaged interfacial stresses.

From previous calculations of section 2.5, the normal and shear stresses acting on the

boundaries of the interface layer were obtained and found to be functions of material, loading,

and geometric characteristics of the composite beam. Figure 6-8(a) shows a schematic view of

such stresses. These stresses are maximum at the crack tip notch and decrease when moving

farther from it. The region in the left side of the crack tip will not carry stresses. The stresses

carried by the interface layer are averaged over the constant moment region to obtain good

approximation of the far field stresses as shown in Figure 6-8(b). Now consider an edge-crack

embedded inside the interface layer as shown in previous figure. The structure is subjected to

mixed-mode loading under plane stress or plane strain conditions. The crack is assumed to be

oriented along the x-axis of a local coordinate system which is originated at the tip of the

crack. When equations that calculate stress intensity factor are developed, a local coordinate

system ($\acute{x} - \acute{y}$) associated with crack geometry is used. The SIFs for the corresponding modes

are expressed as follows.

$$K_I = \sigma_{yy} F_I\left(\frac{a}{L_3}\right) \sqrt{2\pi a}$$
(6-52)

$$K_{II} = \tau_{xy} F_{II}\left(\left(\frac{a}{L_3}\right)\right) \sqrt{2\pi a}$$
(6-53)

σ_{yy} and τ_{xy} are the averaged normal and shear stresses on the interface layer respectively.

They are calculated based on the following equations:

$$\sigma_{yy}(x) = \frac{1}{L_3} \int_{L_1+a}^{L_2} \sigma_p(x)\, dx$$

$$= \frac{1}{L_3} \int_{L_1+a}^{L_2} [R_1 e^{-\beta x} \cos(\beta x) + R_3 e^{\beta x} \cos(\beta x) - n_1 \frac{d\tau_1(x)}{dx}]\, dx$$
(6-54)

$$\tau_{xy}(x) = \frac{1}{L_3} \int_{L_1+a}^{L_2} \tau_1(x)\, dx$$

$$= \frac{1}{L_3} \int_{L_1+a}^{L_2} [B_1 \exp(-\lambda x) + B_2 \exp(\lambda x)]\, dx$$
(6-55)

The complete expansions of Eqs.(6-54) and (6-55) are listed in appendix B. $F_I(\frac{a}{L_3}), F_{II}(\frac{a}{L_3})$ are

the geometric factors for mode 1 and 2 respectively. They are defined into polynomial

expressions [31, 36-37] as follows.

$$F_I\left(\frac{a}{L_3}\right)=1.121\left(\frac{a}{L_3}\right)+3.740\left(\frac{a}{L_3}\right)^2+3.873\left(\frac{a}{L_3}\right)^3-19.05\left(\frac{a}{L_3}\right)^4+22.55\left(\frac{a}{L_3}\right)^5 \quad 0\leq\frac{a}{L_3}\leq0.7 \tag{6-56}$$

$$F_{II}\left(\frac{a}{L_3}\right)=7.264-9.37\left(\frac{a}{L_3}\right)+2.74\left(\frac{a}{L_3}\right)^2+1.87\left(\frac{a}{L_3}\right)^3-1.04\left(\frac{a}{L_3}\right)^4 ;0\leq\frac{a}{L_3}\leq1 \tag{6-57}$$

where

$$L_3=L_2-L_1 \tag{6-58}$$

a and L_2 are the crack length and the half distance between the inner loading points,

respectively. The total ERR in combined mode cracking can be obtained by summing up the

energies for different modes based on the relationship between the ERR and SIFs as follows

[3]:

$$G=G_1+G_2=\frac{1}{\bar{E}}\left[K_I^2+K_{II}^2\right] \tag{6-59}$$

$\bar{E}$ is the elastic modulus of the IMC layer and is equal to:

$\bar{E} = E_a$ for plane stress, and $\bar{E} = {E_a}/{(1-v^2)}$ for plane-strain problems.

The critical ERR can be obtained based on the critical SIF for mode I and mode II which are

determined at the critical load where a crack of specific length starts to grow. This critical

ERR also can be calculated based on energy equilibrium which was used by previous works

[34-35]. For a crack located between the inner loading points, the moment is constant, causing

the strain energy release rate to exhibit steady-state characteristics. Considering the Euler-

Bernoulli beam theory, the steady-state energy release rate is basically the difference in the

strain energy in the un-cracked and cracked beams which can be expressed based on the Euler-Bernoulli beam theory as follows [34-35]:

$$G_c = \frac{M^2(1-v^2)}{4E_2}\left(\frac{1}{I_{uc}} - \frac{1}{I_c}\right)$$

(6-60)

where M is the constant applied moment and is equal to $M = Pl$, P, and l are the applied force and the spacing between inner and outer load points. I_{uc} and I_c are the second moments of inertia for cracked and un-cracked beams, respectively.

$$I_{uc} = \frac{h_1^3}{12}$$

(6-61)

$$I_c = \frac{h_1^3}{3} + \kappa\frac{h_a^3}{3} + \mu\left(\frac{h_2^3}{3} + h_2^2 h_a + h_a^2 h_2\right) - \frac{\left[h_1^2 - \kappa h_a^2 - \mu\left(h_2^2 + 2h_a h_2\right)\right]^2}{4(h_1 + \kappa h_a + \mu h_2)}$$

(6-62)

$$\mu = \frac{E_a(1-v_1^2)}{E_1(1-v_a^2)}, \quad \kappa = \frac{E_2(1-v_1^2)}{E_1(1-v_2^2)}$$

(6-63)

Knowing the stresses at the interface at the time crack starts to grow, the critical stress intensity factors can be determined from Eq.(6-53) and (6-53) and the critical energy release rate, then, can be calculated from Eq.(6-59). This procedure has been validated through an experiment and using the alternative available model, Eq.(6-60).

6.2.5.1 Numerical Example and Discussion

The applicability of the proposed approach of evaluating stress intensity factor of mixed-mode problem based on the far-field interfacial stresses is used to determine the critical SIFs and critical ERR. Based on the example of Section 6.2.4.3, an experimental work is conducted in this study using a four-point bend specimen. The specimen is fabricated according to materials and geometries data implemented in the numerical example of Section 6.2.4.3. The specimen was tested under load control in four-point bend test configuration and subjected to loading increments using high-precision Instron Micro-tester. The load versus displacement

was monitored and recorded. Figure 6-9 shows the typical load versus displacement curve

obtained during testing. It can be seen that the critical load value, which indicates the

occurrence of crack growth, is specified based on the sudden drop in the load value. The

sudden drop is *an indicator* of the energy dissipation upon crack propagation of initially

cracked structure. In this test, the critical interfacial fracture energy of bonding layer is

determined based on calculation of critical stress intensity factors of existing modes. The

results are compared with the values obtained from Eq.(6-60). It was found that a critical

four-point load of 42.5N (4.33 kgf) causes further propagation of an initial crack of length

0.50 mm at the interface layer of the specimen. This critical load value is used to evaluate the

interfacial stresses using Eqs.(6-54) and (6-55). The critical stress intensity factors are

evaluated based on Eqs.(6-52) and (6-53). The obtained critical SIFs values are used to

evaluate the critical energy release rate. The value of critical energy release rate based on

Eq.(6-59) is found to be 53.17 J/m2. When Eq.(6-60) is used to determine the critical energy

release rate, the value was obtained as 51.70 J/m2. The variation of both approaches is within

the standard limits. This consistency means that the SIF-based approach can be an alternative

technique for evaluating the fracture toughness of an interface layer.
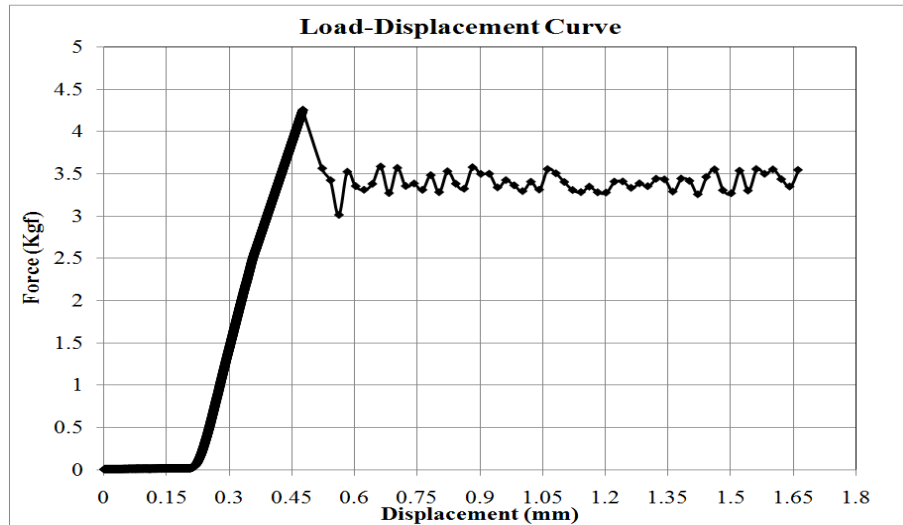
Figure 6-9: Typical load versus displacement curve of four-point bend test

6.3 Summary and Conclusions

An analytical model is developed to calculate interfacial shear and normal stresses in notched tri-layer assembly. It is built based upon the compatibility conditions of displacements and curvatures. The model is used to evaluate the stresses at bond interface for IMC material. Knowing interfacial stresses developed at the bond, an alternative approach of calculating fracture toughness of bond layer is established based on evaluating SIFs for each loading mode exist due to four-point bending test. The proposed approach was used in evaluating critical energy release rate of interface bond for the example given in Section 2.4.3. The result was validated using the energy equilibrium method stated in equation 6-60.

The derivation of interfacial shear and peeling stresses makes it possible to calculate and monitor the critical stress levels at the notch. This approach provides a simple technique of capturing the variations of shear and peeling stresses due to mechanical loading as well as elastic and geometric parameters at the interfaces of electronic components. It should be pointed out here, that FEA analyses are inaccurate in regions of stress singularity. The present study could assist in future studies that deal with finding the effective design and fabricating

methods for components in which parameters such as interfacial modulus, length, and applied load can be purposely controlled to achieve optimum combination of product design and functionality. The study also can help in evaluation of fracture behavior which is a critical aspect in crack and rupture analysis in electronic packaging by finding the corresponding stress intensity factors for mixed-mode loading of a four-point bending specimen.

References

[1]. Song, F., Lee, S. W. R., Newman, K., Sykes, B., and Clark, S., "Brittle Failure Mechanisms of SnAgCu and SnPb Solder Balls during High Speed Ball Shear and Cold Balls Pull Tests," Electronic Components and Technology Conference, Reno, NV, pp. 364-372, June 2007.

[2]. Sohn, Y. Ch., Yn, J., "Correlation between chemical reaction and brittle fracture found in electroless Ni(P)/ immersion gold-solder interconnection," Journal of Materials Research, Vol. 20, No. 8, pp. 1931-1934, 2005.

[3]. Anderson, T.L., "Fracture Mechanics: Fundamentals and Applications, "CRC Press, Boca Raton, 2005.

[4]. Vallin, Ö., Jonsson, K., and Lindberg, U., "Adhesion Quantification Methods for Wafer Bonding," Materials Science and Engineering: R: Reports, Vol. R**50**, No. 4-5, pp. 109–165, 2005.

[5]. Tsau, Ch. H., Spearing, S. M., and Schmidt, M. A., "Fabrication of Wafer-Level Thermo-Compression Bonds," Journal of Micro-electro-mechanical Systems, Vol. 11, No. 6, pp. 641-647, 2002.

[6]. Timoshenko, S., "Analysis of Bi-Metal Thermo-sets," Journal of Optical Society of America A, Vol.11, No. 3, pp. 233-255, 1925.

[7]. Suhir, E., "Stresses in Bi-material Thermostats," Journal of Applied Mechanics. Vol. 53, No. 3, pp. 657-660, 1986.

[8]. Suhir, E., "Analysis of Interfacial Thermal Stresses in a tri-material assembly". Journal of Applied physics. Vol. 89, No. 7, pp. 3685-3694, 2001.

[9]. Ru, C. Q., "Interfacial Thermal Stresses in Bi-material Elastic Beams: Modified Beam Models Revisited," Journal of Electric Packaging, Vol. 124, No. 3, pp. 141-146, 2002.

[10]. Chen, W. T., and Nelson, C. W., "Thermal stresses in Bonded Joints," IBM Journal of Research and Development, Vol. 23, No. 2, pp.179-188, 1979.

[11]. Mirman, I. B., "Effects of Peeling Stresses in Bi-material Assembly," Journal of Electronic Packaging, Vol. 113, No. 4, pp. 431-433, 1991.

[12]. Ghorbani, H. R., and Spelt, J. K., "Interfacial Thermal Stresses in Solder Joints of Leadless Chip Resistors," Journal of Microelectronics and Reliability, Vol. 46, Nos. 5-6, pp. 873-884, 2006.

[13]. Pao, Y. H., and Eisele, E., "Interfacial Shear and Peel Stresses in Multilayered Thin Stacks Subjected to Uniform Thermal Loading," Journal of Electronic Packaging, Vol. 113, No. 2, pp. 164-172, 1991.

[14]. Suhir, E., "Interfacial Stresses in Bi-material Thermostats," Journal of Applied Mechanics, Vol. 56, No. 3, pp. 595-600, 1989.

[15]. Suhir, E., "Predicted Thermal Stresses in a Bi-material assembly Adhesively Bonded at The Ends," Journal of Applied physics, Vol. 89, No. 1, pp. 120-129, 2001.

[16]. Suhir, E., and Vujosevic, M., "Interfacial Stresses in a Bi-material Assembly with a Compliant Bonding Layer," Journal of Physics D: Applied Physics, Vol. 41, pp. 1-9, 2008.

[17]. Taljsten, B. "Strengthening of Beams by Plate Bonding," Journal of Material in Civil Engineering, ASCE Vol. 9, No. 4, pp. 206-212, 1997.

[18]. Smith, S. T., and Teng, J. G., "Interfacial Stresses in Plated Beams," Engineering Structure, Vol. 23, No. 7, pp. 857-871, 2001.

[19]. Abdelouahed, T., "Improved Theoretical Solution for Interfacial Stresses in Concrete Beams Strengthened with FRP Plate," International Journal of Solids and Structures, Vol. 43, Nos. 14-15, pp. 4154-4174, 2006.

[20]. Abdelouahed, Daouadji, Benyoucef, and Addabedia, "Interfacial Stresses in FRP-Plated RC Beams: Effect of Adherend," International Journal of Adhesion and Adhesives, Vol. 29, No. 4, pp. 343-351, 2009.

[21]. Morais, A. B., "Calculation of Stress Intensity Factor by the Force Method," Journal of Engineering Fracture Mechanics, Vol. 74, pp. 739-750, 2007.

[22]. Ichikawa, M., "A Note on Mixed Mode Energy Release Rate," Journal of Engineering Fracture Mechanics," Vol. 26, No. 2, pp. 311-312, 1987.

[23]. Ishikwa, H., Kitagawa, H., and Okamura, H., "J-Integral of a Mixed Mode Crack and its Application in: Mechanical Behavior of Materials," Mechanical behavior of materials; Proceedings of the Third International Conference, Cambridge, England; United Kingdom; 20-24 Aug. 1979. pp. 447-455. 1980

[24]. Banks-Sills, L., Hershovitz I., Wawrznek, P., A., Eliasi, R., and Ingraffea, A. R., "Methods for Calculating Stress Intensity Factors in Anisotropic Materials: Part I- Z=0 is a Symmetric Plane," Journal of Engineering fracture Mechanics, Vol. 72, No. 15, pp. 2328-2358, 2005.

[25]. Banks- Sills, L., Wawrzynek, P. A., Carter, B., Ingraffea, A. R., and Hershkovitz, I., "Methods for Calculating Stress Intensity Factors in Anisotropic Materials: Part II- Arbitrary Geometry," Journal of Engineering fracture Mechanics, Vol. 74, No. 8, pp. 1293-1307, 2007.

[26]. Wang, SS., Yau, F. F., and Corten, H. T., "A Mixed-Mode Crack Analysis of Rectilinear Anisotropic Solids using Conservation Laws of Elasticity," International Journal of Fracture, Vol. 16, No. 3, pp. 247-259, 1980.

[27]. Raju, I. S., and Newmann, J. C., "Three- dimensional Finite-Element Analysis of Finite-Thickness Fracture Specimen," NASA TN D-8414, 1977.

[28]. Toya, M., "Fracture Mechanics of Interfaces," JSME International Journal Series I- Solid Mechanics Strength of Materials, Vol. 33, No. 4, pp. 413-424, 1990.

[29]. Zhigang, S., and Hutchinson, J. W., "Sandwich Test Specimens for Measuring Interface Crack Toughness," Materials Science and Engineering: A, Proceedings of the Symposium on Interfacial Phenomena in Composites: Processing Characterization and Mechanical Properties, Vol. 107, pp. 135-143, 1989.

[30]. Hutchinson, J. W., and Suo, Z., "Mixed Mode Cracking in Layered Materials," Journal of Advances in Applied Mechanics, Vol. 29, pp. 63-191, 1992.

[31]. He, M. and Hutchinson, J. W., "Asymmetric Four-Point Crack Specimen," Journal of Applied Mechanics, Vol. 67, No. 1, pp. 207-209, 2000.

[32]. Shahani, A. R. and Tabatabaei, S. A., "Computation of Mixed Mode Stress Intensity Factors in a Four-Point Bend Specimen," Journal of Applied Mathematical Modeling, Vol. 32, No. 7, pp. 1281-1288, 2008.

[33]. Fett, T., "Stress Intensity Factors for edge Crack Subjected to Mixed Mode Four-Point Bending," Journal of theoretical and Applied Fracture Mechanics, Vol. 15, No. 1, pp. 99-104, 1991.

[34]. Hofinger, I., "Modified Four-Point Bending Specimen for Determining the Interface Fracture Energy for Thin, Brittle Layers," International Journal of Fracture, Vol. 92, No. 3, pp. 213-220, 1998.

[35]. Charalambides, P.G., Lund, J., Evans, A.G. and McMeeking, R.M., "A Test Specimen for Determining the Fracture Resistance of Bi-Material Interfaces," ASME Journal of Applied Mechanics, Vol. 56, No. 1, pp. 77-82, 1989.

[36]. Y. Murakami, "Stress Intensity Factors Handbook," Pergamon Press, New York, 1987.

[37]. H. Tada, P.C. Paris and G.R. Irwin, "The stress analysis of cracks handbook," Del Research Corp., St. Louis, MO (1985).

Appendix A

Expressions for coefficients R1, R2, R3, and R4 of eqs.45 and 46 are given as follows:

$$R1 = \left(\frac{1}{2}\right) * \left[\left(\beta \sin(\beta L1) * ha * E1 * I1 * n1 * \exp(-\beta L2) * \exp(\beta L1) * \frac{d^2\tau_2}{dx^2}l_{x=L_2} * \exp(\beta * L3) * \cos(\beta L3) \right. \right.$$

$$+ \beta * \sin(\beta L1) * ha * E1 * I1 * n1 * \exp(-\beta L2) * \exp(\beta L1) * \frac{d^2\tau_2}{dx^2}l_{x=L_2} * \exp(\beta L3)$$

$$* \cos(\beta L3) * \tan(\beta L3) - \beta * \sin(\beta L1) * ha * E1 * I1 * n1 * \exp(-\beta L2) * \exp(\beta L1)$$

$$* \frac{d^2\tau_1}{dx^2}l_{x=L_2} * \exp(\beta L3) * \cos(\beta L3) - \beta \sin(\beta L1) * ha * E1 * I1 * n1 * \exp(-\beta L2)$$

$$* \exp(\beta L1) * \frac{d^2\tau_1}{dx^2}l_{x=L_2} * \exp(\beta L3) * \cos(\beta L3) * \tan(\beta L3) - n1 * \frac{d^3\tau_1}{dx^3}l_{x=L_1} * ha * E1$$

$$* I1 * \exp(\beta L2) * \exp(-\beta L2) * \cos(\beta L2) * \exp(\beta L3) * \cos(\beta L3) - n1 * \frac{d^3\tau_1}{dx^3}l_{x=L_1} * ha$$

$$* E1 * I1 * \exp(\beta L2) * \exp(-\beta L2) * \cos(\beta L2) * \exp(\beta L3) * \cos(\beta L3) * \tan(\beta L3) - Ea$$

$$* MT * \exp(\beta L2) * \exp(-\beta L2) * \cos(\beta L2) * \exp(\beta L3) * \cos(\beta L3) - Ea * MT * \exp(\beta L2)$$

$$* \exp(-\beta L2) * \cos(\beta L2) * \exp(\beta L3) * \cos(\beta L3) * \tan(\beta L3) - 2 * \beta * n1 * \frac{d^2\tau_2}{dx^2}l_{x=L_3}$$

$$* \exp(\beta L1) * \sin(\beta L1) * ha * E1 * I1 * \exp(\beta * L2) * \exp(-\beta L2) * \cos(\beta L2) + n1 * \beta$$

$$* \sin(\beta L1) * ha * E1 * I1 * \cos(\beta L3) * \exp(\beta L2) * \frac{d^2\tau_2}{dx^2}l_{x=L_2} * \exp(-\beta L3) * \exp(\beta L1)$$

$$+ n1 * \beta * \sin(\beta L1) * ha * E1 * I1 * \cos(\beta L3) * \exp(\beta L2) * \frac{d^2\tau_2}{dx^2}l_{x=L_2} * \exp(-\beta L3)$$

$$* \exp(\beta L1) * \tan(\beta L3) - n1 * \beta \sin(\beta L1) * ha * E1 * I1 * \cos(\beta L3) * \exp(\beta L2)$$

$$* \frac{d^2\tau_1}{dx^2}l_{x=L_2} * \exp(-\beta L3) * \exp(\beta L1) - n1 * \beta \sin(\beta L1) * ha * E1 * I1 * \cos(\beta L3)$$

$$\left. * \exp(\beta L2) * \frac{d^2\tau_1}{dx^2}l_{x=L_2} * \exp(-\beta L3) * \exp(\beta L1) * \tan(\beta L3) \right)$$

$$\left. / \left[\left(\beta^2 * \sin(\beta L1) * ha * E1 * I1 * (-\exp(-\beta L1) * \exp(\beta L3) + \exp(-\beta L3) * \exp(\beta L1)) \right. \right. \right.$$

$$\left. \left. \left. * \cos(\beta L3) * (1 + \tan(\beta L3)) * \exp(\beta L2) * \exp(-\beta L2) * \cos(\beta L2) \right) \right] \right]$$

$$\text{(A1)}$$

$$R2 = -\left(\frac{1}{2}\right) * \Big[exp\left(-\beta * L3\right) * Ea * MT * exp(\beta * L2) * exp\left(-\beta * L2\right) * cos(\beta * L2) * cos(\beta * L3)$$

$$+ exp\left(-\beta * L3\right) * Ea * MT * exp(\beta * L2) * exp\left(-\beta * L2\right) * cos(\beta * L2) * cos(\beta * L3)$$

$$* tan(\beta * L3) - exp\left(-\beta * L2\right) * \beta * sin(\beta * L1) * ha * E1 * I1 * n1 * exp\left(-\beta * L1\right)$$

$$* \frac{d^2\tau_2}{dx^2} l_{x=L_2} * exp(\beta * L3) * cos(\beta * L3) - exp\left(-\beta * L2\right) * \beta * sin(\beta * L1) * ha * E1 * I1$$

$$* n1 * exp\left(-\beta * L1\right) * \frac{d^2\tau_2}{dx^2} l_{x=L_2} * exp(\beta * L3) * cos(\beta * L3) * tan(\beta * L3) + exp\left(-\beta * L2\right)$$

$$* \beta * sin(\beta * L1) * ha * E1 * I1 * n1 * exp\left(-\beta * L1\right) * \frac{d^2\tau_1}{dx^2} l_{x=L_2} * exp(\beta * L3)$$

$$* cos(\beta * L3) + exp\left(-\beta * L2\right) * \beta * sin(\beta * L1) * ha * E1 * I1 * n1 * exp\left(-\beta * L1\right)$$

$$* \frac{d^2\tau_1}{dx^2} l_{x=L_2} * exp(\beta * L3) * cos(\beta * L3) * tan(\beta * L3) - exp\left(-\beta * L3\right) * \beta * sin(\beta * L1)$$

$$* ha * E1 * I1 * n1 * exp\left(-\beta * L1\right) * exp(\beta * L2) * \frac{d^2\tau_2}{dx^2} l_{x=L_2} * cos(\beta * L3) - exp\left(-\beta * L3\right)$$

$$* \beta * sin(\beta * L1) * ha * E1 * I1 * n1 * exp\left(-\beta * L1\right) * exp(\beta * L2) * \frac{d^2\tau_2}{dx^2} l_{x=L_2}$$

$$* cos(\beta * L3) * tan(\beta * L3) + exp\left(-\beta * L3\right) * \beta * sin(\beta * L1) * ha * E1 * I1 * n1$$

$$* exp\left(-\beta * L1\right) * exp(\beta * L2) * \frac{d^2\tau_1}{dx^2} l_{x=L_2} * cos(\beta * L3) + exp\left(-\beta * L3\right) * \beta * sin(\beta * L1)$$

$$* ha * E1 * I1 * n_1 * exp\left(-\beta * L1\right) * exp(\beta * L2) * \frac{d^2\tau_1}{dx^2} l_{x=L_2} * cos(\beta * L3) * tan(\beta * L3)$$

$$+ exp\left(-\beta * L3\right) * n1 * \frac{d^3\tau_1}{dx^3} l_{x=L_1} * ha * E1 * I1 * exp(\beta * L2) * exp\left(-\beta * L2\right)$$

$$* cos(\beta * L2) * cos(\beta * L3) + exp\left(-\beta * L3\right) * n1 * \frac{d^3\tau_1}{dx^3} l_{x=L_1} * ha * E1 * I1 * exp(\beta * L2)$$

$$* exp\left(-\beta * L2\right) * cos(\beta * L2) * cos(\beta * L3) * tan(\beta * L3) + 2 * n1 * \frac{d^2\tau_2}{dx^2} l_{x=L_3} * \beta$$

$$* sin(\beta * L1) * ha * E1 * I1 * exp(\beta * L2) * exp\left(-\beta * L2\right) * cos(\beta * L2) * exp\left(-\beta * L1\right) \Big]$$

$$/ \Big[exp(\beta * L2) * \beta^2 * sin(\beta * L1) * ha * E1 * I1$$

$$* \left(-exp\left(-\beta * L1\right) * exp(\beta * L3) + exp\left(-\beta * L3\right) * exp(\beta * L1)\right) * cos(\beta * L3)$$

$$* \left(1 + tan(\beta * L3)\right) * cos(\beta * L2) * exp\left(-\beta * L2\right) \Big]$$

<div align="right">(A2)</div>

$$R3 = -\left(\frac{1}{2}\right) * \left[\left(-\beta sin(\beta L1) * ha * E1 * I1 * n1 * exp(-\beta L2) * exp(\beta L1) * \frac{d^2\tau_2}{dx^2}l_{x=L_2} * exp(\beta L3)\right.\right.$$

$$* cos(\beta L3) - \beta sin(\beta L1) * ha * E1 * I1 * n1 * exp(-\beta L2) * exp(\beta L1) * \frac{d^2\tau_2}{dx^2}l_{x=L_2}$$

$$* exp(\beta L3) * cos(\beta L3) * tan(\beta L3) + \beta sin(\beta L1) * ha * E1 * I1 * n1 * exp(-\beta L2)$$

$$* exp(\beta L1) * \frac{d^2\tau_1}{dx^2}l_{x=L_2} * exp(\beta L3) * cos(\beta L3) + \beta sin(\beta L1) * ha * E1 * I1 * n1$$

$$* exp(-\beta L2) * exp(\beta L1) * \frac{d^2\tau_1}{dx^2}l_{x=L_2} * exp(\beta L3) * cos(\beta L3) * tan(\beta L3) - \beta sin(\beta L1) * ha$$

$$* E1 * I1 * n1 * exp(-\beta L1) * exp(\beta L2) * \frac{d^2\tau_2}{dx^2}l_{x=L_2} * exp(\beta L3) * cos(\beta L3) - \beta sin(\beta L1)$$

$$* ha * E1 * I1 * n1 * exp(-\beta L1) * exp(\beta L2) * \frac{d^2\tau_2}{dx^2}l_{x=L_2} * exp(\beta L3) * cos(\beta L3)$$

$$* tan(\beta L3) + \beta sin(\beta L1) * ha * E1 * I1 * n1 * exp(-\beta L1) * exp(\beta L2) * \frac{d^2\tau_2}{dx^2}l_{x=L_3}$$

$$* exp(\beta L3) * cos(\beta L3) + \beta sin(\beta L1) * ha * E1 * I1 * n1 * exp(-\beta L1) * exp(\beta L2)$$

$$* \frac{d^2\tau_1}{dx^2}l_{x=L_2} * exp(\beta L3) * cos(\beta L3) * tan(\beta L3) + n1 * \frac{d^3\tau_1}{dx^3}l_{x=L_1} * ha * E1 * I1 * exp(\beta L2)$$

$$* exp(-\beta L2) * cos(\beta L2) * exp(\beta L3) * cos(\beta L3) + n1 * \frac{d^3\tau_1}{dx^3}l_{x=L_1} * ha * E1 * I1$$

$$* exp(\beta L2) * exp(-\beta L2) * cos(\beta L2) * exp(\beta L3) * cos(\beta L3) * tan(\beta L3) + Ea * MT$$

$$* exp(\beta L2) * exp(-\beta L2) * cos(\beta L2) * exp(\beta L3) * cos(\beta L3) + Ea * MT * exp(\beta L2)$$

$$* exp(-\beta L2) * cos(\beta L2) * exp(\beta L3) * cos(\beta L3) * tan(\beta L3) + 2 * \beta * n1 * \frac{d^2\tau_2}{dx^2}l_{x=L_3}$$

$$\left.\left.* exp(\beta L1) * sin(\beta L1) * ha * E1 * I1 * exp(\beta L2) * exp(-\beta L2) * cos(\beta L2)\right)\right]$$

$$/ \left[\left(\beta^2 sin(\beta L1) * ha * E1 * I1 * \left(-exp(-\beta L1) * exp(\beta L3) + exp(-\beta L3) * exp(\beta L1)\right)\right.\right.$$

$$\left.\left.* cos(\beta L3) * \left(1 + tan(\beta L3)\right) * exp(\beta L2) * exp(-\beta L2) * cos(\beta L2)\right)\right]$$

(A3)

$$R4 = -\left(\frac{1}{2}\right) * \left[\left(-\exp(-\beta L3) * \beta \sin(\beta L1) * ha * E1 * I1 * n1 * \exp(-\beta L2) * \exp(\beta L1) * \frac{d^2\tau_2}{dx^2}l_{x=L_2} * \cos(\beta L3)\right.\right.$$

$$- \exp(-\beta L3) * \beta * \sin(\beta L1) * ha * E1 * I1 * n1 * \exp(-\beta L2) * \exp(\beta L1) * \frac{d^2\tau_2}{dx^2}l_{x=L_2}$$

$$* \cos(\beta L3) * \tan(\beta L3) + \exp(-\beta L3) * \beta * \sin(\beta * L1) * ha * E1 * I1 * n1 * \exp(-\beta L2)$$

$$* \exp(\beta * L1) * \frac{d^2\tau_1}{dx^2}l_{x=L_2} * \cos(\beta L3) + \exp(-\beta L3) * \beta\sin(\beta L1) * ha * E1 * I1 * n1$$

$$* \exp(-\beta L2) * \exp(\beta L1) * \frac{d^2\tau_1}{dx^2}l_{x=L_2} * \cos(\beta L3) * \tan(\beta L3) - \exp(-\beta L3) * \beta\sin(\beta L1) * ha$$

$$* E1 * I1 * n1 * \exp(-\beta L1) * \exp(\beta L2) * \frac{d^2\tau_2}{dx^2}l_{x=L_2} * \cos(\beta L3) - \exp(-\beta L3) * \beta * \sin(\beta L1)$$

$$* ha * E1 * I1 * n1 * \exp(-\beta L1) * \exp(\beta L2) * \frac{d^2\tau_2}{dx^2}l_{x=L_2} * \cos(\beta L3) * \tan(\beta L3) + \exp(-\beta L3)$$

$$* \beta * \sin(\beta L1) * ha * E1 * I1 * n1 * \exp(-\beta L1) * \exp(\beta L2) * \frac{d^2\tau_2}{dx^2}l_{x=L_3} * \cos(\beta L3)$$

$$+ \exp(-\beta L3) * \beta * \sin(\beta L1) * ha * E1 * I1 * n1 * \exp(-\beta L1) * \exp(\beta L2) * \frac{d^2\tau_1}{dx^2}l_{x=L_2}$$

$$* \cos(\beta L3) * \tan(\beta L3) + \exp(-\beta L3) * n1 * \frac{d^3\tau_1}{dx^3}l_{x=L_1} * ha * E1 * I1 * \exp(\beta L2) * \exp(-\beta L2)$$

$$* \cos(\beta L2) * \cos(\beta L3) + \exp(-\beta L3) * n1 * \frac{d^3\tau_1}{dx^3}l_{x=L_1} * ha * E1 * I1 * \exp(\beta L2) * \exp(-\beta L2)$$

$$* \cos(\beta L2) * \cos(\beta L3) * \tan(\beta L3) + \exp(-\beta L3) * Ea * MT * \exp(\beta L2) * \exp(-\beta L2)$$

$$* \cos(\beta L2) * \cos(\beta L3) + \exp(-\beta L3) * Ea * MT * \exp(\beta L2) * \exp(-\beta L2) * \cos(\beta L2)$$

$$* \cos(\beta L3) * \tan(\beta L3) + 2 * n1 * \frac{d^2\tau_2}{dx^2}l_{x=L_3} * \beta\sin(\beta L1) * ha * E1 * I1 * \exp(\beta L2)$$

$$\left.\left.* \exp(-\beta L2) * \cos(\beta L2) * \exp(-\beta L1)\right)\right]$$

$$/ \left[\left(\beta^2\sin(\beta L1) * ha * E1 * I1 * \left(-\exp(-\beta L1) * \exp(\beta L3) + \exp(-\beta L3) * \exp(\beta L1)\right)\right.\right.$$

$$\left.\left.* \cos(\beta L3) * \left(1 + \tan(\beta L3)\right) * \exp(\beta L2) * \exp(-\beta L2) * \cos(\beta L2)\right)\right]$$

`

$$(A4)$$

Appendix B

The expanded form of the integrals in equations 54 and 55

$$\sigma_{yy}(x) = \frac{1}{L_3}\int_{L_1+a}^{L_2} \sigma_p(x)\,dx$$

$$= \frac{1}{L_3}\int_{L_1+a}^{L_2}\left[R_1 e^{-\beta x}\cos(\beta x) + R_3 e^{\beta x}\cos(\beta x) - n_1\frac{d\tau_1(x)}{dx}\right]dx$$

$$= \frac{1}{L_3}\left\{R_1\, e^{-\beta(L_1+L_2+a)}\frac{1}{2\beta}\left[e^{-\beta L_2}[\cos(\beta(L_1+a))-\sin(\beta(L_1+a))]\right.\right.$$
$$-(\cos(\beta L_2)-\sin(\beta L_2))\,]$$
$$-R_2\,\frac{1}{2\beta}\left[e^{(\beta(L_1+a))}[\cos(\beta(L_1+a))+\sin(\beta(L_1+a))]\right.$$
$$\left.\left.-(\cos(\beta L_2)+\sin(\beta L_2))\,]-n_1\tau_1(x)|_{x=L_1+a}^{x=L_2}\right\}$$

$$(B1)$$

$$\tau_{xy}(x)=\frac{1}{L_3}\int_{L_1+a}^{L_2}\tau_1(x)\,dx$$

$$=\frac{1}{L_3}\int_{L_1+a}^{L_2}[B_1\exp(-\lambda x)+B_2\exp(\lambda x)]\,dx$$

$$=\frac{1}{L_3}\left\{\frac{B_1}{\lambda}\left(\exp(-\lambda(L_1+a))-\exp(-\lambda L_2)\right)+\frac{B_2}{\lambda}\left(\exp(\lambda L_2)-\exp(\lambda(L_1+a))-\right)\right\}$$

$$(B2)$$

Chapter 7 : Summary and Conclusions

The effect of size of the joints on kinetics of bond formation and mechanical behavior of Lead-free solder joints was investigated. Several major discoveries were made. A summary of main findings of this research is provided below:

7.1 Major Conclusions

Experimental observation combined with analytical modeling of growth kinetics of η and ε IMC layers formed during Sn-3.5Ag solders/Cu-substrate soldering process shows that the net growth of each IMC phase can be governed by two mechanisms: diffusion and partial chemical-reaction mechanisms. The analytical modeling results show that the increase in the IMC layer thickness during the soldering process follows a linear relationship with time during the chemical reaction-controlled stage of formation of Cu_3Sn IMC layer. However, parabolic relationship between layer growth and time is observed during the diffusion-controlled growth stage. Using this analytical model, the apparent activation energies were calculated for both stages. The model also was able to resolve the possible interaction between the chemical reaction and the diffusion mechanisms during IMC growth process. Further analysis of the effect of the joint size on kinetics of IMC compounds formation and growth showed that while the joint size has no effect on the type of IMCs formed, it indeed has a significant effect on the IMC growth behavior. Thicker IMC layers, particularly ε-phase, were formed in joints with smaller thicknesses. The effects of temperature and time on the IMC growth were found to be the same in all specimen

sizes resulting in similar growth rate constants and activation energies for η-phase. However, for Cu$_3$Sn IMC, the activation energy was found to be size effect dependent. Higher activation energy was associated with smaller solder joints.

In an effort to compare the grain orientation and size in different specimens, EBSD analysis was used. However, specimen preparation is a very critical step in obtaining a successful EBSD image. Additionally, several EBSD parameters play a very strong role in the quality of the images. Our initial effort in obtaining a damage-free surface was unsuccessful, because of existence of combination of different materials with different wear resistance and stiffness. A certain procedure that results in an optimum surface in a certain phase could result in build up and damage in another phase with different surface wear resistance and stiffness. Therefore, we modified the regular specimen preparation procedure by adding certain number of hours of vibratory polishing. Furthermore, EBSD parameters were adjusted in a systematic manner to obtain a quality image in this multilayer specimen.

Our finding suggest that a series of mechanical grinding and polishing followed with vibratory polishing is adequate for preparing damage-free surfaces in multiple-layer specimens. Vibratory polishing and its associated polishing time were found to be the key factor to successfully prepare such difficult specimens. We have also found that EBSD parameters play a critical role in reliably discriminating between phases and measuring the grain size and grain orientation. Obviously mechanical performance of the microelectronic joints is a key function. In order to determine the mechanical properties several different studies were conducted. Because the size of the solder joints and the size of the grains are comparable in micro-scale interconnects, the conventional continuum mechanics assumption in which the properties of a bulk material are assumed to be isotropic and homogeneous is not valid. In this case, the joints behave

199

anisotropically depending on the number and orientation of grains that exist in the joints. Therefore, properties of the grains define the properties of the joints. Consequently, knowledge of mechanical properties of individual grains is very important. Additionally, as the size of the joints becomes smaller, the structural constrains may change the local behavior of the material. Therefore, we have used nanoindentation to investigate (1) the local properties of different phases that exist in the joint by measuring the properties of single grains of materials, (2) determine if there is any difference in the properties of existing phases as the size of the joint changes, and (3) to find the properties of single grain Cu6Sn6 and compare them at different orientation, it is accomplished using nanoindentation combined with a post-test EBSD imaging. Results have shown that the size effects play a major role in the mechanical properties of solder joints. As the joint thickness decreases, the elastic modulus, hardness, and yield strength were found to increase while work hardening exponent decreases in both Cu_6Sn_5 and Cu_3Sn IMCs. Measurement of elastic modulus on single grains of Cu_6Sn_5 IMC indicates that material is stiffer in the orientation of c axis compared to the other crystallographic orientation in hexagonal closed pack crystal structure of this IMC material.

As the joints become smaller, IMC materials make up larger portion of these joints. Intermetallics in general are much more brittle than β-tin phase solder. Therefore, the crack propagation in these materials is better modeled using fracture mechanics concepts. Fracture toughness and energy release rate are important parameters that dictate the crack propagation characteristics in any material. Additionally, stress concentration factors play a very important role in driving crack propagation, further mechanical analysis of the joints at micro scale was conducted to obtain these parameters. The standard fracture toughness measurement tests are not applicable to this microscale because of difficulties in generating a bulk sample solely out of

200

IMCs. Therefore a unique technique of four-point bending test was used to calculate the fracture toughness of IMC materials. An analytical model was developed to obtain the stresses at the interface of the multi-layer four-point bend specimen. The model results were confirmed by finite element simulation. The stresses at the interface were then used to calculate the energy release rate. Our results indicated that the analytical model that was developed to obtain the stress at the interface was accurate and that the energy release rate obtained through these techniques was reasonable and close.

7.2   Contributions

The experiments conducted in this dissertation provide the basic understanding of the size effects on the microstructure and mechanical properties of lead-free solder joints. The local mechanical properties of Cu_6Sn_5 IMC were also experimentally investigated. The contributions of this study can be summarized below:

1- A systematic and methodical investigation of the growth kinetics of the IMC layers in lead-free micro-scale solder joints

2- Understanding the effect of process parameters on the growth kinetics

3- Modification of an existing physics-based analytical model to model the growth kinetics in a complex situation where both chemical reaction- and diffusion-controlled mechanisms exist.

4- First time report of apparent activation energy of ε-(Cu_3Sn) IMC phase growth during the chemical reaction-controlled stage.

5- Understating of the effects of structural constraints on the growth behavior and growth kinetics of IMC layers in Sn-3.5Ag/Cu-substrate soldering system.

6- Experimental values of growth rate constants, and activation energy, for Cu_3Sn IMC layer as a function of thickness for the first time in literature.

7- An improved method of specimen preparation and EBSD analysis for multilayer specimens.

8- Providing the EBSD and specimen preparation community with optimum values to be used for future guidance in analyzing similar type of multilayer structures.

9- Understanding of the effects of structural constraints on the elastic and plastic properties of different IMC layers in Sn-3.5Ag/Cu-substrate soldering system.

10- An improved technique for local probing and mechanical properties measurement using combined nanoindentation and EBSD analysis.

11- Supplying microstructural-based simulation studies with needed local mechanical properties of IMCs formed in lead-free solder joints.

12- Developing closed-form solutions of interfacial peeling and shear stresses in four-point bend structure.

13- Applying the interfacial stresses in calculating fracture toughness of IMC bond using four-point bend test.

14- Providing values of much needed energy release rate for IMC material that can be used in modeling crack and crack propagation in this material.

7.3   Recommendations for Future Research

- Although there was not any influence of the joint size on the type of intermetallics formed in the soldering system under investigation, the effect of joint thickness on the intermetallic morphology such as equiaxed- or scalloped, has not been studied. It is an important factor especially when considering fatigue and fracture.

- In this study, the range of soldering temperature and time were between 260-360 $^{\circ}$C and 20-240 min. A set of different soldering temperatures and times should be considered in future research to cover the possible soldering and operating conditions solder joints might experience.

- The current study has considered one type of lead-free solder alloys; other soldering systems, such as SAC and Sn-Cu should be investigated for size effects.

- Size effects on the mechanical properties of IMCs formed in Sn-3.5Ag/Cu-substrate soldering system were evaluated using nanoindentation, other techniques such as micro-beam bending and micro-tensile testing should also be used to confirm and validate the results obtained from nanoindentation testing.

- Evaluation of local elastic mechanical properties has been done only for Cu_6Sn_5 IMC, other IMC phases should also be investigated. The future work should also consider extracting the plastic properties of IMC.

- Creep and fatigue is also an important subject in soldering. Studies that address the creep and fatigue behaviors of solder joints against size effects should also be considered for future work.

References

[1].Puttlitz K.J., Stalter K.A., "Handbook of Lead-Free Solder Technology for Microelectronic Assemblies," Marcel Dekker AG, Basel, Switzerland, 2004.

[2].Blackwell G.R., "The Electronic Packaging Handbook Ed. Blackwell", G.R. Boca Raton: CRC Press LLC, 2000.

[3].Tu K.N., Zeng K., "Tin-lead (SnPb) solder reaction in flip chip technology", Material science and engineering, Vol. R34, pp. 1-58, 2001.

[4].Quan L., Frear D., Grivas D., Morris Jr J.W., "Tensile behavior of Pb-Sn solder/Cu joints," Journal of Electronic Materials, Vol. 16, No. 3, pp.203-208 , 1987.

[5].Skipor A.F., Harren S. V., and Botsis J., "the effect of mechanical constraint on the flow and fracture of 63/37 Sn/Pb eutectic alloy", Journal of Engineering Fracture Mechanics, Vol. 52, No. 4, pp. 647-669, 1995.

[6].Qi Y., Ghorbani H.R., and Spelt J.K., "Thermal fatigue of SnPb and SAC resistor joints: analysis of stress-strain as a function of cycle parameters", IEEE Transaction Advanced Packaging, Vol. 29, NO. 4, pp.690-700, 2006.

[7].Vianco P., and Arbor A., "Development of alternatives to lead-bearing solders", Center for Solder Science and Technology, Sandia National Laboratories, 1993.

[8].Melton C., "Alternatives of lead bearing solder alloys", IEEE Transaction, Vol. No. pp. 94-97, 1993.

[9].Abtew M., and Selvaduray G., "Lead-free solders in microelectronics", Journal of Materials Science and engineering, Vol. 27, pp. 95-141, 2000.

[10]. Wood E.P., and Nimmo K.L., "In search of new lead-free electronic solders", Journal of Electronic Materials, Vol. 23, No. 8, pp. 709-713, 1994.

[11]. Goodman P., Strudwick P., and Skipper R., "Reliability and failure analysis: Technical adaptation under directive 2002/95/EC (RoHS)-Investigation of exemptions", ERA report 2004-0603.

[12]. Official journal of European Union, "Directive 2002/95/EC of the European parliament and of the council of 27 January 2003 on the restriction of the use of certain hazardous substances in electrical and electronic equipment. 02-13-2003.

[13]. U.S. Congress, Office of Technology Assessment, Miniaturization Technologies, OTA-TCT-514 (Washington, DC: U.S. Government Printing Office, November 1991).

[14]. Sienski K., Eden R., and Schaefer D., "3-D electronic interconnect packaging", IEEE Transaction on Aerospace Applications Conference, 1996. Proceedings, Vol. 1, pp. 363-373, 1996.

[15]. Chew K.H., "Drop in replacement of tin/lead solder alloy in wave soldering process-lead free solders", Quantum Chemical Technologies (S) Pte Ltd.

[16]. Chidambaram V., Hald J., and Hattel J., "Development of Au-Ge based candidate alloys as an alternative to high-lead content solders", Journal of alloys and compounds. Vol. 490, pp. 170-179, 2010.

[17]. Tri-County Health Department, "Electronic and computer waste".2004, www.tchd.org

[18]. Five Winds International, LP, "Toxic and Hazardous Materials in IT and Telecom Products", Final report, October 2001.

[19]. Plumbridge W.J., "Second generation lead-free solder alloys- A challenge to thermodynamics", Journal of Monatshefte Fur Chenie. Chemical Monthly, Vol. 136, pp. 1811-1821, 2005.

[20]. Zeng G., Xue S., Zhang L., Gao L., Dai W., and Luo J., "A review on the interfacial intermetallic compounds between Sn-Ag-Cu based solders and substrates. Journal of Material Science, Vol. 21. Pp. 421-440, 2010.

[21]. ASM International, "ASM handbook, Colume 3: Alloy phase diagrams", The material information company, 1992.

[22]. Ohnuma I., Cui Y., Liu X.J., Inohana Y., Ishihara S., Ohtani H., Kainuma R., and Ishida K., "Phase wuilibria of Sn-In based micro-soldering alloys", Journal of Electronic Materials, Vol. 19, No. 10, pp. 1113-1121, 2000.

[23]. Lee B.L., Seok C., and Shim J.H., "Thermodynamic assessments of the Sn-In and Sn-Bi binary systems", Journal of Electronic Materials, Vol. 25, No. 6, pp. 983-991, 1996.

[24]. Islam R.A., Wu B.Y., Alam M.O., Chan Y.C., and Jillek W., " Investigations on the microhardness of Sn-Zn based lead-free solder alloys as replacement of Sn-Pb solder", Journal of Alloys and Compounds, Vol. 392, pp. 149-158, 2005.

[25]. McCormack M. and Jin S., "Improved mechanical properties in new, Pb-free solder alloys", Journal of Electronic Materials, Vol. 23, No. 8, 1994.

[26]. Humpston G and Jacobson D M, "Principles of Soldering", ASM International 2004.

[27]. Nishikawa H., Piao J.Y., and Takemoto T., "Interfacial reaction between Sn-0.7Cu (-Ni) solder and Cu substrate", Journal of Electronic Materials, Vol. 35, No. 5, pp. 1127-1132, 2006.

[28]. Ma H. and Suhling, "A review of mechanical properties of lead-free solders for electronic packaging", Journal of Material Science, Vol. 44, pp. 1141-1158, 2009.

[29]. Suganuma K., "Lead-free soldering in electronics: Science, technology, and environmental impact," Marcel Dekker, INC, New York-Basel, 2004.

[30]. Siviour C.R., Walley S.M., Proud W.G., and Field J.E., "Mechanical properties of SnPb and lead-free solders at high rates of strain", Journal of Phsics D: Applied Physics, Vol. 38, pp. 4131-4139, 2005.

[31]. Choi S., Bieler T.R., Lucas J.P., and Subramanian K.N., "Characterization of the growth of intermetallic interfacial layers of Sn-Ag and Sn-Pb eutectic solders and their composite solders on Cu substrate during isothermal long-term aging", Journal of Electronic Materials, Vol. 28, No. 11, pp. 1209-1215, 1999.

[32]. Lee H.T., Lin H.S., Lee C.S., and Chen P.W., "Reliability of Sn-Ag-Sb lead-free solder joints," Materials Science and Engineering, Vol. A407, No. 1-2, pp. 36-44, 2005.

[33]. Li J.F., Mannam S.H., Clode M.P., Whalley D.C and Hutt D.A., "Interfacial reactions between molten Sn-Bi-X solders and Cu substrates for liquid solder interconnects", Journal of Acta Materialia, Vol. 54, pp. 2907-2922, 2006.

[34]. Zhoo G., Sheng G., Luo J., and Yuan X., "Solder characteristics of a rapidly solidified Sn-9Zn-0.1Cr alloy and mechanical properties of Cu/solder/Cu joints," Journal of Electronic Materials, Vol. 41, No. 8, pp. 2100-2106, 2012.

[35]. Ichitsubo T., Matsubara E., Fujiwara K., Yamaguchi M., Irie H., Kumamoto S, and Anada T., "Control of compound forming reaction at the interface between SnZn solder and Cu substrate", Journal of Alloys and Compounds, Vol. 392, pp. 200-205, 2005.

[36]. Yu D.Q., Xie H.P., and Wang L., "Investigation of interfacial microstructure nd wetting property of newly developed Sn-Zn-Cu solders with Cu substrate", Journal of Alloys and Compounds, Vol. 385, pp. 119-125, 2004.

[37]. Sundelin J., Nurmi S.T., Lepisto T.K., and Ristolainen E.O., "Mechanical and microstructural properties of SnAgCu solder joints", Journal of Materials Science and Engineering A, Vol. 420, pp. 55-62, 2006.

[38]. Wei C., Liu Y., Gao Z., Wan J., and Ma C., "Effects of thermal aging on the microstructure and microhardness of Sn-3.7Ag-0.9Zn-1In solder," Journal of Electronic Materials, Vol. 38, No. 2, pp. 345-350, 2009.

[39]. Kattner U., "Phase diagrams for lead-free solder alloys", JOM-Journal of the minerals, metals and materials society, Vol. 54, No. 12, pp. 45-51, 2002.

[40]. Yoon J.W., Lee C.B., Kim D. U., and Jung S.B., "Reaction diffusions of Cu6Sn5 and Cu3Sn intermetallic compounds in the couple of Sn-3.5Ag eutectic solder and copper substrate," Metals and Materials International, Vol. 9, No. 2, pp. 193-199, 2003.

[41]. Yang W., Felton L.E., and Messler JR.W., "The effect of soldering process variables on the microstructure and mechanical properties of eutectic Sn-Ag/Cu solder joints", Journal of Electronic Materials, Vol. 24, No. 10, pp. 1465-1472, 1995.

[42]. Frear D.R., Jang J.W., Lin J.K., and Zhang C., "Pb-free solders for flip-chip interconnects," LOM-Journal of the minerals, metals, and materials society, Vol. 53, No. 1, pp. 28-33, 2001.

[43]. Roman J.W. and Eagar T.W., "Low stress die attach by low temperature transient liquid phase bonding," Proceeding of the 1992 International symposium on Microelectronics, CA, 19-21, October 1992, pp. 1-6, 1992.

[44]. Venkatadri V., "Quantitative assessment of long term aging effects on the mechanical properties of lead free solder joints, Thesis, Binghamton University-State university of New York, 2009.

[45]. Osenbach J., Amin A., Bachman M., Baiocchi F., Bitting D., Crouthamel D., Delucca J., Goodell J., Peridier C., Stahley M., and Weachock R., "Stability of Flip-chip interconnects assembled with Al/Ni(v)/Cu-UBM and eutectic Pb-Sn solder during exposure to high-temperature storage," Journal of Electronic Materials, Vol. 38, No. 2, pp. 303-324, 2009.

[46]. Ghosh M., Kar A., Das S.K., and Ray A.K., "Aging characteristics of Sn-Ag eutectic solder alloy with the addition of Cu, In, and Mn", The minerals, Metals, and Material Society and ASM International, Vol. 40A, pp. 2369-2376, 2009.

[47]. Yoon J.W., Noh B.I., and Jung S.B., "Mechanical reliability of Sn-Ag BGA solder joints with various electroless Ni-P and Ni-B plating layers," IEEE Transaction on Components and Packaging Technologies, Vol. 33, No. 1, pp. 222-228, 2010.

[48]. Salam B., Ekere N.N., and Rajkumar D., "Study of the interface microstructure of Sn-Ag-Cu lead-free solders and the effect of solder volume on the intermetallic layer formation," Electronic Components and Technology Conference, 2001, Proceedings., 51st, pp. 471-477, Orlando, FL, USA.

[49]. Made R.I., Gan C.L., Yan L.L., Yu A., Yoon S.W., Lau J.H., and Lee C., "Study of low-temperature thermo-compression bonding in Ag-In solder for packaging applications," Journal of Electronic Materials, Vol. 38, No. 2, pp. 365-371, 2009.

[50]. Arzt E., "Overview No. 130, Size effects in materials due to microstructural and dimensional constraints: a comparative review," Journal of Acta Materialia, Vol. 46, No. 16, pp. 5611-5626, 1998.

[51]. Anderson E.R. and Groza J.R., "Microstructural size effects in high-strength high-conductivity Cu-Cr-Nb alloys," Metallurgical and Materials Transactions A, Vol. 32A, pp. 1211-1224, 2001.

[52]. Keller C., Hug E., and Feaugas X., "Microstructural size effects on the mechanical properties of high purity nickel," International Journal of Plasticity, Vol. 27, pp. 635-654, 2011.

[53]. Geers M.G.D., Brekelmans W.A.M., and Janssen P.J.M., "Size effects in miniaturized polycrystalline FCC samples: strengthening versus weakening," International Journal of Solids and Structures, Vol. 43, pp. 7304-7321, 2006.

[54]. Simons G., Weippert Ch., Dual J., and Villain J., " Size effects in tensile testing of thin cold rolled and annealed Cu foils," Materials Science and Engineering A, Vol. 416, pp. 190-299, 2006.

[55]. Klein M., Hadrboletz A., Weiss B., and Khatibi G., "The size effect on the stress-strain, fatigue and fracture properties of thin metallic foils," Materials Science and Engineering A, Vol. 319, pp. 924-928, 2001.

[56]. Janssen P.J.M., Keijser Th.H.de., and Geers M.G.D., "An experimental assessment of grain size effects in the uniaxial straining of thin Al sheet with a few grains across the thickness," Materials Science and Engineering A, Vol. 419, pp. 238-248, 2006.

[57]. Lanssen P.J.M., Hoefnagels J.P.M., Keijser Th.H.de., and Geers M.G.D., "Processing induced size effects in plastic yielding upon miniaturization," Journal of the Mechanics and Physics of Solids, Vol. 56, pp. 1687-2706, 2008.

[58]. Benzerga A.A., Hong S.S., Kim K.S., Needleman A., and Giessen E.V.D., "Smaller is softer: an inverse size effect in a cast aluminum alloy," Journal of Acta Materialia, Vol. 49, pp. 3071-3083, 2001.

[59]. Sevillano J.G., Arizcorreta I.O., and Kubin L.P., "Intrinsic size effects in plasticity by dislocation glide," Materials Science and Engineering A, Vol. 309-310, pp. 393-405, 2001.

[60]. Zhao Y.H., Guo Y.A., Wei Q., Dangelewicz A.M., Xu C., Zhu Y.T., Langdon T.G., Zhou Y.Z., and Lavernia E.J., "Influence of specimen dimensions on the tensile behavior of ultrafine-grained Cu," Scripta Materialia, Vol. 59, pp. 627-630, 2008.

[61]. Lederer M., Groger V., Khatibi G., and Weiss B., "Size dependency of mechanical properties of high purity aluminum foils," Material Science and Engineering A Vol. 577, pp. 590-599, 2010.

[62]. Kang Y.L., Zhang Z.F., Wang H.W., and Qin Q.H., "Experimental investigations of the effect of thickness on fracture toughness of metallic foils," Materials Science and Engineering A, Vol. 394, pp. 312-319, 2005.

[63]. Venkatraman R and Bravman J, "Separation of film thickness and grain boundary strengthening effects in Al thin films on Si," Journal of Materials Research, Vol. 7, No. 8, pp. 2040-2049, 1992.

[64]. Weertman J.R., "Hall-Petch strengthening in nanocrystalline metals," Materials Science and Engineering A, Vol. 166, pp. 161-167, 1993.

[65]. Mann G., Griffiths L.R., and Caceres C.H., "Hall-Petch parameters in tension and compression in cast Mg-2Zn alloys," Journal of Alloys and Compounds, Vol. 378, pp. 188-191, 2004.

[66]. Keller C., and Hug E., "Hall-Petch behavior of Ni polycrystals with a few grains per thickness," Mterilas Letters, Vol. 62, pp. 1718-1720, 2008.

[67]. Sylwestrowicz W., and Hall E.O., "The deformation and aging of mild steel," Proceedings of the Physical Society. Section B, Vol. 64, No. 6, pp. 495-502, 1951.

[68]. Meyers M.A., and Chawla K.K., "Mechanical behavior of materials," Cambridge University Press 2009, p. 306.

[69]. Friedel L., Gennes P.G.De., and Matricon J., "Nature of the driving force in flux creep phenomena," Applied Physics Letters, Vol. 2, No. 6, pp. 119-121. 1963.

[70]. Fulop T., Brekelmans W.A.M., and Grees M.G.D., "Size effects from grain statistics in ultra-thin metal sheets," Journal of Materials Processing Technology, Vol. 174, pp. 233-238, 2006.

[71]. Han Ch-S., Hartmaier A., Gao H., and Huang Y., "Discrete dislocation dynamics simulations of surface induced size effects in plasticity," Materials Science and Engineering A, Vol. 415, pp. 225-233, 2006.

[72]. Henning M. and Vehoff H., "Statistical size effects based on grain size and texture in thin sheets," Materials Science and Engineering A, Vol. 452-453, pp. 602-613, 2007.

[73]. Bayley C.J., Brekelmans W.A.M., and Grees M.G.D., "A three-dimensional dislocation field crystal plasticity approach applied to miniaturized structures," Philosophical Magazine and Philosophical Letters, Vol. 87, No. 8-9, pp. 1361-1378, 2007.

[74]. Bernstein L., "Semiconductor joining by the solid-liquid-interdiffusion (SLID) process," Journal of the Electrochemical Society, Vol. 113, No. 12, 1966.

[75]. Bernstein L. and Batholomew H., "Application of solid-liquid interdiffusion (SLID) bonding in integrated-circuit fabrication," Transactions of the Metallurgical Society of AIME, Vol. 236, No. 3, pp. 405-412, 1966.

[76]. Bartels F. and Morris JR. J. W., "Intermetallic phase formation in thin solid-liquid diffusion couples," Journal of Electronic Materials, Vol. 23, No. 8, pp. 787-790, 1994.

[77]. Lee C.C. and Wanh C.Y., "A low temperature bonding process using deposited gold-tin composites," Journal of Thin Solid Films, Vol. 208, pp. 202-209, 1992.

[78]. Bader S., Gust W., and Hieber H., "Rapid formation of intermetallic compounds by interdiffusion in the Cu-Sn and Ni-Sn systems," Acta Materialia, Vol. 43, No. 1, pp. 329-337, 1995.

[79]. Lin J.C., Huang L.W., Jang G.Y., and Lee S.L., "Solid-liquid interdiffusion bonding between In-coated silver thick films," Journal of Thin Solid Films, Vol. 410, pp. 212-221, 2002.

[80]. Bosco N.S. and Zok F.W., "Strength of joints produced by transient liquid phase bonding in the Cu-Sn system," Acta Materialia, Vol. 53, pp. 2019-2027, 2005.

[81]. Bobzin K., Lugscheider E., Zhuang H., Ernst F., Bagcivan N., Maes M., Rosing J., Ferrara S., Erdle A., and Kramer A., "New soldering processes and solder systems for hybrid

microsystems: developments and applications," Microsystem Technology, Vol. 12, pp. 620-625, 2006.

[82]. Zou H.F. and Zhang Z.F., "Solid-liquid and liquid-state interfacial reactions between Sn-based solders and single crystal Ag substrate," Journal of Alloys and Compounds, Col. 469, pp. 207-214, 2009.

[83]. Li J.F., Agyakwa P.A., and Johnson C.M., "Interfacial reaction in Cu/Sn/Cu system during the transient liquid phase soldering process," Acta Materialia, Vol. 59, pp. 1198-1211, 2011.

[84]. Deng X., Chawla N., Chawla K.K., and Koopman M., "Deformation behavior of (Cu, Ag)-Sn intermetallics by nanoindentation," Acta Materialia, Vol. 52, pp. 4219-4303, 2004.

[85]. Li J.F., Mannan S.H., Clode M.P., Whalley D.C., and Hutt D.A., "Interfacial reaction between molten Sn-Bi-X solders and Cu substrates for liquid solder interconnects," Acta Materialia, Vol. 54, pp. 2907-2922, 2006.

[86]. Ladani L.J., Razmi J., and Bentley J., "Microstructural and mechanical strength of snag-based solid liquid inter-diffusion bonds for 3 dimensional integrated circuits," Journal of Thin Solid Films, Vol. 518, pp. 4948-4954, 2010.

[87]. Ladani L.J. and Razmi J., "Bonding strength and microstructure of SnAg-based solid liquid inter-diffusion bonds," Proceeding of the ASME 2009 International Engineering Congress and Exposition, IMCE2009, November 13-19, Lake Buena Vista, Florida, USA.

[88]. Islam M.N., Sharif A., and Chan Y.C., "Effect of volume in interfacial reaction between eutectic Sn-3.5%Ag-0.5%Cu solder and Cu metallization in microelectronic packaging," Journal of Electronic Materials, Vol. 34, No. 2, pp. 143-149, 2005.

[89]. Sharif A., Chan C., and Islam R.A., "Effect of volume in interfacial reaction between eutectic Sn-Pb solder and Cu metallization in microelectronic packaging," Journal of Material Science and Engineering, Vol.B106, pp. 120-125, 2004.

[90]. Huang Z., Conway P.P., Liu C., and Thomson R.C., "Effect of solder bump geometry on the microstructure of Sn-3.5%Ag on electroless nickel immersion gold during solder dipping," Journal of Materials Research Society, Vol. 20, No. 3, pp. 649-658, 2005.

[91]. Huanh Z., Conway P.P., Jung E., Thomson R.C., Liu C., Loeher T., and Minkus M., "Reliability issues in Pb-free solder joint miniaturization," Journal of Electronic Materials, Vol. 35, No. 9, pp. 1761-1772, 2006.

[92]. Ochoa F., Williams J.J., and Chawla N., "The effect of cooling rate on microstructure and mechanical behavior of Sn-3.5Ag solder," JOM-Journal of the minerals, metals and materials society, Vol. 55, No. 6, pp. 56-60, 2003.

[93]. Kim K.S., Huh S.H., and Suganuma K., "Effects of cooling speed on microstructure and tensile properties of Sn-Ag-Cu alloys," Material Science and Engineering, Vol. A333, pp. 106-114, 2002.

[94]. Huang Y.C., Wu K.S., and Chen S.W., "Size and substrate effects upon undercooling of Pb-free solder," Microsystems, Packaging, Assembly and Circuits Technology Conference, IMPACT 2009. 4th International, 21-23 Oct. 2009, pp. 662-665, Taipei, China, 2009.

[95]. Huang Y.C. and Chen S.W., "Co alloying and size effects on solidification and interfacial reactions in the Sn-Zn-(Co)/Cu couples," Journal of Materials Research, Vol. 25, No. 12, pp. 2430-2438, 2010.

[96]. Cugnoni J., Botsis J., Sivasubramanian V., and Rusch J.J., "Experimental and numerical studies on size and constraining effects in lead-free solder joints," Fatigue and Fracture of Engineering Materials and Structures, Vol. 30, No. 5, pp. 387-399, 2007.

[97]. Wu F., Wang B., Du B.B., and Wu Y., "Effect of stand-off height on microstructure and tensile strength of the Cu/Sn9Zn/Cu solder joint," Journal of Electronics Materials, Vol. 38, No. 6, pp. 860-865, 2009.

[98]. Zhang N., Shi Y., Xia Z., Lei Y., Guo F., and Li X., "Investigation on impact strength of the as-soldered Sn37PB and Sn3.8Ag0.7Cu solder joints," Journal of Materials Scieence: Materials for Electronics, Vol. 20, pp. 499-506, 2009.

[99]. Wiese S. and Wolter K.J., " Microstructure and creep behavior of eutectic SnAg and SnAgCu solders," Microelectronics Reliability, Vol. 44, pp. 1923-1931, 2004.

[100]. Wiese S., Roellig M., and Wolter K.J., "The effect of downscaling the dimensions of solder interconnects on their creep properties," Journal of Microelectronics Reliability, Vol. 48, pp. 843-850, 2008.

[101]. Shen Y.L., Chawla N., Ege E.S., and Deng X., "Deformation analysis of lap-shear testing of solder joints," Acta Materialia, Vol. 53, pp. 2633-2642, 2005.

[102]. Zimprich P., Saeed U., Weiss B., and Ipser H., "Constraining effects of lead-free solder joints during stress relaxation," Journal of Electronic Materials, Vol. 38, No. 3, pp. 392-399, 2009.

[103]. Cho M.G., Kang S.K., and Lee H.M., "Undercooling and microhardness of Pb-free solders on various under bump metallurgies," Journal of Materilas Research, Vol. 23, No. 4, pp. 1147-1154, 2008.

[104]. Castro W.B.de, Maia M.de.L, Kiminami C.S., and Bolfarini C., "Microstructure of undercooled Pb-Sn alloys," Materials Research, Vol. 4, No. 2, pp. 83-86, 2001.

[105]. Yang S., Rian Y., and Wang C., "Investigation on Sn grain number and crystal orientation in the Sn-Ag-Cu/Cu solder joints of different sizes," Journal of Materials Science: Materials for Electronics, Vol. 21, pp. 1174-1180, 2010.

[106]. Gong J., Liu C., Conway P.P., and Siberschmidt V.V., "Micromechanical modeling of SnAgCu solder joint under cyclic loading: Effect of grain orientation," Journal of Computational Materials Scienace, Vol. 39, pp. 187-197, 2007.

[107]. Bonda N.R. and Noyan I.C., "Deformation in-homogeneity and representative volume in Pb/Sn solder alloys," Metallurgical and Materials Transactions A, Vol. 23, No. 2, pp. 479-484, 1992.

[108]. Bonda N.R. and Noyan I.C., "Effect of the specimen size in predicting the mechanical properties of PbSn solder alloys," IEEE Transactions on Components, Packaging, and Manufacturing Technology-Part A, Vol. 19, No. 2, pp. 208-212, 1996.

[109]. Ranieri J.P., Lauten F.S., and Avery D.H., "Plastic constraint of large aspect ratio solder joints," Journal of Electronic Materials, Vol. 24, No. 10, pp. 1419-1428, 1995.

[110]. Yin L.M., Zhang X.P., and Lu C., "Size and volume effects on the strength of microscale lead-free solder joints," Journal of Electronic Materials, Vol. 38, No. 10, pp. 2179-2183, 2009.

[111]. Li B., Tin L., Yang Y., and Zhang X., "FE simulation of size effects on interface fracture characteristics of micro scale lead-free solder interconnects," International Conference on Electronic Packaging Technology & High Density Packaging (ICEPT-HDP), pp. 242 – 247, 10-13 Aug. 2009, Beijing, China.

[112]. Lee W.W., Nguyen L.T., and Selvaduray G.S., "Solder joint fatigue models: review and applicability to chip scale packages," Microelectronics Reliability, Vol. 40, No. 2, pp. 231-244, 2000.

[113]. Shang J.K., Zeng Q.L., Zhang L., and Zhu Q.S., "Mechanical fatigue of Sn-rich Pb-free solder alloys," Journal of Materials Science: Materials in Electronics, Vol. 18, No. 1-3, pp. 211-227, 2007.

[114]. Song, F., Lee, S. W. R., Newman, K., Sykes, B., and Clark, S., "Brittle Failure Mechanisms of SnAgCu and SnPb Solder Balls during High Speed Ball Shear and Cold Balls Pull Tests," Electronic Components and Technology Conference, Reno, NV, pp. 364-372, June 2007.

[115]. Sohn, Y. Ch., Yn, J., "Correlation between chemical reaction and brittle fracture found in electroless Ni(P)/ immersion gold-solder interconnection," Journal of Materials Research, Vol. 20, No. 8, pp. 1931-1934, 2005.

[116]. Anderson, T.L., "Fracture Mechanics: Fundamentals and Applications, "CRC Press, Boca Raton, 2005.

[117]. Vallin, Ö., Jonsson, K., and Lindberg, U., "Adhesion Quantification Methods for Wafer Bonding," Materials Science and Engineering: R: Reports, Vol. R50, No. 4-5, pp. 109–165, 2005.

[118]. Tsau, Ch. H., Spearing, S. M., and Schmidt, M. A., "Fabrication of Wafer-Level Thermo-Compression Bonds," Journal of Micro-electro-mechanical Systems, Vol. 11, No. 6, pp. 641-647, 2002.

[119]. Timoshenko, S., "Analysis of Bi-Metal Thermo-sets," Journal of Optical Society of America A, Vol.11, No. 3, pp. 233-255, 1925.

[120]. Suhir, E., "Stresses in Bi-material Thermostats," Journal of Applied Mechanics. Vol. 53, No. 3, pp. 657-660, 1986.

[121]. Suhir, E., "Analysis of Interfacial Thermal Stresses in a tri-material assembly". Journal of Applied physics. Vol. 89, No. 7, pp. 3685-3694, 2001.

[122]. Ru, C. Q., "Interfacial Thermal Stresses in Bi-material Elastic Beams: Modified Beam Models Revisited," Journal of Electric Packaging, Vol. 124, No. 3, pp. 141-146, 2002.

[123]. Chen, W. T., and Nelson, C. W., "Thermal stresses in Bonded Joints," IBM Journal of Research and Development, Vol. 23, No. 2, pp.179-188, 1979.

[124]. Mirman, I. B., "Effects of Peeling Stresses in Bi-material Assembly," Journal of Electronic Packaging, Vol. 113, No. 4, pp. 431-433, 1991.

[125]. Ghorbani, H. R., and Spelt, J. K., "Interfacial Thermal Stresses in Solder Joints of Leadless Chip Resistors," Journal of Microelectronics and Reliability, Vol. 46, Nos. 5-6, pp. 873-884, 2006.

[126]. Pao, Y. H., and Eisele, E., "Interfacial Shear and Peel Stresses in Multilayered Thin Stacks Subjected to Uniform Thermal Loading," Journal of Electronic Packaging, Vol. 113, No. 2, pp. 164-172, 1991.

[127]. Suhir, E., "Interfacial Stresses in Bi-material Thermostats," Journal of Applied Mechanics, Vol. 56, No. 3, pp. 595-600, 1989.

[128]. Suhir, E., "Predicted Thermal Stresses in a Bi-material assembly Adhesively Bonded at The Ends," Journal of Applied physics, Vol. 89, No. 1, pp. 120-129, 2001.

[129]. Suhir, E., and Vujosevic, M., "Interfacial Stresses in a Bi-material Assembly with a Compliant Bonding Layer," Journal of Physics D: Applied Physics, Vol. 41, pp. 1-9, 2008.

[130]. Taljsten, B. "Strengthening of Beams by Plate Bonding," Journal of Material in Civil Engineering, ASCE Vol. 9, No. 4, pp. 206-212, 1997.

[131]. Smith, S. T., and Teng, J. G., "Interfacial Stresses in Plated Beams," Engineering Structure, Vol. 23, No. 7, pp. 857-871, 2001.

[132]. Abdelouahed, T., "Improved Theoretical Solution for Interfacial Stresses in Concrete Beams Strengthened with FRP Plate," International Journal of Solids and Structures, Vol. 43, Nos. 14-15, pp. 4154-4174, 2006.

[133]. Abdelouahed, Daouadji, Benyoucef, and Addabedia, "Interfacial Stresses in FRP-Plated RC Beams: Effect of Adherend," International Journal of Adhesion and Adhesives, Vol. 29, No. 4, pp. 343-351, 2009.

[134]. Yin L.M., Zhang X.P., and Lu Ch., "Size and volume effects on the strength of micro scale lead-free solder joints," Journal of Electronic Materials, Vol. 38, No. 10, pp. 2179-2183, 2009.

[135]. Zimprich P., Kotas A., Khatibi G., Weiss B., and Ipser H., "Size effects in small scaled lead-free solder joints," Journal of Materials Science: Materials in Electronics, Vol. 19, pp. 383-388, 2008.

[136]. Zimprich P., Saeed U., Betzwar-Kotas A., Weiss B., and Ipser H., "Mechanical size effects in Miniaturized lead-free solder joints," Journal of Electronic Materials, Vol. 37, No. 1, pp. 102-109, 2007.